THE UNIVERSITY *of* EDINBURGH

A multi-scale analysis of the influence of particle shape on the mechanical response of granular materials

Behzad Soltanbeigi

THE UNIVERSITY *of* EDINBURGH

This dissertation is submitted for the degree of
Doctor of Philosophy

School of Engineering
Institute for Infrastructure and Environment

2018

Declaration of authorship

This thesis entitled, "*A multi-scale analysis of the influence of particle shape on the mechanical response of granular materials*" is submitted to the University of Edinburgh for the degree of Doctor of Philosophy. The research work described and reported in this thesis has been completed solely by Behzad Soltanbeigi under the supervision of Dr. Stefanos-Aldo Papanicolopulos and Prof. Jin Y. Ooi.

Hereby, I confirm that:

- Where I have consulted the published work of others, this is always clearly attributed.
- Where I have quoted from the work of others, the source is given.
- I have acknowledged all main sources of help.
- Where the thesis is based on work done by myself jointly with others, I have made clear exactly what was done by others and what I have contributed myself. This applies in the area of simulating superquadric shape particles in Chapters 4 and 5, and simulating EPSD rolling resistance model in Chapter 5, where work has been carried out jointly with Dr. Alexander Podlozhnyuk.

Journal papers, peer reviewed conference papers and extended abstracts:

- Soltanbeigi, B., Podlozhnyuk, A., Papanicolopulos, S.A., Kloss, C., Pirker, S. and Ooi, J.Y., 2018. "DEM study of mechanical characteristics of multi-spherical and superquadric particles at micro and macro scales." *Powder Technology*, 329, pp.288-303.
- Soltanbeigi, B., Podlozhnyuk A., Ooi, J.Y., Kloss, C., and Papanicolopulos, S.A., 2017. "Comparison of multi-sphere and superquadric particle representation for modelling shearing and flow characteristics of granular assemblies."*European Physical Journal Web of Conferences*, 140, 06015.

- Podlozhnyuk, A., Soltanbeigi, B., Papanicolopulos, S.A., Kloss, C., Pirker, S. and Ooi, J.Y., "Characteristics of different particle shape descriptors in predicting avalanching, packing and shearing response of granular material", *To be submitted for Granular Matter*.

- Soltanbeigi, B., Papanicolopulos, S.A. and Ooi, J.Y., "A study on influence of different rolling resistance models on packing and discharge of spherical particles in a flat-bottom silo", *To be submitted for review*.

- Soltanbeigi, B., Papanicolopulos, S.A., Zetzener, H., Ooi, J.Y. and Kwade, A., "Experimental study of particle shape effect on flow characteristics of granular materials" *1st International Conference of the Greek Society of Experimental Mechanics of Materials*, Athens, Greece, May 2018.

- Soltanbeigi, B., Papanicolopulos, S.A. and Ooi, J.Y., "Particle shape effect on deformation localization during quasi-static flow at active state" *5th International conferences on Geotechnical Engineering and soil mechanics*, Tehran, Iran, November 2016.

Conference presentations:

- Soltanbeigi, B., Weinhart, T., Papanicolopulos, S.A., Luding, S., and Ooi, J.Y., "Flowing characteristics of spherical particles with restrained rotation" Conference on Computational Solid and Structural Mechanics, Glasgow, UK, June 2018.

- Soltanbeigi, B., Podlozhnyuk, A., Papanicolopulos, S.A., Kloss, C. and Ooi, J.Y., "Influence of blockiness and bumpiness on modelling dense granular flows of non-spherical particles", *Particles conference*, Hannover, Germany, September 2017.

- Soltanbeigi, B., Papanicolopulos, S.A. and Ooi, J.Y. An exploration of the micromechanism of the directional constant torque rolling friction model in quasi-static flow. *CFDEM®project user meeting workshop*, Linz, Austria, March 2016.

- Soltanbeigi, B., Papanicolopulos, S.A. and Ooi, J.Y. DEM investigation of flow in silos: the effect of particle shape and rolling resistance. *Particles conference*, Barcelona, Spain, October 2015.

Signed:

_____

Date:

_____

Acknowledgements

" This is to remind myself that I'll be indebted to my colleagues, friends and FAMILY for all my success."
'Behzad Soltanbeigi, September 2018'

I greatly appreciate my supervisors *Dr. Stefanos-A. Papanicolopulos* and *Prof. Jin Y. Ooi*, as this thesis work would not have been possible without their skilfulness, profound knowledge, constructive discussions and most importantly endless patience. I bothered them with all means of communication when I was in Germany, loads of e-mails, teleconferences and video-calls. Stefanos even devoted his time during holidays to guide me through different milestones, for which I would always be grateful.

This thesis has been carried out as a part of the *T-MAPPP* project, an EU-funded FP7 Marie Curie Initial Training Network under grant agreement no. ITN 607453. The financial support provided by the European Commission is gratefully acknowledged.

Profound gratitude goes to *Prof. Arno Kwade* and *Dr. Harald Zetzener*. They hosted me at the Institute for Particle Technology (Braunschweig, Germany) at the third year of my PhD. In addition to their invaluable academic support, they bestowed me the state-of-the-art experimental facilities at TU Braunschweig. Our collaboration did not end at the final point of the *T-MAPPP* project and I was lucky to be offered an extra year to pursue my research at their institute.

A remarkable point during my PhD was the collaboration that I had with *Dr. Alexander Podlozhnyuk*. Alexander, as the ESR, worked at DCS Computing GmbH (Linz, Austria). Our collaboration led to a more productive PhD research, which has been disseminated in conferences and journal publications. Alexander was not only a wonderful colleague, but also a decent and sympathetic friend, who was always there for moral support. I was fortunate to have many useful discussions and comments from *Dr. Christoph Kloss* (DCS) and *Prof. Stefan Pirker* (Johannes Kepler University, Linz, Austria).

One of my secondments took place at *University of Twente*, where I had the golden opportunity to collaborate with *Prof. Stefan Luding*, *Dr. Vanessa Magnanimo* and *Dr. Thomas Weinhart*. Their supports during my project is greatly acknowledged. Specifi-

cally, thanks to Vanessa, who was our Senior Training Mentor during *T-MAPPP* project and her great efforts provided all ESRs and ERs with outstanding training events.

T-MAPPP was definitely a high quality research platform for me. In addition, I got to know many cool folks and we had many encouraging discussions during our regular project meetings and conferences. I remember all those joyful moments that we spent together in the evenings after the presentations and discussions were over. Thanks *Ahmad, Hao, Giuseppe, Ilaria, Kostas, Nikoletta, Rahul, Ramon, Tim, Tomaz, Xizhong* and *Yuosef*. However, Among all, I want to highlight the positive influence of these guys on my professional and personal life: *Alexander, Behrad, Kianoosh, Rohit* and *Somik*. They were colleagues, friends and I reckon we ended up with a brotherhood.

Many thanks to *Dr. Alvaro Janda* and *Dr. Carlos Labra* from *Particle Analytics Ltd* who supported me with using *P4* post-processing tool.

I am thankful to all my colleagues at University of Edinburgh (IIE), who made it easier for me to handle the stressful days. I have been blessed with their friendship: *Dhiraj, Fahad, Gelly, Konstantina, Lige, Payam, Pratap, Sina, Utibe, Zeynep*. Additionally, assistance and friendship received from *Dr. John P. Morrissey* was invaluable and greatly appreciated.

I am filled with gratitude to all my colleagues at iPAT. Many names come to my mind: *Alexander, Ann-kathrin, Benedikt, Bilal, Cedric, Didem, Victor, Ajmal, Matthaus, Paul, Reza (I) - Reza (II), Steffen, Tobias* and many more. Great support from workshop by *Detlev Hille and Uwe Stüwe* is appreciated. I am many thankful to our student assistants *Selin Altın* and *Ksenia Ragozina*.

I must mention also my friends from IDCOM, whom were probably equal in number to my friends from IIE. We had great times together on weekends when we were only guys in the institute and also during launch breaks for almost two years, thanks guys: *Alessandro, Hossein - Elham, Iman - Mahdiye, Kim, Mehdi, Mehrdad, Tezcan, Yuki*. I greatly appreciate friendship and accompany from *Mohammad* and *Hamed*, who were house-mates, colleague and kind code debuggers.

Thanks to our Research Support Officers *Nicola McRobbie*. Without her supports I would not be able to deal with all those visa issues and other administrative chores.

Many thanks to my colleagues and friends at Boğaziçi University (Istanbul, Turkey) for their lifelong support. Thanks to *Dr. Çinicioğlu, Dr. Altunbaş, Ahmet* and *Emirhan*.

Last but not the least, with all my heart and soul I thank my family, *Ali, Behnaz* and *Sara*. I am sure this journey would not have been possible without your immense supports. I also send my regards to soul of my two grandfathers and one of my grandmothers and my cousin *Vahid*.

Abstract

Particle-scale characteristics govern the behaviour of particulate materials at the macro-scale. An important factor that dominates the interaction of individual particles is shape, which generates particle interlocking. The resulting geometric interlocking affects the contact force network and the particle motion which lead to change in rheology, as well as stress distribution in the granular system. Accordingly, both numerical, by means of Discrete Element Modelling (DEM) simulations, and experimental, by use of direct shear and silo discharge tests, approaches are considered to determine the influence of particle shape on the mechanical response of granular assemblies at the micro- and macro-scales.

The Discrete Element Modelling (DEM) has been utilized to track the interaction of particles and obtain particle-scale information. In DEM simulations, shape factor is addressed through multiple approaches, but most of the studies use spherical particles due to the simplicity of contact detection algorithm resulting in faster simulation times. However, the lack of interlocking in spheres necessitates the need to better capture the shape effect. This is usually done by applying a rotational constraint at contacts, which is referred to as a rolling resistance model. The first part of this study investigates the influence of such implementations, through considering two different rolling resistance models, on the flow characteristics of spherical particles in a silo. Using a coarse-graining technique, the particle-scale DEM data was converted to continuum fields, which allowed a better understanding of stress and density distribution. It is seen that the flow profiles, packing density and stress distribution are highly dependent on the applied rolling resistance. Morevover, the possibility of obtaining comparable bulk response through both models is investigated. Accordingly, a procedure has been suggested to compensate for the differences in the calculation of torque for the two models using a proposed dimensionless parameter.

Meanwhile, there exist other approaches which try to simulate the most representative shape by allowing to adjust surface or edge properties and also aspect ratio of a particle. Two of the most widely used approaches, namely ‘Multi-spheres’ and ‘Superquadrics’, are employed here and the influence of changing particle surface and edge complexities on the micro- and macro- scale response is assessed for the two

cases: direct shear test and silo flow. For direct shear test, the density of the sample determines the level of change in bulk response due to the shape factor. In the case of silo flow, beyond a certain level of shape complexity, the edge and surface properties show no significant influence on the material flow. The comparison between the two methods of shape description provides useful insights into the particle shape effect during shearing and flow.

Additionally, it is not yet fully known whether introducing a rolling resistance in spherical particle contacts can adequately capture the granular friction in non-spherical particles. In this respect, the response of spherical particles with restricted rotational freedom is compared to the particles simulated using the multi-sphere and superquadric approaches. The results indicate that certain characteristics of the particles with complex shapes can be replicated with spherical particles, such as: angle of repose (AoR), dilative behaviour and shear strength (only with the Elastic-Plastic Spring-Dashpot model).

Lastly, in order to validate the numerical observations, experiments were performed including angle of repose, Jenike shear and silo discharge (at 1g and also different accelerations with flat-bottom and wedge shape hopper). Additionally, the validity of Beverloo's assumption for predicting the mass flow rate and velocity profiles inside the silo (at higher accelerations) is analysed in detail (Beverloo suggests that the mass flow rate at increased acceleration is proportional to the square root of the gravity). The results from AoR, Jenike and 1g silo discharge showed a great dependency on the particle shape factor. Comparing the mass flow rate at 1g with those of at different gravitational accelerations (in normalized form) suggest the validity of Beverloo's approach only in case of spherical particles. Additionally, analysis of the normalized velocity of the particles shows that while the mass flow region for the spherical particles follows Beverloo's assumption, the region near the outlet diverges to some extent. Furthermore, particles with shape irregularity show different flow profiles in presence of high gravitational forces compared to those of the 1g case.

In summary, this thesis presents an extensive investigation of the particle shape parameter on DEM simulation of granular assemblies. On the numerical side, the influence of different rolling resistance models on the interaction of the spherical particles is clarified. Moreover, the effect of the particle surface and edge characteristics of multi-sphere and superquadrics shapes is quantified at both micro and macro-scales. The comparison of the three shape descriptors suggests that spherical particles together with rolling resistance can mimic several key mechanical properties of complex shape particles. Finally, the experimental observations have provided further insights into the particle flow at different gravitational stress states. Results suggest that it is yet challenging to predict the flow profiles of the discharging granular material with complex shapes, at different gravitational levels.

Lay Summary

Granular materials exist in large quantity in nature and it is estimated that over 75% of all raw materials in the industry are in granular form. Although individual grains are solid in nature, granular materials behave differently in various circumstances and are often considered as a new state of matter with properties of solids, liquids and gases. These materials are present in a wide range of usage such as pharmaceutical powders, agricultural products, sands and gravels, and chemical pellets. Despite their prevalence in the majority of industrial applications, there is still a large discrepancy between the results predicted by analytical or numerical solutions and the real granular material behaviour. The lack of knowledge on estimation of the granular material response can lead to the inefficient design of operations, increasing the risk of material handling issues and wastage of materials, which ultimately increase industrial downtime and financial loses.

Thus, the principal aim of this Ph.D. study is to characterize the flow properties of granular materials to develop an understanding of the material behaviour that can lead to improved efficiencies of bulk material handling processes. Among the many physical properties of individual particles in particulate materials, the particle shape plays an important role in the shear strength and flowability of the bulk material. Accordingly, this project has incorporated results from a numerical solution, which simulates interaction of individual particles, and also advanced experimental tools to provide a clear explanation on influence of particle shape parameter on overall response of granular material.

In summary, the thesis presents an extensive investigation on various aspects of particle shape effect on mechanical response of the granular material. As a result, it will help other researchers to consider the appropriate approach for considering shape parameter in their numerical simulations. Furthermore, the experimental observations will provide an outline over the predictability of the flow for granular materials.

Table of contents

List of figures

List of tables

Abbreviations

AoR	Angle of Repose
AR	Aspect Ratio
CDT	Constant Directional Torque
CG	Coarse Graining
CN	Coordination Number
DCC	Direct Cross Correlation
DEM	Discrete Element Method
EDIP	Equally Dense Initial Packing
EPSD	Elastic-Plastic Spring Dash-pot
FEM	Finite Element Method
DDT	Fast Fourier transform
MS	Multi-sphere particles
PIV	Particle Image Velocimetry
RoI	Region of Interest
SQ	Superquadric Particles

Symbols

A	Area
A_0	Mechanical Work by Friction Force
b	Width of Outlet
C	Beverloo's constant
C_T	Total Computational Time
D	Shear Cell Displacement
D_o	Outlet Diameter
D_L	Lid Vertical Displacement
d	Particle Diameter
e	Void Ratio
e_P	Coefficient of Restitution
ff_c	Flowability Function
F_d	Dynamic Coulomb Friction
F_D	Dissipative Force
f_i	Contact Force
F_s	Coulomb Friction
g	Earth Gravity
G_P	Shear Modulus
H	Sample Height
I_i	Moment of Inertia
k	Beverloo's Coefficient
k_c	Correction Factor
K_0	At Rest Lateral Stress Ratio
K_f	Modified Lateral Stress Ratio
K_n	Normal Stiffness
K_R	Total Rotational Kinetic Energy
L	Length of Outlet
l_i	Branch Vector
m_i	Particle Mass
M_D	Mass Discharged

N	Blockiness Parameter
N_C	Number of contacts
N_P	Number of Particles
r_i	Particle radius
R^*	Equivalent Radius
S_i	Cross-sectional Area
S_n	Normal Stiffness
S_T	Total Simulation Time with Perfect Spheres
t	Time
T_i	Torque
V	Velocity
V_t	Tangential Velocity
V_T	Total volume
V_S	Volume of Solids
V_V	Volume of Voids
V_W	Velocity Function
W	Mass Flow Rate
w	Spatial Averaging Scale
x_i	Particle Position
$\boldsymbol{X}_{Ck}$	Centre of Mass
α_1	Sliding Angle
β	Damping Coefficient
δ	Shape Parameter
δ_n	Normal Overlap Distance
ΔT	Temporal Averaging Scale
Δt	Time-step
Δx	Displacement
$\boldsymbol{\delta}_n$	Normal Overlap Vector
θ	Angle of Conical Hopper
$\boldsymbol{\theta}_i$	Cumulative Rotation
θ_i	Cumulative Rotation Magnitude
κ	Strength Parameter
μ	Friction Coefficient
μ_r	Rolling Friction Coefficient
μ^s_{pp}	Particle-Particle Friction Coefficient
μ^s_{pw}	Particle-Wall Friction Coefficient
$\nu_{(P)}$	Poisson's Ratio
ρ_{bulk}	Bulk Density
ρ_p	Particle Density

σ_1	Major Principal Stress
σ_c	Unconfined Yield Stress
σ_v	Normal Consolidation Stress
σ_{xx}	Horizontal Stress
σ_{zz}	Vertical Stress
τ	Shear Stress
ϕ	Porosity
ϕ_{init}	Initial Porosity
ϕ_{end}	Final Porosity
ϕ_s	Solid Fraction
Φ_p	Peak Friction Angle
ψ_i	Angle of Internal Friction
ω_i	Rotational Velocity

Chapter 1

Introduction

Granular materials are one of the most ubiquitous media on the earth. This type of material can act as solid and carry large loads (e.g. soil under a foundation), or flow as a liquid (e.g. during landslides) and as a gas (e.g. inside is fluidized bed), see Jaeger et al. (1996). The variety in the response of these materials, which is sensitive to many different conditions, makes it difficult to have a single solution for predicting their behaviour.

Handling granular material is of great importance, since nearly 75% of the raw materials in industries are particulate in nature (Nedderman, 1992). Accordingly, numerous industrial applications, such as: pharmaceutical, food, chemical and mining are dealing with granular materials to a very large extent. Each of these applications treats bulk solids in a different way, for instance: in pharmaceutical processes, the compaction of powders, which makes the final tablet, is of great importance or in case of mining, being able to efficiently crush the raw material is crucial.

Additionally, a safe and efficient storage process is very important for granular materials (safe is referring here to structural endurance of the handling infrastructures, whereas efficient is pointing to the continuous flow of the stored material, without any clogging). Silos (also referred as bunkers, bins and hoppers) are the large containers that are used for storing purposes. These structures are usually in cylindrical shape, filled from top and have an opening in the bottom for discharge. Each silo must be designed according to the specific bulk solid that will be ensiled, otherwise the discharge of stored material will face severe problems.

Despite extensive studies that have been conducted to optimise silo structures, the number of failures for these structure are much higher than for any other industry-related infrastructures (Dogangun et al., 2009; Ravenet, 1981; Tejchman, 2013). Most failures are due to lack of knowledge regarding the dynamic phenomena that occurs during the discharge process. Main reasons for silo failure are listed by Tejchman (2013) as: non-symmetric wall pressures, earthquakes, wind loads, stresses induced

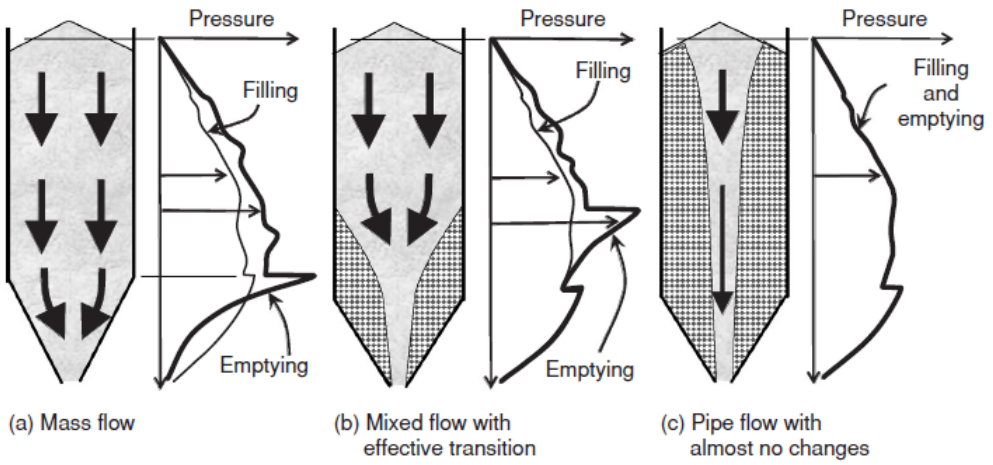

Figure 1.1 Dependency of the wall pressure on the flow characteristics of the granular media (Rotter, 2008).

from difference in temperature between stored material and silo walls, possible explosion (resulted from chemical reactions), failure in bearing capacity of the foundation or the support columns. Accordingly, it can be concluded that it is essential to characterize the effects of both material properties and boundary conditions.

The flow of the particulate materials in silos is categorized into two main types: mass flow and funnel flow (called as mixed flow and pipe flow also), see Figure 1.1. In case of mass flow, the whole material moves down the barrel section of the silo with an equal average velocity. In this type of flow the grains are discharged with respect to their elevation in the silo (i.e. first-in and first-out type). This type of flow is provided in silos with smooth and steep hoppers and relatively large outlet diameters. Most of industries prefer this kind of silos, since they can overcome difficulties regarding segregation, flooding, hang-ups, caking and formation of stagnant regions (these problems are common with funnel flow silos). The major draw-back for mass flow silos is the requirement of steeper angles for the hopper walls, which leads to taller silo walls. Additionally, thicker silo walls might be required, due to dynamic loads that are created by continuous discharge of material Wójcik et al. (2012).

Various experimental approaches have been employed to better understand the flow kinematics inside a silo, such as: coloured sand layer (Nedderman and Laohakul, 1980; Tejchman and Gudehus, 2000), x-rays (Babout et al., 2013; Baxter et al., 1990; Drescher, 1992; Drescher et al., 1978; Maiti et al., 2016),stereo-photogrammetry (Drescher, 1998), electrical capacitance tomography (Niedostatkiewicz et al., 2009, 2010), X-ray tomography (Grudzień et al., 2011) and particle image velocimetry (Ostendorf and Schwedes, 2005).

Numerical approaches, on the other hand, are extensively used for identifying the influential factors on macro-scale response of granular material. A general recommen-

dation in the literature is to use continuum approach to study the slow (quasi-static) flow, whereas for rapid or dynamic flow, use of discrete methods are more beneficial (Tejchman, 2013). The important advantages of continuum approaches are the applicability of simulating large systems and the possibility of feeding material constants in the models (which can be calibrated by standard tests), see (Tejchman, 2008; Tejchman and Wu, 2009). Finite element method (FEM), as a continuum approach, is a powerful tool for obtaining real loads inside and on silo walls, see (Chen et al., 2001; Holst et al., 1999; Ooi and Rotter, 1990, 1991; Sanad et al., 2001; Wang et al., 2014; Yang et al., 2011).

Additionally, the improvements in computational power has increased the popularity of DEM (Cundall and Strack, 1979). This powerful numerical tool is capable of modelling complicated particulate systems with arbitrary boundary effects. In DEM, the particulate material is treated as an assembly of distinct interacting granules. Correspondingly, the position, velocity and contact forces for each particle are tracked in fractions of a second. Further explanation and formulation of this approach is presented in Section 2.2.

The main intention of this thesis is to investigate the importance of the shape factor in the micro- and macro-scale response of particulate materials. A major part of the study includes numerical simulation of different shape particles by means of DEM. The shape representation techniques that are used include spheres (with/without presence of rolling resistance), multi-spheres and superquadrics. In this thesis a comprehensive sensitivity analysis on the discharge process of spherical particles, in the presence of rolling resistance, have been performed. The results clearly contribute to a deep understanding of the macro-scale characteristics of the spherical particles. Moreover, mechanical characteristics of complex shape particles are assessed for multi-spheres and superquadrics. The performed tests at multi-scale, greatly informs the current understandings regarding the effect of considering shape complexities by means of surface bumpiness and edge blockiness. Moreover, comparing the bulk response of complex shape particles with those of spherical particles (with constrained rotation) has provided a clear answer towards possibility of using such artificial shape representations (i.e. rolling resistance models) to predict the realistic macro-scale response for granular materials. On the experimental side of the study, the great dependence of flowing and shearing characteristics on the shape factor has been verified. Finally, simulating realistic stress states (with a silo centrifuge), the predictability of flow under higher gravitational accelerations is assessed for the ensiled granular assemblies.

1.1 Objectives and motivation

The predictability of bulk response in granular materials is essential for a safe and optimised design. Particle shape is an important factor that can highly influence the behaviour of the single particles in contact-level and accordingly, affect the macro-scale characteristics. Namely, irregular shapes result in geometric interlocking between particles, which hinders the motion of the particles and this led to change in rheology of the granular assemblies. Our aim is to investigate the influence of shape parameter in different scales to construct frameworks for understanding the behaviour of granular materials. Given that, granular material can be exposed to different loading and shearing scenarios, while having various density states (dilute to dense), which might affect the degree of sensitivity to micro-scale parameters. Accordingly, the main aim of this research is to evaluate the importance of the shape parameter in different testing conditions.

In DEM simulations, shape complexity can be addressed through various techniques. The utilized methods are spherical (with and without rolling resistance), multi-spherical and superquadrics, which have their own unique way of including shape complexity. Accordingly, other main objective in this thesis is to determine the mechanical characteristics of each approach, at different level of complexity, in single-particle and bulk-level conditions. It is also of high interest to evaluate the capability of the simplest approach (spherical particles with constrained rotation) to mimic the behaviour of more complex techniques (i.e. multi-spheres and superquadrics).

Additionally, an experimental study is conducted to evaluate the influence of shape parameter in real testing conditions. In this context, it is essential to clarify the influence of shape parameter on avalanching, shearing and flowing characteristics of granular assemblies. Additionally, stress state, as an important boundary condition, can drastically affect the bulk response in particulate systems. Particularly, in silo discharge process, our observations might be severely influenced by the boundary effects, since real-scale silos store thousands of tons of materials, while in laboratory we are considering a tiny fraction of this amount. To this end, using a silo centrifuge device, the presence of real stress states is facilitated in a small-scale model silo. Subsequently, running silo discharge tests at various gravitational accelerations, the predictability of the flow characteristics is assessed and compared to the well-known Beverloo's empirical approach.

1.2 Thesis Structure

A brief outline of the thesis is presented here:

Chapter 1: An introduction is given about necessities of characterizing granular materials in many multi-disciplinary applications. Additionally, the motivations behind this study are stated as well. A brief description of each chapter is also mentioned.

Chapter 2: The common experimental methodologies for characterizing the granular materials are presented. The background of DEM simulation and its formulation is briefly described. DEM input parameters are defined and the methods to obtain these parameters are discussed.

Chapter 3: The mechanisms by which two rolling resistance models control the rotational freedom of the spherical particles are discussed. Moreover, the influences of considering rolling resistance at contacts is studied at grain-level and bulk-scale. The possibility of obtaining similar bulk response from both models is evaluated by means of tuning rolling friction coefficient. Finally, dependence of discharge characteristics on the initial packing is studied.

Chapter 4: Two different approaches are considered two address the shape parameters in DEM analyses of granular materials. The influences of surface bumpiness, in multi-spheres, and corner sharpness, in superquadrics, are investigated in multi-scale. The assessments are clarifying the importance of shape factor during single particle contact, avalanching, shearing and flowing of granular assemblies.

Chapter 5: The bulk response of three rolling resistance models are compared with those of complex shape particles to evaluate the capability of these models in addressing shape parameters. Cubical and cylindrical shapes are simulated by means of superquadrics and multi-spheres. Another level of shape complexity is considered by increasing aspect ratio of the particles. The bulk responses are evaluated through heap formation, porosity, dilative behaviour and shear strength of the samples.

Chapter 6: In this chapter, the importance of the shape parameter is evaluated through experimental studies. The influence of particle shape is investigated in angle of repose, Jenike shear test and 1g silo discharge. Additionally, response of ensiled granular material in presence of higher stress state is evaluated in a silo centrifuge device. The observations are compared to those of empirical approaches that are available in the literature. DEM analyses are also conducted, by simulating the silo centrifuge, to study the problem in micro-scale.

Chapter 7: An overview of the conducted study is given. The conclusions drawn from each chapter are summarized. Recommendations and future studies are presented.

Chapter 2

State of the art

Majority of the raw materials that is used in many different industries, and also part of the final products, are known to have granular structure. A granular material is composed of solid individual particulates that can either make a stable heap or flow as a liquid. Interaction of the single particles in micro-scale and their response as an assembly in macro-scale have been studied for many decades. There are many disciplines that are encountered in the study of this field, such as: Geotechnical, Chemical and Process Engineering and some fundamental studies in applied Physics and Mathematics. The mutual goal of these studies is to determine the dependency of the bulk response on various influencing factors (i.e. particle-scale properties and/or boundary conditions). Additionally, further attempts have been carried out to evaluate the predictability of the bulk solid response based on micro-scale characteristics of a granular assembly. The particle-scale studies are usually conducted by considering factors such as: size, shape and cohesion, while studies that are conducted over importance of boundary conditions consider factors such as geometry, stress path, heat and vibration.

This chapter will go through the methods that are used for characterising the particulate materials by means of experimental and numerical approaches.

2.1 Experimental study of granular materials

Granular materials have different micro-scale characteristics that influences certain bulk properties of the assembly, which can affect handling and storage processes. A useful explanation is provided by StanleyWood (2008), regarding particle-scale features that influence properties of the bulk solids, as shown in Figure 2.1.

There are several important factors, which are essential to characterise a certain type of granular material, namely: packing density, flow rate and flowability. The definition of each factor and the methodology to obtain the representative parameters is discussed hereafter.

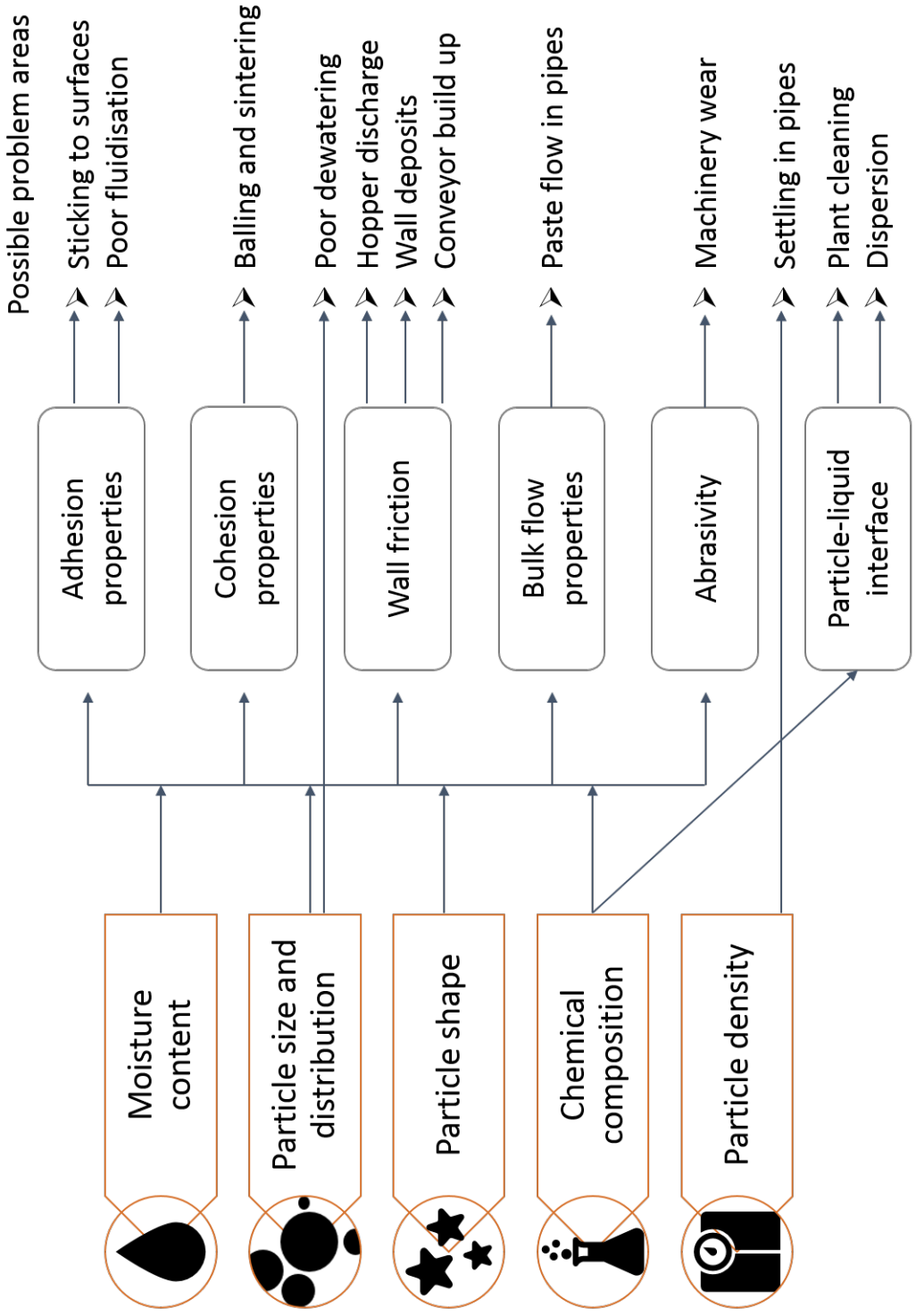

Figure 2.1 Micro-scale features that influence the properties of granular assemblies and the respective possible problem areas (StanleyWood, 2008).

2.1.1 Packing density

Ratio of the solids in a granular system to bulk volume of the specimen is known as packing/bulk density. There are various standards for performing this test, however the most general approach is: using a funnel which has a tap or stop (to control the initiation of the outflow), a container with known volume is filled. Height of the container is usually considered to be 2 times the diameter. A sensitivity test must be carried out to determine the effect of pouring height on the measured mass (pouring height affects the compaction of the bulk solid).

There are several other parameters for quantifying density state for a powder or soil sample which are defined as following:

Void ratio

Mostly used in soil mechanics field, void ratio is defined as the volume of the voids (V_V) over the volume of the solids (V_S):

$$e = \frac{V_V}{V_S} \tag{2.1}$$

Porosity

Frequently used parameter to describe how densely the grains are packed. Range of variation is always between 0 to 1, where the smaller the value of porosity, the denser the packing is, defined as:

$$\phi = \frac{V_V}{V_T} = \frac{e}{1+e}, \tag{2.2}$$

where, V_T is the total volume of the system. Additionally, it is possible to relate the porosity with particle density (ρ_p) and bulk density (ρ_{bulk}):

$$\phi = 1 - \frac{\rho_{bulk}}{\rho_p} \tag{2.3}$$

2.1.2 Flow rate

Flow rate is a quantity which measures the outflow of a bulk solid from an orifice in a certain time. Both particle-scale characteristics of a granular material (e.g. size distribution, shape, cohesion), and boundary conditions (e.g. orifice size and hopper angle) affects the flow rate.

For bulk material handling process, it is important to predict the flow rate, and in this respect, several attempts have been conducted to relate flow rate to the flow con-

ditions and material properties (empirically or with dimensional analysis), see (Brown and Richards, 1970; Nedderman et al., 1982; Schulze, 2008).

Most of predicting approaches originates from observations related to the discharge of liquids under earth gravity. Considering a tank filled with liquid (to height of h), it is possible to obtain the velocity (V) of the discharging liquid from a hole in the bottom of the tank by the Torricelli approach (Torricelli, 1644):

$$V = \sqrt{2gh} \tag{2.4}$$

where, g is the Earth gravity and the system is frictionless. This holds true for liquids since the pressure along the height is changing due to hydrostatic pressure. However, in case of granular material, due to Janssen effect (Janssen, 1895), the pressure in the bottom of silo remains unchanged (stress state near outlet is independent of h), and this lead to an almost constant flow rate. Therefore, only diameter of the outlet D_o must be considered for obtaining V, as follow:

$$V \propto \sqrt{gD_o} \tag{2.5}$$

Then, to obtain the mass flow rate W, the cross section area of the out-flowing bulk A and bulk density ρ_b must be taken into consideration and multiplied by the velocity at the outlet, accordingly:

$$W = A.\rho_b.V \propto A.\rho_b.\sqrt{gD_o} \propto \rho_b.\sqrt{g}.{D_o}^2.5 \tag{2.6}$$

However, considering the point that the cross-section of out-flowing bulk is smaller than the cross-section of the opening, Hagen (1852) suggested that D_o must be reduced. Thus, a new term as kx, in which x is a function of the particle diameter, is subtracted from D_o:

$$W \propto \rho_b.\sqrt{gD_o}(D_o - kx)^{2.5} \tag{2.7}$$

Equation 2.7 is the general form of the most of the proposed approaches in the literature (Schulze, 2008). Among all, Beverloo's approach is known to be the most frequent (Beverloo et al., 1961):

$$W = C\rho_b\sqrt{g}(D_o - kx)^{2.5} \tag{2.8}$$

where, C and k are fitting parameters and Beverloo et al. (1961) pointed out following ranges accordingly: $0.55 \leq C \leq 0.65$ and $1.5 \leq k \leq 3$.

British Materials Handling Board suggested a similar approach for free flowing bulk solid (particle size with range of $3\% < 250\mu m$). Here, the rectangular and circular orifices are separated:

For a circular orifice:

$$W = 0.58\rho_b\sqrt{g}(D_o - kx)^{2.5}K_\Theta \tag{2.9}$$

and for rectangular orifice (where b is the width and L is the length, considering $L > 3b$):

$$W = 1.03\rho_b\sqrt{g}(L - kx)(b - kx)^{1.5}K_\Theta \tag{2.10}$$

In the equations above, k is treated as shape factor (for spherical particle $k = 1.6$ and for irregular shapes $k = 2.5$). Additionally, hopper inclination Θ is directly affecting W and included as:

$K_\Theta = (\tan\Theta)^{-0.35}$ for $\Theta < 45^\circ$

$K_\Theta = 1$ for $\Theta \geq 45^\circ$

Beside the mentioned studies, there are a couple of other suggested equations, for determination of the mass flow rate, which are listed here (see McGlinchey (2008) for more details):

Johanson (1966) (applicable for cohesionless powders):

$$W = \rho\frac{\pi D_o^2}{4}[\frac{D_o g}{4\tan\theta}]^{0.5} \tag{2.11}$$

Brown and Richards (1970) (applicable for cohesionless powders):

$$W = \rho g^{1/2}{D_o}^{5/2}(\frac{\pi}{6})(1 - \frac{\cos^{3/2}\theta}{\sin^{5/2}\theta}) \tag{2.12}$$

Williams (1977) (applicable for cohesive powders):

$$W = k_c\rho g^{1/2}{D_o}^{5/2} \tag{2.13}$$

where, θ is the semi-included angle of a conical hopper, V_w is the function of the velocity along the hopper wall, k_c is the correction factor for hopper outlet diameter.

2.1.3 Flowability

In contrast to soil mechanics, where it is usually desirable to limit soil deformations to be elastic, in the case of powder technology the flow (failure) of the granular material is needed in order to ensure feeding process (Schwedes, 1975). For most of bulk solid

handling processes (e.g. hoppers and chutes), the flow of granular medium is enabled through a gravity-driven operation. Thus, it is essential to identify the force distribution among particles and ensure the occurrence of failure in the granular system. The force distribution among particles is not equivalent, but it is rather concentrated on a random network of particles (referred as force chains). While material is under pressure, the particles are closely packed and form the force chain, however, during shearing the force chain consistently collapses and then forms among a distinct network of particles.

One pioneer failure or yield criterion is proposed by Coulomb (1776), in which the shear stress at failure is a function of the normal stress (the correlation is controlled by the inter-particle friction). Additionally, it is also suggested that the yield shear stress is dependent on a stress independent component, which is referred as cohesion (bonding strength among particles). The failure strength in granular materials is mostly stress-history dependent, unless the material is free flowing (the applied consolidation stress does not increase the shear strength). Therefore, it is necessary to utilize standard tests to evaluate the flowability of the powders within various stress ranges. Consequently, shear testers are the most common means of characterization methods for evaluating the flowability, see (Fulchini et al., 2017; Moreno-Atanasio et al., 2005; Zafar et al., 2015, 2017).

Flowability is an indication of how easily a bulk solid can flow in different conditions. The range for flowability varies from not flowing to cohesive and free flowing. The shear strength of a sample usually provides a quantitative measurement of flowability. Accordingly, a common methodology that is used for determining flowability is defined under Coulomb failure concept (Jenike et al., 1960), which states: once shear stresses in a granular body reaches the limiting shear (note that particles do not experience plastics deformations), plastic flow (failure of the material) occurs.

Two essential parameters that must be obtained from experiments are the unconfined yield stress (σ_c) and major principal stress (σ_1). Following is the definition of the both parameters:

One of the most preferred tests is uniaxial compression, which provides the force that is needed for breaking or deforming a granular sample that has no surrounding confinement. The test consists of a couple of steps (see Figure 2.2): a) the sample is poured in the hollow cylinder, which has smooth walls b) the levelled surface of the specimen is then vertically loaded with σ_1 (called consolidation stress as well), and thus it gets compressed c) the specimen is unloaded and the hollow cylinder is carefully raised d) the sample undergoes an increasing vertical load (σ_c) and at a certain point it start to fail (shear bands emerge and deformations localize).

Uniaxial compression test is repeated for couple of different vertical loads the results are plotted between varied σ_1 and σ_c, and next, connecting the points, a curve

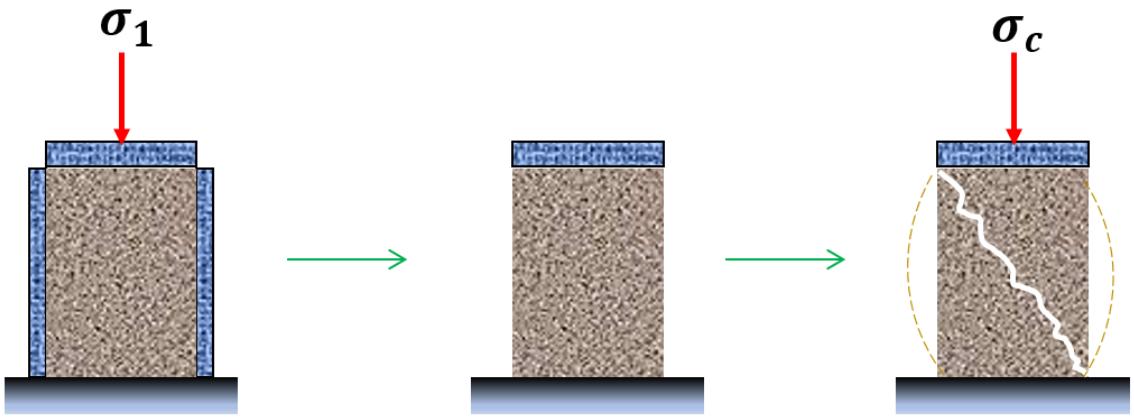

Figure 2.2 Uniaxial compression (test steps), Schulze (2008).

forms which is known as flow function. Accordingly, flowability is defined as a ratio:

$$ff_c = \frac{\sigma_1}{\sigma_c} \tag{2.14}$$

Jenike (1964); Jenike et al. (1960) has provided a criteria for flowability of the granular materials based on obtained ff_c, which is summarized in Figure 2.3.

2.2 The Discrete Element Method (DEM)

Complexity in behaviour of particles assembly and their wide usage encouraged many researchers to study them in detail and this led to development of several numerical and experimental methods to characterise bulk materials. Developed by Cundall and Strack (1979), Discrete Element Method (DEM) is a good example of numerical solutions that treats the bulk solid as a system of distinct interacting bodies. DEM simulates particle interactions and provides an insight into overall response. Each particle is identified separately having its own mass, velocity and contact properties. Therefore, it can provide a clear explanation on particle-scale behaviour of granular solids to characterize bulk mechanical responses.

Figure 2.4 displays a schematic flowchart of the loop for calculations done in a DEM simulation. The initial step in DEM is to define the geometry of the system, where particles are free to overlap while they come into contact. In each time-step, the positions of the particles are determined. The distance between two adjacent spheres deduces the contact; if the centre-to-centre interval of adjacent particles becomes less than the sum of both radii, then particles are overlapped and considered as in contact (for complex shape particles there are various contact detection algorithms, see Podlozhnyuk et al. (2017)). Once the overlap occurs between particles, using a constitutive contact model, normal and tangential forces are calculated. DEM employs Newton's

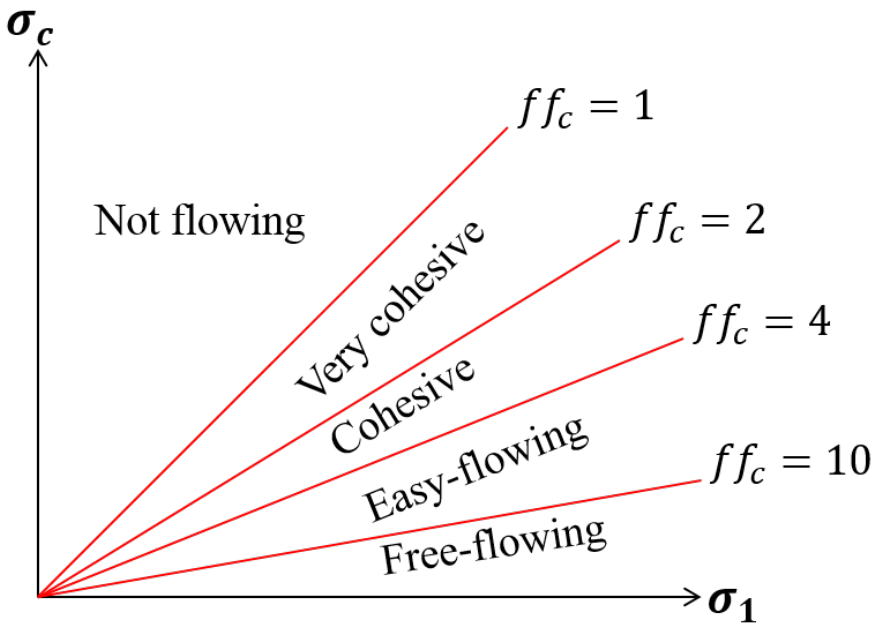

Figure 2.3 Flow characteristics based on flow function (Jenike et al., 1960; Schulze, 2008).

second law of motion to acquire the acceleration of individual particles resulting from any unbalanced force (including contact forces and body forces) acting on the particle. This way, force displacement law relates the acting forces at the contacts among particles to the resulting displacements.

For particle i the equation of motion is defined as:

$$m_i \frac{d^2}{dt^2} \vec{x_i} = \vec{f_i} + m_i \vec{g} \tag{2.15}$$

where, m_i is the mass of the particle, t is time, x_i is its position, g is the acceleration due to gravity and f_i is the force acting on the particle due to particle contacts and given by:

$$\vec{f_i} = \sum_c \vec{f_i^c} \tag{2.16}$$

The rotational motion equation for particle i is obtained through:

$$I_i \frac{d}{dt} \vec{\omega_i} = \vec{T_i} \tag{2.17}$$

where, I_i is the moment of inertia, ω_i is the angular velocity and T_i is the total torque acting on particle i and defined as:

$$\vec{T_i} = \sum_{i=1}^{N_c} \vec{l_i^c} \times \vec{f_i^c} \tag{2.18}$$

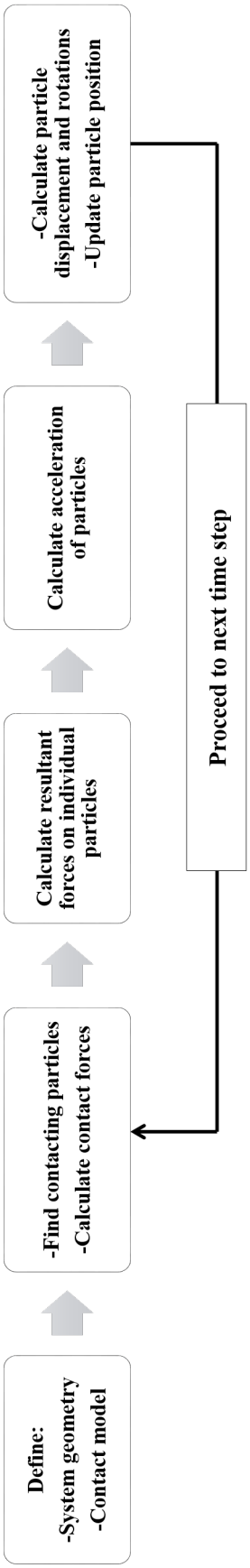

Figure 2.4 Necessary step for running DEM simulation (O'Sullivan, 2011).

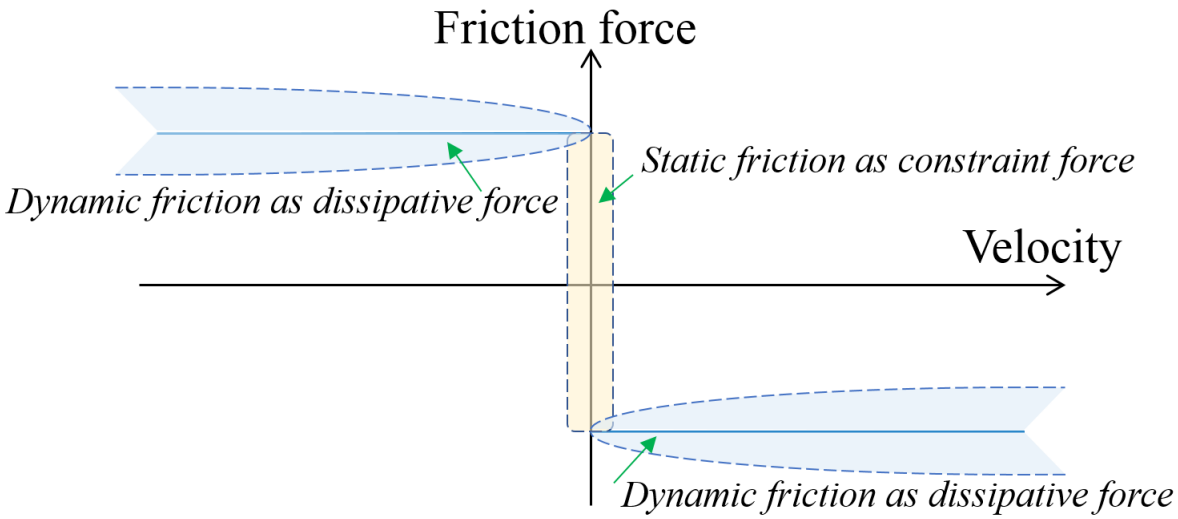

Figure 2.5 Graphical description of friction acting as constraint and dissipative force (i.e. dependence of the friction on velocity), Matuttis and Chen (2014).

where, l_i is the branch vector, given by:

$$\overrightarrow{l_i} = \overrightarrow{r_i} - \overrightarrow{r_j} \tag{2.19}$$

where, r is the radius of particle. Details of contact detection, time integration scheme, contact models and boundary conditions (periodic, rigid) are already available in the literature, see (Matuttis and Chen, 2014; O'Sullivan, 2011). Following sections summarize methodologies associated with measuring input parameters for DEM.

2.2.1 Sliding friction

A simple definition for friction is: the force that resists against relative motion of contacting bodies. For two solids sliding along one dimension (in dry conditions), with F_n is the normal force, dynamic Coulomb friction is defined as:

$$F_d = -F_n \mu \text{sgn}(\eta) \tag{2.20}$$

where, F_d is a dissipative force that acts in opposite to the sliding (tangential to the contact) and *sgn* is the usual step function. In case of no-sliding, F_d is defined as the extrema of the static Coulomb friction F_s, in other words:

$$-F_n \mu \leq F_s \leq F_n \mu \tag{2.21}$$

here, F_s is acting as constraint force.

As a common approach, calibration process is pursued to include a realistic friction coefficient in DEM simulations, see Coetzee (2017). In this respect, internal friction coefficient of the material is obtained through a shear tester or angle of repose, and then, the particle-particle friction coefficient is varied iteratively in DEM to obtain overlapping bulk friction (Barrios et al., 2013; Combarros Garcia et al., 2016; Härtl and Ooi, 2011; Marigo and Stitt, 2015).

More sophisticated approaches have also been considered for calibration process, such as: statistical analyses (Yan et al., 2015) and artificial neural networks (Benvenuti et al., 2016).

Friction between the particle and surface is also an important parameter, and several methodologies have been developed to measure it. Chung (2006) used a simple apparatus to obtain friction between corn grains and acrylic, steel and aluminium surfaces. Initially, three random grains were glued to a base plate and a test plate was located above the grains. Test starts with gradually rotating the base plate around the hinge and it continues up to the point which sliding of the test plate occurs. The tangent of the angle which base plate makes with the horizontal is regarded as particle-geometry friction coefficient.

The influence of friction coefficient on bulk response of granular material has been assessed in various tests, such as:

Huang et al. (2014) and Hanley et al. (2017) studied the influence of inter-particle friction on the critical state response of a specimen during conventional drained triaxial compression tests. They have observed that varying the friction coefficient influences the critical state parameters and the position of critical state line.

Taghizadeh et al. (2015) investigated the sensitivity of the elastic moduli of granular materials on inter-particle contact friction. Accordingly, they have considered frictionless and frictional spherical particles and simulated an isotropic deformation mode. Their study suggests that with higher inter-particle contact friction, the bulk modulus drops systematically.

Yan et al. (2015) have considered the effect of static friction coefficients in angle of repose test. Comparing the profiles for the discharged materials, they have seen that increasing friction leads to steeper slopes and the width of the sandpile shrinks.

2.2.2 Rolling friction

For real materials, a rolling friction can be defined only when there is a deformation at contact (i.e. rolling friction is applicable for elastic material). However, in DEM simulations, though particles are overlapping, deformation is not allowed at contacts. Accordingly, the rolling resistance must be defined artificially in particle-particle and

particle-geometry contacts. This is essential particularly for spherical particles, where particles have more rotational freedom (due to lack of interlocking).

In past decades, number of experimental (Calvetti et al., 1997; Oda et al., 1982) and numerical (Bardet, 1994; Iwashita and Oda, 1998) studies have been conducted considering disk (in 2D) and spherical (3D) shape particles. The mutual observation of these studies was that, without a resisting torque, these particles can only resist small shear or frictional forces.

In order to include the rolling friction in DEM simulations, various approaches have been suggested in the literature. Two chapters of this thesis are devoted for evaluation of such models and assess their capability in addressing the shape parameter.

2.2.3 Restitution coefficient

The dissipation of energy at contacts is a direct function of the restitution characteristics of a material. Both normal and tangential restitution coefficient are obtained though measuring the normal and tangential components of the incoming and rebounding velocities at a contact. The restitution coefficient between a particle and geometry can be measured by a simple impact test. Generally, a high-speed camera is used for measuring velocity of the particle at pre and post-collision, see Chung (2006).

Yan et al. (2015) studied the influence of restitution coefficient on the angle of repose tests and concluded that varying this parameter, the profiles of the heaps do not change. However, it is reported that the effects of friction and coefficient of restitution are cross correlated.

Anand et al. (2008) simulated granular flow in a quasi-3D, wedge-shaped hopper and investigated the influence of different parameters on flow characteristics. They have observed that coefficient of restitution has insignificant influence on the discharge rate (due to having mostly long duration, highly frictional and sliding contacts).

Hastie (2013) made an effort to measure the restitution coefficient for non-spherical particles. He considered polyethylene pellets and recorded the random behaviour, using high-speed video recorder, of these particles in 3D. It is seen that finding a single proper value that can feed DEM simulations, for non-spherical particles, is still ambiguous. However, it is suggested that a sensitivity analyses must be conducted to account for variation of the restitution, angular displacement and angular velocity.

2.2.4 Shape implementation techniques utilized in DEM

The inclusion of realistic particle shape has been always a concern in DEM simulations. As discussed already, a simple approach is to consider the spherical particles and include a constraint over the rotational freedom of the particles. However, num-

ber of investigations are also carried out to simulate complex shape particles, such as: multi-spheres (Abbaspour-Fard, 2000; Favier et al., 1999), superquadrics (Cleary, 2004; Podlozhnyuk et al., 2017), digitisation (developed by Jia et al. (2007)), spherodiscs (Li et al., 2004), polyhedrons (Azéma et al., 2009), spherosimplices (Pournin et al., 2005). A good review over the incorporation of shape factor in DEM in many different applications has provided by Lu et al. (2015).

Rolling resistance models and applications

Following is a summary of the works that have been done by researchers to incorporate rolling resistance through different approaches, see Ai et al. (2011) for a detailed list:

Sakaguchi et al. (1993) reported that the disks, in the conventional DEM, are not capable of forming arches since these elements are geometrically unstable and roll freely. Thus, in order to express the plugging of granular flow by DEM, Sakaguchi et al. have employed rolling friction scheme. The resisting moment derived from multiplying coefficient of rolling friction and normal contact force. They have concluded that including a rolling friction moment in DEM simulation of silo discharge leads to a good agreement of the predicted flow patterns and formation of arches with experimental measures.

Iwashita and Oda (1998), comparing the DEM results of a biaxial compression test with experiments done by Oda and Kazama (1998), asserted that the microstructure developed in shear bands is completely different. Oda and Kazama suggested that the primary mechanism that controls the dilatancy inside a shear band is rolling of the particles. Hence, Iwashita and Oda proposed a modified model of conventional DEM (called MDEM) that considers rolling resistance at contacts. MDEM has an additional set of elastic spring, dashpot, no-tension joint and a slider at each contact, which responds to the resisting moment. Elastic spring and the dash-pot are balancing the resisting moment, while the slider only activates if the moments exceeds a threshold. Using MDEM, Iwashita and Oda successfully predicted shear bands. They also observed the large voids inside these shear bands and the high gradient of particle rotation along the shear band boundaries as well.

Zhou et al. (1999) proposed a simulation method that was based on original DEM algorithm and was capable of modelling formation of a stable heap of spheres in 3D conditions. The suggested modification was established upon the experimental and theoretical analysis of Beer et al. (1972) and Brilliantov and Pöschel (1998). Accordingly, a rolling friction torque that opposes the rotation of each particle was introduced to original DEM code. Two different approaches are followed to obtain the rolling friction torque, which differ based on consideration or ignorance of the angular velocity. They showed that both methods can provide relatively similar results, however, it

was shown that the model independent of angular velocity is more effective. It must be also noted that, the coefficients of rolling friction in the study by Zhou et al. (1999) had physical units, which introduced another complexity to the proposed models.

Jiang et al. (2005) suggested a modification on model provided by Iwashita and Oda (1998) that avoids limitations of using model parameters chosen separately by try and error. They presented a precise definition of pure sliding and pure rolling, which made it possible to relate general contact displacement to energy dissipation. Moreover, they introduced a shape parameter, which represents the contact width between grains. Incorporating the model in DEM, they conducted biaxial simulations on 2D discs and concluded that new code provides an increase in coefficient of internal friction of the tested material by choosing a proper value for the shape parameter. They also stated that the model can help the microanalysis of the strain localization phenomenon.

Chang et al. (2012) proposed a modified eccentric circle model for incorporation of rolling resistance in DEM simulations. The model first relocates the centre of mass for circular particles, to achieve eccentricity, then to dissipate energy in the rotational direction, a local damping moment is applied. The applicability of the model is approved through comparison of simulation results with experimental observations on repose and landslide characteristics of chalk rod assemblies.

Additionally, new 3D rolling resistance models have been recently developed and implemented in DEM, which claim to predict macro-scale parameters more realistically. The following is two examples of such models:

Jiang et. al. (2015) developed a new 3D contact model that account for rolling and twisting resistances at inter-particle contacts. Using the new contact model, conventional triaxial compression and plane-strain compression tests are simulated. Two new parameters as shape parameter β and local crushing parameter ξ_c , are introduced with clear physical meanings. It is shown that assigning a proper value of β provides an increase in peak strength of the sample (similar to that of observed for a real sand). Additionally, a high strain-softening rate is reported during plane-strain compression tests. Additionally, it is shown that once rolling resistance is excluded from contacts, the strength and dilatancy reduce more (compared to the case where twisting resistance is off), which suggests the importance of rolling resistance.

Huang et. al. (2017) developed a rotational resistance model with a physical basis, which consists of two parameters: a) a shape parameter δ (defining particle irregularity) b) a strength parameter κ (linking the strength of asperities to the normal force). For a particle assembly, subjected to triaxial shearing, both δ and κ parameters have notable influences on increasing the shear strength. Additionally, conducting a sensitivity analysis, it is shown that dilative volumetric strain is always a function of δ.

Thus, it is concluded that surface topology has a more significant influence on interlocking than asperity strength.

Groups of researchers have investigated the influences of various rolling resistance models on the bulk response in different applications:

Balevičius et al. (2012) studied the influence of rolling torque on bulk response of granular assembly inside a bin and compared the obtained result with experimental measurements. They showed that the effect of rolling friction, which was experimentally obtained through an inclined plain test, on wall pressure distribution is minimal (especially at filling state). Additionally, they showed that presence of rolling resistance is decreasing the horizontal velocity across the bin. Whereas, the vertical velocity at the centre of the bin is slightly increased in presence of rolling resistance (this is justified by the tendency of the rolling resistance in increasing voidage distribution, which reduces the energy dissipation due to less collision of the particle during the discharge). Finally, they mentioned that the recorded numerical outflow of the ensiled mass shows better agreement with experimental data by including the rolling friction effect.

Zhao and Guo (2014) assessed the capability of spherical particles in presence of rotational resistance to account for the shape irregularity in triaxial undrained shear test. It is shown that the shearing strength of the packing is increased in presence of rotational resistance and the granular system becomes less susceptible to liquefaction. Additionally, they conclude that the rotational resistance influences the critical void ratio and critical fabric anisotropy.

Incorporation of complex shapes in DEM studies

Number of researchers have considered various shape representation techniques to predict realistic bulk response for granular materials in different testing conditions. Here is a brief list of recent studies that mainly focused on importance of shape factor:

Shamsi and Mirghasemi (2012) utilized multi-sphere (MS) particles to investigate the influence of particle angularity on the bulk response of a granular assembly in a triaxial test. They observed that the more angular the single particles are (at a specified confining pressure), the higher mobilized friction angle and dilation is reached. Additionally, they reported that the shear strength is more affected by angularity once higher friction coefficients are applied.

Höhner et al. (2011) studied the adequacy of the MS and polyhedral (PH) approach to approximate particle-wall collisions of ellipsoidal particles. They showed that both approaches require significantly less computational time compared to the ellipsoid contact algorithm while still yielding acceptable results at micro-level.

Höhner et al. (2012, 2013) conducted DEM simulations with spherical, PH and MS particles and examined the macroscopic features of the flow during hopper discharge. The results revealed that polyhedral particles increase the flow resistance compared to MS particles, and suggested that this might be due to the relatively smooth surfaces of the MS particles, while PH surfaces have multiple sharp vertices and edges. Moreover, Höhner et al. (2012) stated that smoother particles form a V-shaped flow that reaches the hopper walls, while increasing the angularity of the particles leads to a core flow above the opening. They also mentioned that particles with sharper edges have a tendency to build arches that can clog the flow.

Cleary and Sawley (2002) compared the discharge of superquadric (SQ) and spherical particles from a hopper and showed that the non-sphericity causes a slower flow up to 30% and also changes the flow kinematics. They found that the hopper flows are not sensitive to any further increase of particle angularity if SQ blockiness (N) is greater than 8 (description of the blockiness is provided in Chapter 4).

Pereira and Cleary (2017) studied segregation of a binary granular mixture composed of cubes modelled as SQ and spheres in a slowly rotating cylindrical tumbler. They found that cubical particles segregate to the inner core of the particle bed while the spherical particles segregate to the curved walls of the tumbler. It was shown that blocky particles dissipate energy faster than spherical ones and hence move more slowly as they travel down the free surface.

Härtl and Ooi (2011), considering spherical and non-spherical (consist of two glued beads), investigated the influence of particle shape and on the bulk friction in a Jenike direct shear test. It is shown that particle interlocking has a more pronounced impact than porosity on the bulk friction.

Tao et al. (2010) used the MS approach to represent corn-shape particles and compared the flow properties with spherical particles. They showed that the downward velocity of the clusters shows higher variation, compared to spheres, along the width of the silo (the maximum is seen in the centre and decreases towards the walls). Furthermore, they observed that the mean voidage of packings for non-spherical particles is smaller than that of the spherical particles.

Markauskas et al. (2009) evaluated the capability of the MS method to describe ellipsoidal particles, which can replace the perfectly smooth ellipsoids generated using the SQ technique. Varying the number of sub-spheres, the MS particles were characterized through studying the angle of repose, porosity and coordination numbers. They observed a non-linear increase of computational time with the increase in the number of sub-spheres compared to the case of ideal spherical particles. It was pointed out that increasing the number of sub-spheres exhibits a clear tendency to mimic macroscopic parameters of a smooth ellipsoid.

2.3 Experimental studies on particle shape effect on flow characteristics

Beside numerical study of granular materials, some researchers have monitored the flow in lab-scale silos. Following is a summary of the experimental studies, which tried to clarify the particle shape effect on the flow properties:

Sukumaran and Ashmawy (2003) introduced Shape Factor and Angularity Factor for better characterizing the particle geometry. It is shown that as the angularity and shape factor increases, the mass flow rate drops. It is also reported that the strength properties of the granular material can be linked to the flow rate; an approximately linear relationship is obtained between the large strain friction angle of the materials and the mass flow rate.

Zuriguel et al. (2005) studied experimentally the jamming phenomenon during discharge of particulate material from a silo (transparent walls are utilized). To investigate the influence of particle shape, the study included spherical glass beads, pasta grains, lentils and rice. For spherical particles a mix flow is observed, in which a mass flow develops in the upper region of the silo and a funnel flow forms below a certain height. In case of nonspherical particles, a funnel flow is always available. Additionally, it is shown that particle shape parameter strongly influences the arch formation probability (increases). A critical radius (outlet size) is also defined beyond which no arching happens. It is reported that the critical radius is highly dependent on particle shape characteristics.

Börzsönyi et al. (2016) studied the clogging of flow, for spherical and nonspherical, in a 3D hopper by means of x-ray tomography. For elongated particles, it is shown that particles in the flowing zone are oriented approximately parallel to the streamlines. However, near the silo walls, it is seen that most of particle are tangentially aligned. Additionally, the packing density of the particles is lower in the flow zone (compared to the stagnant zone), and this difference is less pronounced in case of spherical particles. Moreover, it is seen that dome height (the 3D analogies of a 2D arch) is dependent on the aspect ratio of the particles (i.e. it decreases with increasing aspect ratio).

Calderón et al. (2017) investigated experimentally the flow characteristics of three different seeds with different shapes (ellipsoids, spheres and parallelepipeds). The considered silo has hoppers of conical and flat-bottomed, in which the orifice size can be varied. The main objective was to correlate the flow parameters involved in Beverloo's equation (C and k) to the geometry of the grains. It is shown that for the various hopper shapes and different seed types the parameter C in Beverloo's equation is not changing (not sensitive). However, it is shown that k parameter can be well correlated with the size, circularity and specific area of the seeds. It is also noticed that

for obtaining k value it is essential to consider the size and surface area of the particles (i.e. k value cannot be predicted solely by circularity).

2.4 Centrifuge modelling

In Geotechnical Engineering field, centrifuges are used for decades to tackle with complexity of the soil response during various stress state. The centrifuge modelling is beneficial once loading condition is unusual or extreme, and when constitutive models are missing or not well defined for the specific soil type (Madabhushi, 2014). Several researchers used centrifuge to model various geotechnical problems such as: Estimation of hydraulic conductivity (Singh and Kuriyan, 2002), Earthquake simulation (Coe et al., 1985), Liquefaction (Popescu and Prevost, 1993), Tunnelling (Idinger et al., 2011; Loganathan et al., 2000), Retaining walls (Powrie and Daly, 2007) and soil slopes reinforcement (Porbaha and Goodings, 1996; Sonnenberg et al., 2010).

The use of centrifuge modelling to study silos is first introduced by Molerus and Schöneborn (1977) and Nielsen and Askegaard (1977), in which the former investigated the critical outlet dimension and the latter studied the scale errors in model tests. Kristiansen et al. (1988) conducted centrifuge tests on Limestone and reported that the filling procedure affects the stress distribution in the hopper section. Moreover, it is observed that the obtained critical outlet dimension is larger than Jenike's prediction.

After the mentioned preliminary studies, there was a pause on utilization of silo centrifuge until Großstück and Schwedes (2005) revisited the critical outlet dimension problem. Considering a moderately cohesive bulk solid, they compared the critical outlet dimension obtained both from Jenike design procedure and silo centrifuge. They reported that both methods lead to similar dimensions for the outlet.

Ittershagen et al. (2013), using a silo centrifuge, made an attempt to study the pipe dimensions for an active state of stress. In their study a new powder tester is also utilized to measure both the unconfined yield strength in the uniaxial direction, and the anisotropic unconfined yield strength. It is shown that both methods yield reasonably overlapping results.

Chapter 3

Rolling resistance as a technique for particle shape representation [1]

Spheres are the most frequently used shape in Discrete Element Modelling (DEM) simulations. For spheres, the mechanical interlocking is missing and the motion of the individual particles is restricted merely by frictional forces. Meanwhile, it has already been suggested that controlling the rotational freedom (by means of rolling resistance models) can overcome the inherent deficiency of the spheres in providing geometric interlocking. This chapter focuses on the influence of two popular rolling resistance models on the micro and macro response of spherical particle assemblies. In this regard, the mechanism of each model for retardation of angular velocity will be extensively discussed. Additionally, simulating particles in a silo geometry, the effect of each model on single-particle, packing and flow characteristics of the ensiled material will be assessed. Moreover, a coarse-graining technique will be utilized to convey the particle-scale DEM data to the continuum field, which allows a better understanding of stress and density distribution. Finally, results will qualitatively be compared to responses of non-spherical particles that are available in the literature, to determine the capability of such models in predicting the effects of the particle shape factor.

[1] Results of this chapter are included in a paper draft:

Soltanbeigi, B., Papanicolopulos, S.A. and Ooi, J.Y., "A study on influence of different rolling resistance models on packing and discharge of spherical particles in a flat-bottom silo", *To be submitted for review*,

and presented in:

Soltanbeigi, B., Weinhart, T., Papanicolopulos, S.A., Luding, S., and Ooi, J.Y., "Flowing characteristics of spherical particles with restrained rotation" Conference on Computational Solid and Structural Mechanics, Glasgow, UK, June 2018.

Soltanbeigi, B., Papanicolopulos, S.A. and Ooi, J.Y. An exploration of the micro-mechanism of the directional constant torque rolling friction model in quasi-static flow. *CFDEM®project user meeting workshop*, Linz, Austria - March 2016.

Soltanbeigi, B., Papanicolopulos, S.A. and Ooi, J.Y. DEM investigation of flow in silos: the effect of particle shape and rolling resistance. *Particles conference*, Barcelona, Spain, October 2015.

3.1 Introduction

Recent DEM studies on flow of ensiled material are mostly focused on assessing the influence of particle-level properties and boundary effects on the flow kinematics (Anand et al., 2008; González-Montellano et al., 2011; Höhner et al., 2012; Ketterhagen et al., 2009; Langston et al., 1995; Liu et al., 2014; Masson and Martinez, 2000; Vidyapati and Subramaniam, 2013). Among the particle scale features that control the behaviour of a granular material, shape factor plays an important role. Real particles, usually with asymmetric shape and surface asperities, show interlocking behaviour, which affects both the rotational and translational characteristics of these particles. Accordingly, the difference between the shape of real particles and idealized spheres, used in conventional DEM, leads to fundamental differences in estimation of material characteristics.

Various techniques have been introduced to represent non-spherical particle geometries in DEM: multi-spheres (Abbaspour-Fard, 2004; Favier et al., 1999; Härtl and Ooi, 2011), superquadrics (Cleary, 2010; Podlozhnyuk et al., 2017) and polyhedrals (Azéma et al., 2009; Jaelee, 2014). Moreover, a common practical approach, for considering the particle shape effect in discrete element simulations, is to add a resisting moment to rotating particles (Iwashita and Oda, 1998; Jiang et al., 2005; Sakaguchi et al., 1993; Wensrich and Katterfeld, 2012; Zhou et al., 1999). Additionally, an extreme case is also available, in which the rotation of the spheres are completely suppressed (Fleischmann et al., 2013).

There are various mechanisms for defining the magnitude and direction of the shape-representative rolling resistant moment, which are classified into categories by Ai et al. (2011). According to Ai et al. (2011) the available rolling resistance models can be classified into four categories:

a) Directional constant torque models: in this category, a constant torque is calculated and applies to the particles in contact, which is independent of the rotational velocity, see Zhou et al. 1999. The general form of the equation for obtaining the torque is further explained in Section 3.2.

b) Viscous models: in such models, the angular velocity of the particles is directly influencing the magnitude of calculated torque. A model from this category is proposed by Zhou et al. (1999):

$$\vec{M}_r = -\mu_r R_r \vec{F}_n (\vec{\omega}_i r_i - \vec{\omega}_j r_j) \tag{3.1}$$

c) Elastic-plastic spring-dashpot models: the torque in the models in this category are composed of two part: a mechanical spring torque and a viscous damping torque (see Iwashita and Oda 1998 and Jiang et al. 2005). Further details of this model is

presented in Chapter 5.

d) Contact-independent models: in this models, the obtained torque is independent of the relative rotation or rotational velocity of a pair of particles in contact. Instead, the torque is dependent on the total rotation or rotational velocity of a particle (e.g., Bardet and Huang 1992; Sakaguchi et al. 1993)

Most of the mentioned studies consider static and dynamic problems and evaluate: a) the influence of various rolling resistance models on the granular system and b) capability of these models to replicate the shape factor. For a quasi-static flow, however, a comprehensive study that considers the effect of rolling resistance at micro level and relates this to bulk response, is still missing. Accordingly, this chapter focuses on simulation of the discharge of spherical particles from a flat bottom silo and applies two different rolling resistance models to determine both objectives above (in terms of packing and discharging) and also evaluates the possibility of predicting similar bulk response with both models by tuning the rolling friction parameter.

3.1.1 Coarse-graining methodology

In order to compute the continuum fields through micro–scale data, an appropriate averaging methodology must be followed. The averaging procedure removes the unnecessary fluctuations at particle-scale and thus enhances obtaining well-defined bulk–scale information for the problem of interest. In this study, we are using averaging or coarse graining (*CG*) technique, described by Babic (1997) and Goldhirsch (2010), to attain macro-scale features of the granular assembly such as density, velocity and stress. The toolbox for performing *CG* (know as P4) is developed at University of Edinburgh (in 2015 it has started as a spin-out company as Particle Analytics Limited).

The detail of assumptions and disciplines where *CG* has been applied successfully is summarized in Weinhart et al. (2016). Coarse-graining utilizes both spatial and temporal options for averaging the DEM results, in which the former regulates the size of the solid contributing to the field data at each point and the latter is employed to reduce the temporal fluctuations (Weinhart et al. (2016)). Both the spatial (w) and the temporal (ΔT) scales are problem-dependent and vary with the kinematic characteristics of the system. The principal aim of this section is to specify what temporal and spatial averaging scales must be used and also to determine the effect of each on bulk results. The optimum values for w and ΔT provide scale-independent macroscopic fields (Weinhart et al. (2016)). Accordingly, the variation of the solid faction and horizontal stresses, based on applied w and ΔT, are evaluated for the granular assembly with μ_r=0 (see Figure 3.1). Furthermore, it is an established fact that the continuum fields can be averaged over directions in which the flow is homogeneous. In this respect, since

applied periodic boundary in depth of silo provides a homogeneous flow, the results are averaged over y-direction.

For problems with steady flow, where the time scale considered has insignificant effect, the magnitude of the w can be calculated based on particle size (Labra et al., 2013). Therefore, a series of values, which are multiples of the mean particle radius (r), are assigned for w. On the other hand, for showing the effect of ΔT, both instantaneous and time averaged values are presented in Figure 3.1 (averaging is conducted over ΔT= 0.2 and 0.4 seconds, which represents approximately 5 and 10% of the discharge). The chosen time is at 1 second after opening of the outlet (i.e. start of discharge), in which the flow is in steady state (here 1 s is midpoint of the averaging window). Moreover, the sample point is at the centre of silo in the mass flow zone.

Solid fraction results show a clear plateau, scale independent condition, for $w > 3r$, as shown in Figure 3.1a. Additionally, it can be deduced that the highest influence of temporal average is for $w < 2r$. Figure 3.1b shows that stress is more sensitive to the temporal average and applying ΔT=0.2 reduces the fluctuations considerably. Moreover, spatial average over $2r < w < 4r$ provides a plateau with both values of ΔT. Consequently, based on spatio-temporally averaged results in this section, the optimum values of w and ΔT is defined as $3r$ and 0.2 s respectively.

3.2 Rolling resistance consideration in the contact model

The Hertz-Mindlin (No Slip) contact model is the default model used in the current study due to its accurate and efficient force calculation (DEM Solutions Ltd. (2014)).

As suggested by Jiang et al. (2015) the relative rotation of two 3D particles in contact, can be decomposed into two components: a) about the contact normal direction, which renders a twisting resistance torque b) on the tangential contact plane, which leads to rolling resistance moment. It is shown that both components are influencing the relative motion of the particles, which results in increased dilation (in sample volume) at both triaxial and plane-strain compression tests. However, it is shown that once rolling resistance is excluded from contacts, the strength and dilatancy reduce more (compared to the case where twisting resistance is off), which suggests the importance of rolling resistance. Consequently, in this thesis, to minimize the varying parameters and to highlight the influence of the rolling resistance component, the twisting resistance is overlooked.

Two popular rolling resistance models, which already implemented in EDEM along with Hertz-Mindlin, are used in this chapter. The fundamental idea behind both the models is to generate a torque ($\vec{\tau}$) which opposes the rotation of the particles in contact. The general form of the torque equation is:

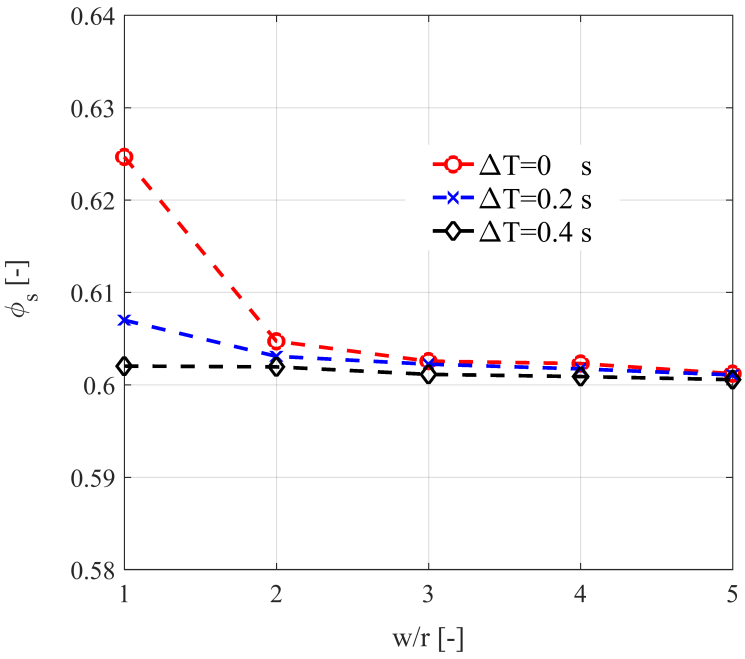

(a)

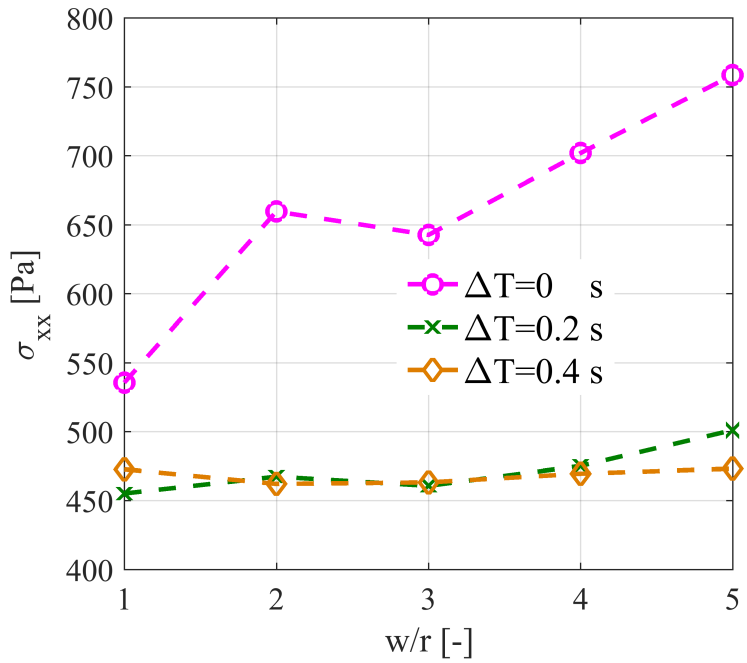

(b)

Figure 3.1 Effect of coarse-graining parameters (coarse-graining width (w) and temporal scale (ΔT)) on bulk results a) solid fraction (ϕ_s) b) horizontal stress (σ_{xx}), results are for the case with $\mu_r = 0$.

$$\vec{\tau} = -\mu_r R \mid \vec{F}_n \mid \hat{\vec{\omega}} \tag{3.2}$$

Both models consider the magnitude of the normal contact force ($\mid F_n \mid$) and a dimensionless rolling friction coefficient (μ_r) to determine the magnitude of the torque. The models that are considered here differ in the way they include the radius (R) and rotational velocity (ω).

The first model is referred as "Relative Velocity Dependent (RVD) rolling friction model" in EDEM documentation (hereafter called as Model A). Model A considers an equivalent radius (R^*) and unit average rotational velocity vector ($\vec{\omega}_{rel}$) of the particles in contact.

The second model is the default rolling resistance model in EDEM (hereafter referred as Model B), which incorporates the radius R_i and unit rotational velocity vector $\vec{\omega}_i$ of individual particle into torque calculation.

Equations 3.3 and 3.4 define the torque equations for Model A and B respectively:

$$\vec{\tau}_{ij(A)} = -\mu_{r(A)} R^* \mid F_n \mid \hat{\vec{\omega}}_{rel} \tag{3.3}$$

$$\vec{\tau}_{i(B)} = -\mu_{r(B)} R_i \mid F_n \mid \hat{\vec{\omega}}_i \tag{3.4}$$

where,

$$R^* = \frac{R_i R_j}{R_i + R_j} \tag{3.5}$$

$$\hat{\vec{\omega}}_{rel} = \hat{\vec{n}}_{ij} \times \vec{v}_{t_{ij}} / \mid v_{t_{ij}} \mid \tag{3.6}$$

$$\vec{v}_{t_{ij}} = \begin{cases} -\frac{1}{2}(\vec{\omega}_i + \vec{\omega}_j) \times \vec{r}_{ij}, \ particle - particle\ contacts \\ -R_i \vec{\omega}_i \times \hat{\vec{n}}_{ij}, \ particle - geometry\ contacts \end{cases} \tag{3.7}$$

$$r_{ij} = r_i - r_j \tag{3.8}$$

Here, $\hat{\vec{n}}_{ij}$ is a unit vector pointing from particle i to the point of contact, see Figure 3.2. $\vec{V}_{tij}$ is the relative tangential velocity contributed by angular velocities at the contact point between particles i and j.

The characteristics of the two models during a two particle collision are summarized here:

Keeping F_n and μ_r constant, R^* and R_i control the magnitude of the applied torque for both models. However, if the contacting particles have equal radii, according to Equation 3.5, the torque generated in Model A ($\vec{\tau}_{ij(A)}$) will be half the torque in Model B ($\vec{\tau}_{i(B)}$), see Figure 3.3. Moreover, the magnitude of $\vec{\tau}_{ij(A)}$ further decreases, if contacting particles do not have equal radii (i.e. system has polydispersity), see Figure

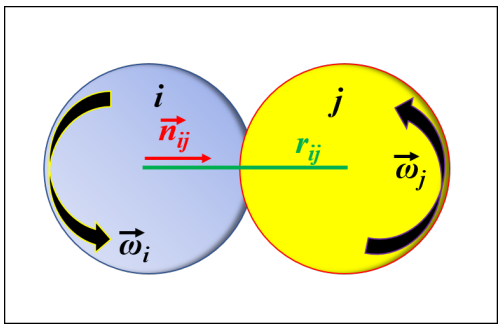

Figure 3.2 Schematics of particle-particle collision (DEM Solutions Ltd. (2014)), schematic representation of unit vector .

3.4. On the other hand, both models have a similar torque magnitude while contacting a geometry.

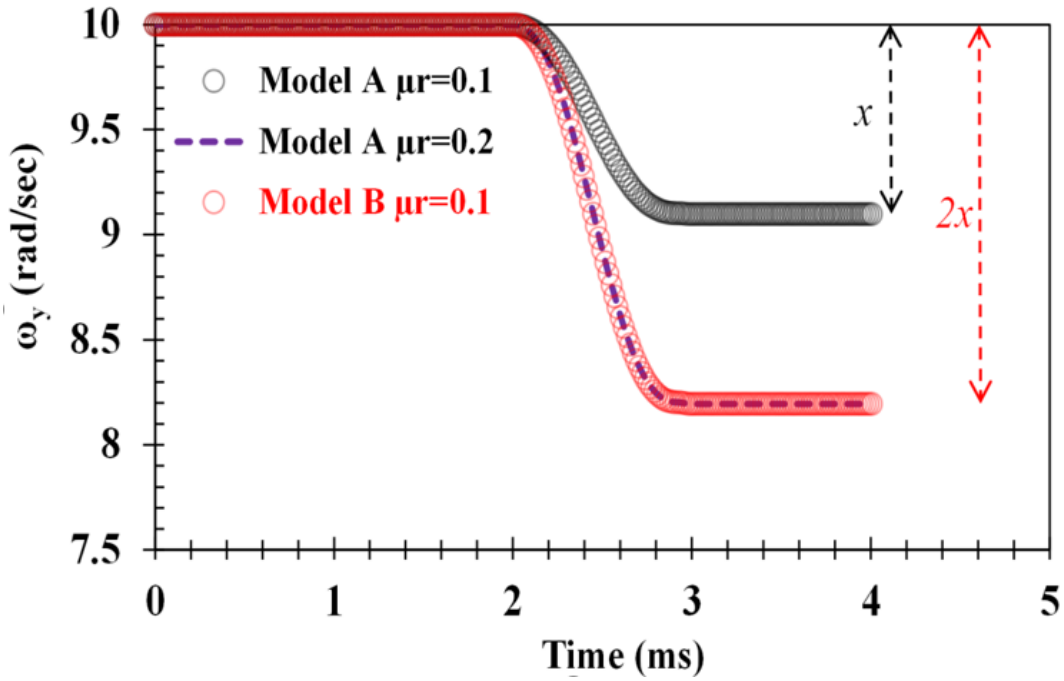

Figure 3.3 Change in angular velocity of single particle after collision (two spheres with equal radius and $\mu_{r(A)}$=$\mu_{r(B)}$ and $\mu_{r(A)}$=2$\mu_{r(B)}$).

Furthermore, if particles in contact have $|\vec{\omega}_i| = |\vec{\omega}_j|$ with opposite directions of rotation, Model A will apply no torque to the particles in contact (see Equation 3.7 and Figure 3.5a, and for $\vec{\omega}_i = \vec{\omega}_j$ see Figure 3.5b). Furthermore, since in Model A equivalent torque is applied to the particles in contact (i.e. $\vec{\tau}_i = \vec{\tau}_j$), if particles have different magnitude of ω in opposite directions $\vec{\omega}_i \neq \vec{\omega}_j$, the torque will accelerate the rotation of the slower particle and will decrease rotational speed of the faster one, see Figure 3.5c (note that sliding friction is off in both cases). Nevertheless, in case of Model B, the applied torque reduces the rotational velocity of the particles in all conditions, see

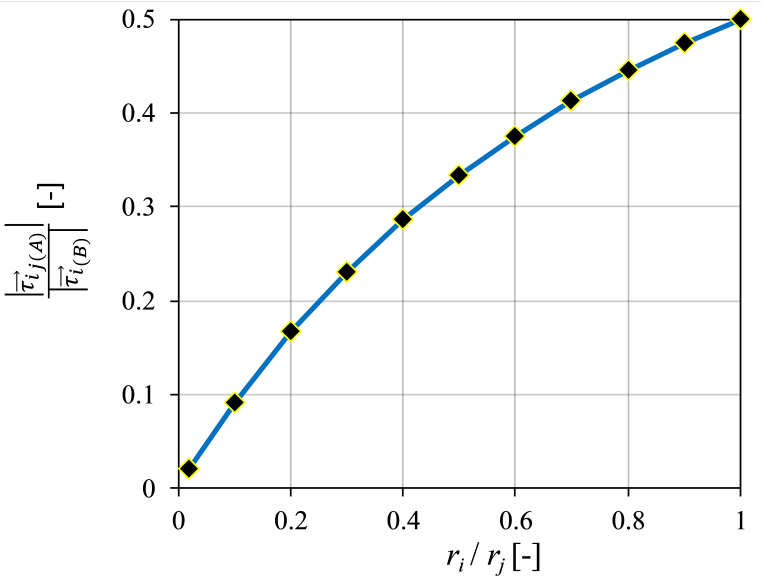

Figure 3.4 Effect of polydispersity on the magnitude of the applied torque for Model A.

Figure 3.6. Note that in these simulations, sliding friction is off, restitution coefficient is assigned as unity and rolling resistance coefficient is given as 0.1 for both models.

According to Ai et al. (2011), any model in the form of Equation 3.1 (depending on how ω is considered in the model) can be categorised as: a) directional constant torque model (Type A) or b) contact-independent model (Type D). It must be noted that despite some resemblance between "Model A" and "Type A" rolling resistance models, there is difference in calculating ω_{rel}; "Model A" considers an average value of the rotational velocity between particles in contact, whereas, "Type A" takes a relative value into account.

It must be noted that the way ω_{rel} is obtained in Model A results in some deficiencies; as shown earlier in Figure 3.5a (which represents pure rolling case) rotational resistance model does nothing to control the rotation of particles in contact. Moreover, in Figure 3.5b (which represents pure sling case), the rotation of particles are retrained inaccurately (angular velocity should remain unchanged). Consequently, despite the availability of Model A in some DEM codes, it is necessary to be cautious regarding deficiencies of this model (i.e. Model A differs from most rolling resistance models and indeed fails to resist pure rolling at all).

The chosen two rolling resistance models are among simplest models available in the literature, however they are yet popular and applicable in certain applications, see (Barrios et al., 2013; Cabiscol et al., 2018; Freireich et al., 2011; Goniva et al., 2012; González-Montellano et al., 2011; Horabik et al., 2018; Marigo et al., 2011; Thakur et al., 2016; Wang et al., 2017; Yu and Saxén, 2014). Since the utilized models are still in use among researchers, it was of high interest to evaluate the capabilities

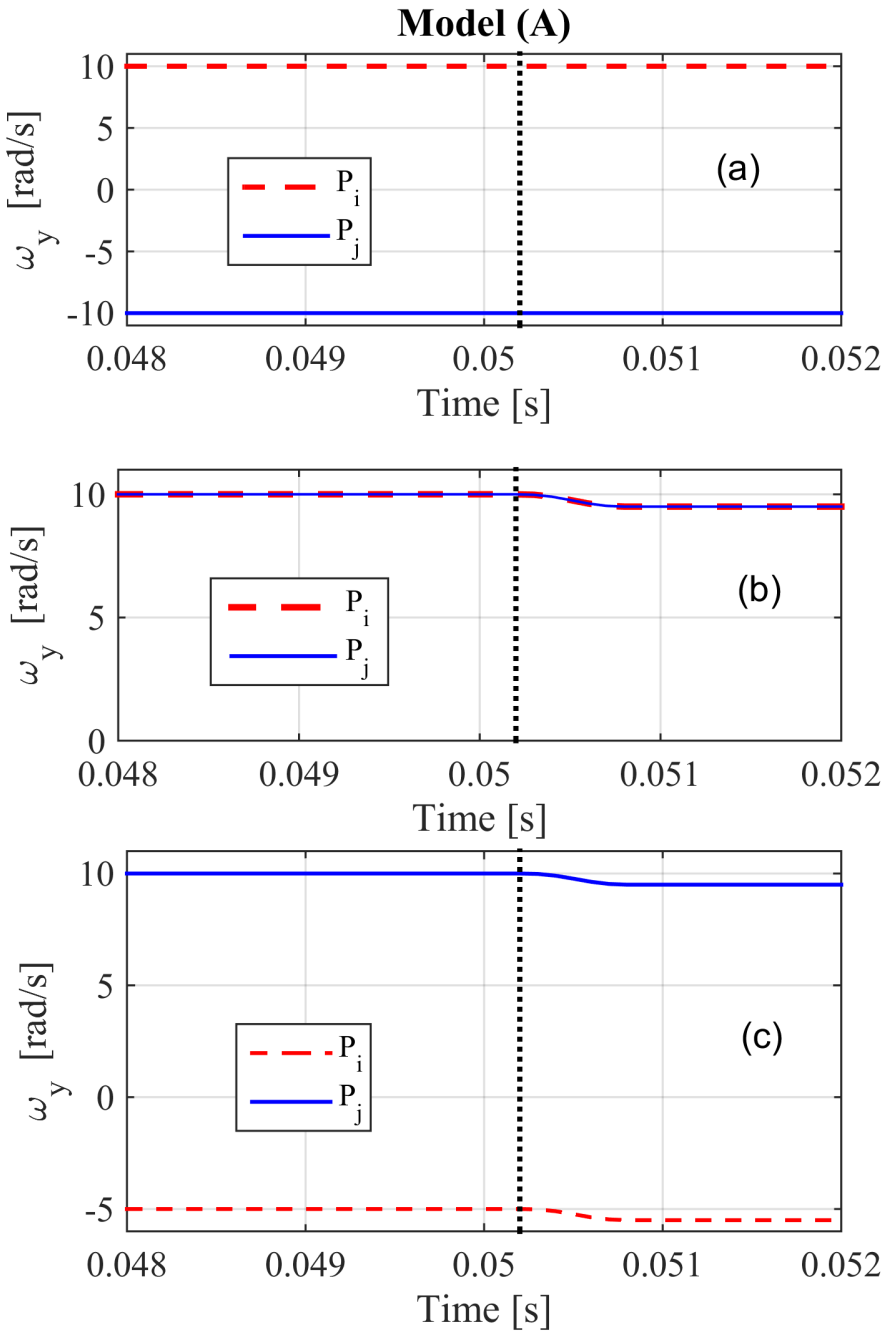

Figure 3.5 Different scenarios for two particle collision and respective change in rotation velocity for Model A (pre and post collision is shown in all plots) a) two particle have equal magnitude of ω but in opposite directions b) two particle have equal magnitude and direction of ω c) two particle have different magnitude of ω in opposite directions. Dotted line represents the instance of contact.

of these models during various loading and shearing conditions. As first step, the properties of the both models at single particle contact level are clarified, which then correlated to their effect on macro-scale properties. Furthermore, in case of Model

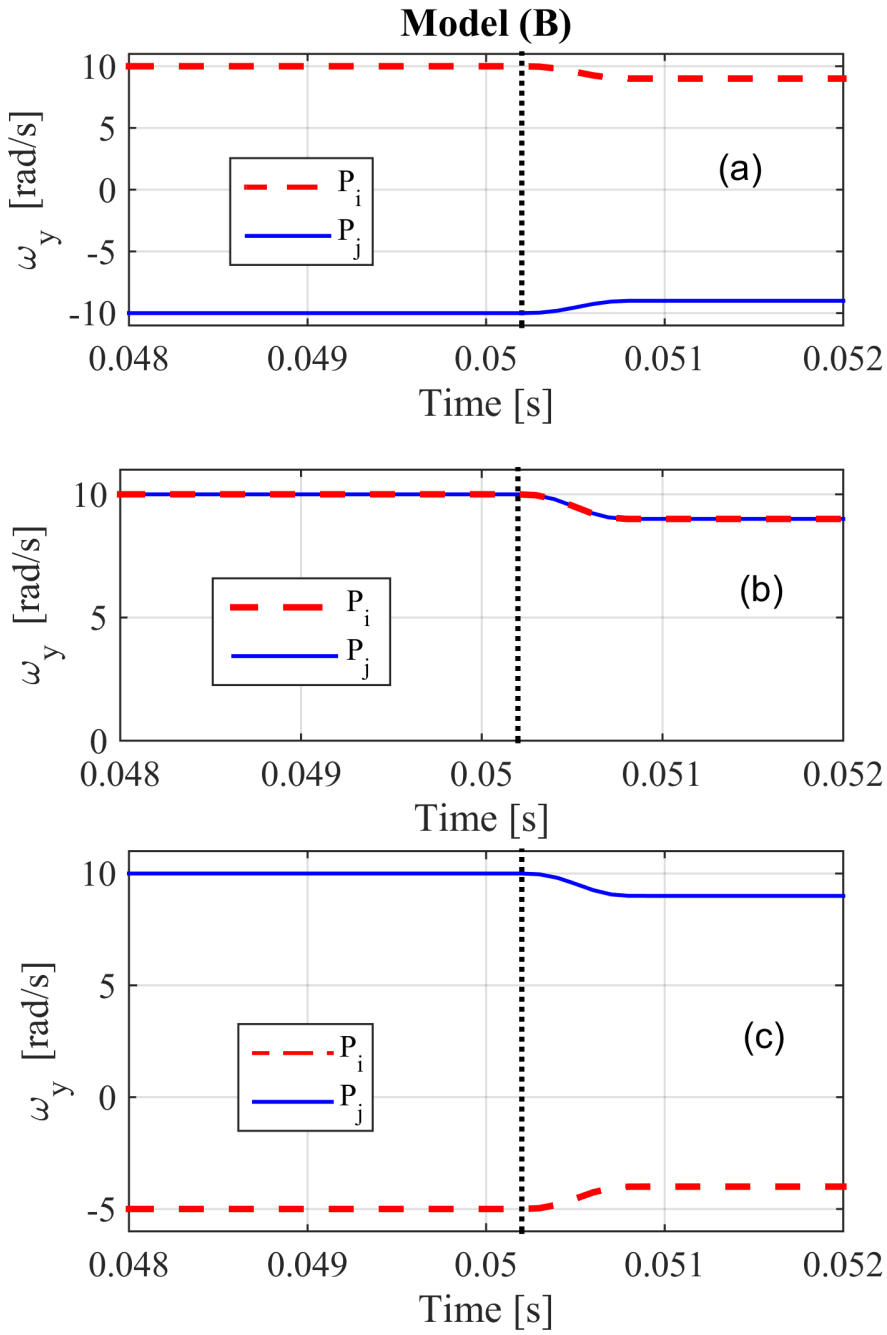

Figure 3.6 Different scenarios for two particle collision and respective change in rotation velocity for Model B (pre and post collision is shown in all plots) a) two particle have equal magnitude of ω but in opposite directions b) two particle have equal magnitude and direction of ω c) two particle have different magnitude of ω in opposite directions. Dotted line represents the instance of contact.

A, although it was known that the oscillation happens for static packings, there was no studies that investigate the presence of this deficiency at a quasi-static flow (i.e. determine possible influences on the flow characteristics). Results from Chapter 3

supported the idea that both models are effective during discharge of particles from a silo (i.e. affecting all the macro-scale parameters). Meanwhile, in Chapter 5, the comparison among results from Model A and Model B with those of Model C (which considered as a proper rolling resistance model) are included. Additionally, results are compared to that of real shape particles also, and this leads to better understanding of the effectiveness/imperfections of the considered rolling resistance models.

3.3 Single-particle level characteristics

This section investigates the influence the both rolling resistance models on single particle level characteristics. As a first step, the collision of two particles is simulated and the rotational velocity is monitored. To distinguish between the effect of rolling friction and sliding friction, a set of simulations has been conducted in the following order: a) with μ_r=0, increase sliding friction (Figure 3.7a) b) increase μ_r with sliding friction off (Figure 3.7b). It is clear from Figure 3.7 that both parameters contribute to decrease in ω after collision (only the mechanism, by which rotational velocity is reduced, differs).

3.3.1 A single disk rolling on a flat surface

To further investigate the frequently employed rolling resistance models, Ai et al. (2011) have conducted an extensive study in 2D. A part of their study is concentrated on the ability of the various models to control the motion of the single particles. The work reports oscillatory motion for particles in the presence of "directional constant rolling friction model" (naming is according to Ai et al. (2011)). They have considered several test cases and proved the occurrence of this phenomenon. On the other hand, the default model in EDEM is similar (in general form) to Model A (there are some fundamental differences that have been discussed before). Thus, it is necessary to conduct test cases (similar to those of employed by Ai et al. (2011)) and determine the occurrence of the oscillations for the default rolling friction model in EDEM. In this respect a simple test, rolling of a single particle on a surface, is repeated for this model as well and results are presented.

As stated in Ai et al. (2011), a single sphere is generated and left to settle under 1g gravity on a flat surface. The translational velocity is set to $V_x i$ =1.0 m/s (as initial velocity), while no angular velocity (ω) is considered for the disk, see Figure 3.8. As motion of the particle starts, due to friction between surface and the particle, the translational velocity decreases and the rotational velocity becomes non-zero (see Figure 3.9a). As it can be seen in Figure 3.9b, the rolling distance increase moderately (up to approximately 0.2 m) and then saturates (particle stops horizontal movement). More-

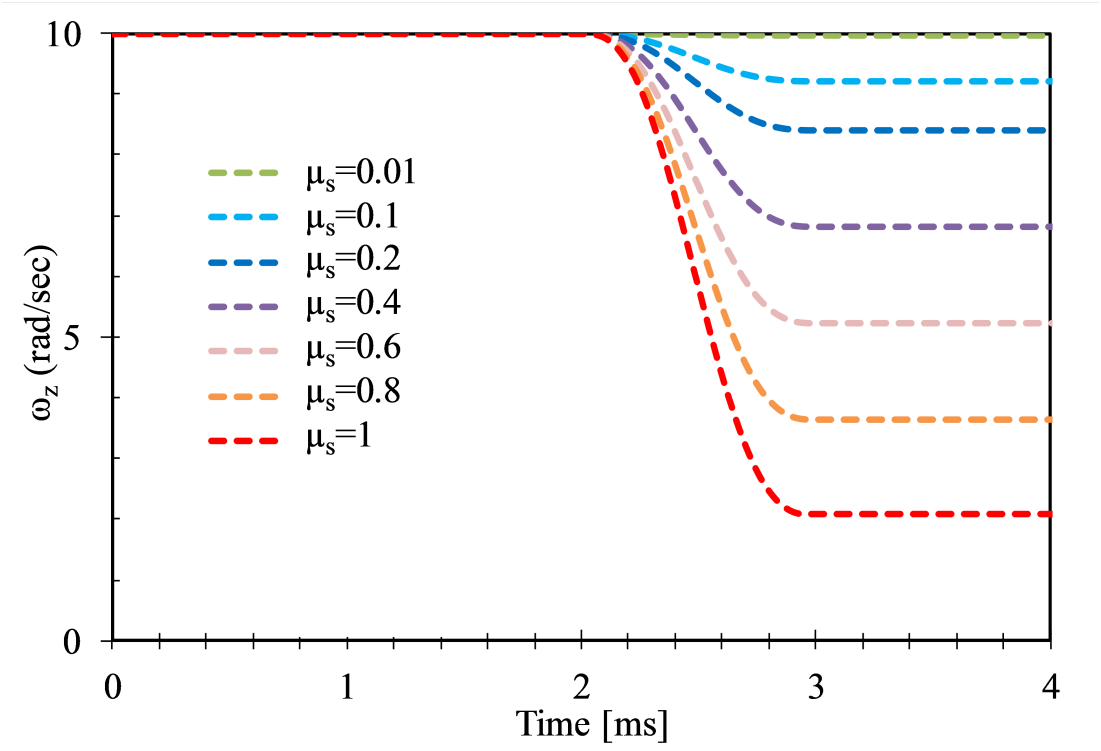

(a)

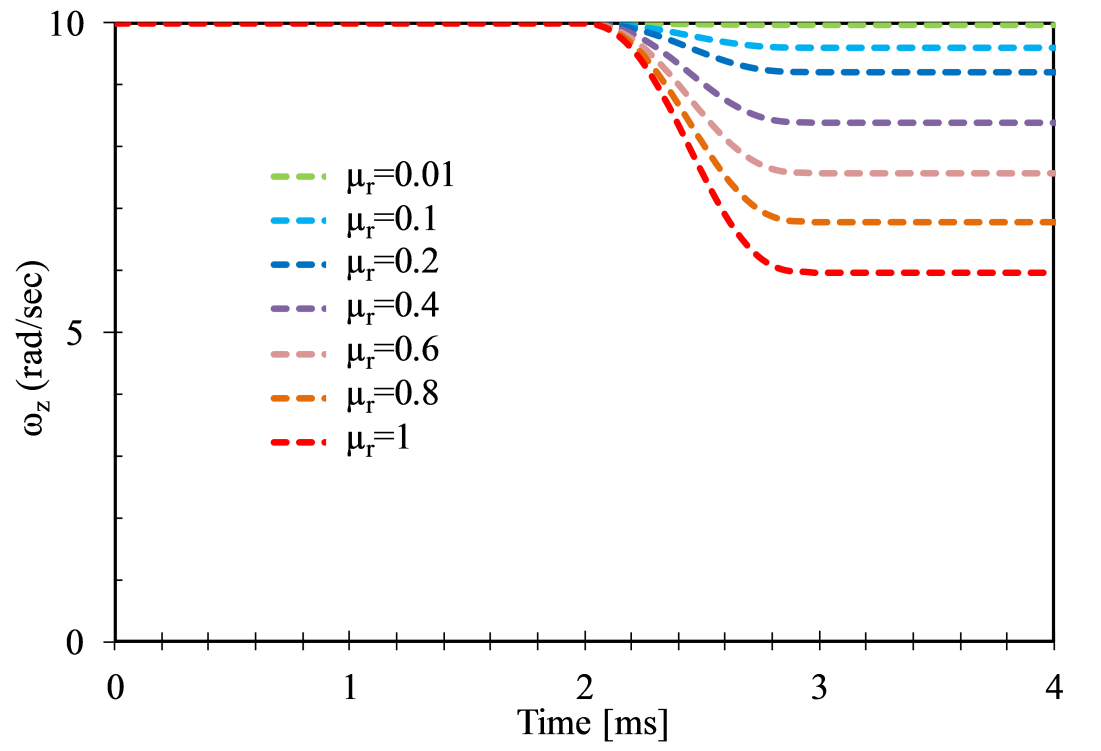

(b)

Figure 3.7 Rotational velocity of a single particle pre and post collision (the initial rotational velocity of the particle is assigned as $10 rad/s$ in clockwise direction) a) rolling resistance is off and only sliding friction is increasing b) sliding friction is off, while rolling friction is increasing.

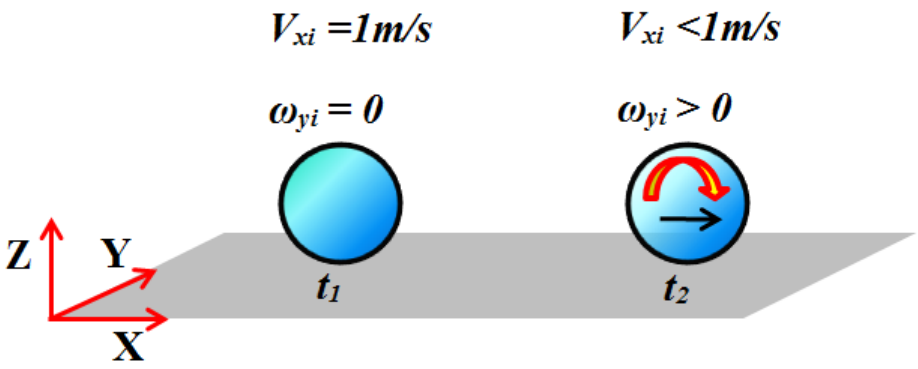

Figure 3.8 Single particle rolling on a flat surface.

over, the rotational velocity reaches a peak value in the initial portion of the motion, which gradually decreases. Additionally, when the particle gets to zero translational velocity, a torque will be applied to the particle and will rotate it backward (since the torque is constantly calculated and applied independent of the magnitude of rotational velocity). At the next time-step, since the direction of the rotation is changed, a torque will be applied in the opposite direction, see Figure 3.10. The successive applied torque leads to a back and forth motion in the resting particle (it is not clear in the Figure 3.9b, however zooming in the area where the particle is stationary clarifies this phenomenon, see Figure 3.9c). The oscillation of the particles results in higher kinetic energy in the system and causes instabilities in the static packings.

The above observations are in line with those of reported by Ai et al. 2011, for Model A. Despite the detailed study in the static case, the existence of this numerical artefact in dense granular flow scenarios (i.e. quasi-static) has not been assessed.

3.4 Effect of the alternating torque on silo flow

Ai et al. (2011) have reported an oscillatory motion for particles when “Directional constant torque” rolling friction model is employed in granular systems. Despite the detailed study in the static case, the effect of this numerical artefact in dense granular flow scenarios (i.e. quasi-static) has not been assessed. In this respect, a model flat bottom silo is simulated to confirm the characteristics of the oscillation of the particles and also, to investigate the influences of the alternating torque on flow characteristics.

The details of the considered granular system are provided in the following sections. The geometric specifications and boundary conditions of the flat bottom silo can be found in section 3.4.1. Additionally, section 3.4.1 summarises the DEM parameters that are assigned for the particle-particle and particle-wall contacts.

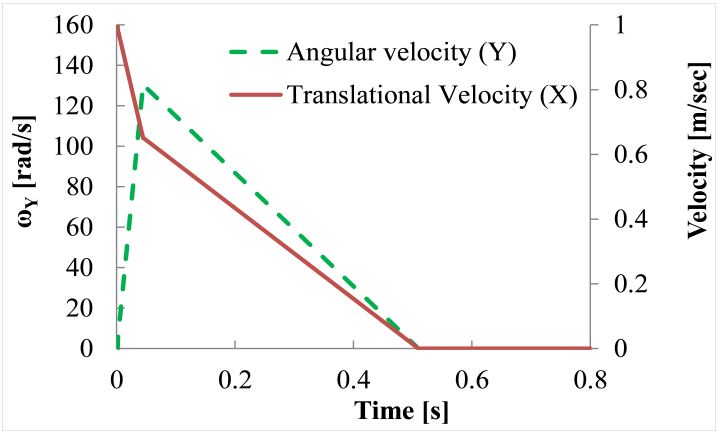

(a)

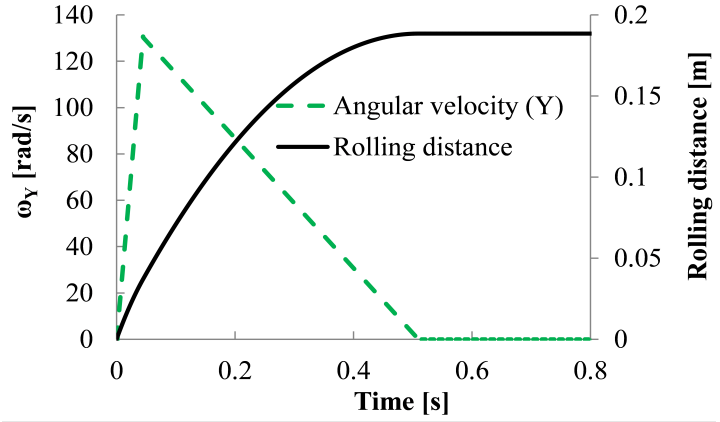

(b)

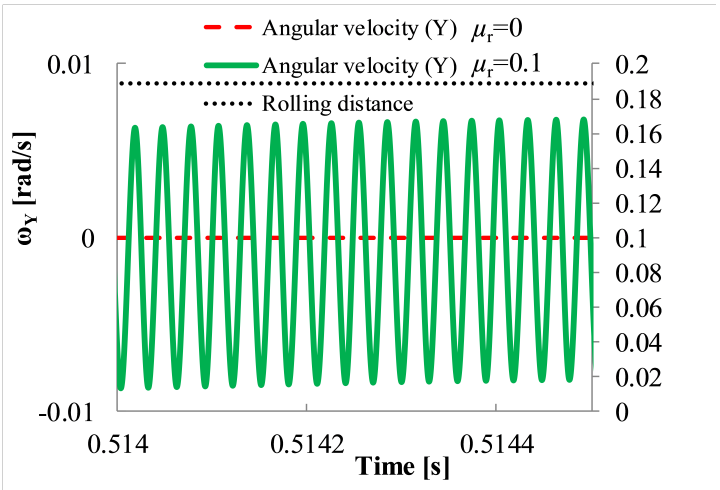

(c)

Figure 3.9 Single particle rolling on the flat surface a) variation of the translational and rotational velocity b) variation of the angular velocity and rolling distance c) smaller temporal window for variation of the angular velocity and rolling distance (for visualisation of oscillation).

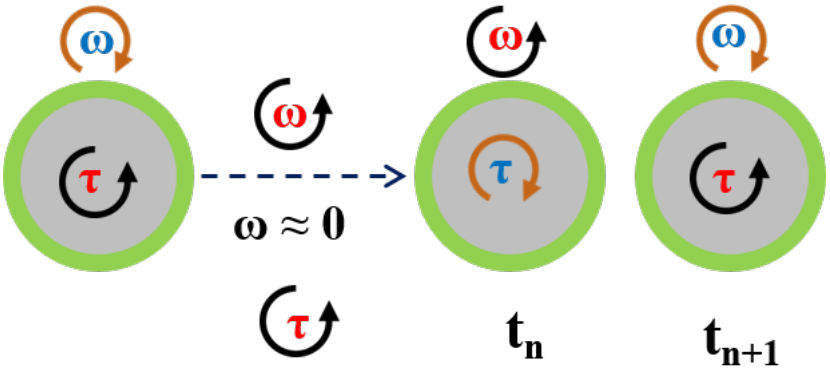

Figure 3.10 Graphical explanation of the oscillation process for a single particle.

3.4.1 Granular system

Current study employed EDEM® 2.7 as particle simulation software (DEM Solutions Ltd. (2014)). A flat bottom silo is considered as the main geometry, as shown in Figure 3.11. Periodic boundary is considered for the model silo in y-direction (depth of silo). The model considers almost 30000 poly-disperse particles. The granular system consists of spherical particles with diameter ranging from 2.8 to 3.2 mm and following a normal distribution (with a mean diameter of 3 mm and a standard deviation of 0.2). The parameters that have been used during the simulations are listed on Table 3.1. A sampling frequency of 200 Hz is considered for saving the particle data.

Table 3.1 DEM parameters.

Parameter	Symbol	Unit	Value
Density	$\rho_{(P)^*}$	kg/m^3	950
Static friction	$\mu_{s(P-P)}$	-	0.577
	$\mu_{s(P-G)^{**}}$	-	0.5
Poisson's ratio	$\nu_{(P)}$	-	0.4
Shear Modulus	$G_{(P)}$	Pa	1E+08
Rolling friction	$\mu_{r(P-G)}$	-	0.001
Coefficient of restitution	$e_{(P)}$	-	0.0001
Particle radius	r	mm	1.5

*P: Particle
**G: Geometry

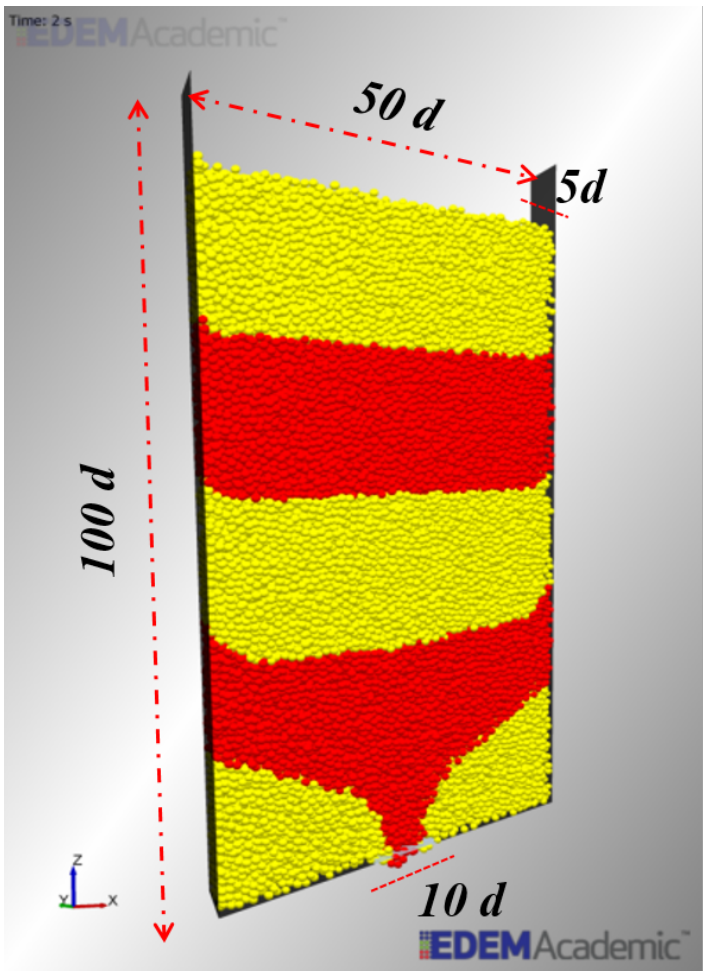

Figure 3.11 Silo geometry (in particle diameter d).

3.4.2 Single particle behaviour

Angular velocity of the particles was extracted with default saving frequency (200 Hz). However, initial observations suggested that the considered saving interval can lead to crude raw data for study of the particle oscillation. Accordingly, the first step was to adjust the appropriate saving period and frequency. Results for 5, 0.1 and 0.01 msec saving intervals have been shown in Figure 3.12. It is clear that 5 msec interval is missing necessary details for study of the oscillation, whereas 0.01 and 0.1 msec intervals seem reasonable. However, saving with 0.01 msec interval leads to dump files which are too large. Thus, a saving interval of 0.1 msec is selected for the rest of the studies.

In order to detect the oscillation inside the silo, several particles have been selected from various regions (bottom (S_1 and S_2), top (S_3 and S_4), mid-height (S_5 and S_6), near the outlet (S_7)), see Figure 3.13. These particles are selected at the end of filling, and then the rotational behaviour of each particle is monitored during the discharge. The location of particle are representing different regions in the silo (i.e. S_1 and S_2

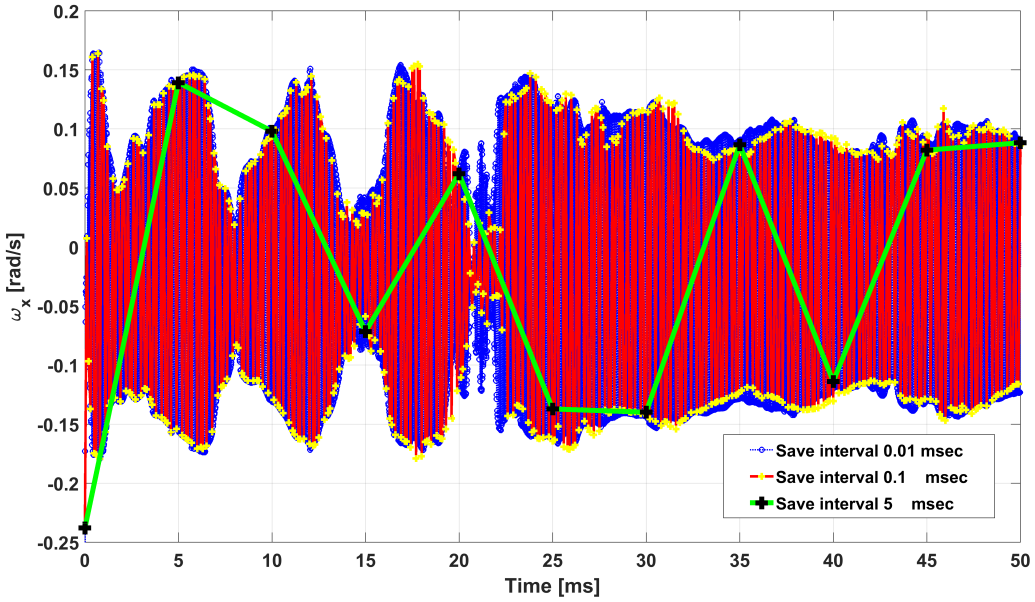

(a)

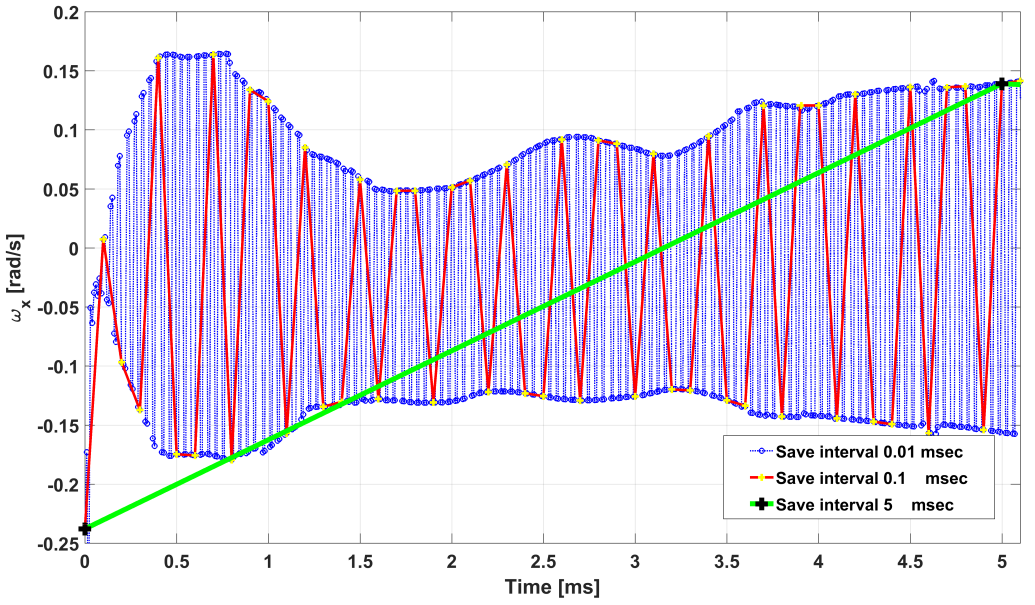

(b)

Figure 3.12 Angular velocity of a single particle with different saving time frequencies.

represent the particles in the dead-zone, S_3, S_4 and S_5 represent mass flow region, S_6 represents the transition between mass flow and stagnant zone and S_7 represents fast flow channel). The detailed rotational velocity around X, Y and Z axis are shown for the considered particles in Figures 3.14, 3.16, 3.17, 3.18 (note that the case with $\mu_{r(A)}$=0.1 is considered for this section, and results shown are for 10 % of discharge duration). The time trace for single particle angular velocity confirms the alternating rotation around zero, except S_7, which seems to follow a different trend of oscillation (due to its location, S_7 can be considered as a free falling case). Accordingly, it holds true to conclude that if a particle is in a densely packed region (e.g. stagnant zone or mass flow zone), it can be susceptible for oscillation. A cumulative rotation map for the particles during discharged has been provided (see Figure 3.19), which depicts the location of the shear bands. It is seen that near the boundaries (i.e. side walls) and the area between stagnant and flowing zone, there exists a high rotational velocity. As a result, based on the observations, it can be concluded that any particle laying out of shear band region is most probably undergoing oscillation. Additionally, for S_1 particle, oscillations has been shown on a smaller temporal window (see Figure 3.15a), which clarifies the magnitudes of the oscillation around different axis. Moreover, displacement in X, Y and Z directions are also presented for S_1 and S_7, respectively in Figures 3.15b and 3.18b. It is clear that S_1 is almost stationary, whereas S_7 experiences large displacements.

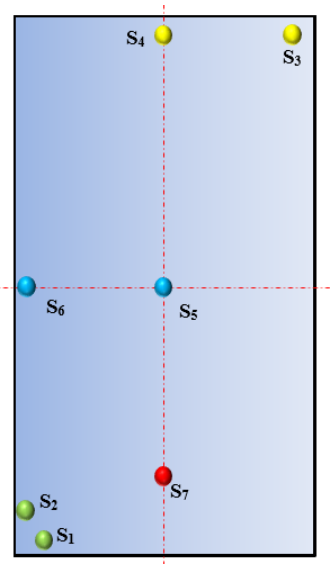

Figure 3.13 Location of the selected particles for further analysis of the oscillation inside the silo.

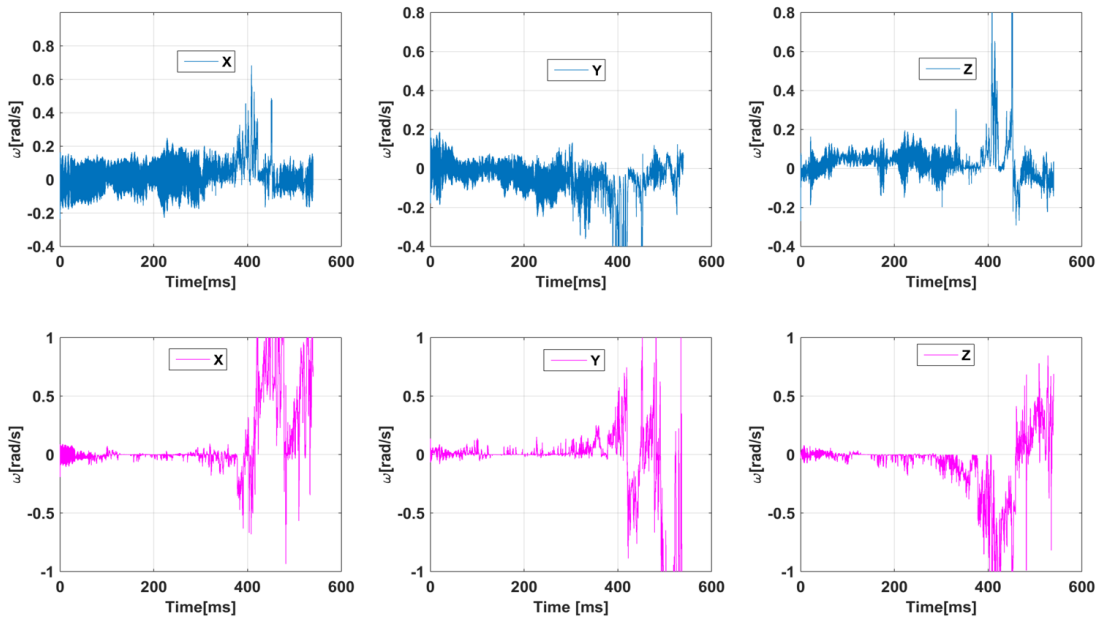

Figure 3.14 Time trace for single particle angular velocity around X, Y and Z axis for selected particles a) S_1 b) S_2.

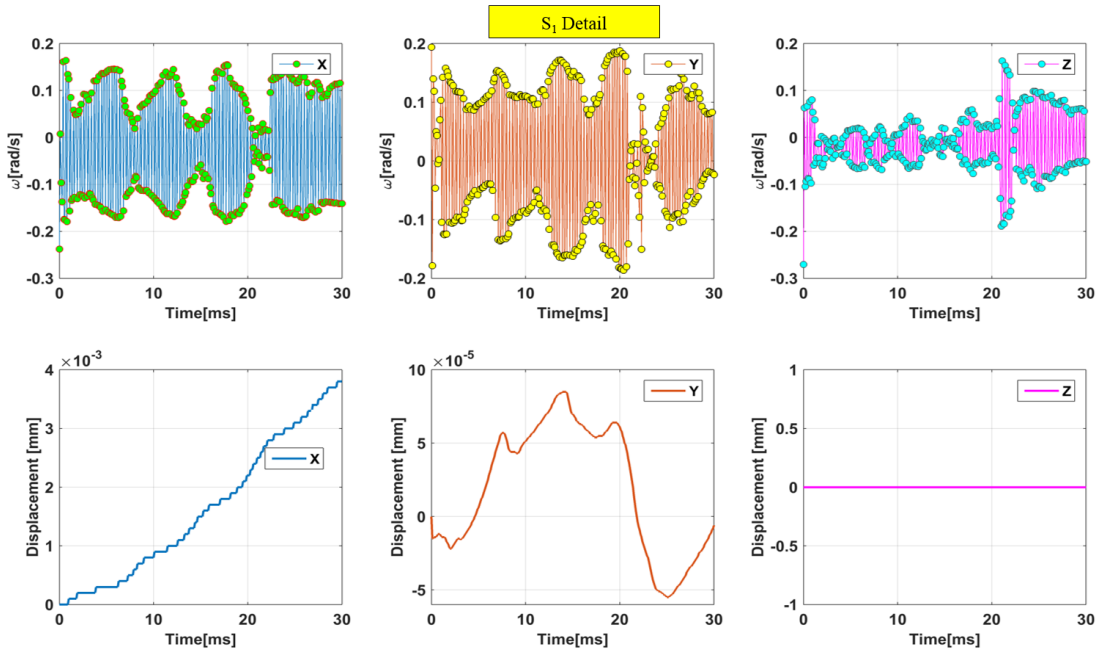

Figure 3.15 Detailed motion of S_1 particle a) rotational velocity around X, Y and Z axis in temporal window b) displacement of the particle in X, Y and Z directions.

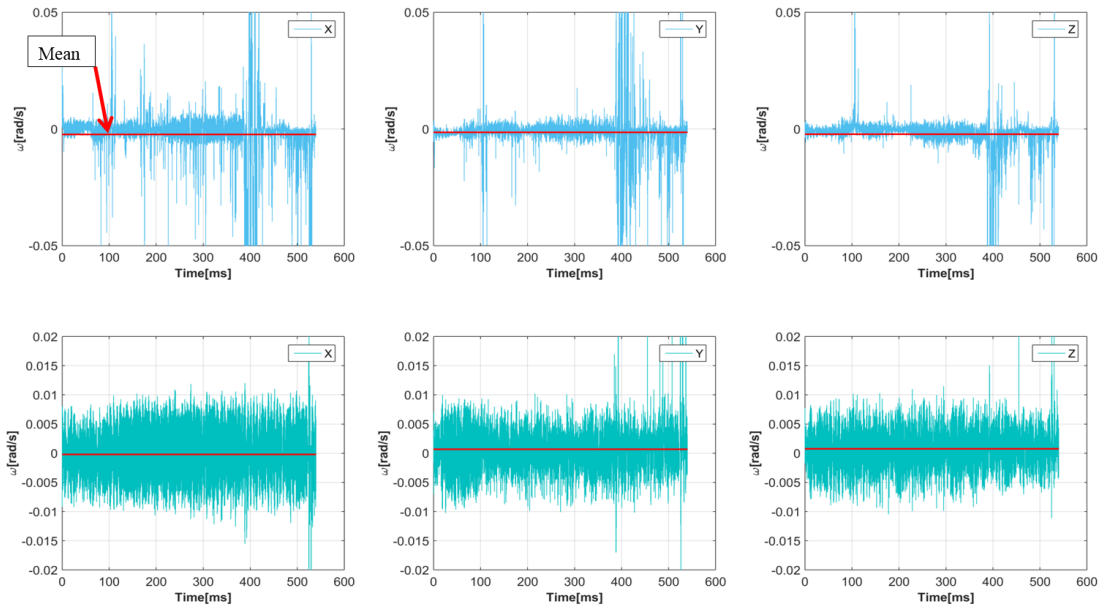

Figure 3.16 Time trace for single particle angular velocity around X, Y and Z axis for selected particles a) S_3 b) S_4.

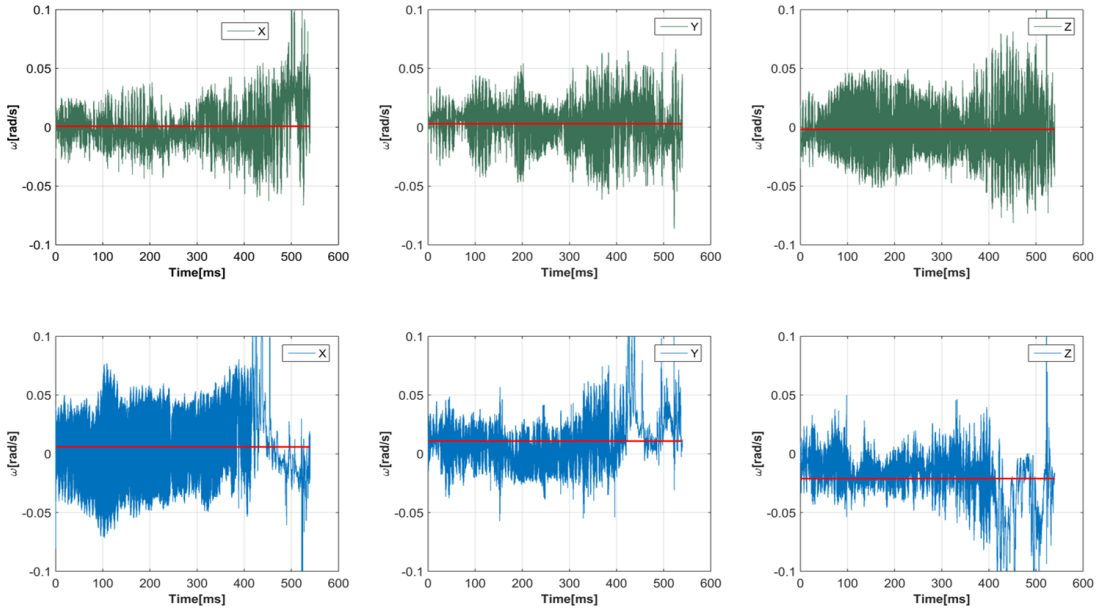

Figure 3.17 Time trace for single particle angular velocity around X, Y and Z axis for selected particles a) S_5 b) S_6.

3.4.3 Fast Fourier transform analysis

Fast Fourier transform (FFT) is a useful mathematical tool, which converts time domain data to frequency domain representation. In our case, FFT allows obtaining the

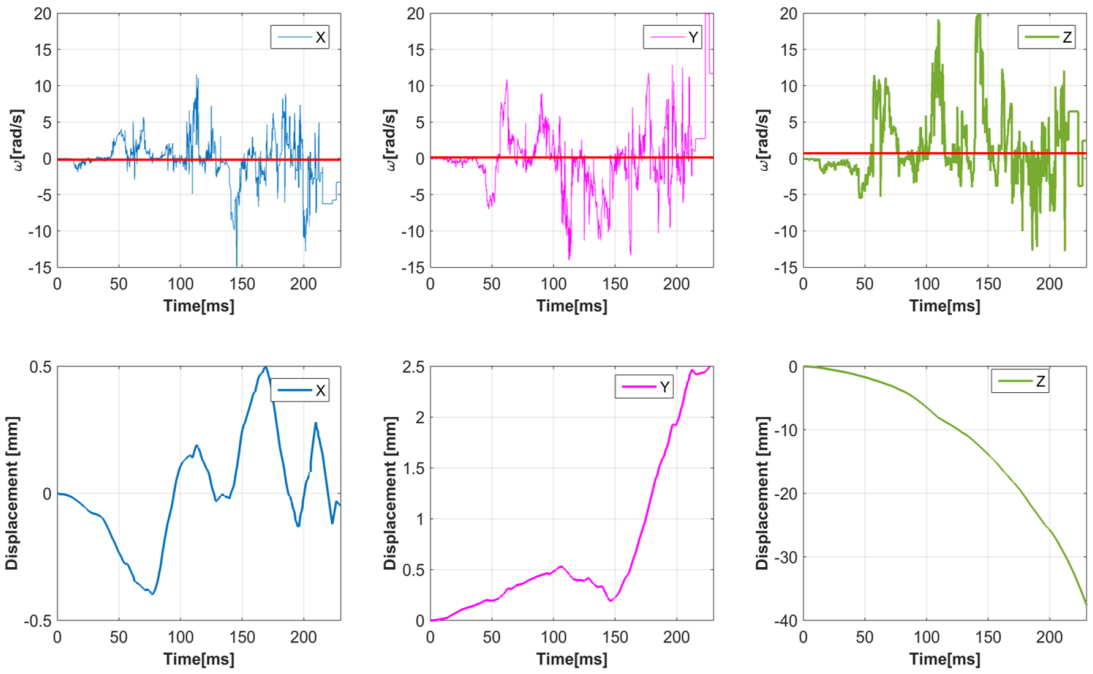

Figure 3.18 Detailed motion of S_7 particle a) rotational velocity around X, Y and Z axis b) displacement of the particle in X, Y and Z directions.

main frequency of the rotational velocity fluctuations. Power spectrum analysis supports the existence of the alternating motions in the granular system, see Figure 3.20. It is clear that the frequency of the fluctuation are around the same magnitude (i.e. 166 kHz). Considering the point that the time-step considered for the simulation is 3e-6 (which equals to 333 kHz), it can be deduced that the dominant frequency is half the time-step frequency.

Further analysis has been carried out to determine whether the frequency of the oscillation changes over the time. In this respect, the angular velocity for a single particle is extracted over 400 msec and evaluated over successive 50 msec spans (i.e. the main frequency is obtained at 8 intervals), see Figure 3.21. Results depicts that even though the power of the fluctuations changes, the frequency remains constant (supports the observations in 3.20).

To evaluate the influence of the magnitude of μ_r on the oscillation characteristics of the single particles, an additional simulation has been conducted with half of the initial rolling resistance coefficient (i.e. $\mu_{r(A)} = 0.05$). The results from power spectrum analysis show that the frequency of the oscillation is independent of the considered μ_r value, see Figure 3.22.

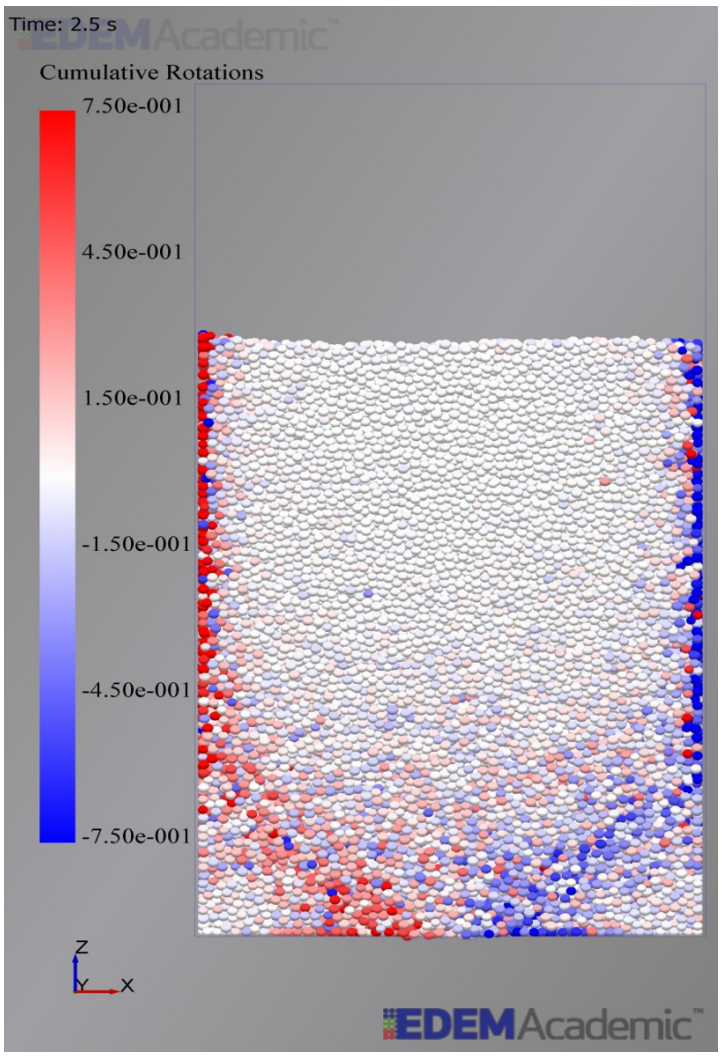

Figure 3.19 Cumulative rotation representation for the discharging particles (note that clockwise direction is considered as positive, and simulation is for $\mu_r = 0$ case at 30% of discharge).

3.4.4 Time-step effect

Though, the presence of oscillation in the single particles has been confirmed, it is not yet known if the bulk response is affected by this. Moreover, since the frequency of the oscillations is shown to be a function of the assigned time-step, a two set of simulations with different time-steps are conducted: for the first one time-step is assigned as 4 % of the Rayleigh time-step (5.5e-7 s) and the second one has 20 % of the Rayleigh time-step (3e-6 s). It is seen from Figure 3.23 that the power (amplitude) of the oscillation is also a function of the assigned time-step (i.e. larger time-step causes smaller frequency but larger amplitude).

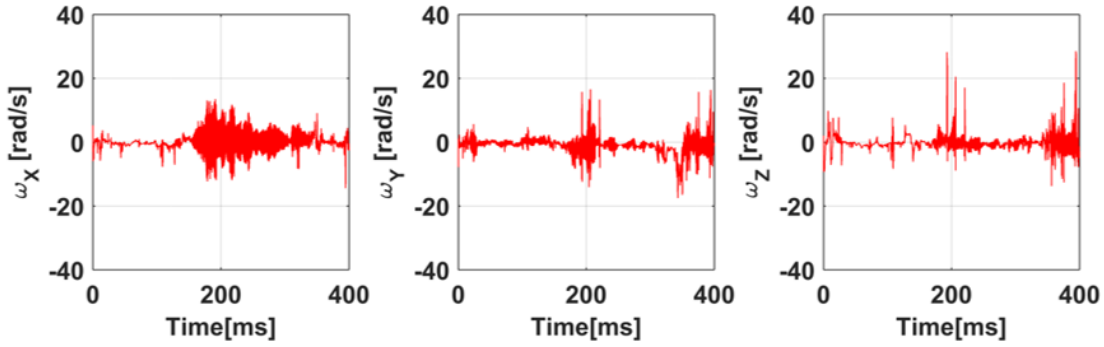

(a)

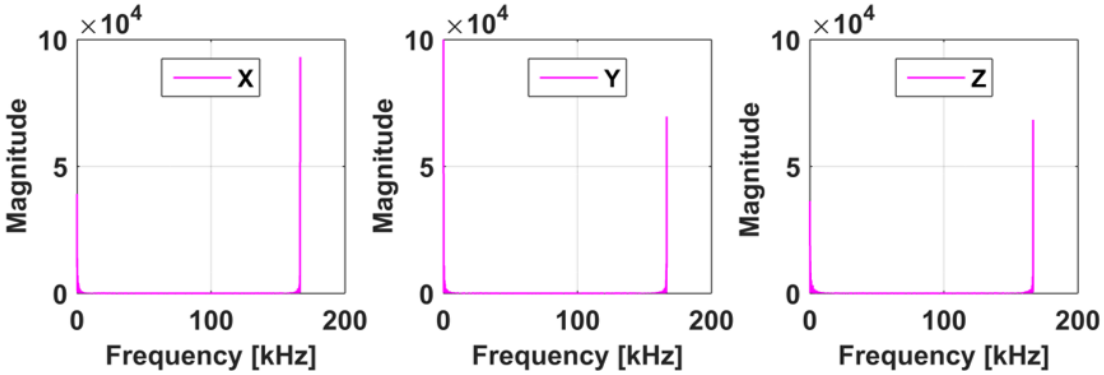

(b)

Figure 3.20 Power spectrum analyses of angular velocity for single particle (it is located at similar position to S_3 in Figure 3.13).

To investigate the effect of changing the time-step on flow characteristics, the cumulative mass discharge, total rotational kinetic energy, vertical and horizontal velocity profiles of both cases with different time-steps are compared.

Results in Figure 3.24 shows that the cumulative mass discharge is only affected by less than 3 %, which in this case is not significant (this may become more influential in static regimes). Additionally, for one of the cases mass flow rate is also computed and since it is fluctuating, power spectrum analysis is performed over the results, see Figure 3.25. It is clear that there exist no such dominant frequency in the mass flow rate over time.

The total rotational kinetic energy (K_R) of both granular assemblies has also been computed for the whole discharge process and presented in Figure 3.26. Similar to the results of cumulative mass discharge over time, the total rotational kinetic energy of the granular systems has been affected to a small extent by the adopted time-step. K_R is defined as (note that the total value is obtained by summing K_R value of individual particles):

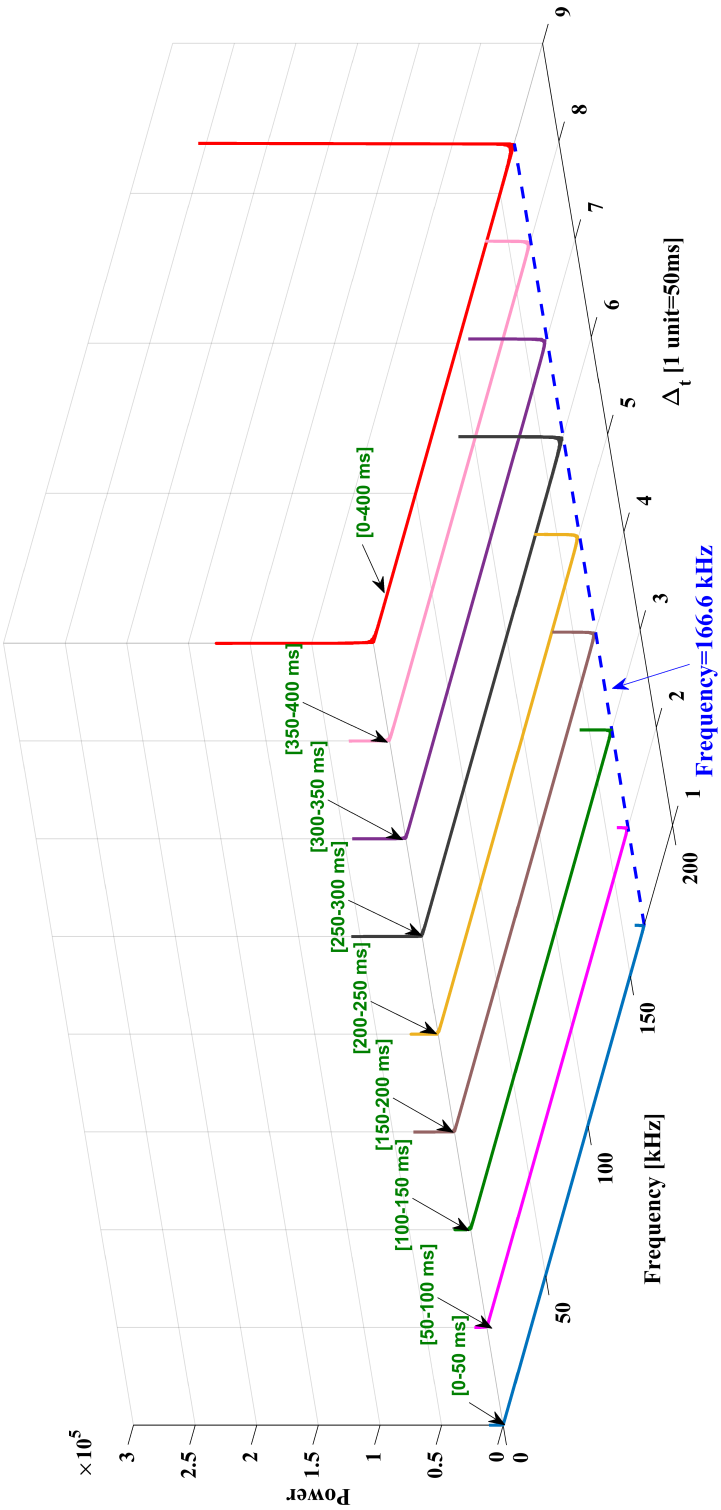

Figure 3.21 Determining the variation of oscillation frequency at various steps of the discharge process.

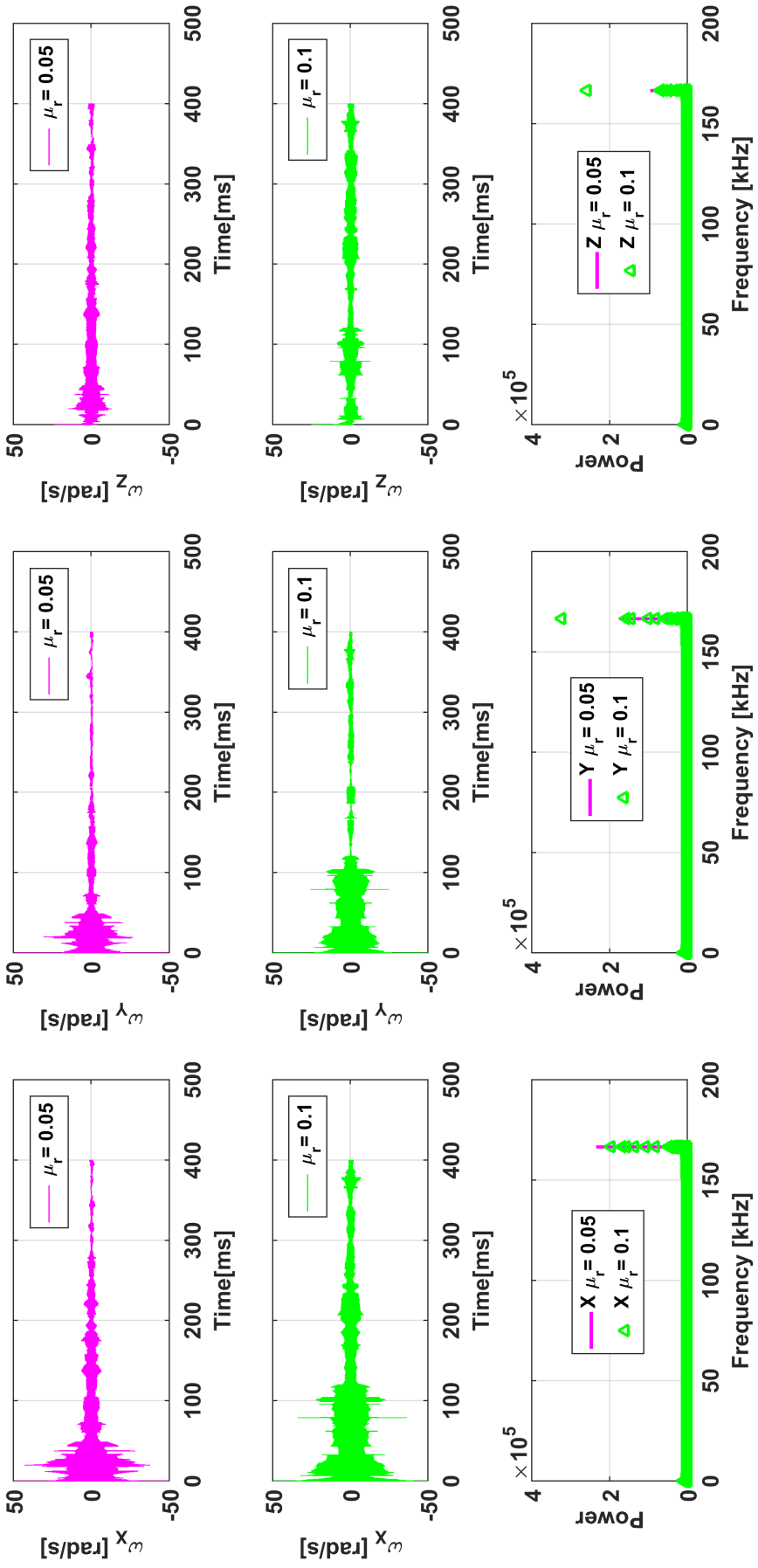

Figure 3.22 Effect of rolling resistance coefficient on oscillation characteristics of the single particles.

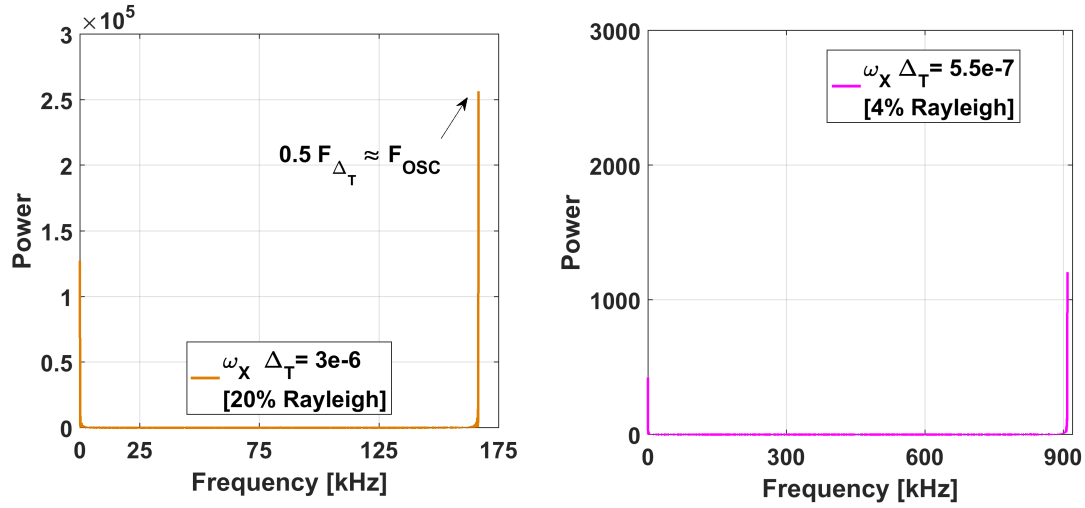

Figure 3.23 Power spectrum analysis for the cases with different time-steps (4 % and 20 % of the Rayleigh time-step).

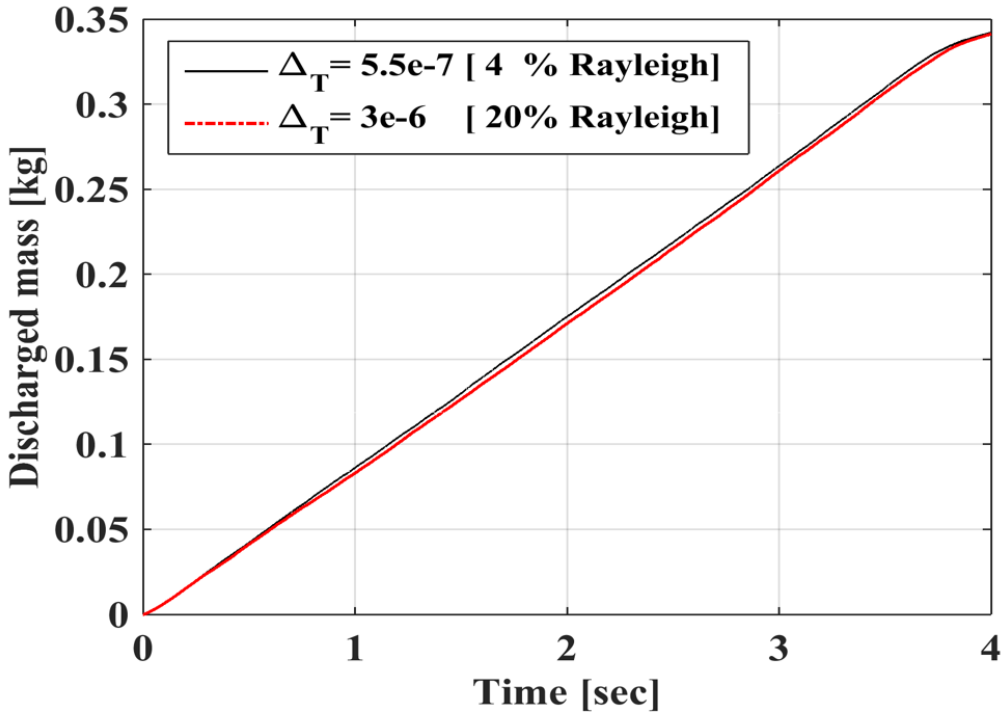

Figure 3.24 Cumulative mass discharge over time for the cases with different time-steps (4 % and 20 % of the Rayleigh time-step).

$$K_R = \sum_{n=1}^{N_p} 0.5 I \omega^2 \tag{3.9}$$

where, I is the moment of inertia and N_p is number of particles.

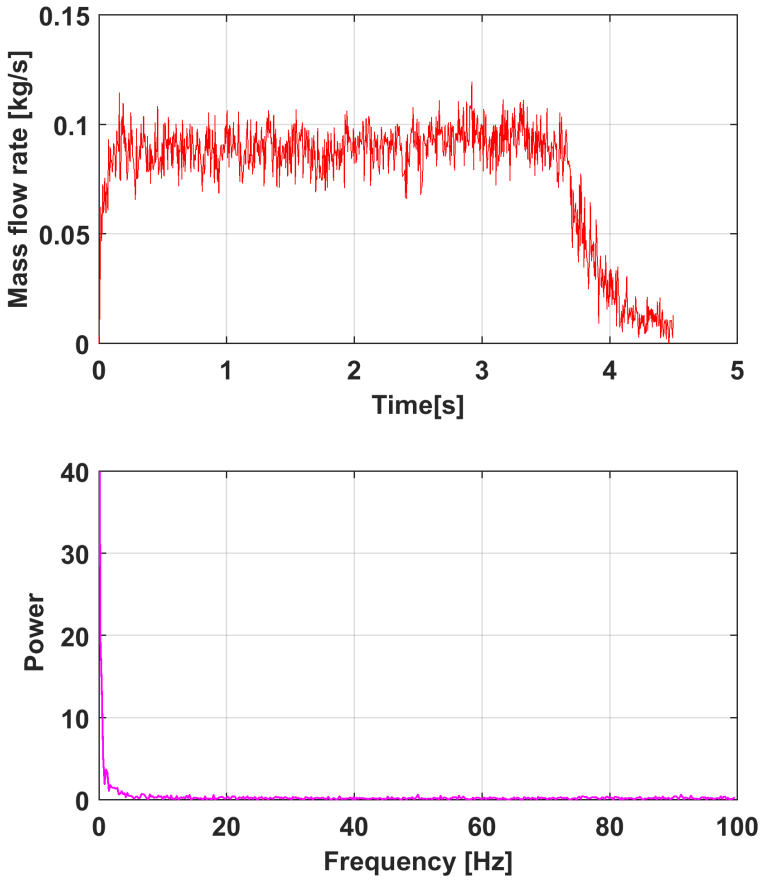

Figure 3.25 Power spectrum analysis for mass flow rate over time a) mass flow rate (for 4 % of the Rayleigh time-step) b) frequency domain representation of the mass flow rate.

Velocity distribution of the particles are obtained from P4 (coarse-graining tool, see Section 3.1.1) and cross-sections have been defined at two different heights, as shown in Figure 3.27. The velocity data has been obtained at three different stages of the discharge (0.45, 0.85 and 1.45 s). The vertical velocity plots for two time-step diverges at H=50 and 100 mm. It is seen that the increase in time-step slows down the vertical velocity. This can be a mutual influence of change in the calculated contact forces (which is dependent on the time-step) and also the presence of the alternating torque (a further study needs to be foreseen, which is independent of the time-step). On the other hand, time-step dependency is smaller in case of the horizontal velocity distribution (except in one time window 1.45 s at 100 mm height), see Figure 3.29.

Finally, comparing results of two cases, one with small and the other with relatively larger time-step, it is clear that the bulk scale response of the granular assemblies can be affected to some extent by the presence of oscillations. However, to minimize the

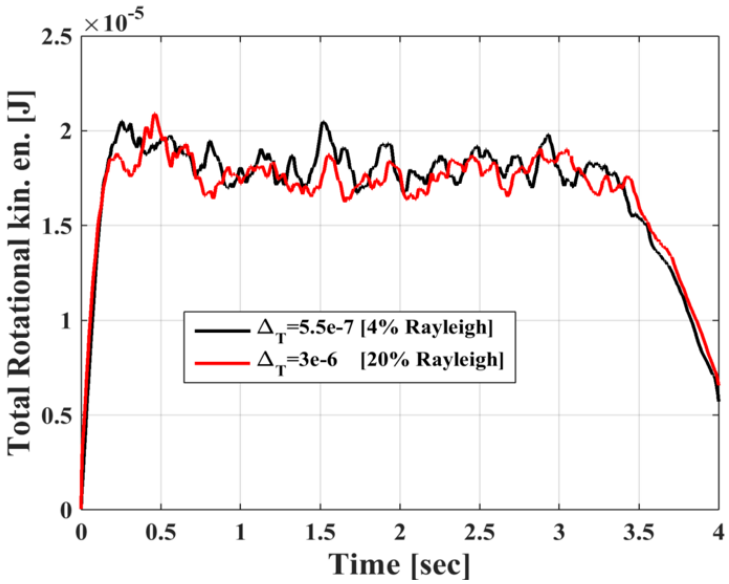

Figure 3.26 Total rotational kinetic energy over time is shown for the cases with different time-steps (4 % and 20 % of the Rayleigh time-step).

effect of oscillations, smaller time-steps must be considered while utilizing this type of rolling resistance models.

3.5 Effect of rolling friction models on filling state

This section shows the sensitivity of the bulk results to the applied rolling resistance models. Accordingly, the evolution of macro-scale data, by means of solid fraction, stress distribution, flow pattern and mass discharge rate, is evaluated at both filling and discharge states. In all simulations, the value of the rolling friction coefficient is considered equal for particle-particle and particle-wall contacts. Additionally, for all the results the case without rolling friction (μ_r=0) is also presented to enhance the isolation of rolling resistance effect.

3.5.1 Initial packing

The packing of the grain assembly at the end of the filling is described here in terms of the solid fraction (ϕ_s), here obtained as the ratio of the total volume of particles in a horizontal slice of the silo to the volume of the slice (the height of silo is divided into 15 equal-size slices). Figure 3.30 presents the variation of ϕ_s along the height (H) of the silo for different values of μ_r for each model, showing that increasing rolling resistance results in decreasing solid fraction for both models, which is in line with observations of Fukumoto et al. (2013). This is expected, since the rolling resistance at contacts, provide a more stable arrangement of the particles, and thus the voids are

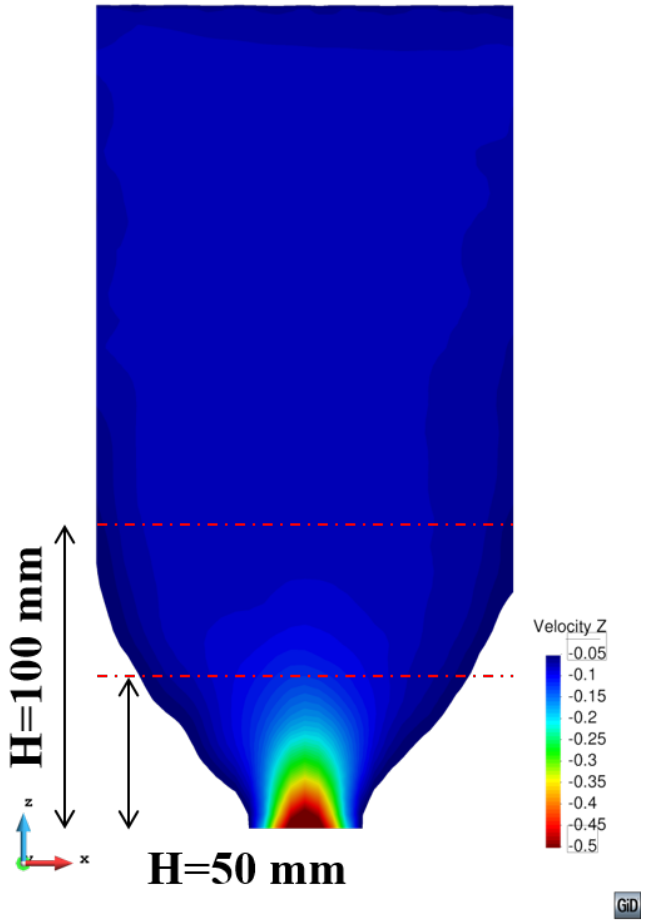

Figure 3.27 Velocity distribution in Z direction (downward), obtained through *CG* (this is for μ_r =0 at 10% of discharge).

increased (increasing in number of stable contacts, by considering rolling resistance, is also reported by Shen (2013)).

In general, every rolling resistance model aims to mimic the attributes of irregular shapes from various aspects. Meanwhile, packing of granular material is not always following a simple trend toward shape complexity; for instance, in case of aspect ratio, Li et al. (2010) observed the following: for cone particles, packing density increases only up to aspect ratio of 0.8 and then reduces, whereas, for cylinders, increase in packing density is limited to aspect ratio of 0.9. Consequently, despite the direct proportionality of rolling resistance and solid fraction, the effect of shape complexity on packing characteristics is more complex and depends on various factors.

3.5.2 Stress distribution (end of filling)

Determination of stress distribution inside a silo, both during filling and discharge states, is essential for a safe and economical design. The lateral stress ratio, which

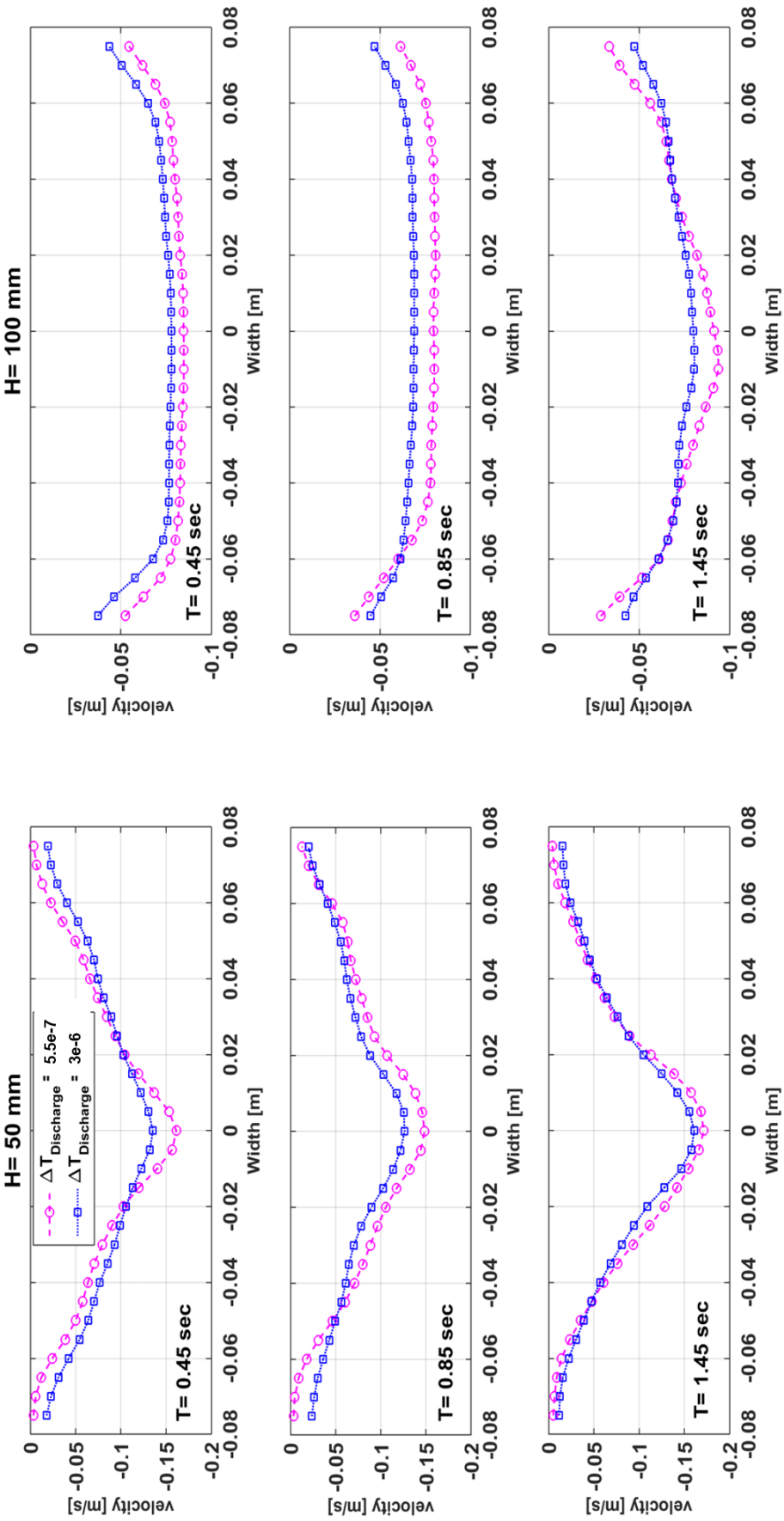

Figure 3.28 Vertical velocity distribution for two cases with different time-steps (results are obtained at 3 consecutive times and 2 two different heights

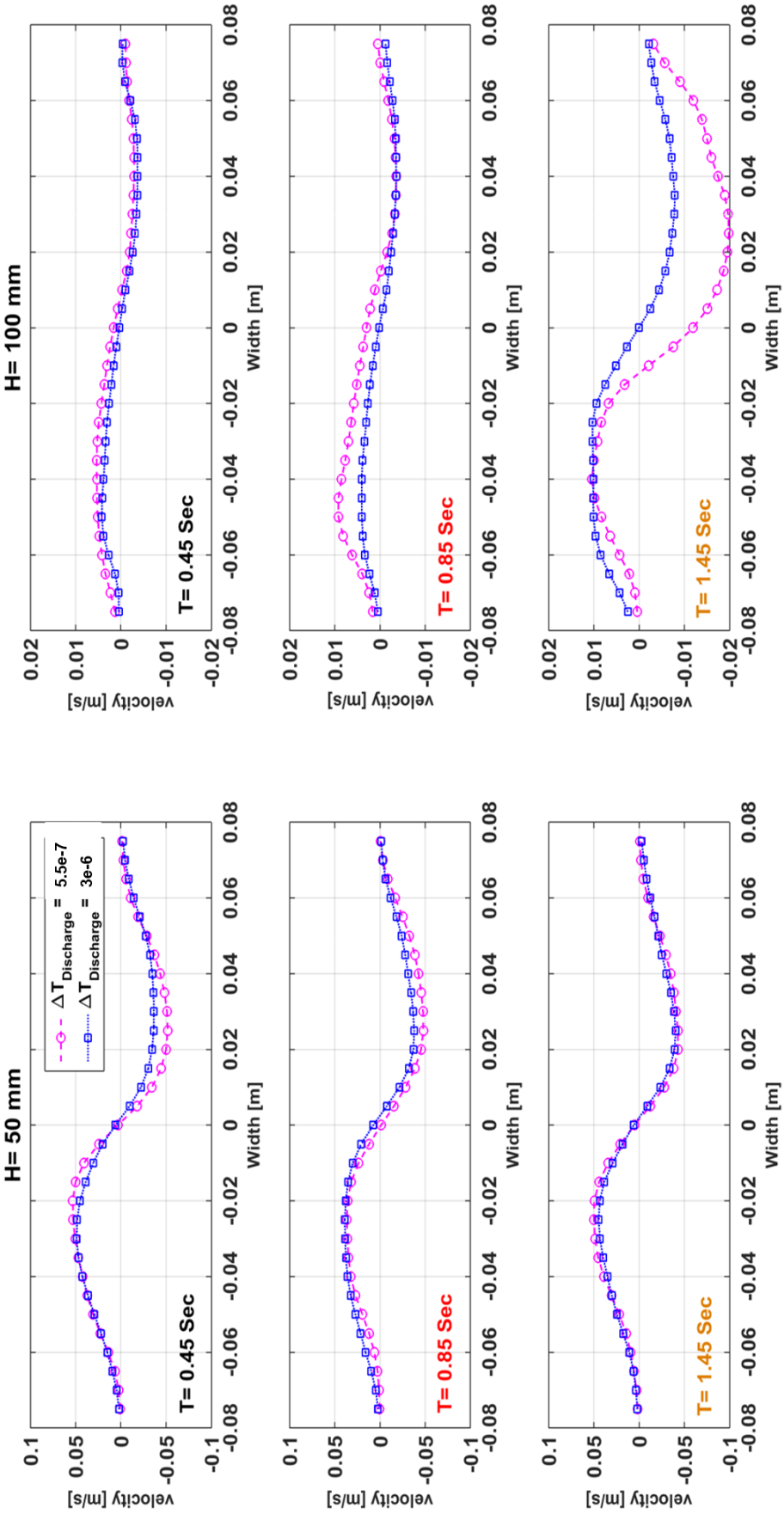

Figure 3.29 Horizontal velocity distribution for two cases with different time-steps (results are obtained at 3 consecutive times and 2 two different heights).

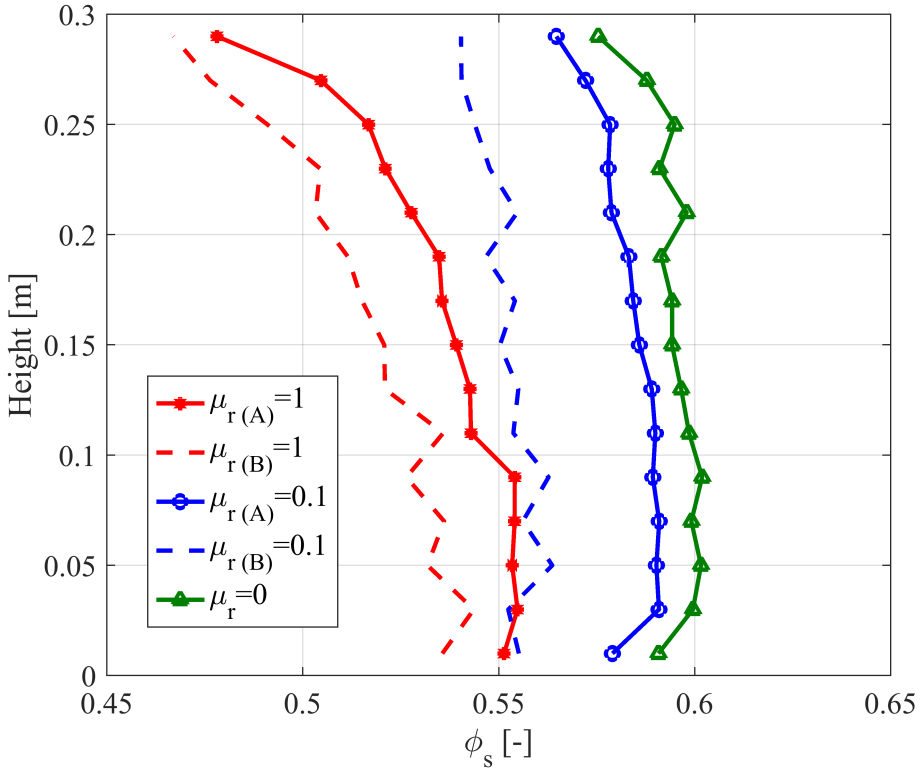

Figure 3.30 Influence of rolling resistance on solid fraction at the end of filling.

is the ratio of the wall normal stress to the mean vertical stress, is known as a good indication of the stress distribution in the granular systems. The lateral stress ratio can vary usually between 0.3 and 0.6 (Kwade et al. (1994)) and barely exceeds these values. However, lateral stress ratio is 0 for a perfectly rigid, inelastic solid body, whereas it equals 1 for a Newtonian fluid (Schulze (2008)). The lateral stress ratio inside a filled silo, which is known as at rest lateral pressure ratio (K_0), has been approximately related to the angle of internal friction ψ_i of the solid as (proposed by Jaky (1948)):

$$K_0 = 1 - \sin(\psi_i) \tag{3.10}$$

The K_0 value in Equation 3.10 is valid for an ideal condition, where the vertical and horizontal stresses are principal stresses, and both are uniform and walls are frictionless. In contrast, within a filled silo, the major principal stress is only oriented vertically along the silo axis and deviates from vertical toward the walls. Considering this heterogeneity in the stress distribution, the European standard EN 1991–4 (2007) defines the filling value of K_f for design purposes as:

$$K_f = 1.1(1 - \sin(\psi_i)) \tag{3.11}$$

For the currently studied granular system, with $\sin(\psi_i)$ =0.577, the K_f value is approximately 0.55 (according to Equation 3.11).

The coarse graining (CG) provides maps of horizontal and vertical stress distribution in the silo, which makes it is possible to monitor local variation of stress in the system (it is important to note that CG faces deficiencies near the boundaries, where the particle data is averaged with the space beyond the boundary). Figure 3.31 shows the distribution of stress ratio (i.e. the ratio of horizontal to vertical stress) for the three different cases (note that the presented values are slightly different from K, which is defined as the wall normal stress to mean vertical stress); packing with no rolling resistance μ_r =0 and also two cases with a very high value of rolling friction coefficient for each of the models (i.e. $\mu_{r(A)}$= 1, $\mu_{r(B)}$= 1). Results show that with μ_r>0, there is a smaller stress ratio in the system. Masson and Martinez (2000) have compared the

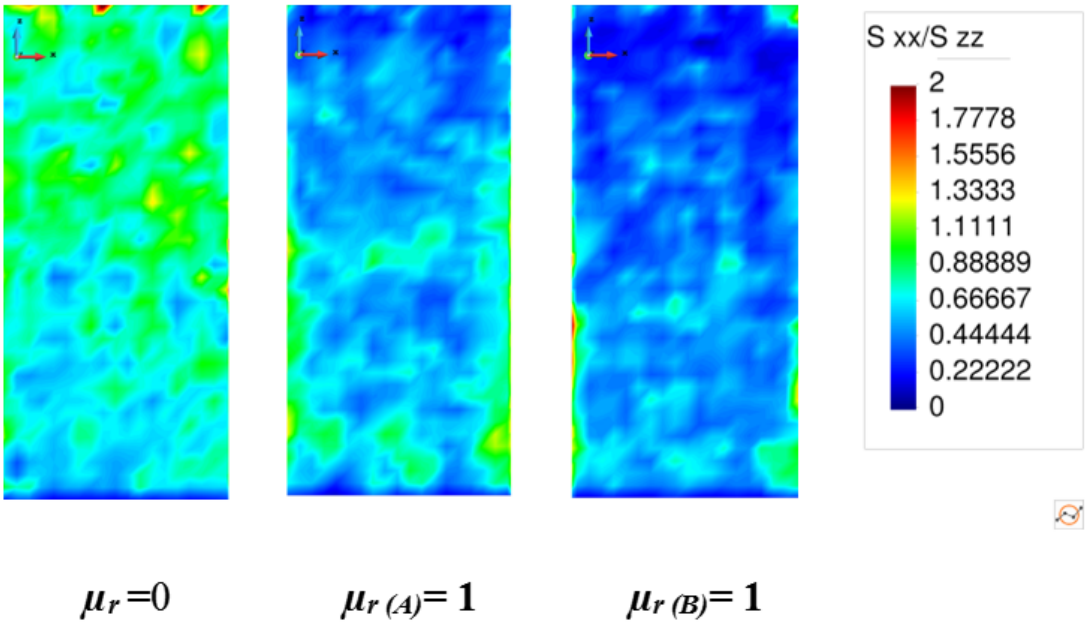

Figure 3.31 Effect of rolling resistance on stress distribution (ratio of horizontal to vertical stress).

contact force network for particles with and without friction inside a plane rectangular silo (before start of discharge). It is seen that including friction leads to increase of local heterogeneity of the stress transmission. Whereas, for the frictionless case, the contact force magnitude is relatively uniformly distributed. Additionally, it is shown that for the frictional practices the majority of the contact forces are aligned the gravity direction. Considering the observations by Masson and Martinez (2000), a possible justification for Figure 3.31 can be stated as: rolling resistance is known as an additional friction component, which in our case will contribute to build stronger contact networks (vertically oriented) for $\mu_{r(A)}$= 1 and $\mu_{r(B)}$= 1 packings. Accordingly, most

of the overburden pressure is carried directly to the bottom of the silo (resulting in higher vertical stress), and therefore K_f ratio will be smaller than that of μ_r =0.

3.6 Effect of rolling friction models on discharge

This section explores in depth the influences of considering rolling resistance at contacts, considering mass flow rate, flow profiles and the stress distribution (horizontal and vertical). Results are qualitatively compared to those observed for the non-spherical particles and the capability of mimicking the shape parameter is discussed.

3.6.1 Mass flow rate

The influence of applying both Model A and B rolling resistance torque on flow characteristics is further explored by showing the mass flow rate over time. As expected, both rolling resistance models suppress the rotational freedom of the discharging particles, which results in lower mass discharge, as shown in Figure 3.32.

Moreover, total mass discharge percentage for both models (at a certain temporal window) is represented in a single graph as function of μ_r, see Figure 3.33. It is clear that Model A presents a linear decrease in amount of mass discharged and saturates at $\mu_{r(A)}$= 1. As it is clear from Figure 3.31, Model B has lower mass flow rate than Model A for similar values of μ_r. Accordingly, a sharper drop is clearly observed for Model B in Figure 3.32, and it saturates at $\mu_{r(B)}$= 0.5.

3.6.2 Flow profiles

Figure 3.34 shows different snapshots of the discharge process (at 10, 50 and 80% of mass discharged (M_D)) for Model A and B with various μ_r values. The case with no rolling resistance (μ_r= 0) is also shown to help better understanding of the change in flow behaviour. The obtained results are consistent with the nature of a flat bottom bin, which gives rise to funnel flow. Following is a description of flow characteristics for μ_r = 0, $\mu_{r(A)}$=0.2, $\mu_{r(A)}$=1, $\mu_{r(B)}$=0.1 and $\mu_{r(B)}$=0.5:

Looking at M_D=10%, it is clear that depending on the value of the applied μ_r, the flow propagates at different angles with respect to the horizontal. This leads to a change in height of the effective transition zone, where the flow channels intersect the silo walls (i.e. it is transferred to a higher elevation in both cases by increasing μ_r). Accordingly, flow is separated into upper and lower section at in which the former has mass flow and the latter presents funnel flow in both models and also in μ_r= 0. Additionally, it can be seen that increasing μ_r value, for the both models, results in a narrower flow channel and also causes enlargement of the not flowing (stagnant) zones.

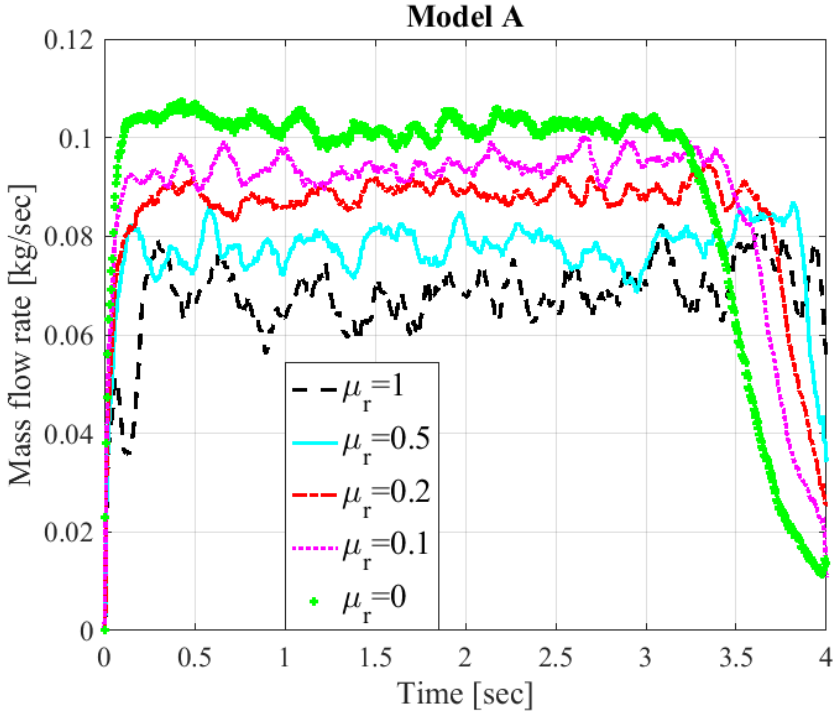

(a)

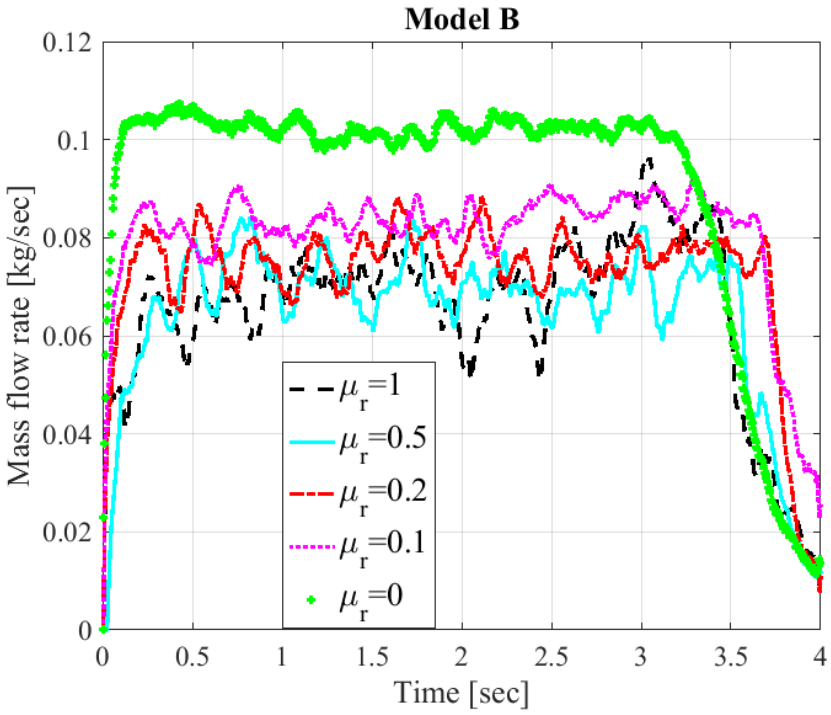

(b)

Figure 3.32 Mass flow rate over time a) for Model A b)for Model B.

Moreover, comparing the profiles for assemblies with $\mu_{r(A)}$=1 and $\mu_{r(B)}$=0.5 (i.e. μ_r values at which each model is saturated according to Figure 3.33), reveals that fast flow channel for Model B propagates to a higher elevation (1.5 times higher than for Model

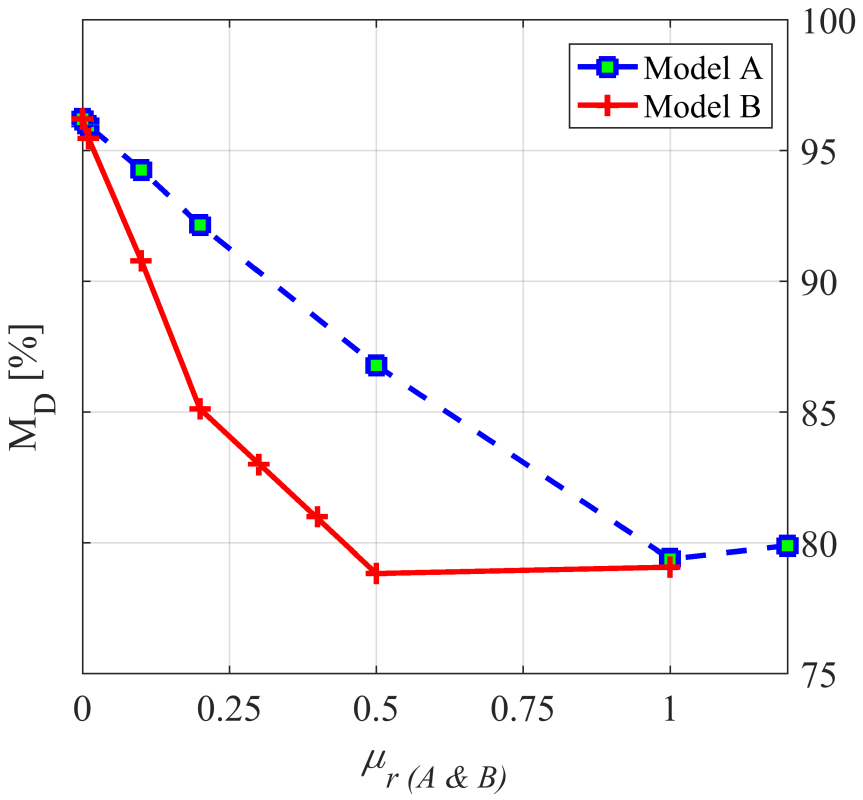

Figure 3.33 Effect of rolling friction on the total mass discharged (all the results are obtained at the end of 4 seconds from removing of the opening).

A). This differences in flow profiles are affecting the stress distribution inside to silo (see the next section). Liu et al. (2014) have monitored the discharge of particles with various shapes, ranging from spherical particles (aspect ratio =1) to prolate spheroid (aspect ratio > 1, polar radius is greater than the equatorial radius) and oblate spheroid (aspect ratio < 1, equatorial radius is greater than the polar radius). Comparing flow profiles, it is reported that diverging from spherical particles, the interlocking of the particles lead to a 'rat-hole', which is more considerable for particles with aspect ratio >1. The rat-hole is defined as condition in which a central fast flow core is formed above the orifice and stagnant zones are formed at both sides. A similar observation has also been reported in Chapter 4 for particles with different surface and edge properties. It is pointed out that increasing shape complexity affects the flow kinematics and contributes to development of larger dead-zones and faster active central flow.

In a mixed flow, similar to the studied cases here, the mass flow region (upper part of silo) feeds the fast flow zone and this continues until all the mass flow region is discharged (Wang et al., 2015; Zhang and Ooi, 1998). Later, once the discharge height reaches the transition height, the particles in dead-zones start to contribute to discharge process. This phenomenon can be seen at M_D=50% (i.e. discharge has reached the

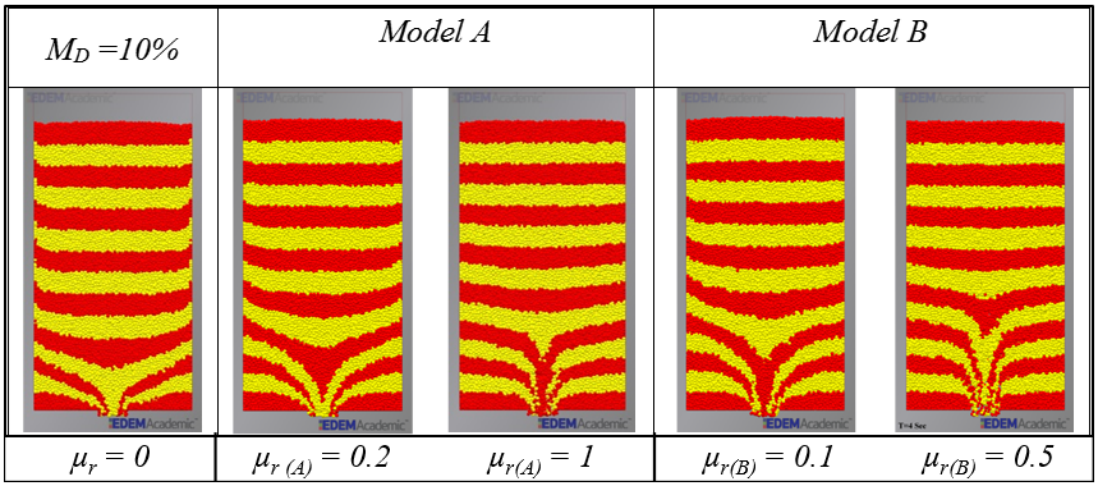

(a)

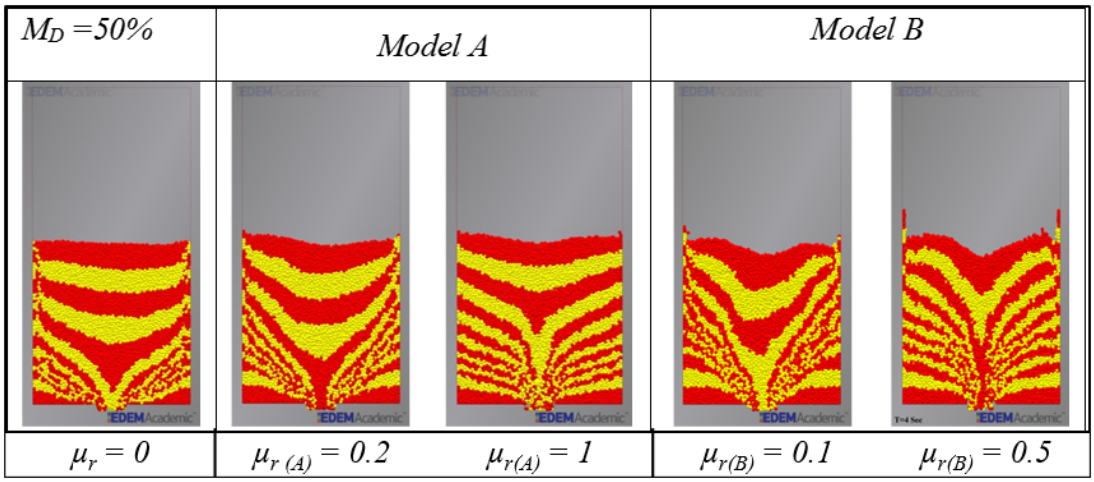

(b)

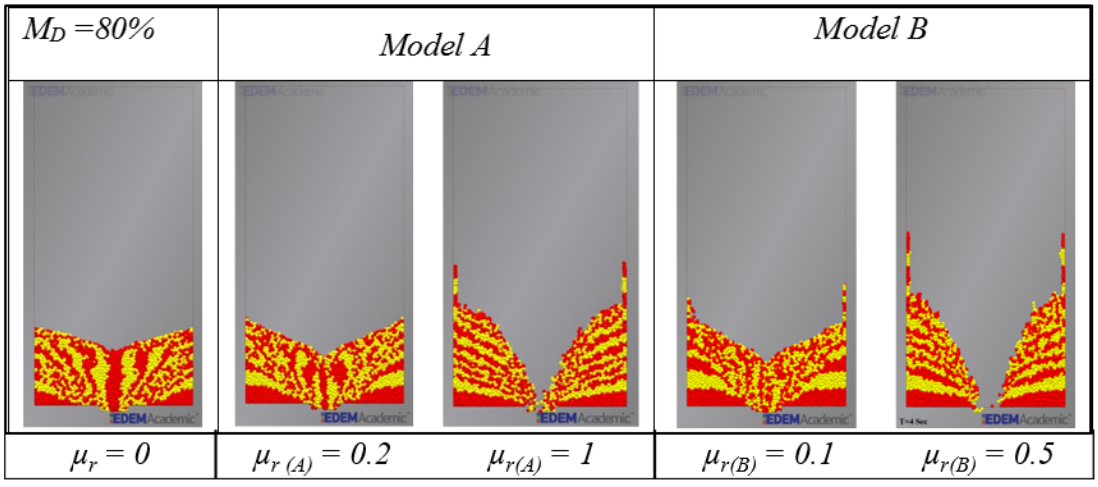

(c)

Figure 3.34 Effect of rolling resistance models on flow patterns at three stage of discharge a) M_D=10, b) M_D=50 a) c) M_D=10.

transition zone) for the two cases of Model B, while all other cases are yet following the flow characteristics discussed at M_D=10%.

Additionally, flow profiles are presented at M_D=80% to get a clear understanding about the geometry of the stagnant zones and also to discuss the final stages of the discharge process. Moreover, studying the not-flowing zone is considered as a supplementary information for identifying static properties of the packing (i.e. measuring angle of repose and evaluate avalanching phenomena). It is deduced from Figure 3.34 that the formation and geometry of the dead-zones are highly dependent on the magnitude of μ_r. The higher value of μ_r contributes to formation of larger stagnant zones. Additionally, as expected, the packing without rolling resistance is yet discharging without forming a considerable dead-zone. The stated effects are in line with the observations of Liu et al. (2014), which suggested that not-flowing zones for the non-spherical particles are enlarging with increase of aspect ratio.

All in all, it can be pointed out that the influences of considering rolling resistance is well coinciding with the influences of non-sphericity for predicting the flow profiles. However, the question of "to what extent or for which type of particles, consideration of rolling resistance can address the shape parameter" is going to be answered in Chapter 5.

3.6.3 Velocity profiles

The velocity profiles provide (along width of silo) a clear understanding of evolution of both the fast flow and stagnant zone. As presented in Figure 3.35, increasing μ_r in mass flow zone (i.e. H=0.15 m) reduces the velocity along the width of silo. Furthermore, flow velocity at below transition zone (i.e. H=0.075), clarifies the formation of the stagnant zone and its enlargement by increasing μ_r in both models. Moreover, it is observed that by increase of μ_r, flow concentrates only in the fast flow zone in centre of the silo, which contributes to higher V magnitudes. Figure 3.35 also shows that both models have a different flow channel characteristics at saturation level (i.e. at $\mu_{r(A)}$ = 1 and $\mu_{r(B)}$ = 0.5), in which Model B makes a more pronounced flow channel.

3.6.4 Stress distribution

Influence of rolling resistance on shearing response of spherical particles in shear testers (i.e. triaxial, direct and simple shear) have been extensively studied both at micro (i.e. evaluation of contact forces, orientation and anisotropy) and macro scales (total shear stress curves and elastic response), refer to (Estrada et al., 2013; Mohamed and Gutierrez, 2010; Zhou et al., 2013). However, in case of quasi-static flow, specifically discharge of particles from a silo, the rolling resistance effect is only studied on

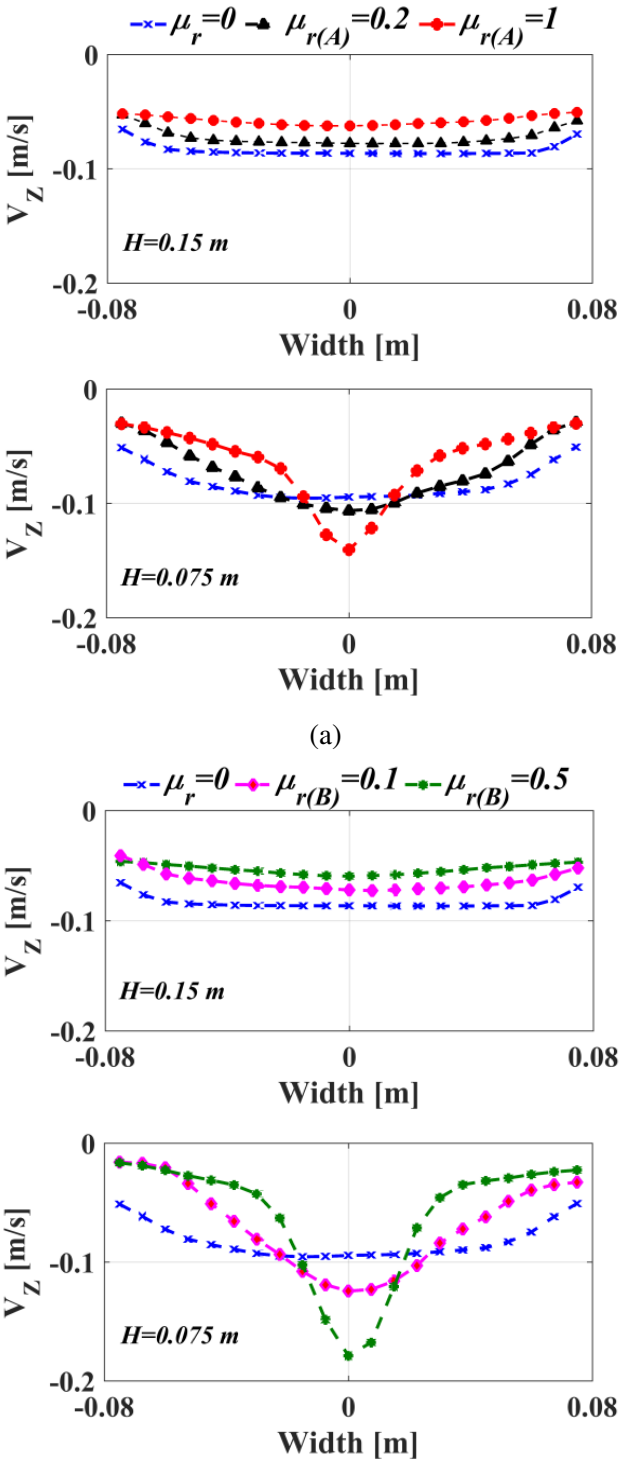

Figure 3.35 Quantitative representation of velocity along the width of silo a) for Model A b)for Model B.

wall pressure distribution (Balevičius et al. (2012)). As a result, it is of high interest to investigate the stress distribution locally for discharging granular assemblies.

Using coarse-graining technique, the horizontal and vertical stresses are obtained and further evaluated in this section. Figures 3.36 and 3.37 reveal that the presence of the rolling resistance has altered the stress distribution inside the silo. Figures 3.36a and 3.37a show the horizontal stress (σ_{xx}) distribution for both models, with different values of rolling friction coefficient, at M_D=10% (please note that μ_r=0 is repeated in both figures). Results show that distribution of σ_{xx} is very dependent on the flow pattern. To assess thoroughly all parts of the silo, it is reasonable to separate the height of the silo into three sections:

I. The σ_{xx} in the bottom section of the silo, which encompasses the flow channel, is relatively high for the case with μ_r=0, whereas by increasing rolling resistance, σ_{xx} decreases to a great extent in this region. The reduction of σ_{xx}, in the cases with μ_r>0, is mainly due to the formation of the fast flow channel and its further development, which breaks the contact network constantly and avoids building strong arches. The flow channel can be distinguished well in the vertical stress σ_{zz} distribution plots (see the region with very low stress adjacent to the highest vertical stress distribution area), as shown in Figures 3.36b and 3.37b.

II. The mass flow section, which is located immediately above the transition zone (where mass flow section meets the flow channel), gives rise to formation of strong arches. Accordingly, the highest horizontal stresses are developed in this section (high-stress zone). The formed arches convey the available pressure to the side walls and to the stagnant zone, respectively. Consequently, in the vertical stress plots, a column-like load transmission behaviour can be seen near the side walls, see Figure 3.36b and 3.37b. Moreover, it is also clear that for high values of rolling resistance (i.e. $\mu_{r(B)}$=0.5, $\mu_{r(A)}$=1), due to the further development of flow channel, σ_{xx} drops drastically in the mass flow zone as well.

III. Additionally, there is a low-stress section in σ_{xx} plots, just above the high-stress zone. This section has a weak contact network due to lower overburden pressure and seems to be common in all packings regardless of the rolling resistance.

To verify the local variation of stress in a dimensionless field, the lateral pressure ratio (σ_{xx}/σ_{zz}) plots are presented in Figure 3.36c and 3.37c. The plots indicate the location of the transition height and also the geometry of the flow channel. The area in the centre with $\sigma_{xx}/\sigma_{zz} > 1.5$ can be the representative of the flow channel, in which due to drop in vertical stress magnitude, the σ_{xx}/σ_{zz} ratio is presenting very high values. Additionally, there is low-stress area at the sides of the flow channel, in which represents the stagnant zone. In this region $\sigma_{xx}/\sigma_{zz} <0.5$ condition is dominant due to presence of higher magnitudes of σ_{zz}.

Next step is to compare the current observations, regarding stress distribution, with those of non-spherical particles; a part of study by Liu et al. (2014) has already been discussed in Section 3.3.2, where they have compared the flow profiles of oblate, prolate and spherical particles. They plotted the normal contact force network of the particles with different shapes and pointed out that flow features are directly affecting the force distribution inside the silo. For the spheres, the force magnitude is rather small, but distributed all over the silo, while for particles with aspect ratio$\neq$0, large forces are developed in vicinity of the wall region. They also reported that as the non-sphericity increases, the arches are forming in a higher elevation. Another important observation was that going far from spherical particles, the wall pressure will undergo a noticeable reduction. Additionally, results in Chapter 4 is in agreement with the above observations; while increasing surface bumpiness and corner sharpness, the horizontal stress distribution is showing a reduction due to change in both flow and contact characteristics.

3.7 Interchangeability of $\mu_{r(A)}$ and $\mu_{r(B)}$ (toward similar bulk response)

3.7.1 Calibration of rolling resistance models

Both Model A and B are popular among researchers for incorporation of shape effects, however it is not fully understood that whether it is possible to compensate the differences in the calculation of torque for the two models by only tuning the dimensionless parameter μ_r. Accordingly, a series of simulations have been conducted to calibrate models based on discharged mass over time. Figure 3.38 shows 8 sets of simulations, in which cumulative discharges are largely overlapping for pairs of μ_r values for both models. In order to see the quantitative correlation between both models for calibrated simulations, the variation of $\mu_{r(A)}/\mu_{r(B)}$ with $\mu_{r(A)}$ is plotted in Figure 3.39. The results depict that for values of $\mu_{r(A)}$ <0.2, the equivalent coefficient of rolling friction for Model B is 4 times less (which will lead to equivalent discharge rate for both models). Furthermore, for values of 0.2<$\mu_{r(A)}$<1 there is a linear relationship with $\mu_{r(B)}$, in which, at saturation point of Model A (i.e. $\mu_{r(A)}$=1), the equivalence coefficient reduces to 2 (i.e. $\mu_{r(B)}$=0.5). It must be noted that the calibration procedure, explained in the current section, in not generally applicable (i.e. it is particularly limited to the silo discharge application).

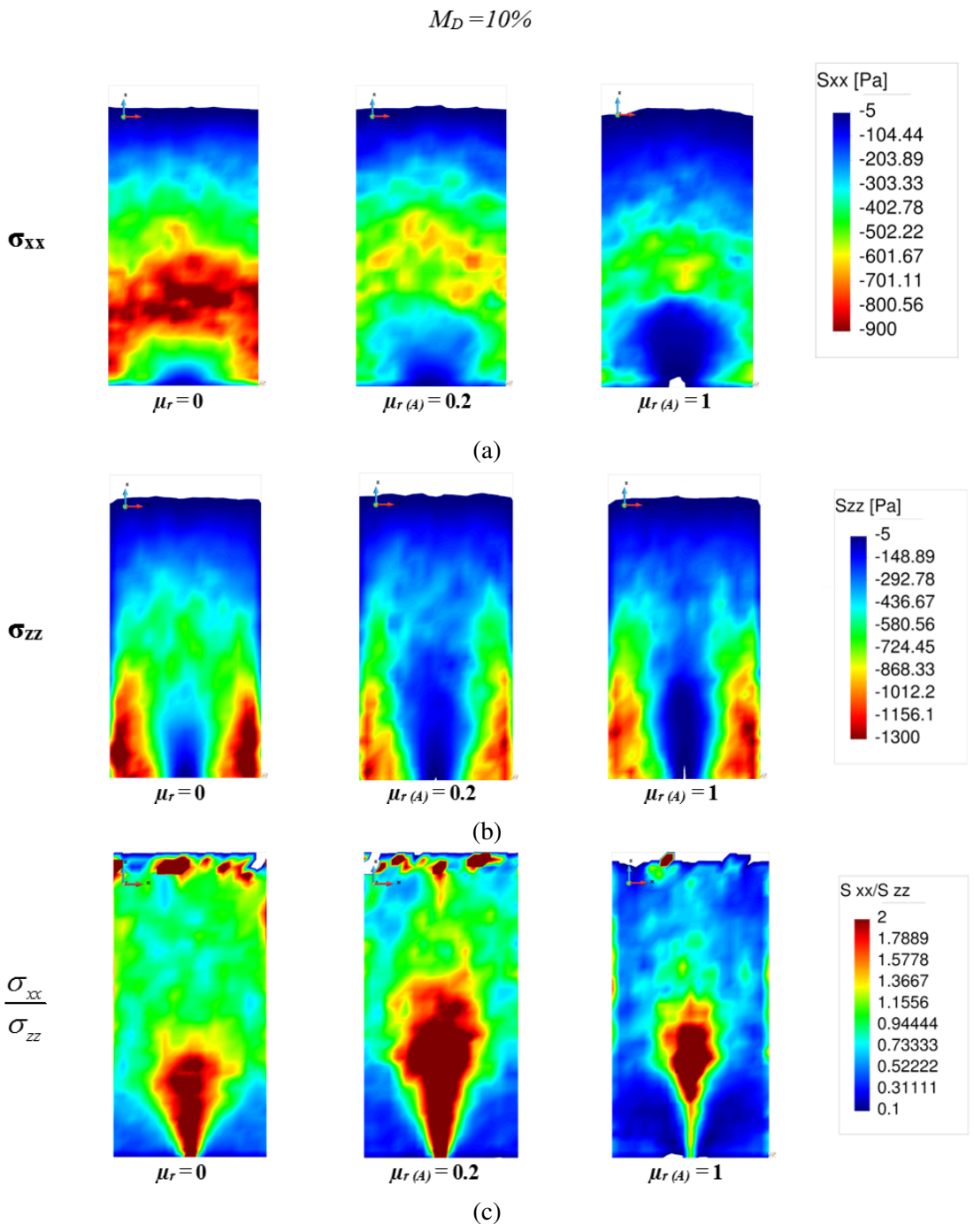

Figure 3.36 Influence of rolling resistance on stress distribution during discharge (Model A), a) horizontal stress b) vertical stress c) ratio of horizontal to vertical stress. Note that compression state of stress is represented by negative sign.

Validation of μ_r calibration

After calibrating the models based on cumulative discharge, the next step is to check whether other bulk scale properties of the calibrated simulations also match. Commonly, the range of $\mu_{r(A)}$ that is used in the literature changes depending on the stud-

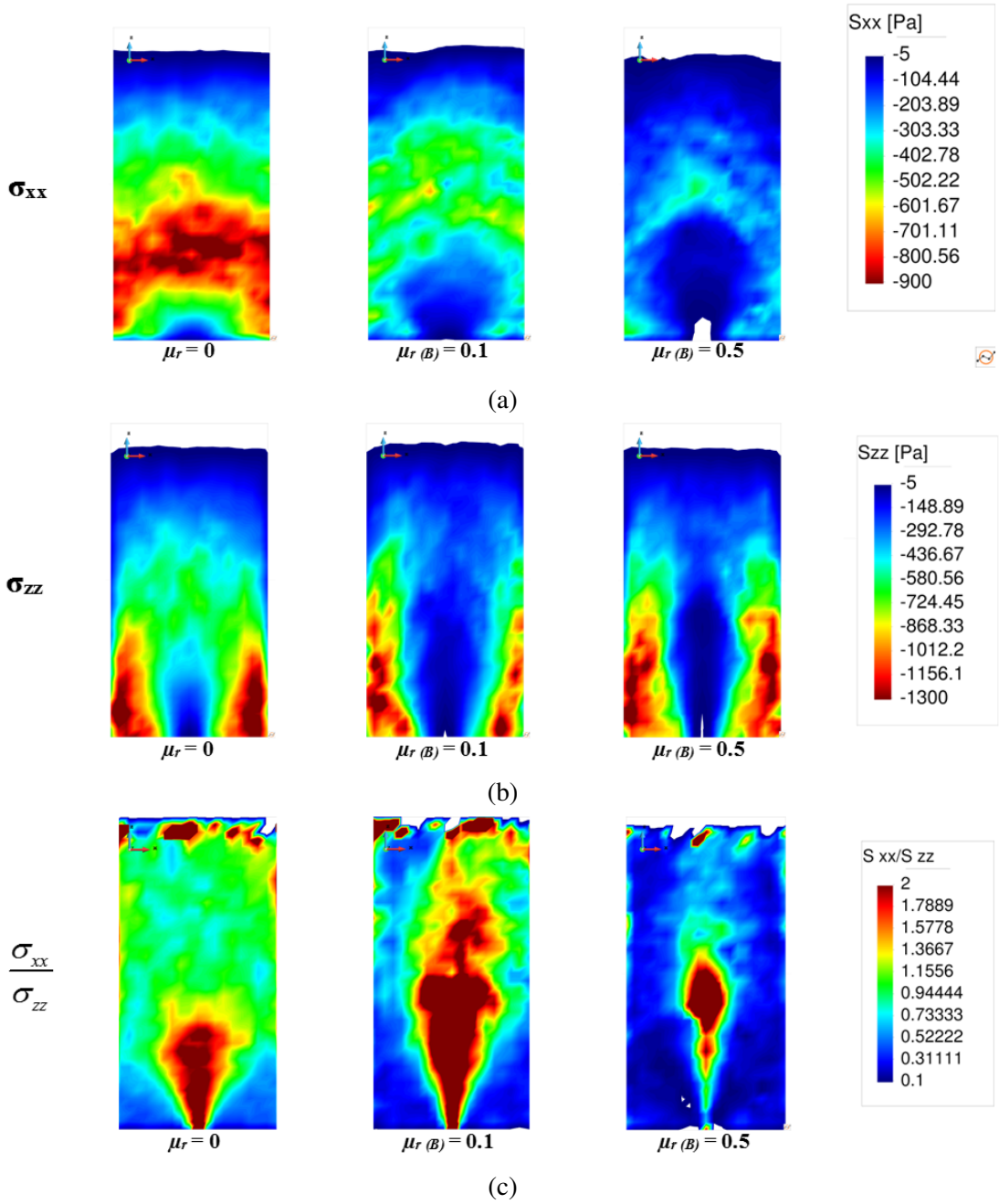

Figure 3.37 Influence of rolling resistance on stress distribution during discharge (Model B), a) horizontal stress b) vertical stress c) ratio of horizontal to vertical stress. Note that compression state of stress is represented by negative sign.

ied problem, however based on our survey it is seen that the assigned values are in the range $0.01<\mu_{r(A)}<0.2$ (Barrios et al., 2013; Cabiscol et al., 2018; Freireich et al., 2011; Goniva et al., 2012; González-Montellano et al., 2011; Horabik et al., 2018; Marigo et al., 2011; Thakur et al., 2016; Wang et al., 2017; Yu and Saxén, 2014). By selecting $\mu_{r(A)}=0.2$ and knowing that the equivalence coefficient is 4 for the two models at this value, the value $\mu_{r(B)}=0.05$ is selected for the comparison. In this respect, the plots for

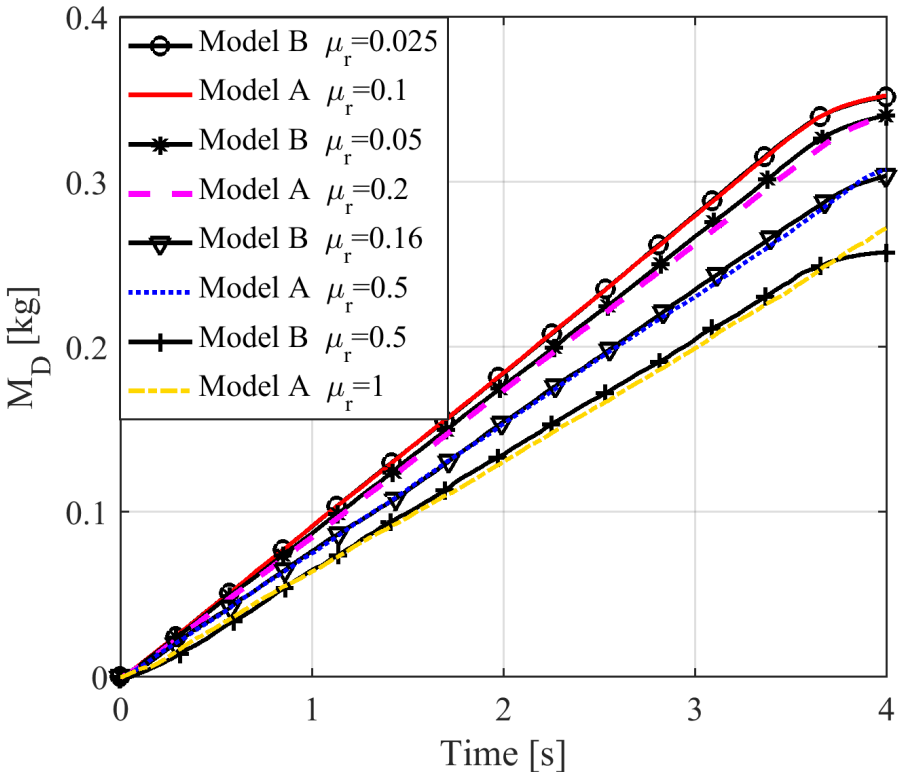

Figure 3.38 Cumulative discharged mass (for the cases in which mass flow rate is overlapping for the both rolling resistance models).

solid fraction, velocity profiles and stress distribution for $\mu_{r(A)}$=0.2 and $\mu_{r(B)}$=0.05 are compared at various stages.

Solid fraction

The solid fraction (ϕ_s) results are compared at the end of filling and during discharge for $\mu_{r(A)}$=0.2 and $\mu_{r(B)}$=0.05. Figure 3.40a shows the capability of calibrated values of $_r$ for both models in producing similar packing. Furthermore, the variation of ϕ_s at M_D=25% is also plotted in Figure 3.40b, which clearly suggests the similarity of both packing during the discharge process.

Velocity profiles

Figure 3.41 shows the velocity profiles, both horizontal (Vx) and vertical (V_Z), of the calibrated simulations at 0.075 and 0.15 m elevations (corresponds to 0.5 and 0.25 of H). The results obtained at M_D=25% are showing the similarity in flow kinematics during discharge at various parts of the silo.

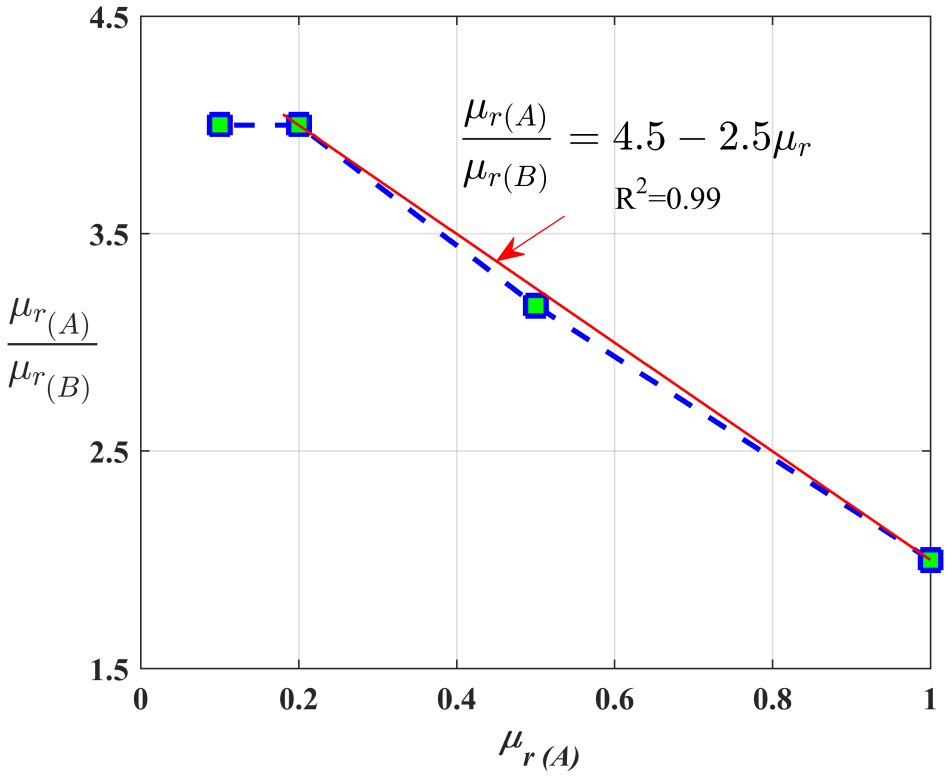

Figure 3.39 Equivalency map for $\mu_{r(A)}$ and $\mu_{r(B)}$.

Stress distribution

Stress distribution is also evaluated, through comparing the ratio of σ_{xx}/σ_{zz} for the calibrated simulations, and results are presented in Figure 3.42. The comparison is done at two different heights of the silo at 10 and 40% of the full discharge. It is clear that a good match is available for lateral pressure ratio between granular assemblies with $\mu_{r(A)}$=0.2 and $\mu_{r(B)}$=0.05.

To generalize the key findings in this section, we further compare the bulk scale results for both models in the predefined range of $0.01<\mu_{r(A)}<0.2$. Accordingly, we selected $\mu_{r(A)}$=0.1 and $\mu_{r(B)}$=0.025 and similar to what have been seen already, the obtained results were in a good agreement for this set of simulations as well.

3.7.2 Dependence of calibrated μ_r on the sliding friction

A set of simulations are conducted to determine the dependence of the calibrated rolling resistance models on the sliding friction coefficient (μ_s). For this purpose, mass discharged results over time for four set of simulations are compared. Two of calibrated simulations, with $\mu_{r(A)}$=0.2 and $\mu_{r(B)}$=0.05 having μ_s=0.577, are compared

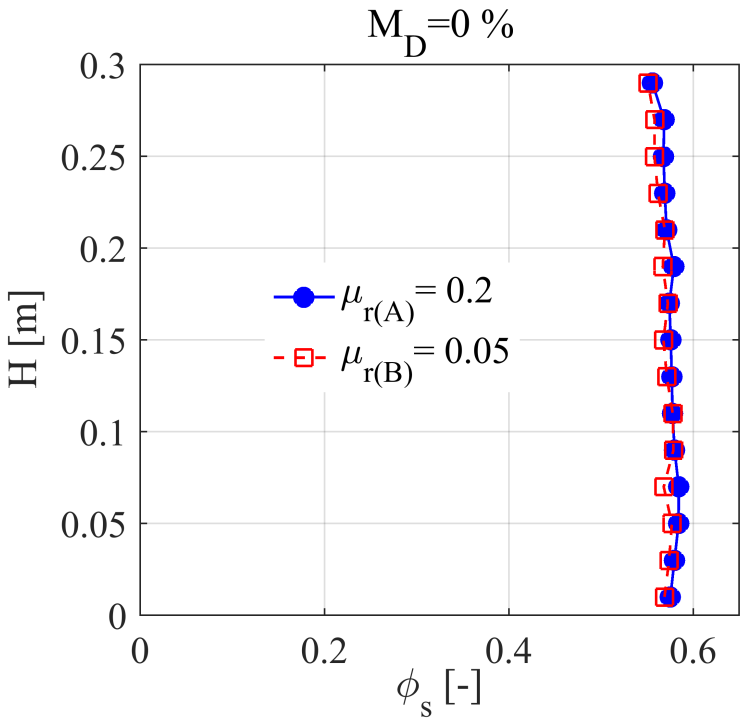

(a)

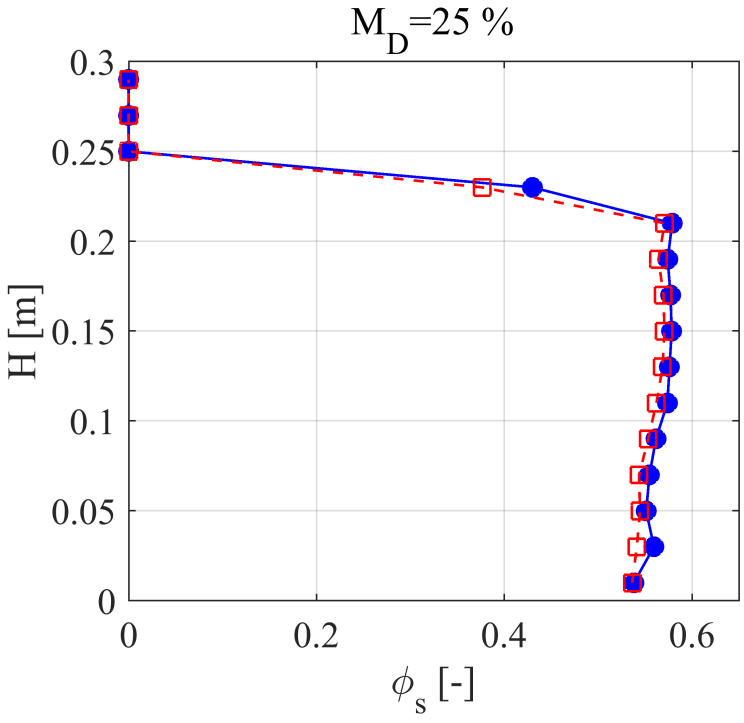

(b)

Figure 3.40 Solid fraction comparison a) end of filling and b) during discharge.

with results of simulations with the same μ_r having a sliding coefficient equal to half that of the first set of simulations. Figure 3.43 shows that reducing the sliding friction

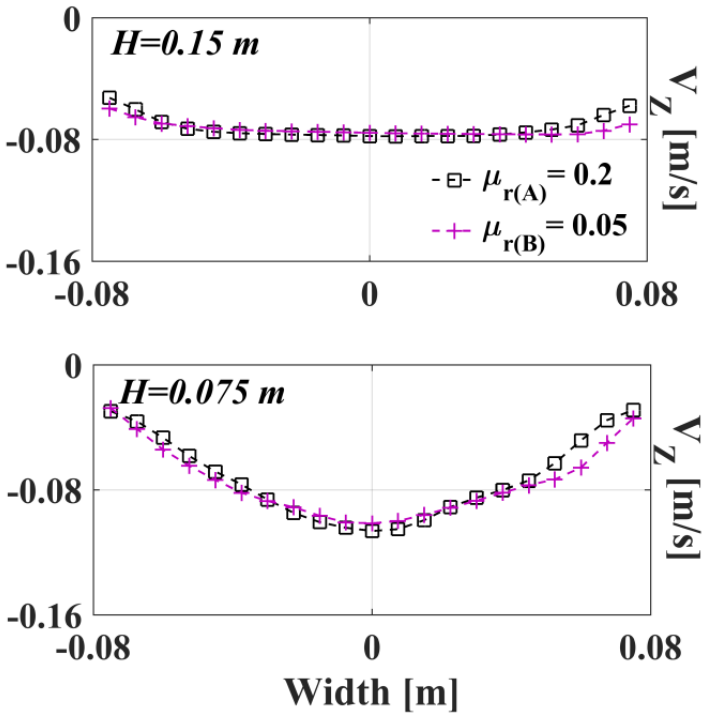

(a)

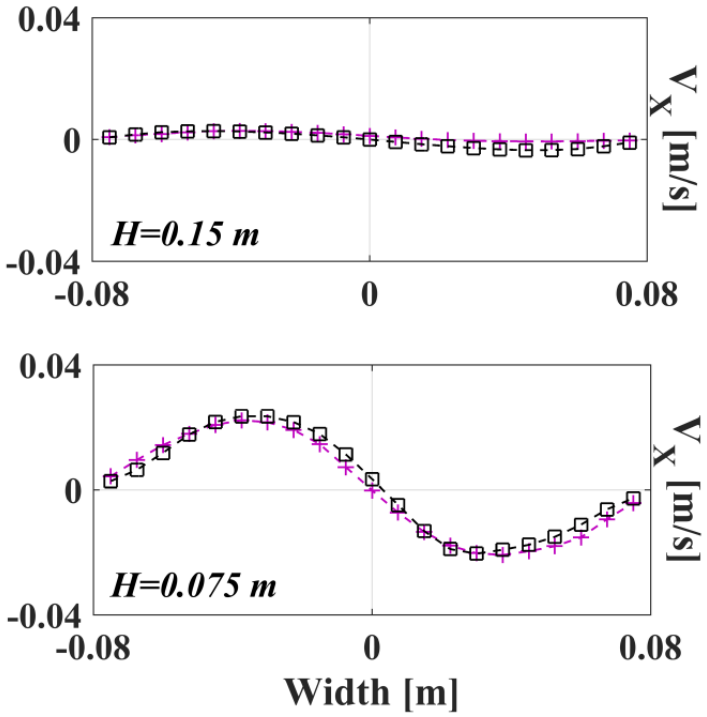

(b)

Figure 3.41 Comparison of velocity profiles at two elevation along the height of silo (at M_D =25 %) a) vertical velocity variation b) horizontal velocity variation.

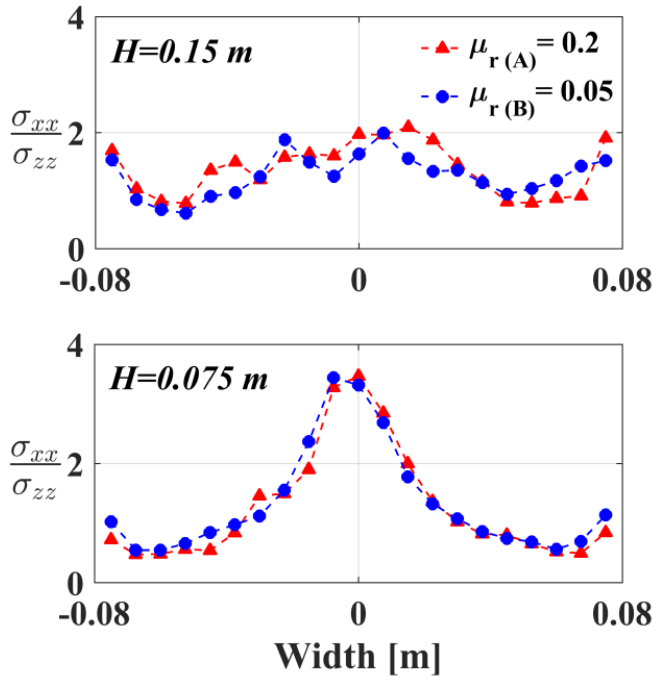

(a)

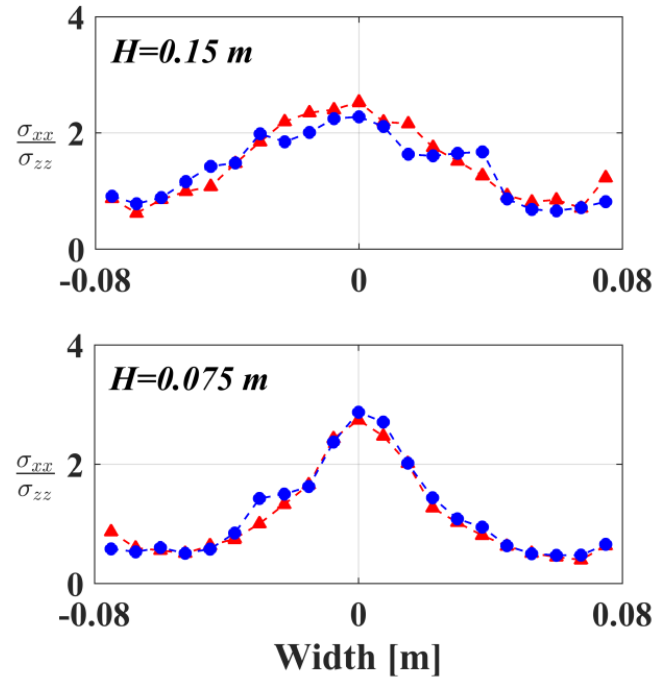

(b)

Figure 3.42 Comparison of dimensionless stress distribution (horizontal stress/vertical stress) at two elevation along the height of silo a) at 10% of total mass discharged b) at 40% of total mass discharged.

by half has led to a faster discharge for both models. Nevertheless, the results of the calibrated simulations are still mostly overlapping, which suggests that the effect of μ_s is negligible on the calibration procedure of the two models. Additionally, it is clear that the applied rolling friction coefficient is fairly large, and since Models A and B are both active in the pure sliding case, the influence of sliding friction diminishes.

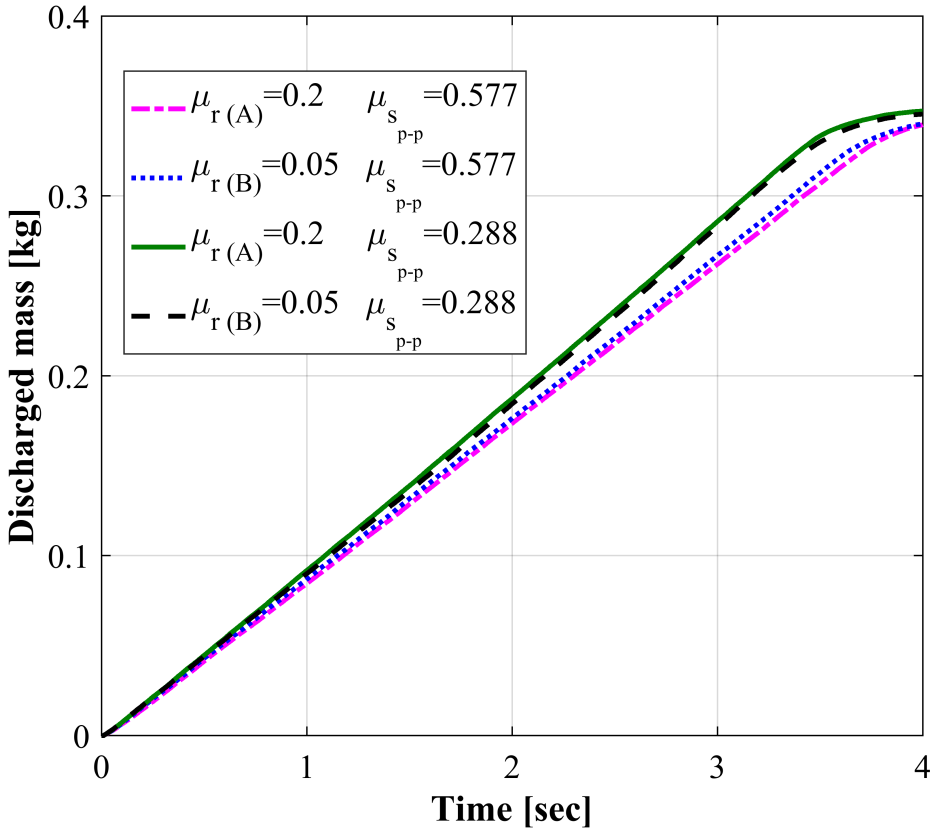

Figure 3.43 Comparison of the cumulative discharged mass, in order to evaluate the dependency of calibrated rolling resistance models on the sliding friction.

3.7.3 Initial packing effect on bulk behaviour

In order to distinguish the effect of rolling resistance models from the influence of initial packing on the discharge process, a set of simulations with different initial packing is obtained through applying $\mu_{r(A)}$=0.5 and $\mu_{r(B)}$=0.16 to spheres (selected from pairs with overlapping cumulative discharge, which are presented in Figure 3.38). Before discharge, the rolling resistance models and μ_r values are swapped for the packings (i.e. from $\mu_{r(A)}$=0.5 to $\mu_{r(B)}$=0.16 and from $\mu_{r(B)}$=0.16 to $\mu_{r(A)}$=0.5), see Figure 3.44a. The simulations were then run for over 0.5 seconds in order to allow the particles to rest in new condition. It is clear that changing from $\mu_{r(A)}$=0.5 to $\mu_{r(B)}$=0.16 (I) had no effect on the particle configuration, whereas changing from $\mu_{r(B)}$=0.16 to $\mu_{r(A)}$=0.5

(II) had loosen the packing and there is particle settlement, as shown in Figure 3.44a. This is due to the fact that Model B is always active (for pure sliding/rolling or any combination), whereas Model A, is only active for sliding.

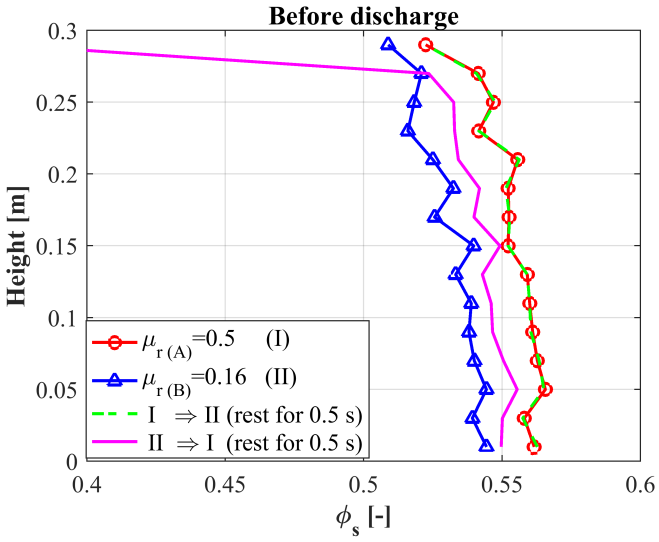

(a)

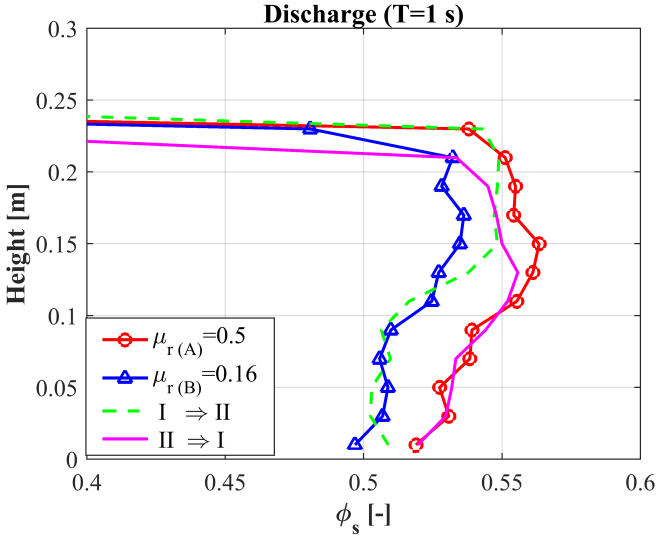

(b)

Figure 3.44 Solid fraction (interchanging rolling resistance models) a) end of filling (T=0 s) b) at 1 s after initiation of the discharge.

Subsequently, the solid fraction of the modified and the original packings are compared during the discharge (T=1 s after initiation of the discharge), see Figure 3.44b. It can be noticed that as discharge progresses, the modified cases are following the same trend for ϕ_s according to the applied rolling friction coefficients, up to the transition height (this suggest that the applied rolling resistance forms its unique flow channel

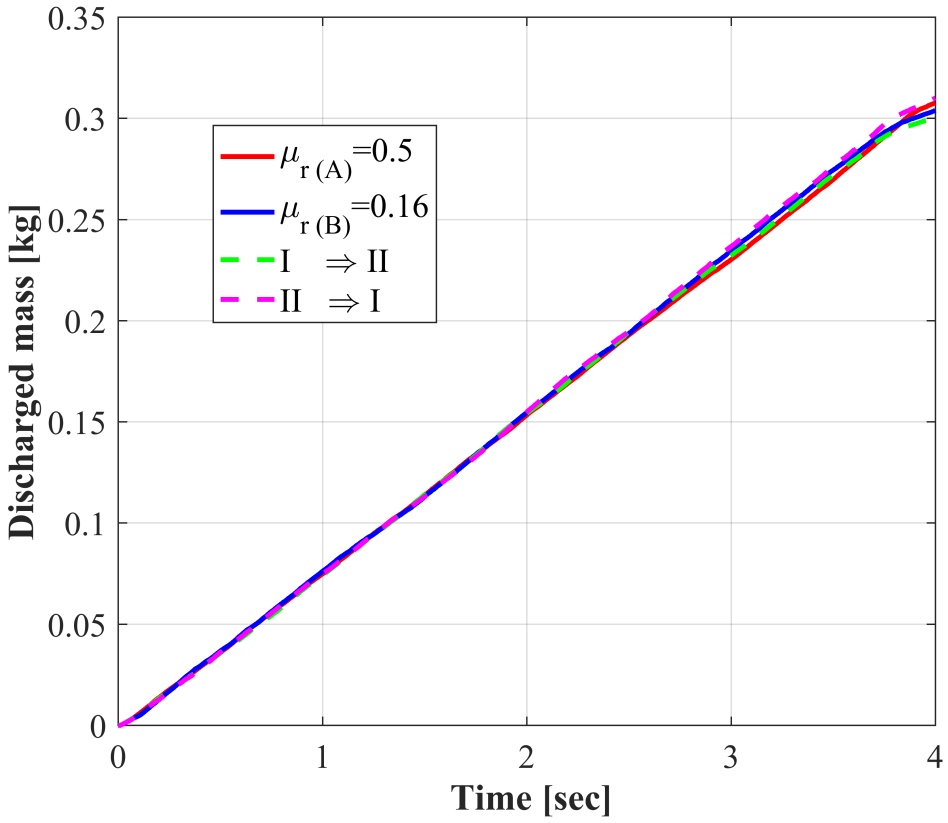

Figure 3.45 Comparison of cumulative discharged mass for simulations with distinct initial packing (rolling resistance models are interchanged during the discharge).

and stagnant zones independent of the initial packing). Furthermore, the plot for discharged mass versus time (Figure 3.45 shows that the slope of the cumulative discharge for both cases is overlapping, which indicates the equality of the mass flow rate. Consequently, it can be deduced that the rolling resistance model and the respective flow channel, rather than the initial packing, govern the discharge rate in silo simulations.

The drawn conclusion is evaluated with another example, where the initial packings of the considered packings are similar (for $\mu_{r(A)}$=1 and $\mu_{r(B)}$=0.2). Moreover, a different packing to those of considered is obtained by assigning μ_r=0, see Figure 3.46a. For two identical packings with μ_r=0, immediately before discharge, rolling resistance is enabled (one with $\mu_{r(A)}$=1 and the other with $\mu_{r(B)}$=0.2). Then, all four packings are discharged and followings are pointed out:

The comparison of the packings during discharge suggest the similarity of the observations with previous example in Figure 3.44b. On the other hand, cumulative discharge for all packings are compared in Figure 3.47, in which it is clear that the discharge characteristic in cases with similar packings ($F_{\mu_r=0}$), is influenced by the applied rolling resistance.

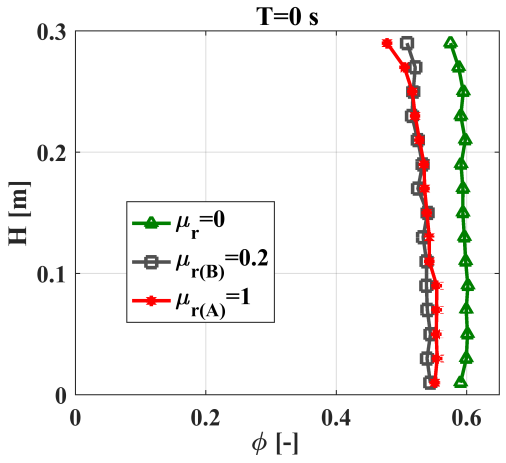

(a)

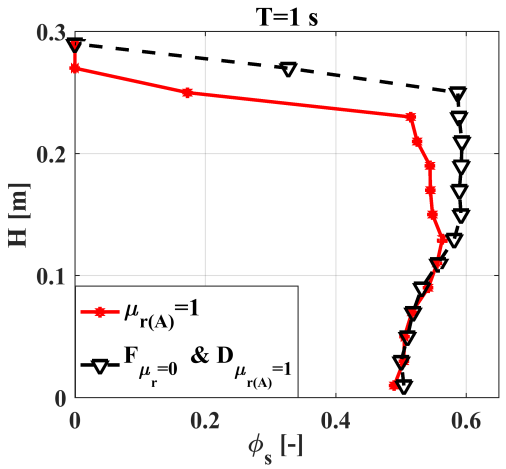

(b)

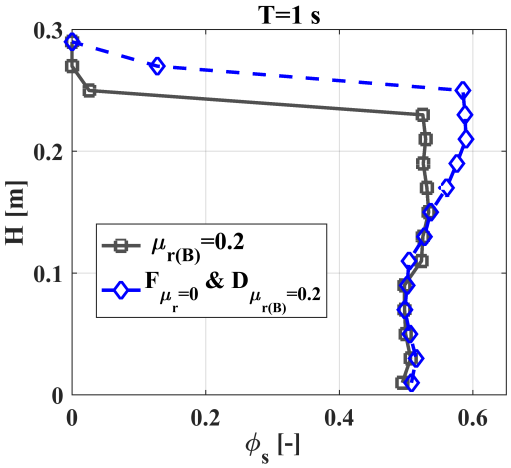

(c)

Figure 3.46 Solid fraction a) end of filling (T=0 s) b,c) at 1 s after initiation of the discharge.

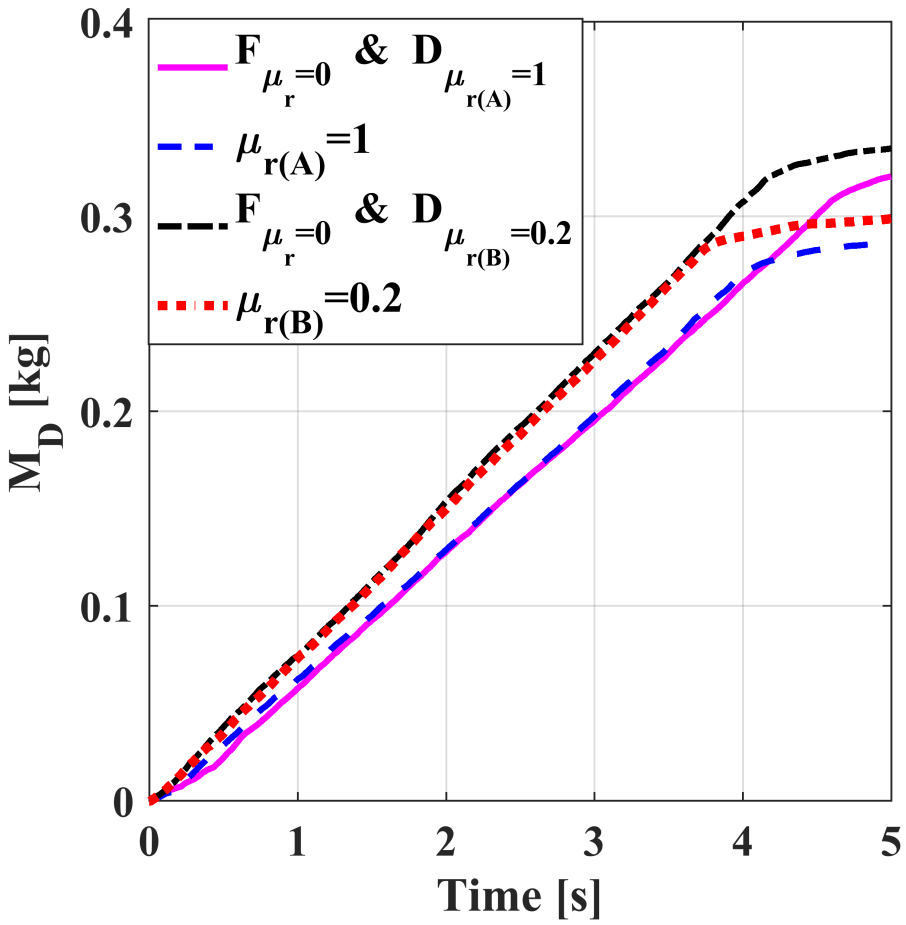

Figure 3.47 Comparison of cumulative discharged mass for simulations with similar initial packing (rolling resistance is included during the discharge). Note that filling is represented by “F”, and discharge process is represented by “D”.

The results in Figure 3.47 also shows the independence of the calibration methodology, presented in Section 4.1, from the initial packing density (in other words, mass flow rate is a function of the applied rolling and sliding frictions and is not affected by the initial packing).

3.8 Summary

This chapter has investigated the behaviour of spherical particles, in presence of two rolling resistance models, both in micro and macro-scales.

Firstly, the mechanism by which both models are applying the artificial torque is thoroughly assessed. Next, the presence and characteristics of oscillation of the single particles due to independence of the generated torque from the value of rotational velocity has been evaluated. Accordingly, the observations suggested that the frequency

of the oscillations is a function of the assigned time-step. Furthermore, it is seen that the influence of this known deficiency in the considered rolling resistance models is negligible on the flow characteristics of the spheres (smaller time-steps are recommended to minimize the unforeseen affects).

Secondly, the influence of applying rolling resistance to the packing and flow characteristics of spherical assemblies has been investigated. Results show that the packing of granular system is highly affected by considering the rotational constrain at contacts (i.e. looser packings are provided). Furthermore, the influences of incorporation of rolling resistance at contacts are further evaluated by means of discharge rates and flow patterns. Results suggest that both models are affecting kinematics of the discharging particles and contribute to retardation of the flow. Hence, it was of a great interest to detect effects of the change in flow characteristics on the stress distribution. Accordingly, it is observed that a fast flow channel is built up in the centre of the silo, which avoids emergence of the strong arches. Accordingly, the horizontal stress distribution alters greatly for the packings with enabled rolling resistance, this is while vertical stress is not affected significantly. Eventually, it is concluded that in case of predicting a clogged flow and reduction in stress distribution, the considered models are mimicking the behaviour of non-spherical particles. However, caution must be taken while predicting the packing density with the spherical particles and accompanying torque (contrary to rolling resistance effect, shape complexity is not always contributing to the increase of solid fraction).

Moreover, considering the different mechanisms of the applied torque in both models, the potential for providing similar bulk responses, by tuning the unitless rolling friction coefficient, is evaluated. It is seen that both models can provide exact discharge rates for all the possible rolling friction coefficients. Additionally, it is shown that for a reasonable range of rolling friction coefficients, not only discharge rate matches for both models, but also there is a good agreement between flow patterns, stress fields, velocity profiles and density of the packings.

Finally, the dependency of the discharge characteristics on initial packing is studied. It is shown that the applied rolling resistance disregards the density state of the initial packing and it can dictate the solid fraction and the mass flow rate of the assemblies.

Chapter 4

Including shape parameter in DEM; multi-sphere and superquadric approaches [1]

An efficient particle shape representation is a key challenge in DEM. Several methods have been adopted for approximation of non-spherical particles in DEM, of which, the most popular approaches are multi-spheres (MS) and superquadrics (SQ). Each approach has different abilities to account for shape complexity, where MS particles have inherent surface bumpiness and SQ particles are addressing well the edge sharpness. The current chapter will evaluate the mechanical characteristics of two shape representation methods through conducting a series of numerical case studies at both single particle and bulk levels. Accordingly, first part of the study will follow several testing scenarios, which clarify the impact, interlocking, sliding and tilting characteristics of cubical shape particle. Later, the role of the two shape descriptors on bulk response will be evaluated in angle of repose, Jenike shear and silo flow simulations. This will lead to a deep understanding regarding the importance of surface and edge complexities for predicting the behaviour of dense flow regimes. Furthermore, the possibility of compensating the edge sharpness with surface bumpiness will be assessed.

[1] Extended and adapted version on the articles:

Soltanbeigi, B., Podlozhnyuk, A., Papanicolopulos, S.A., Kloss, C., Pirker, S. and Ooi, J.Y., 2018. DEM study of mechanical characteristics of multi-spherical and superquadric particles at micro and macro scales. *Powder Technology*, 329, pp.288-303,

Soltanbeigi, B., Podlozhnyuk A., Ooi, J.Y., Kloss, C., and Papanicolopulos, S.A., 2017. Comparison of multi-sphere and superquadric particle representation for modelling shearing and flow characteristics of granular assemblies.*European Physical Journal Web of Conferences*, 140 (2017) 06015.

Presented in:

Soltanbeigi B., Podlozhnyuk A., Papanicolopulos S.A., Kloss C. and Ooi J.Y., Influence of blockiness and bumpiness on modelling dense granular flows of non-spherical particles *Particles conference*, Hanover, Germany, September 2017.

4.1 Introduction

Most DEM codes use spherical particles to reduce the computational cost of the simulations, although in reality particles are mostly of irregular shape. Several non-spherical shape descriptors have been proposed in the literature, the most frequently used approach in DEM being the multi-sphere approach (MS) (Abbaspour-Fard, 2000; Cabiscol et al., 2018; Favier et al., 1999; Kremmer and Favier, 2001; Kruggel-Emden, Wirtz and Scherer, 2008; Markauskas et al., 2009). In this description, spheres are allowed to overlap and be glued together to approximate an arbitrarily shaped particle. On the other hand, irregular particle shapes can alternatively be idealized to some regular shapes such as spheroids, cuboids or cylinders that can be approximated by superquadric (SQ) shapes (Cleary, 2004; Podlozhnyuk et al., 2017; Soltanbeigi et al., 2017, 2018). It has been suggested that 80% of all shapes can be represented by superquadric functions or derived from superquadrics in higher-dimensional hyperquadrics (Williams and Pentland, 1992; Zhong et al., 2016). SQ particles demonstrate an excellent trade-off between model complexity and shape flexibility. Changing only five shape parameters gives an opportunity to switch from a spherical particle to an ellipsoidal, cylindrical or box-like particles. These particle shapes are able to capture many physical elements of real particles and extend the range of applicability of DEM.

You and Zhao (2018) studied numerically the packing and flowing behaviour of ellipsoids. The ellipsoidal shape particles are modelled in DEM by super-ellipsoid and multi-sphere approaches. It is shown that both methods are capable of providing comparable results to that of experiments (both in terms of flow and packing). However, the multi-sphere approach needs more number of sub-spheres to achieve similar bulk response, which increases the simulation time. Overall, it is recommended that super-ellipsoid method can lead to faster and precise simulations, which can prioritise its utilization in addressing shape complexity. Nevertheless, further investigations are needed to characterise both methods at multi-scale.

4.2 Methodology

This section provides information regarding the material properties and the testing procedures that have been followed. The considered particles have cubical shapes with an edge length of $d = 2$mm (the reason for choosing cubical geometry is to have the aspect ratio as 1 and put emphasis on the surface and edge properties). Cubes were approximated by SQ particles in LIGGGHTS and by MS particles in EDEM (DEM Solutions Ltd., 2014), (except for Section 4.4.1, where MS particles were simulated in LIGGGHTS software). Regarding the use of two distinct DEM codes, it should be noted that the contact detection algorithm and force calculation methodology are dif-

ferent for multi-sphere and superquadric particles. Furthermore, using spherical particles, the consistency of the test conditions for both DEM codes was assessed through comparing the results of several single-particle and bulk-level tests (as also mentioned in the Section 4.4.2).

To simulate a perfect cube, the shape description method must be able to provide sharp edges, which can be obtained perfectly by polyhedral technique, see Wang et al. (2011). However, theoretically, the edge sharpness of MS particles could be increased by using spheres of smaller size to represent the particle edges. However, this would lead to i) a smaller time-step ii) a higher number of sub-spheres per particle and, as a result, iii) higher computational costs. The current study evaluates whether surface bumpiness can compensate the lack of edge sharpness for MS particles approximating cubical particles.

The parameters for the considered material are chosen in a way that the computational cost is reasonable. Table 4.1 shows the material properties for particles and the geometry. Hertz model with viscous damping (modified by Brilliantov et al. (1996)) and Mindlin-Deresiewicz (Mindlin and Deresiewicz, 1953) model are used in all simulations as normal and tangential force models. The normal force is a function of normal overlap δ_n:

$$F_n = \frac{4}{3} E^* \sqrt{R^*} {\delta_n}^{1.5} \tag{4.1}$$

the equivalent Young's Modulus E^*, the equivalent radius R^* are defined as:

$$\frac{1}{E^*} = \frac{1-{\nu_i}^2}{E_i} + \frac{1-{\nu_j}^2}{E_j} \tag{4.2}$$

$$\frac{1}{R^*} = \frac{1}{R_i} + \frac{1}{R_j} \tag{4.3}$$

Additionally there is a damping force, ${F_n}^d$, given by:

$${F_n}^d = -2\sqrt{\frac{5}{6}} \beta \sqrt{S_n m^*} {V_n}^{rel} \tag{4.4}$$

Where m^* is the equivalent mass, ${V_n}^{rel}$ is the normal component of the relative velocity and β and S_n (the normal stiffness) are given by:

$$\beta = \frac{\ln e}{\sqrt{\ln^2 e + \pi^2}} \tag{4.5}$$

$$S_n = 2E^* \sqrt{R^* \delta_n} \tag{4.6}$$

Table 4.1 DEM material properties (for both MS and SQ particles)

Parameter	Value
Density (particle) ρ [kg/m^3]	4100
Coefficient of particle-particle friction μ^s_{pp}	0.56
Coefficient of particle-wall friction μ^s_{pw}	0.45
Coefficient of restitution (particle-particle), ε_p	0.15
Coefficient of restitution (particle-wall), ε_{pw}	0.5
Poisson ratio (particles), ν_p	0.25
Poisson ratio (wall), ν_w	0.25
Shear modulus (particles), G_p[Pa]	10^7
Shear modulus (wall), G_w[Pa]	10^{10}
DEM time-step size, Δt[s]	$2 \cdot 10^{-6}$ (equal to 5% of Rayleigh time-step)
Normal force model	Hertz model with viscous damping Brilliantov et al. (1996)
Tangential force model	Mindlin-Deresiewicz Mindlin and Deresiewicz (1953)
Rolling friction model	off for MS and SQ particles

With e the coefficient of restitution. The tangential force, F_t, depends on the tangential overlap δ_t and the tangential stiffness S_t.

$$F_t = -S_t \delta_t \tag{4.7}$$

$$S_t = 8G^* \sqrt{R^* \delta_n} \tag{4.8}$$

Here G^* is the equivalent shear modulus. Additionally, tangential damping is given by:

$$F_t{}^d = -2\sqrt{\frac{5}{6}}\beta \sqrt{S_t m^*} V_t{}^{rel} \tag{4.9}$$

where $V_t{}^{rel}$ is the relative tangential velocity. The tangential force is limited by Coulomb friction $\mu_s F_n$ where μ_s is the coefficient of static friction, for more details see also (Benvenuti, 2014; Di Renzo and Di Maio, 2004; Podlozhnyuk et al., 2017).

4.2.1 Superquadrics

The equation that governs the shape of a SQ particle in its local coordinate system, given by Barr (1981), is as follows:

$$f(x,y,z) \equiv \left(\left| \frac{x}{a} \right|^{n_2} + \left| \frac{y}{b} \right|^{n_2} \right)^{\frac{n_1}{n_2}} + \left| \frac{z}{c} \right|^{n_1} - 1 = 0, \tag{4.10}$$

where a, b, c are the half-lengths of the particles along its principal axes, and n_1 and n_2 are blockiness parameters that control edge sharpness. Cubical particles can be modeled by superquadrics taking $a = b = c = d/2$ and taking $n_1 = n_2 = N > 2$, where N controls the level of edge sharpness/blockiness. It is worth noting that each k-th SQ

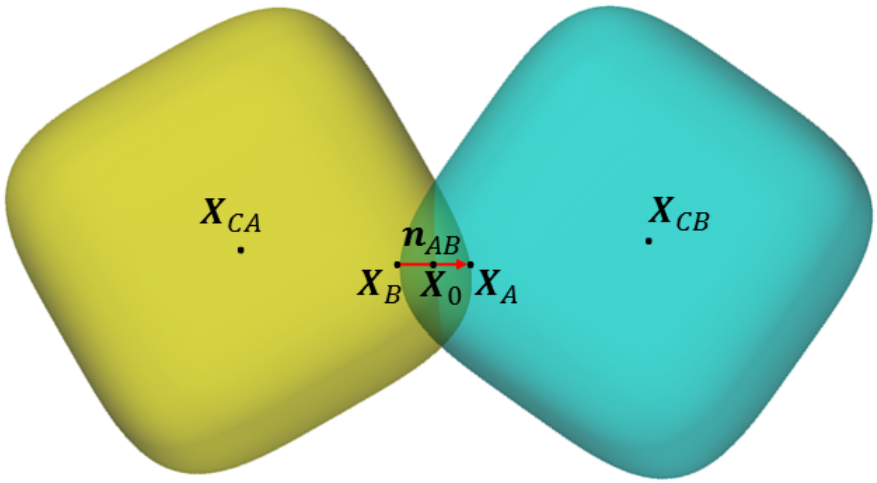

Figure 4.1 Scheme of particle-particle contact for superquadrics.

particle in a simulation can have its own set of parameters $(a_k, b_k, c_k, n_{1k}, n_{2k})$ and, as a result, corresponding shape function $f_k(x, y, z)$.

The contact detection algorithm is based on finding a "midway" point $\boldsymbol{X}_0$ between two superquadric particles A and B (Figure 4.1) that is a solution of the following non-linear system:

$$\begin{cases} \nabla F_A(\boldsymbol{X}) + \mu^2 \nabla F_B(\boldsymbol{X}) = 0 \\ F_A(\boldsymbol{X}) - F_B(\boldsymbol{X}) = 0, \end{cases} \tag{4.11}$$

where μ is the proportionality coefficient, $F_k(\boldsymbol{X}) = f_k(\boldsymbol{Q}_k^T \cdot (\boldsymbol{X} - \boldsymbol{X}_{Ck}))$ is the shape function of particle k defined with respect to a global coordinate system, $\boldsymbol{X}_{Ck}$ is the centre of mass, $\boldsymbol{Q}_k = \boldsymbol{Q}(\boldsymbol{q}_k)$ is the quaternion-based rotation matrix and $\boldsymbol{q}_k$ is the quaternion that tracks orientation of particle k. The contact direction $\boldsymbol{n}_{AB} = \nabla F_A / ||\nabla F_A||$ is calculated at the contact point $\boldsymbol{X}_0$. The normal overlap vector $\boldsymbol{\delta}_n$ is defined as a vector connecting points of intersection $\boldsymbol{X}_B$ and $\boldsymbol{X}_A$ between the contact line and surfaces of particles A and B correspondingly:

$$\begin{aligned} &F_A(\boldsymbol{X}_A) = 0, \text{where } \boldsymbol{X}_A = \boldsymbol{X}_0 + \alpha_A \boldsymbol{n}_{AB}, \\ &F_B(\boldsymbol{X}_B) = 0, \text{where } \boldsymbol{X}_B = \boldsymbol{X}_0 + \alpha_B \boldsymbol{n}_{AB}, \\ &\boldsymbol{\delta}_n \equiv \boldsymbol{X}_A - \boldsymbol{X}_B = (\alpha_A - \alpha_B)\boldsymbol{n}_{AB}. \end{aligned} \tag{4.12}$$

Standard normal and tangential force models (Di Renzo and Di Maio, 2004) can be applied, using local curvature radius as particle radius in force formulations.

Newton's method is employed to solve the system of non-linear equations (4.11) for every potential pair of particles at every DEM time-step. Several techniques can be proposed to reduce the number of potential particle pairs and increase computational efficiency: checking intersections between minimum bounding spheres and oriented

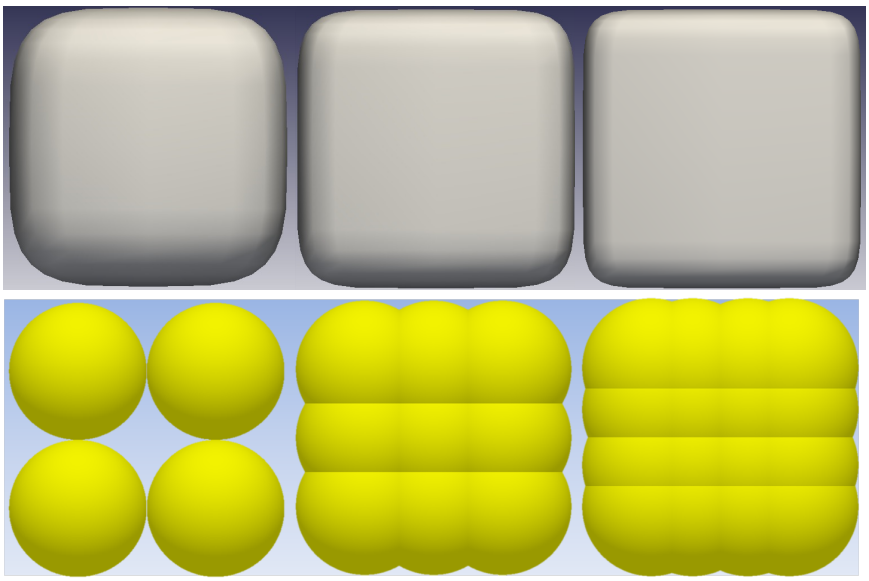

Figure 4.2 Particle shapes used. SQ($N4$),SQ($N6$) and SQ($N8$), top, from left to right. And MS(8), MS(27) and MS(64), bottom, from left to right.

bounding boxes, and using the solution for the contact point from the previous step at a current step as initial guess. Eq. (4.12) must be solved for every pair of overlapping particles. For a more detailed description of contact detection and a contact force algorithms between SQ particles refer to Podlozhnyuk et al. Podlozhnyuk et al. (2017).

Different levels of edge sharpness (between $N = 4$ and $N = 10$, further denoted as SQ($N4$),...,SQ($N10$)) are used in this paper to study the blockiness effect. Figure 5.1 (top row) illustrates particle shapes for SQ($N4$), SQ($N6$) and SQ($N8$).

4.2.2 Multi-sphere approach

Multi-spheres, which approximate the shape of particles by overlapping or touching spheres, are used as an approximation of the real shape irregularities Favier et al. (1999); Zhou and Ooi (2009). In the multi-sphere model, a single particle is represented by a set of rigidly connected spheres, which are inscribed into the shape of the particle such that at each contact point of sphere and real body a tangential plane can be constructed. The sub-spheres are allowed to vary in size and to overlap forming an approximation of any desired shape. The contact force between neighboring particles is calculated from their element spheres, using sphere-sphere contact detection. Each sub-sphere i of particle A is checked for contact against each sub-sphere k of particle B(see Figure 4.3). The normal overlap vector δ_{ABik} is determined for each pair of intersecting sub-spheres in the same way as conducted for single spherical particles:

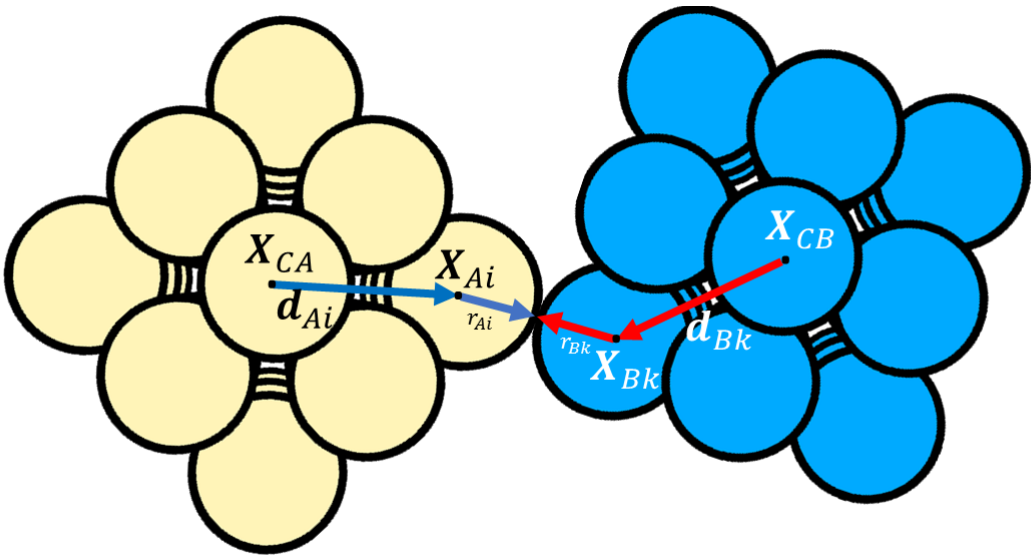

Figure 4.3 Scheme of particle-particle contact for multi-spheres.

$$\begin{aligned} \delta_{ABik} &= \|\boldsymbol{X}_{Ai} - \boldsymbol{X}_{Bk}\| - (r_{Ai} + r_{Bk}) \\ \boldsymbol{X}_{Ai} &= \boldsymbol{X}_{CA} + \boldsymbol{Q}_A \cdot \boldsymbol{d}_{Ai} \\ \boldsymbol{X}_{Bk} &= \boldsymbol{X}_{CB} + \boldsymbol{Q}_B \cdot \boldsymbol{d}_{Bk}, \end{aligned} \tag{4.13}$$

where $\boldsymbol{X}_{CA}$ and $\boldsymbol{X}_{CB}$ are the centres of gravity, $\boldsymbol{Q}_A$ and $\boldsymbol{Q}_B$ are the rotational matrices converting vectors from the body-fixed frame to the global coordinate system, $\boldsymbol{d}_{Ai}$ and $\boldsymbol{d}_{Bk}$ are the vectors in the body-fixed frame pointing from the centres of gravity ($\boldsymbol{X}_{CA}$ and $\boldsymbol{X}_{CB}$) to the centres of sub-spheres i and k for multi-sphere particles A and B correspondingly.

Contact forces F_{ABik} are obtained from the calculated overlaps δ_{ABik} for each pair of overlapping sub-spheres between particles A and B. The resulting overall force acting on particle A from particle B is determined as follows:

$$\boldsymbol{F}_{AB} = \sum_{i,k:\delta_{ABik}<0} \boldsymbol{F}_{ABik}. \tag{4.14}$$

Details of the algorithm and mechanical calculations can be found in (Abbaspour-Fard, 2000; Favier et al., 1999).

Cubes, as multi-spheres, were modeled in EDEM software using equal-radius ($d/4$) overlapping sub-spheres. The number of sub-spheres in each edge of the cubes varies between 2 and 5, resulting in 8, 27, 64, and 125 total sub-spheres per particle (further denoted as MS(8), MS(27), MS(64) and MS(125) correspondingly). Graphical illustrations for MS(8), MS(27), MS(64) are given in Figure 5.1 (bottom row). Note that for the considered MS particles, increasing number of sub-spheres only contributes to

the surface bumpiness, whereas the corners of the particles are identical (i.e. MS(8) and MS(64) have equal curvature at corners).

4.3 Simulation results: micro-level

4.3.1 Particle-wall impact

In this test, a particle impacts a flat wall with a specified translational velocity ($v_{pre} = 0.01\mathrm{m/s}$) normal to the wall and zero angular velocity. The particle has one plane of symmetry parallel to the wall, so that face-wall contact occurs. The post-impact particle velocity v_{post} normal to the wall is computed. The contact is assumed to be frictionless and without gravity. It can be observed from Figure 4.4 that for all particle shapes used the velocity increases again until a certain point, as expected, but then it decreases again slightly. This occurs due to the employed viscous damping model at the end of the contact, when the repulsive force in Eq.(4.1) ($k\delta^n$) component becomes smaller than the viscous part ($\gamma^n U^n$) and the total normal force becomes aligned towards the wall, decreasing the rebound velocity. After the impact is finished, it is clear from Figure 4.4 that the post-impact velocity for superquadric cubes does not depend on the blockiness parameter N and satisfies the coefficient of restitution: $v_{post}/v_{pre} = \varepsilon_{pw}$. On the contrary, the post-impact velocity for multi-spheres decreases with increasing number of sub-spheres. This is a well-known drawback of the standard multi-sphere method (Höhner et al., 2011; Kodam et al., 2009; Kruggel-Emden, Rickelt, Wirtz and Scherer, 2008). To overcome this problem the calculation of the contact forces has to be modified. The total force of the contacting sub-spheres cannot be equivalent to the contact force between contacting MS-particles. Kodam et al. (2009) proposed to adjust the normal spring stiffness that minimizes the error between the summarized contact force of the sub-spheres and reference particle is minimized. An alternative solution as demonstrated by Kruggel-Emden, Rickelt, Wirtz and Scherer (2008) would be to divide the total sum of all component forces by the number of contact points for each contact pair of MS-particles (advanced MS-method). Additionally, for a dense sample, which undergoes a quasi-static flow, this problem can be overlooked (since collisional contacts are missing in such conditions). Another solution can be considered by adjusting the restitution coefficient for the MS particles, which needs further studies.

4.3.2 Degree of interlocking

Particle shape irregularity is quantified in the following section. Particle 1 and Particle 2 stand on a flat surface having centres at $(-r,0,r)$ and $(r,0,r)$ correspondingly and

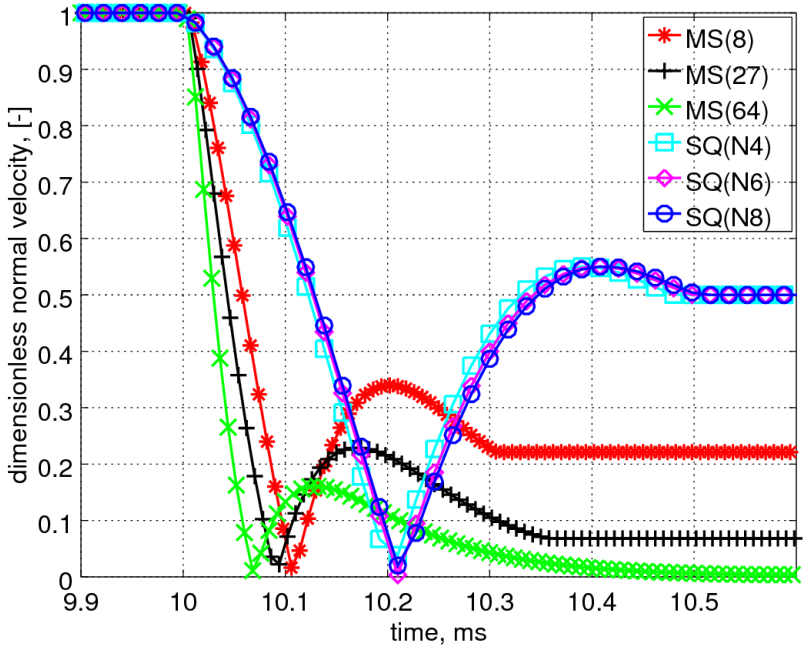

Figure 4.4 The dimensionless particle velocity v/v_{pre} as a function of time during the particle-wall impact.

touching each other at $(0,0,r)$, where $r = d/2$ is the half-edge length of a particle. Particle 3 is initially located at $(-r,0,3r)$ producing zero overlap, and is allowed to fall under gravity over Particle 1 (configuration "1+2", Figure 4.5).

The interlocking value $\delta z = 3r - z$ is calculated, where z is the residual Z-coordinate of the centre of Particle 3. Then, after impact, the initial position of Particle 3 in X-direction is changed by small $\delta x : x := x + \delta x$ and the simulations are iterated from $x = -r$ till $x = r$. The interlocking value δz as a function of initial position in X-direction is presented in Figure4.6.

It is clear from Figure 4.6 that the MS(8) shape has the highest degree of interlocking as can be expected from the surface being represented by two spheres in contact. It must be noted that the interlocking among particles can achieve higher values if particle 3 is shifted in £y£ direction (e.g., $\pm r$ for MS(8)). Moreover, δz decreases with the increase of the number of sub-spheres. The degree of interlocking for SQ particles has its maximum for SQ$(N4)$ and decreases with the increase of superquadric blockiness N.

The effect of particle shape irregularity is further studied in the following set of simulations with 3 particles (in "1+2" configuration). Particle 1,2 and 3 are located initially exactly in the same way as in Figure 4.5. Particle 1 and 2 remain static during the whole simulation. Particle 3 moves from $x = -r$ to $x = r$ with prescribed constant

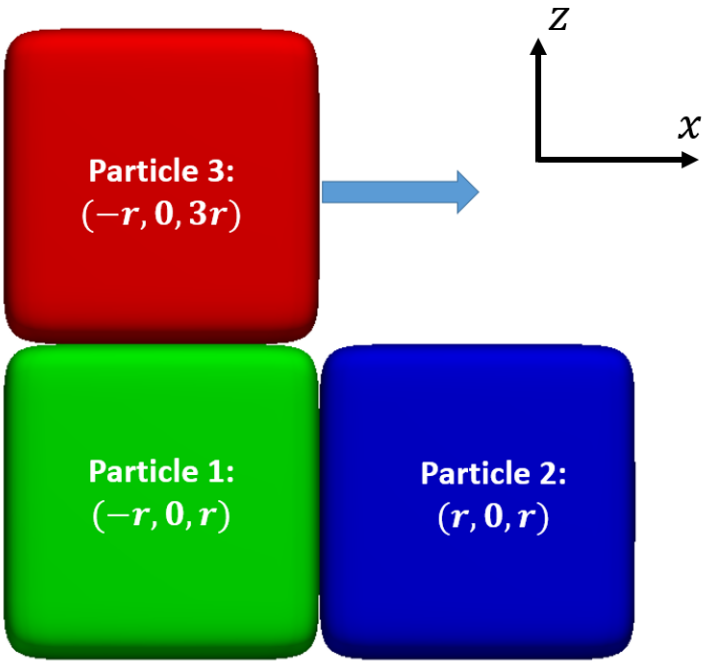

Figure 4.5 Simulation setup for determining the degree of interlocking.

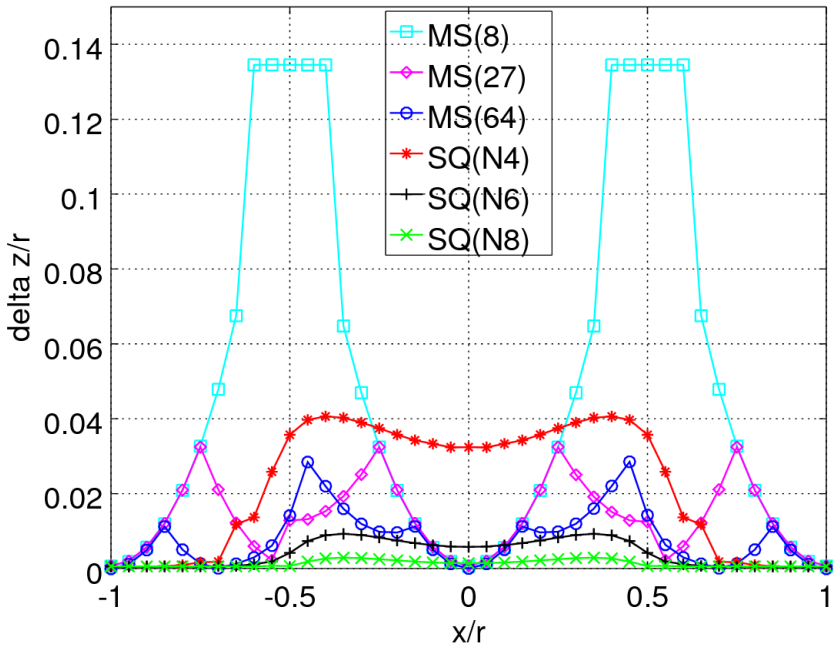

Figure 4.6 Dimensionless interlocking value $\delta z/r$ as a function of dimensionless x/r-coordinate.

translational velocity $u_x = 1\text{mm/s}$ in X-direction, having 1 degree of freedom (along Z-axis, no rotation).

4.3.3 Particle-Particle sliding

The simulation is conducted for different friction coefficients: $\mu^s_{pp} = 0.1, 0.3, 0.56$. Tangential force F_t acting on Particle 3 is calculated as the x-component of the total force (normal+tangential) taken with the negative sign ($-F_x$). In order to cancel out the effect of different masses per single particle, it is plotted (Figure 4.7) in dimensionless form ($F_t/\mu^s_{pp}mg$) as a function of relative displacement x/r. The total mechanical work done by the tangential force F_t is added to the legend in dimensionless form:

$$W = A/A_0, A = \int_{-r}^{r} F_t dx, \tag{4.15}$$

where $A_0 = 2\mu^s_{pp}mgr$ is the mechanical work done by the friction force for a displacement $\Delta x = 2r$ (from $x = -r$ to $x = r$), assuming particles as ideal cubes sliding along a flat surface. It can be seen from Figure 4.7 that the behaviour of the tangential force for MS particles exhibits a "zigzag" pattern. For SQ particles there is always only one local maximum/minimum that is related to the gap at $x = 0$ between particles 1 and 2. It seems that the behaviour of MS and SQ particles (maximum tangential force F_t and its mechanical work) tends to converge to that for ideal cubes ($F_t = \mu^s_{pp}mg = const, A = A_0$) with the increase of the number of subspheres (for MS) and blockiness N (for SQ) and with the increase of the friction coefficient μ^s_{pp}. However, significantly higher MS-particle resolution is required to achieve less than 5% of the maximum relative deviation of the tangential force from the mean value.

4.3.4 Inclined/rotating plate I

Here, a single particle is placed onto a flat surface that starts to rotate with constant angular velocity $\omega = \pi/50$ [rad/s] (the assigned rotational velocity is chosen to be small enough to prevent any sudden movement/jump of the particle while being displaced). The distance between rotation origin and projection of the particle centre onto the surface is $L = 24\text{mm}$ (Figure 4.8). For each particle shape the corresponding critical angle (the angle at which a particle begins to move/tilt) is found for coefficients of friction $\mu_1 = 0.45$ and $\mu_2 = 0.56$ and compared to the sliding angles $\alpha_1 = \arctan(\mu_1) = 24.23^\circ$ and $\alpha_2 = \arctan(\mu_2) = 29.25^\circ$.

Two scenarios are possible during the rotation of the plate: sliding of a particle along the plate without changing the orientation, or tilting of the particle towards the rotation origin. For the SQ particles (Figure 4.9), the results are depending on particle

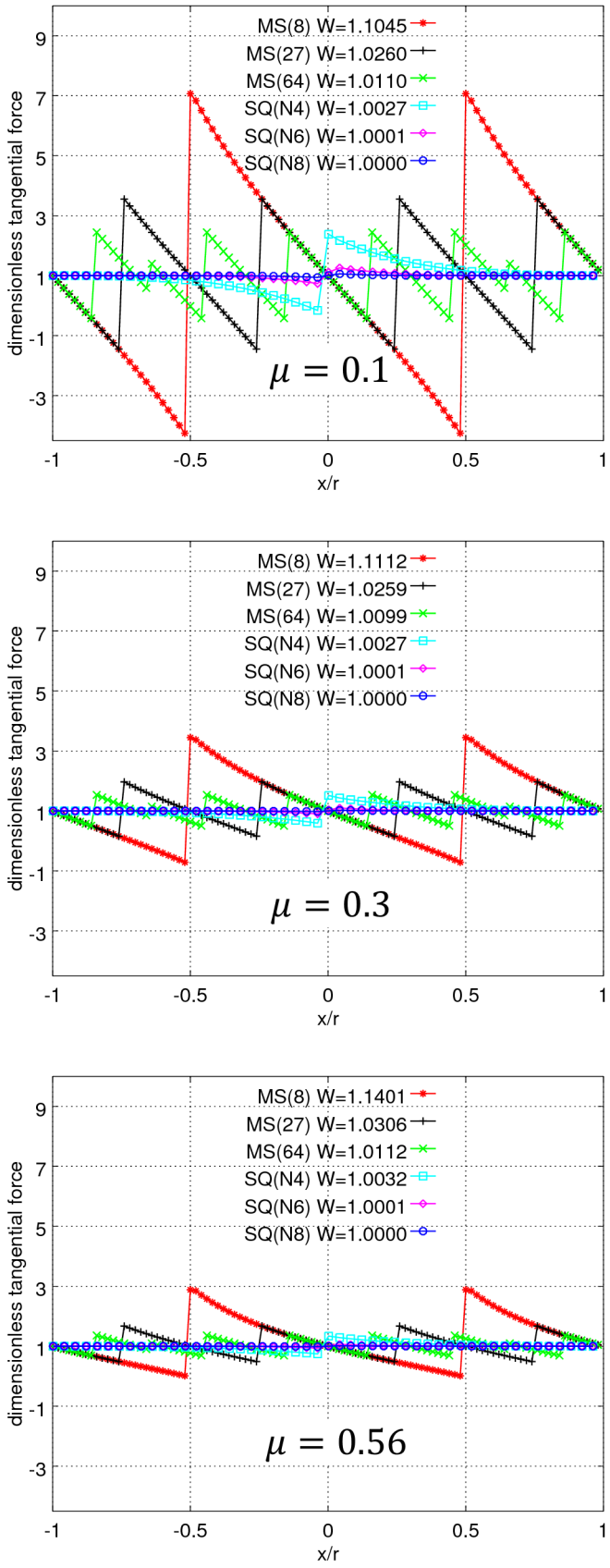

Figure 4.7 Dimensionless tangential force $F_t/\mu^s_{pp}mg$ as a function of initial dimensionless x/r-coordinate for different coefficients of friction $\mu = 0.1, 0.3, 0.56$.

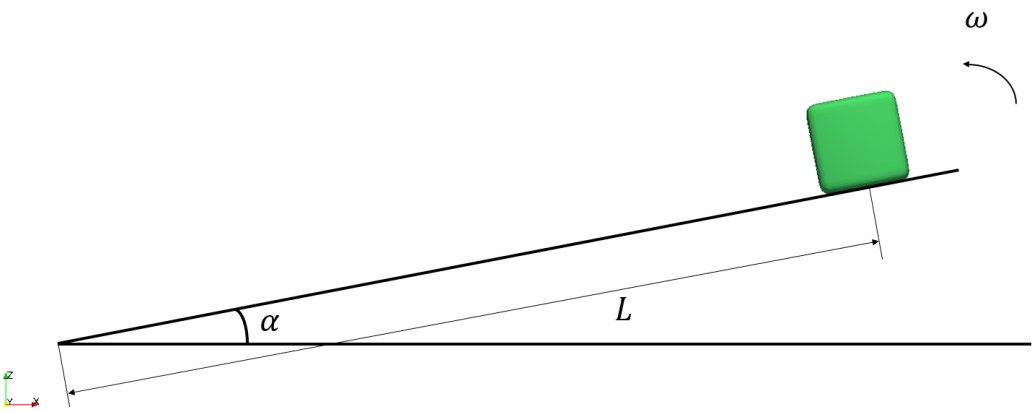

Figure 4.8 Inclined plate I: setup.

blockiness/edge sharpness (N). The SQ($N4$) and SQ($N5$) particles tilt and fall at the same angles irrespective of the coefficient of friction. For coefficient of friction $\mu = \mu_1$, SQ($N6$), SQ($N7$) and SQ($N8$) particles slide at the sliding angle, while for $\mu = \mu_2$, the critical angle increases with the increase of blockiness N. The results show that particles with different levels of edge sharpness can behave differently even at the single grain level (changing the mode of motion from rotational to translational).

It is interesting to note that the behaviour of MS particles does not depend on the number of sub-spheres. For μ_1, MS particles begin to slide exactly at the sliding angle α_1; for μ_2, they begin to tilt and fall from the plate at around 27° (similar to SQ($N6$)), irrespective of the number of sub-spheres for both values of the coefficient of friction studied. This can be explained by the fact that all MS particles have sub-spheres with equal sizes, which give them an alike tilting characteristics.

4.3.5 Inclined/rotating plate II

In this simulation, 3 particles in configuration "1+2" stand on a flat surface. Particle 3 is standing exactly above the gap between particles 1 and 2 (Figure 4.10). The flat surface starts to rotate and the critical angle for particle 3 is measured. The angular velocity ω and the distance L between the rotation origin and the gap between particles 1 and 2 are exactly the same as in the previous section. The particle-wall friction coefficient $\mu^s_{pw} = 1$ was chosen to avoid sliding of particles 1 and 2 along the flat surfaces before particle 3 starts moving. The coefficient of friction between particles was varied: $\mu^s_{pp} = 0.1, 0.2, 0.3, 0.4$, and 0.56. Critical angle as a function of superquadric blockiness (N) and the number of sub-spheres is presented in Figure 4.11. MS(216), MS(343) and MS(729) particles (with 6, 7 and 9 sub-spheres per edge correspondingly) have been additionally simulated. The simulation results ("S") are compared with the analytical solution ("A", case of perfect cubes): $\alpha_{crit} = \arctan(\mu^s_{pp})$ that covers only particle sliding.

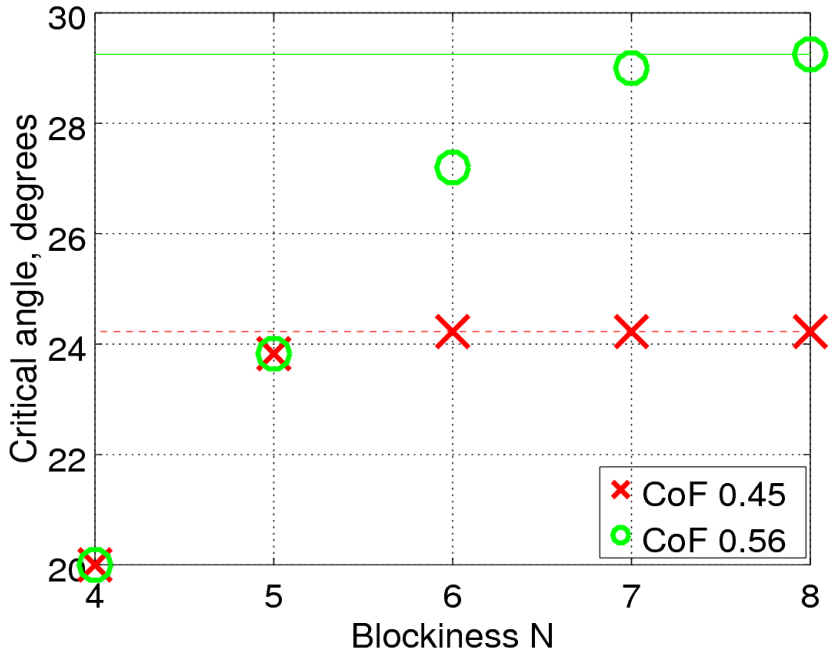

Figure 4.9 Critical sliding/tilting angle as function of superquadric exponent N (blockiness): cross signs for $\mu_1 = 0.45$ ("CoF 0.45"), green circles for $\mu_2 = 0.56$("CoF 0.56"). The red dash line indicates the sliding angle for $\mu_1 = 0.45$, the green solid line represents the sliding angle for $\mu_2 = 0.56$.

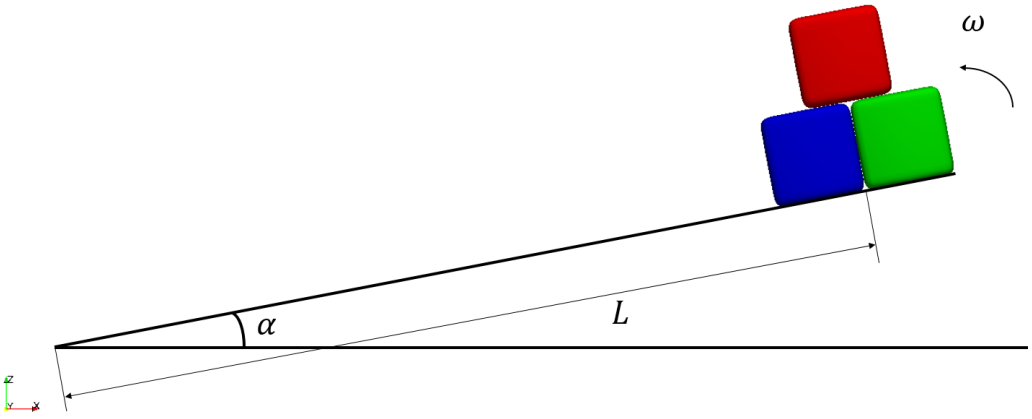

Figure 4.10 Inclined plate II: particle configuration.

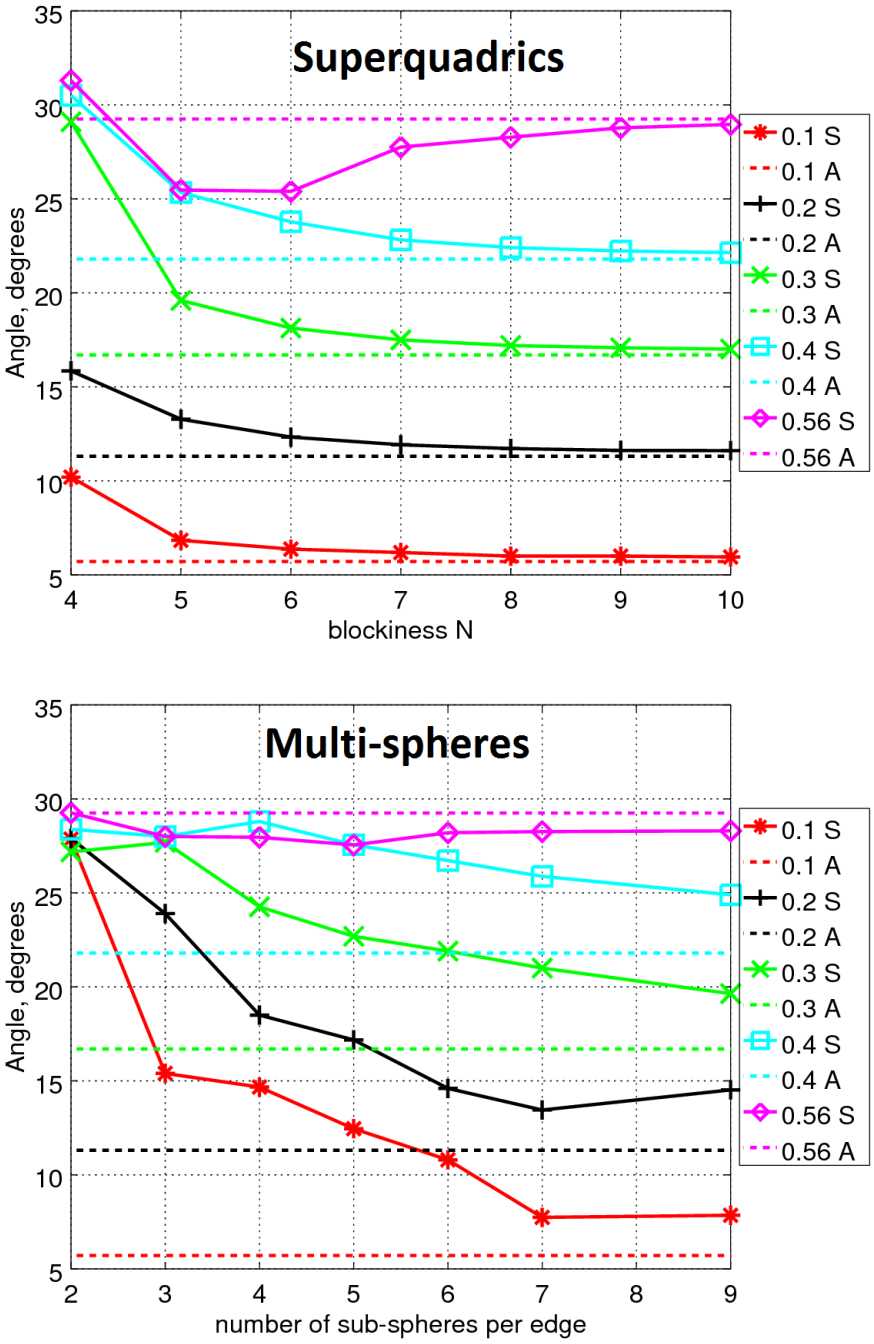

Figure 4.11 Inclined plate II: simulation results. Critical angle vs. superquadric blockiness vs. number of sub-spheres for MS for different coefficients of friction: $\mu^s_{pp} = 0.1, 0.2, 0.3, 0.4$, and 0.56. "S" stands for simulation, "A" stands for analytical solution in case of ideal cubes (dashed lines).

In all cases an increase in blockiness tends to provide results similar to that of analytical solutions. Starting from $N = 8$ the results can be considered as converged to α_{crit}. Except for $\mu_s = 0.56$, all particles with blockiness parameter of 7 or smaller give a larger critical angle, for which it can be suggested that a lower blockiness acts as bumpiness in this case (the top particle is slightly trapped in the free space between two base particles). It seems that there is a threshold for sliding friction, at which the interlocking effect is minimized (this is also seen in case of MS particles, where particles with $\mu_s = 0.56$ are independent of bumpiness).

For MS(8) particles, with maximum interlocking, variation of sliding friction has no significant influence on the critical angle. Whereas, by increasing the number of sub-spheres (having smoother particles), the critical angle becomes dependent on the assigned sliding friction. Moreover, it is seen that for higher values of sliding friction (0.4 and 0.56) the system is not affected by the bumpiness factor.

Based on the results above and the results from previous sections, we can conclude that at low coefficients of friction (≤ 0.2) representation of particle shape using SQ and MS can have significant effect on particle motion, especially for MS particles (interlocking effect). At high contact friction, the effect of particle-interlocking can be relatively neglected.

4.4 Simulation results: macro-level

4.4.1 Angle of repose

In this test an assembly of 6000 particles is distributed randomly in a cone. The system is allowed to settle under gravity (in Z-direction) for 1s of simulation time. Figure 4.12 shows the simulation setup and the dimensions used.

The average residual translational and angular velocities for MS particles after settling were found to be of order $v_{ave}^{MS} = 10^{-13}\text{m/s}$ and $\omega_{ave}^{MS} = 10^{-9}\text{rad/s}$ correspondingly, while for SQ particles the velocities were around $v_{ave}^{SQ} = 10^{-5}\text{m/s}$ and $\omega_{ave}^{MS} = 10^{-2}\text{rad/s}$. A possible explanation for this can be bumpiness of MS particles that produces an artificial sliding and rolling resistance because of multiple contact points between two MS particles. Concerning SQ particles, the contact is based only on a single contact point. Stability of the packings for SQ particles can be increased by applying a rolling friction model, like models B and C in Ai et al. (2011), with a relative small rolling friction coefficient about $\mu_r = 10^{-3}$ or $\mu_r = 10^{-2}$ to dissipate energy. In this case the average residual translational and angular velocities for SQ particles were found to be around one order less for $\mu_r = 10^{-3}$ and 4 orders less for $\mu_r = 10^{-2}$ correspondingly with respect to zero rolling friction coefficient. However,

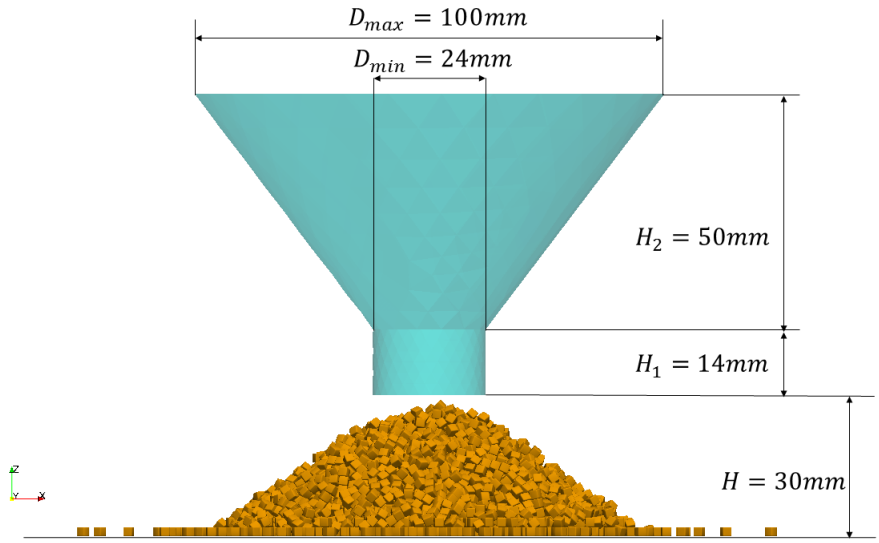

Figure 4.12 Angle of repose simulation setup.

the influence of a small rolling friction coefficient on the superquadric DEM simulation results must be further studied. Hence, zero rolling friction coefficient is used in all simulation results presented further in this paper.

Then, after the packing is formed, the orifice is opened and discharge commences. The simulation continues for 3s until a heap is formed, see Figure 4.13. The heap is then analysed and the angle of repose is estimated. The algorithm that determines the angle of repose of the heap operates by dividing the heap along Z-direction into 20 discs of equal height (instead of dividing into wedge shaped regions as in Wensrich and Katterfeld (2012)). The discs are allowed to overlap by 50% with the neighbors in vertical direction. Then, the average cross-sectional area S_i of each disc is calculated by constructing a convex hull from particle centres in the XY plane. Each disc is assumed to be cylindrical with area equivalent radius $r_i = \sqrt{S_i/\pi}$. This way, it was possible to construct the surface profile function $z_i = z(r_i)$ and plot it for each of particle shapes, see Figure 4.14.

Furthermore, the angle of repose is found as the inclination angle of $z = z(r)$ using linear regression, see Figure 4.15. The first and the last bins are excluded to avoid the influence of the rounded top and flattened foot of the heap. Accordingly, the influence of two interlocking mechanisms (i.e. increased angularity, which is obtained by increasing blockiness of SQ particles, and increased surface bumpiness for MS particles, which achieved by reducing number sub-spheres) on AoR characteristic is evaluated. It can be seen from Figure 4.15 that the results for SQ particles are located within a larger interval than MS particles. The increase of SQ blockiness parameter N from $N = 4$ to $N = 8$ increases monotonically the angle of repose. Meanwhile, it is clear that, for MS particles, increasing the number of sub-spheres decreases bumpiness (which presum-

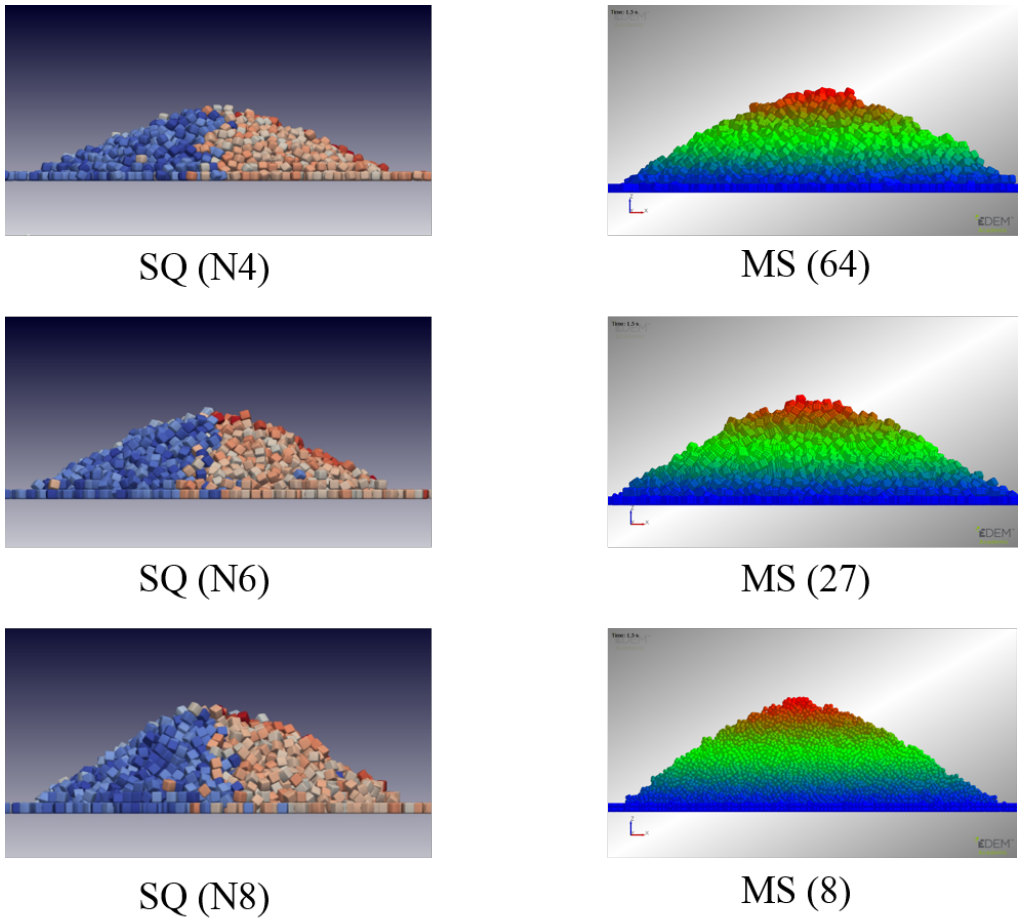

Figure 4.13 Heap formation for the considered cubical particles.

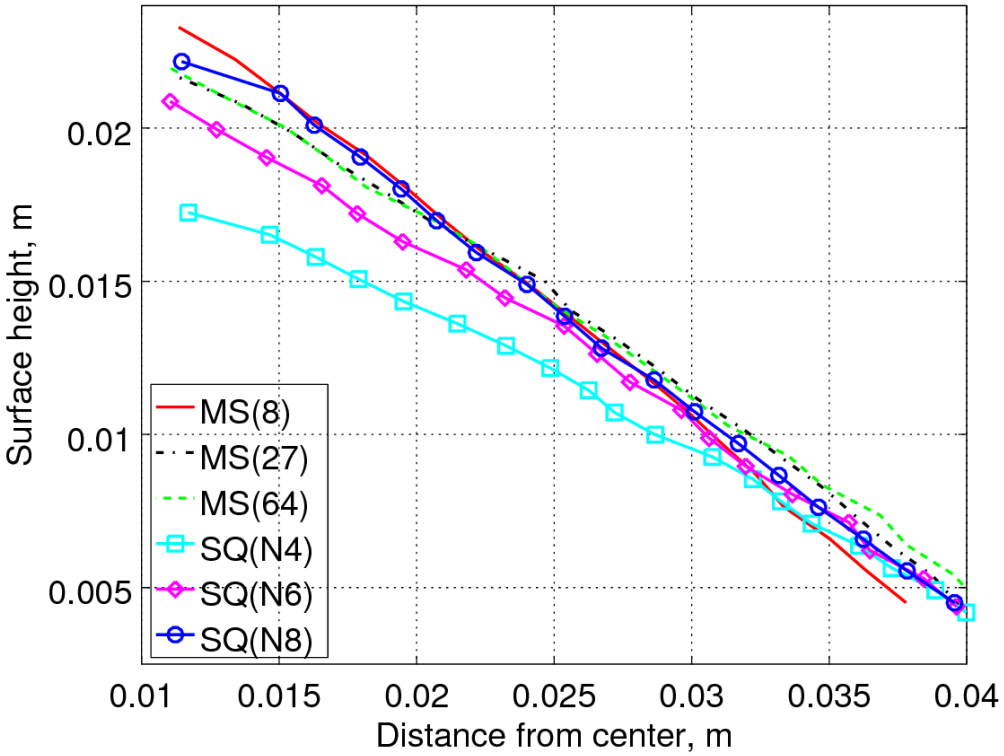

Figure 4.14 Comparison of the surface profiles of particle piles from MS and SQ simulations.

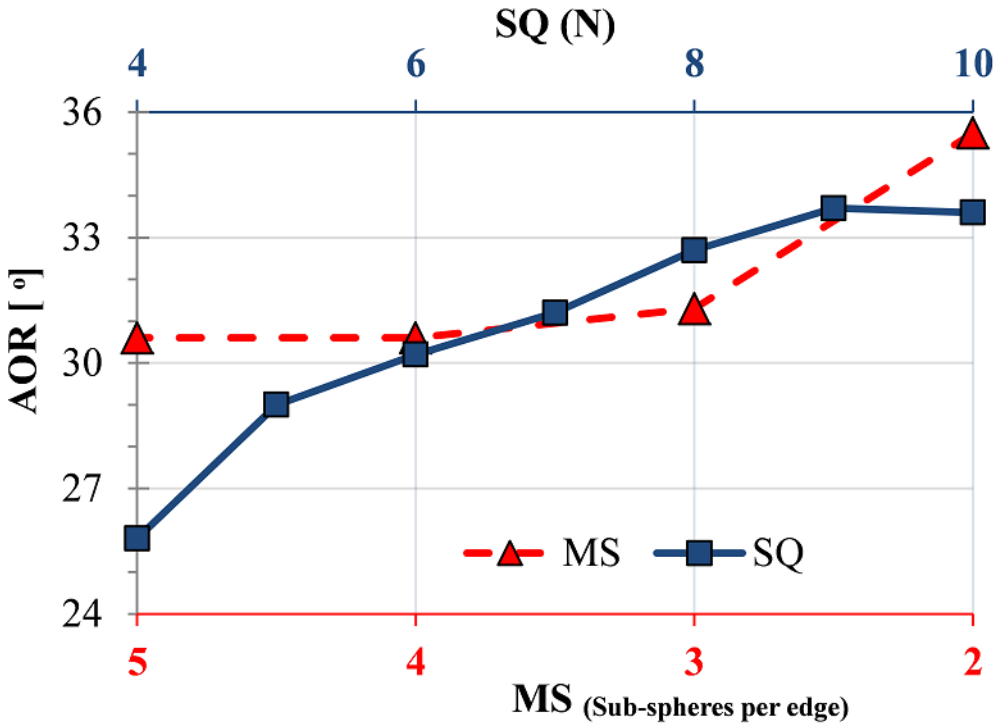

Figure 4.15 Averaged angle of repose for different MS and SQ particles.

ably would affect the angle of repose). Looking at Figure 4.15, it is clear that there is an abrupt change for AoR of MS particles with 2 and 3 particles per edge (i.e. MS8 and MS27). However, it seems that further increase in the number of particles per edge (in this case from 3 to 5), is not affecting the avalanching characteristics of MS particles. A similar effect was observed by Markauskas et al. (2009) for ellipsoidal particles.

Eventually, it is interesting to note that despite the very different interlocking mechanism and surface characteristics between SQ($N8$) and MS(8), both particles show similar heap profiles. Nevertheless, SQ($N4$) and MS(64), which have alike geometric characteristics (both have relatively similar rounded edges, and MS(64) is less bumpy and tend to have a rather smooth surface), present very distinct heap profiles. It can be said that even small surface bumpiness can affect the heap formation of cubic particles (MS(64) has larger AoR than SQ($N4$) and SQ($N6$)). Additionally, it is seen that the SQ particles are more sensitive in AoR test on blockiness parameter.

In order to measure computational efficiency of MS and SQ approaches, the simulations for "Angle of Repose" with SQ and MS particles were conducted on the same machine using the same software (LIGGGHTS). Figure 4.16 illustrates performance degradation C_T/S_t as a function of the number of sub-spheres S_s for MS particles and as a function of blockiness N for SQ-particles, with C_T being the total computational time and S_T being the total simulation time with perfect spheres (can be considered as MS(1)). MS37 and MS61 particles, that are MS64 and MS125 particles with removed interior sub-spheres, were additionally simulated. It can be observed that the computational time for MS particles depends linearly on the number of sub-spheres with a factor of 1.3. MS(125) particles demonstrate the highest computational time and are excluded from further simulations. The total computational time for SQ particles is $10X$ larger than for the case of perfect spheres and it does not grow with the increase of blockiness N (being comparable to C_T of MS8 particles).

Based on the results above and the results from previous sections, only SQ($N4$), SQ($N6$), SQ($N8$) and MS(8), MS(27), MS(64) particles will be used further in this paper and compared to each other.

4.4.2 Jenike shear tester

The Jenike shear tester is widely used for measuring flow properties of particulate solids (Härtl and Ooi, 2011). In this test the granular material is placed in a split cylindrical box. Then, the material is consolidated by applying a constant vertical load σ_v (10 kPa) to the lid section (consolidation state). Later, the top half of the cylinder (ring) is sheared at a constant translational velocity (2 mm/sec), see Figure 4.17. The measured quantity is the force required for this movement that can be converted to an average shear stress τ. Velocity of the lid in LIGGGHTS is controlled by a standard

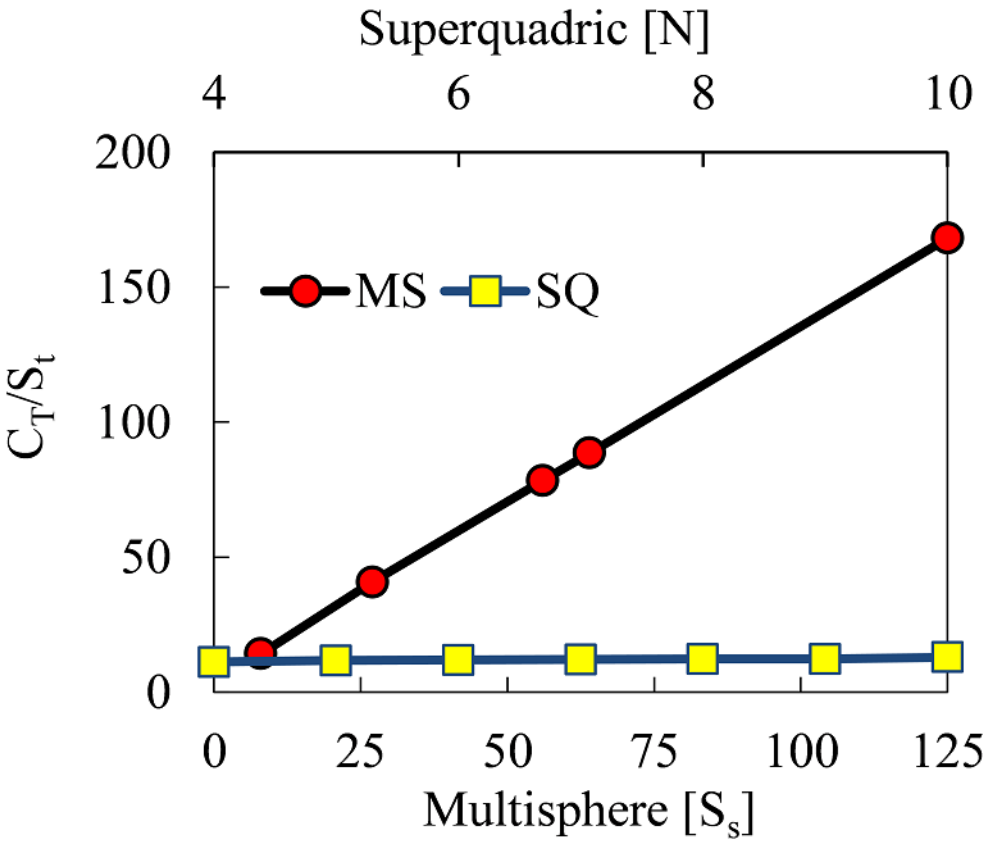

Figure 4.16 Computational time vs. number of sub-spheres for MS particles and vs. blockiness *N* for SQ particles.

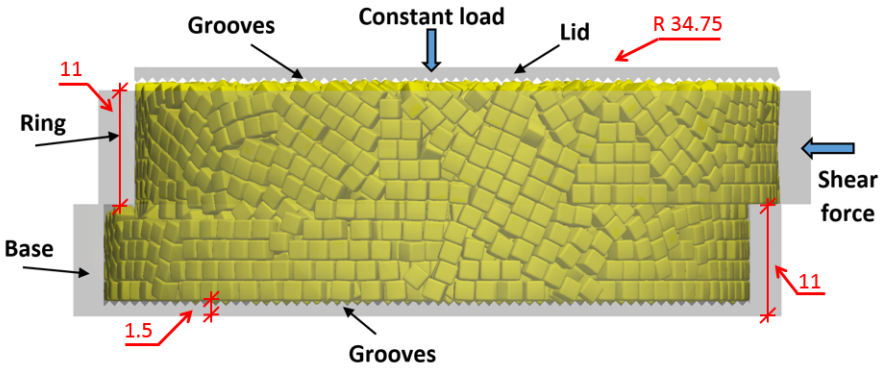

Figure 4.17 Jenike shear tester filled with superquadric particles (dimensions are in mm).

PID controller (Aigner et al., 2013) that compares the current acting force f_{total} with the predefined target value f_{SP}. In EDEM position and velocity of the lid is controlled by multi-body dynamics. Here, the lid is only allowed ro move in Z direction (to allow for dilation/contraction of the specimen). However, it is clear that giving further degree of freedom (i.e. allowing lid tilting) definitely can affect the obtained results.

Before comparing MS and SQ particles, simulations with mono-sized spherical particles were conducted to prove equivalence of the setups in the LIGGGHTS and EDEM codes. Results showed a reasonably good agreement with a maximum difference of 3 % (for stress-displacement curves). This discrepancy can be explained by the difference in initial particle configuration within the generated packings and also the difference in the constant vertical load controller.

The DEM time-step was chosen as $\Delta t = 2 \cdot 10^{-6}$ s (5 % of Rayleigh time) in all simulations. Two types of packing, using MS and SQ particles, were generated to assess the dependence of the results on the density of the initial packing. In the dense packing, the particle-particle friction coefficient μ^s_{pp} was set to zero at the filling stage and changed back to $\mu^s_{pp} = 0.56$ before applying σ_v. On the contrary, the loose packing had $\mu^s_{pp} = 0.56$ during the whole simulation. For all simulations, material properties were kept identical and packings of equivalent bulk volume were generated using SQ($N4$), SQ($N6$), SQ($N8$) and MS(8), MS(27), MS(64) particles. In the following two sections (4.4.2 & 4.4.2), the effects of particle edge and surface properties on the packing density and mode of motion are evaluated. Successively, the shearing response of the particles is assessed in section 4.4.2.

Porosity

The porosity ϕ of the samples was measured by exporting the position of the lid at start and end of shearing. This scalar quantity is an indication of how densely the particles are packed in the system (i.e. by dividing the total volume of the voids over

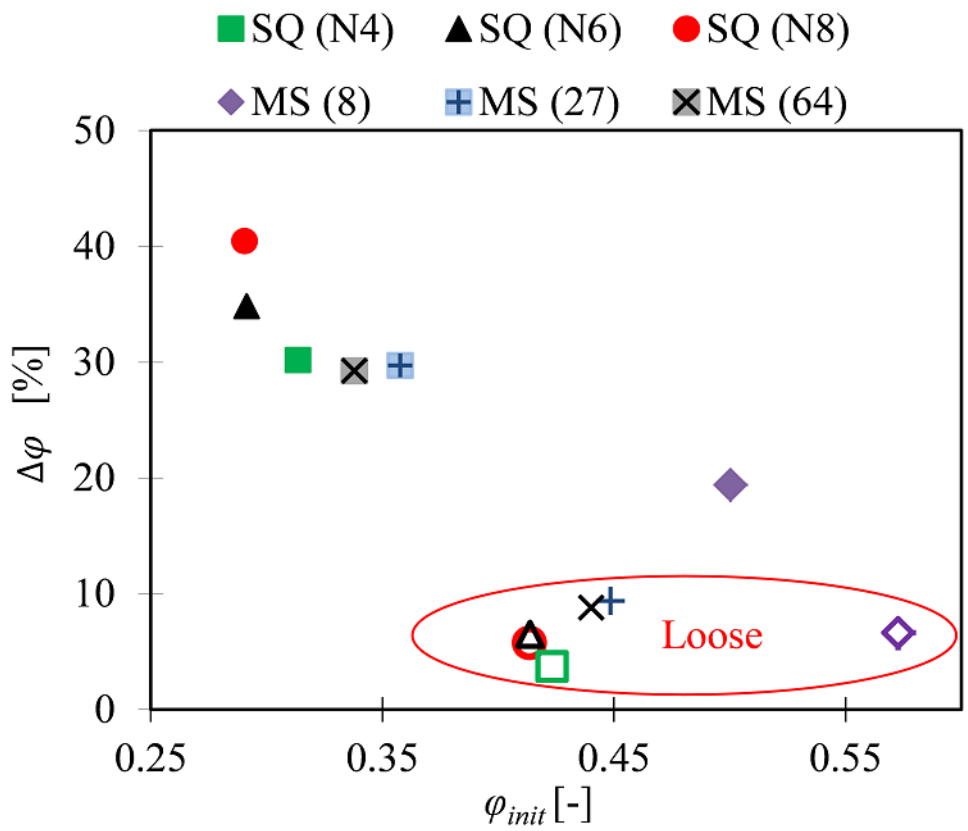

Figure 4.18 Porosity of the packings with different particle shapes (filled markers are for the dense packing).

the volume of the shear tester). As mentioned before, the packings are prepared in dense and loose states by switching the friction coefficient to 0 and 0.56 respectively. Figure 4.18 presents the initial porosity of the samples at $D = 0$ (end of consolidation) and also the relative change of porosity at end of shearing ($\Delta\phi$). The porosity at D = 0 is referred to as "initial porosity" (ϕ_{init}) and $\Delta\phi$ is calculated as:

$$\Delta\phi = \frac{\phi_{end} - \phi_{init}}{\phi_{init}} \cdot 100\% \tag{4.16}$$

where, ϕ_{end} is the final porosity of the sample at $D = 6$ mm.

According to Table 4.2, by increasing N, the number of particles in both density states decrease up to 15 %. Moreover, looking at Figure 4.18, it is clear that the reduction in number of particles is not affecting the initial porosity (ϕ_{init}) of the system (i.e. the extension of edges for SQ($N6$) and SQ($N8$) provides similar total particle volume as the assembly of SQ($N4$) particles) despite the differences in volumes per single particle (Table 4.3). It is also seen that the value $N = 4$ leads to the highest ϕ_{init} for SQ particles (more noticeable for the dense case) and further increase of N from 6 to 8 has no effect on the porosity of the sample.

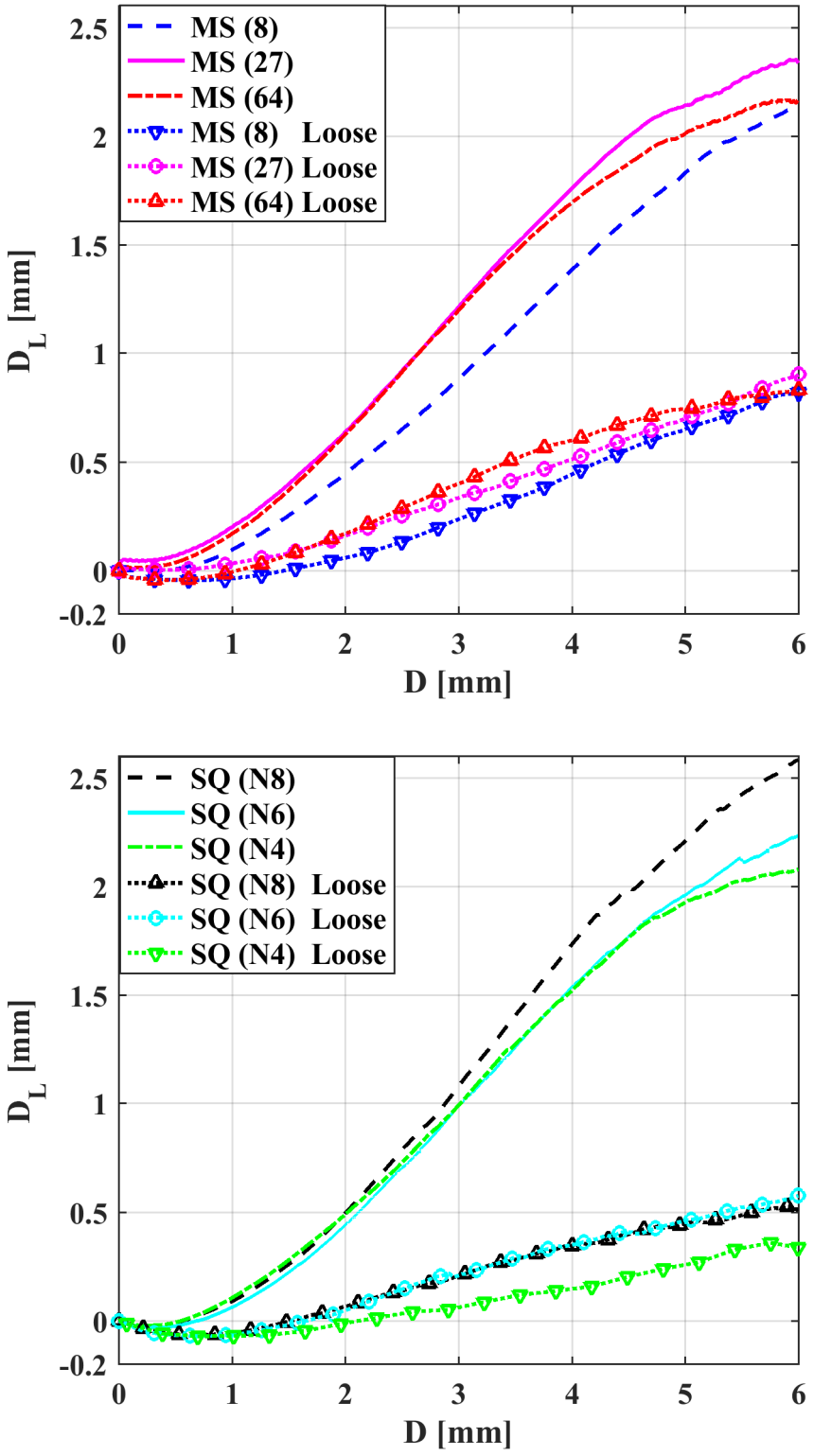

Figure 4.19 The relative vertical displacement of the lid during the shearing for both loose and dense packing of: a) MS particles; b) SQ particles.

Table 4.2 Number of particles in Shear test.

Particle	Packing	Number of particles	Total mass, kg
SQ($N4$)	Loose	6163	0.1637
	Dense	7378	0.1960
SQ($N6$)	Loose	5538	0.1637
	Dense	6848	0.2024
SQ($N8$)	Loose	5225	0.1611
	Dense	6576	0.2027
MS(8)	Loose	6236	0.1071
	Dense	7463	0.1282
MS(27)	Loose	5852	0.1540
	Dense	6975	0.1836
MS(64)	Loose	5719	0.1564
	Dense	6920	0.1892

Table 4.3 Volumes per particle.

Shape	Volume, mm^3	V_p/V_c*
SQ($N4$)	6.4819	0.8102
SQ($N6$)	7.2079	0.9010
SQ($N8$)	7.5167	0.9396
MS(8)	4.1933	0.5242
MS(8) (without central void)	4.6649	0.5832
MS(27)	6.4157	0.8020
MS(64)	6.6653	0.8332

*V_p: volume of single particle
V_c: volume of identical cube

Moreover, results suggest that the bumpiness, in MS particles, can affect the initial porosity of the system and leads to increase of ϕ_{init} in both density states (here, it must be noted that the MS(8) has a void between composing particles which is subtracted from the total voids of the system).

Furthermore, it is seen that all of MS particles provide higher initial porosities than for SQ particles. This is mostly due to the additional void that is available between adjacent overlapping spheres on the surface of the MS particle.

Another important phenomenon that happens during shearing of the granular samples is the dilation of the assemblies. The ϕ_{init} for the samples are plotted in Figure 4.18 with respect to the change in porosity ($\Delta\phi$) at $D = 6$ mm. It is seen that even the samples with initially loose configurations tend to dilate, which might be due to the high level of irregularity that the considered particles have (for both MS and SQ particles $\Delta\phi$ <10 %). On the other hand, the magnitude of $\Delta\phi$ in dense samples is 3 to 4 times larger than for the loose samples (as expected, the dilatant behaviour is more pronounced for the dense packings). Additionally, the increase in blockiness of the SQ particles increases the $\Delta\phi$ magnitude. Unlike this, the effect of bumpiness on dilatancy is not following a specific trend for the considered MS particles. While the difference of $\Delta\phi$ for MS(27) and MS(64) is relatively small, MS(8) presents the lowest $\Delta\phi$. This is due to the higher initial porosity in sample with MS(8) particles. The observed results are well capturing the concept of dilation and its dependency on density state in critical-state theory Altunbas et al. (2017); Wood (1991).

It is also useful to monitor the vertical displacement of the lid, during the shearing of the assembly, to determine the mode of volume change (i.e. contractive or dilative), see Fig 4.19.For the loose packing, SQ$(N4)$ and MS(8) have the lowest amount of lid displacement (this is due to the higher initial porosity, see Figure 16). Furthermore, loose packings are showing a slightly contractive behaviour initially, approximately up to 1.5 mm of the shear displacement, before starting to dilate.

In dense packings, the contraction of the assemblies seems to be insignificant and dilation is the dominant mode of volume change. For the MS particles, the bumpiness effect can be seen in further dilation of MS(27) compared to MS(64), however, MS(8) has the least volume increase due to its initial higher porosity. On the other hand, increase in the corner sharpness of SQ particles is contributing to increased dilation of the assembly during shearing.

Coarse-graining shows the local distribution of the porosity in the Jenike shear tester. Figure 4.20 presents the results for MS(8), with ϕ_{init}=0.5, at $D = 6$ mm. It can be seen that the lowest porosity is formed from top right to bottom left corner. A similar pattern has been observed in the Section 4.4.2 for the normal contact force network.

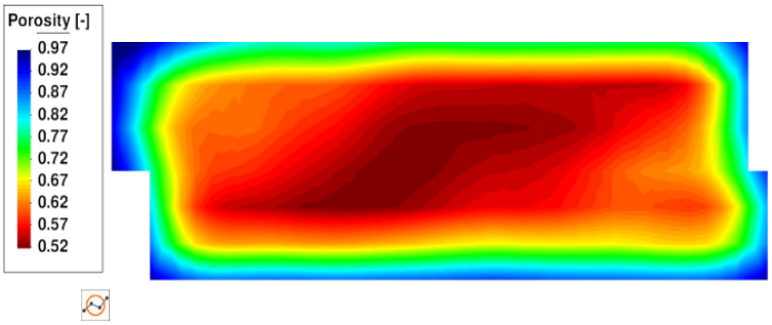

Figure 4.20 Distribution of the voids in Jenike cell (coarse grained results for visualization of the porosity for MS8, at displacement of $D = 6$ mm).

Mode of motion for the particles

The previous section provided information on the effect of surface bumpiness and edge sharpness on the packing density and the dilation of the particles at the initial and final state of a direct shear test. In the current section, an attempt is made to evaluate the mode of motion for the particles during the shearing. Accordingly, the cumulative rotation $\boldsymbol{\theta}_i$ and its magnitude θ_i, for each particle i, is recorded for all the tests:

$$\boldsymbol{\theta}_i(t) = \frac{1}{2\pi}\int_0^t \boldsymbol{\omega}_i d\tau, \theta_i = ||\boldsymbol{\theta}_i||, i = \overline{1, N_p}, \tag{4.17}$$

where, $\boldsymbol{\omega}_i$ is the angular velocity of particle i and N_p is the number of particles in the system.

Figure 4.21a shows the distribution of the cumulative rotation magnitude at $D = 6$ mm for MS(8) particles (since a similar trend was seen for other particles, only the result for MS(8), with $\phi_{init} = 0.57$, is shown here).

It is clear that the rotation of the particles is localized in a layer with a thickness of two to three particles (most rotation belongs to the particles located in the shear band), in the mid height of the shearing cell (this is commonly observed in both MS and SQ particles). The obtained results are in line with the numerical study in Zhang and Thornton (2007). Additionally, a similar simulation has been conducted with spherical particles, where the particles only have sliding friction (no rolling resistance). It is seen from Figure 4.21b that the magnitude of the cumulative rotation is certainly higher for spheres and also the pattern is quite different (mostly near the lid) for two particle shapes.

Similarly, the cumulative rotation around X, Y and Z axes is only presented for MS(8) type particles, see Figure 4.22. It is clear that the highest amount of rotation is happening around Y axis (as shearing happens in X direction). Figure 4.23 compares the magnitude of the cumulative rotation for the dense samples at the end of the shearing. The results in Fig. 4.23 indicate that once sample is dense, bumpy and blocky

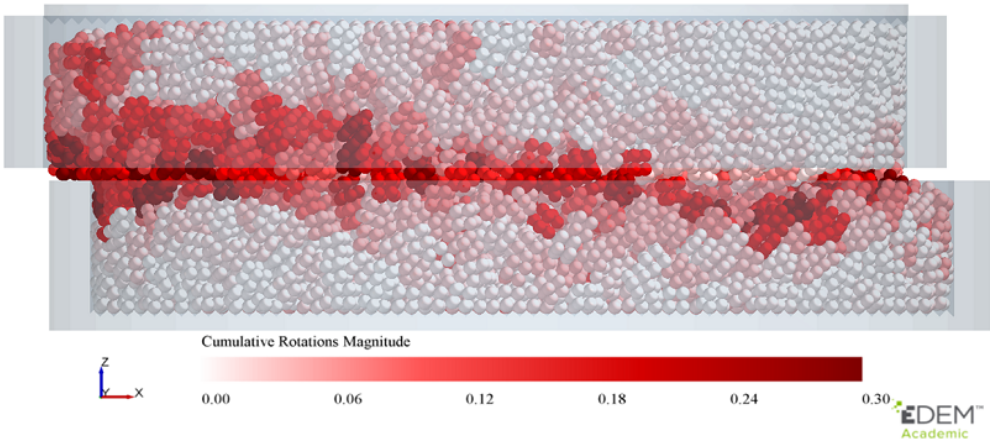

(a)

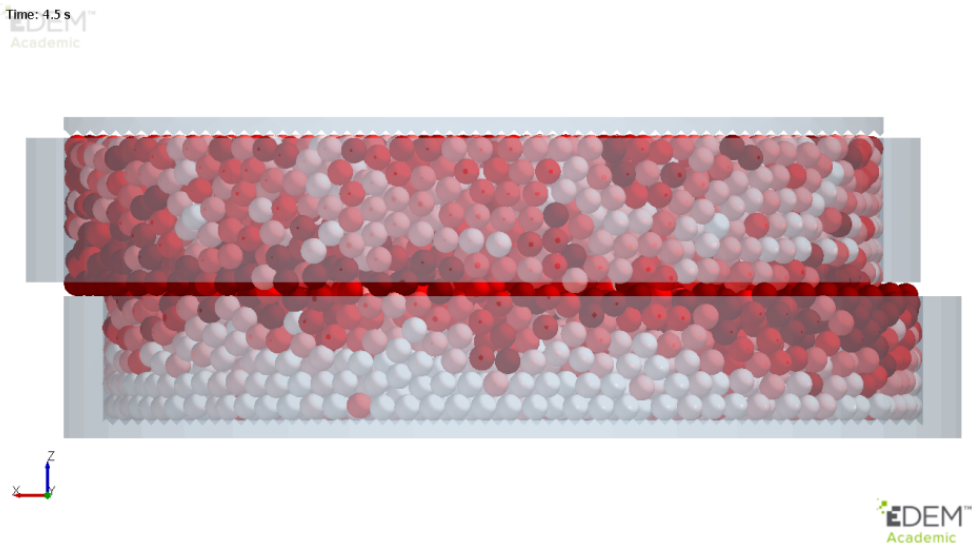

(b)

Figure 4.21 Distribution of the cumulative rotation magnitude at $D = 6$ mm for a) MS(8) b) spherical particles.

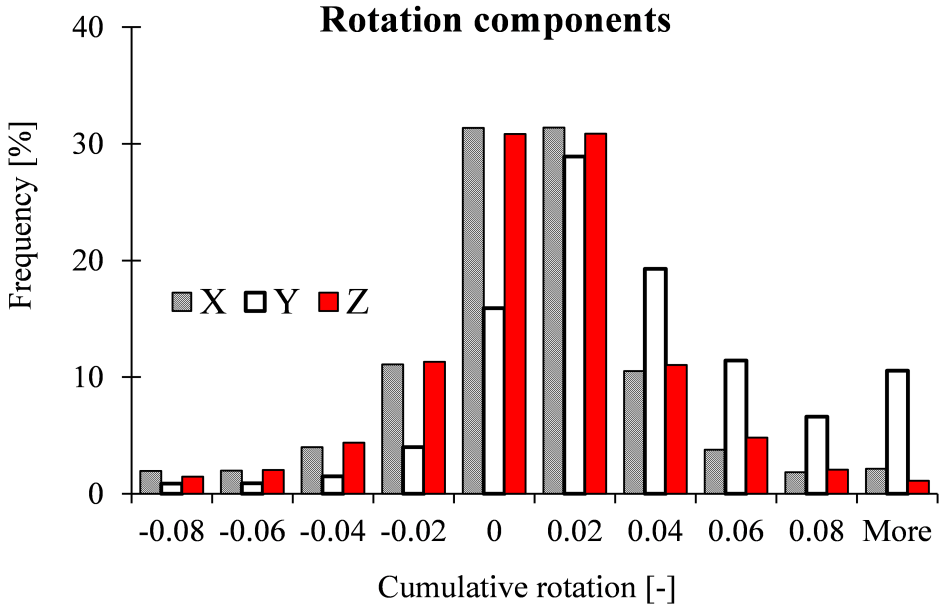

Figure 4.22 Cumulative rotation over different axes for MS(8) particles (at $D = 6$ mm).

particles have less space to rotate. Accordingly, changing number of sub-spheres and blockiness parameter has no considerable effect on the bulk response of the granular sample. Additionally, results imply that for both SQ and MS particles the magnitude of cumulative rotation is independent of the bumpiness and blockiness.

However, for the loose packings, as shown in Figure 4.24, SQ(N8) and MS(8) present the lowest cumulative rotation (true for higher magnitudes of cumulative rotation >0.075). The percentage of MS particles with cumulative rotation magnitude less than or equal to 0.025 is clearly higher than the corresponding percentage for SQ particles, independently of bumpiness/squareness. Nonetheless, for the rest of the cumulative rotation magnitudes, MS and SQ particles show similar values. Consequently, it can be deduced that the additional bumpiness/blockiness results in constraining the rotation of the particles (during shearing) only in loose packings.

Shear strength

Moreover, the distribution of the magnitude of normal contact forces is presented in Figure 4.25 for MS particles. Results suggest that the zone with lower porosity concentration and strong contact forces overlap. Additionally, it is seen that as interlocking increases (i.e. from MS(64) to MS(8)) the strong contact network becomes more pronounced within the shear cell. Furthermore, the coordination number has been obtained for each of the particles types (MS and SQ) during the shearing (for MS particles, coordination number is obtained through considering the total number of contacts among sub-spheres), see Figure 4.26. It is clear that the coordination num-

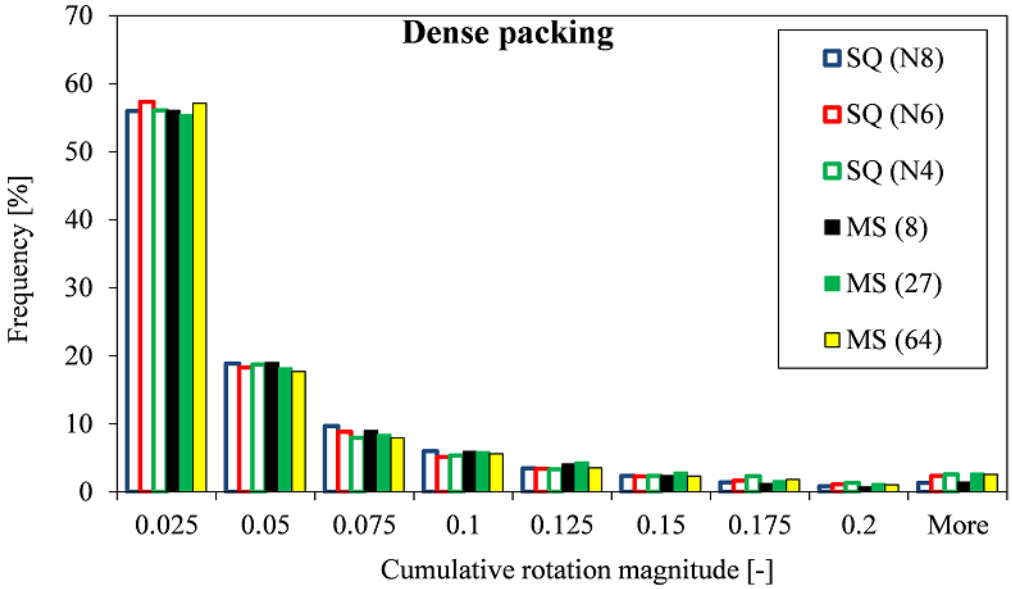

Figure 4.23 Cumulative rotation magnitude for the dense samples.

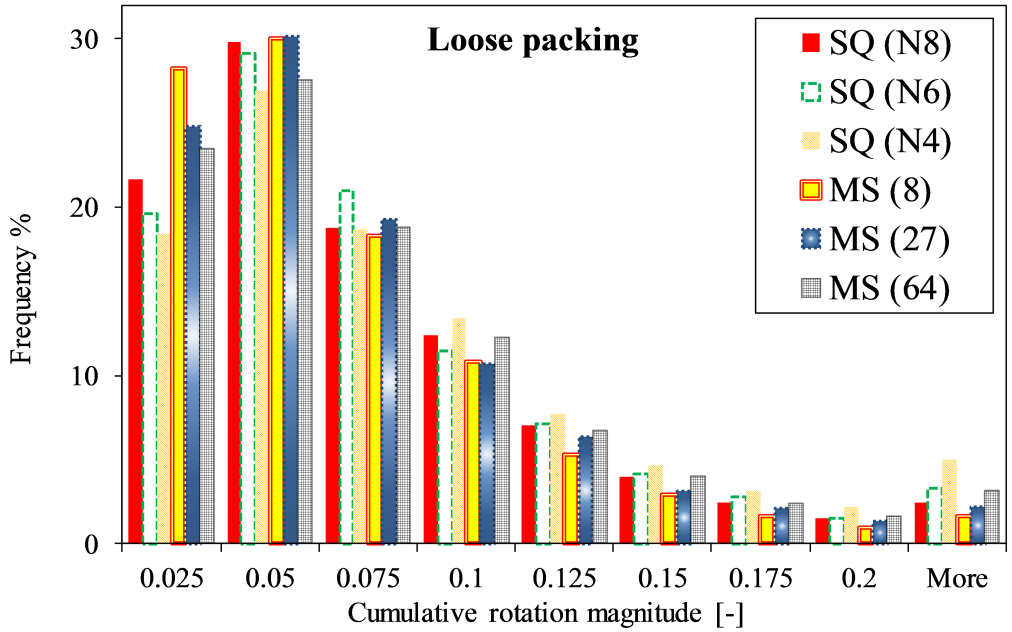

Figure 4.24 Cumulative rotation for the loose samples.

ber is almost constant for SQ particles with different edge sharpness (this suggest that though number of particles for SQ($N6$) and SQ($N8$) are lower than SQ($N4$), sharper edges

The corresponding shear stress curves for SQ and MS particles as a function of shear displacement (D) are shown in Figure 4.27. It can be seen that, in loose packing, SQ($N4$) has the lowest peak strength during shearing. However, it can be noticed that after increasing the blockiness to $N = 6$, the material shows a higher strength, but a further blockiness (i.e. $N = 8$) plays no significant role in the shearing response of the SQ particles. Additionally, one might argue that in shearing strength of the granular material, the fact of packing density matters to a large extent. Looking at Figure 4.18, it can be seen that for the loose packings, cubes with different values of N and various surface bumpiness (except MS(8)) have a similar values of ϕ_{init}.

For the loose packings of the MS particles, the MS(27) and MS(64), which have relatively similar surface roughness, show a comparable peak strength, while a slightly lower residual strength can be seen for the MS(64) (this is due to further smoothness in the surface of the particle). The MS(8) is providing a peak and residual strength larger than for MS(27) and MS(64), which is an indication of increased interlocking among the MS(8) particles. Moreover, a similar residual strength is seen for the following pairs 'SQ($N4$) and MS(64)', and 'SQ($N6$), SQ($N8$) and MS(27)'. According to the shown results, it can be seen that increasing particle bumpiness can compensate to some extent the effect of edge sharpness when approximating particles by multi-spheres. Additionally, comparing the observations here with those in section 4.4.1, it is deducible that in dense shearing regimes having a relatively resembling geometry for the particles can be adequate to capture comparable bulk response from different shape representation techniques.

For the dense packing, increasing blockiness for SQ particles results in higher shear strength of the material. A similar response is seen for the MS particles when the number of sub-spheres is reduced (the influence is roughly 30 % for both particle types). It should be noted that due to the limitation of the displacement in the Jenike tester, the residual strength of the dense samples has not been fully recorded for the particles with the highest amount of bumpiness and blockiness (i.e. MS (8) and SQ ($N6$) and ($N8$)). Accordingly, an alternative way is followed to compare the shear strength of the samples: we compared the peak friction angle (Φ_p), which is obtained through dividing the maximum value of τ by σ_n. The results for all the shapes are summarized in Figure 4.28. Considering the dense packings, MS(8) is in good agreement with SQ($N6$) and SQ($N8$), whereas SQ($N4$) reaches a similar peak as for MS(27) and MS(64). Additionally, in the loose samples, both MS(64) and MS(27) have Φ_p values close to SQ($N6$) and SQ($N8$). Consequently, it can be said that influence of blockiness is increased in dense sample (the Φ_p value for MS(8) is reached by SQ($N6$) and

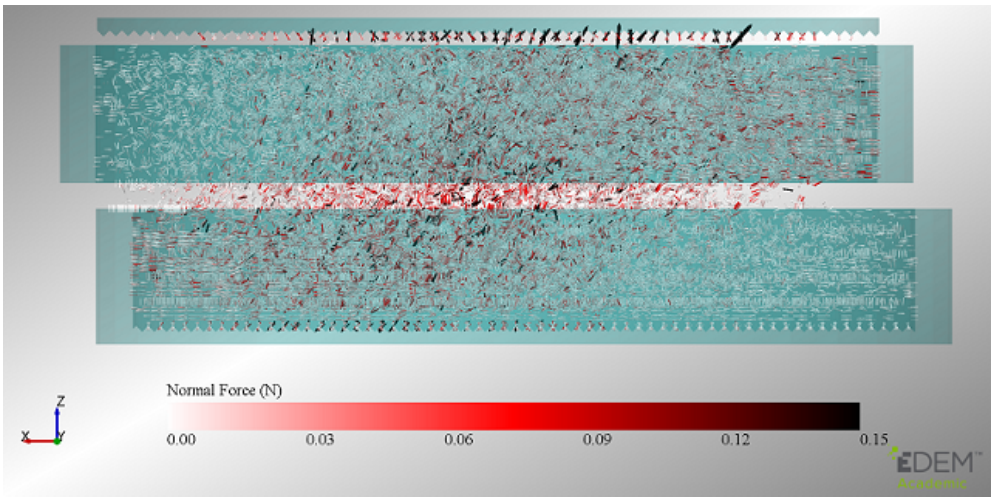

(a)

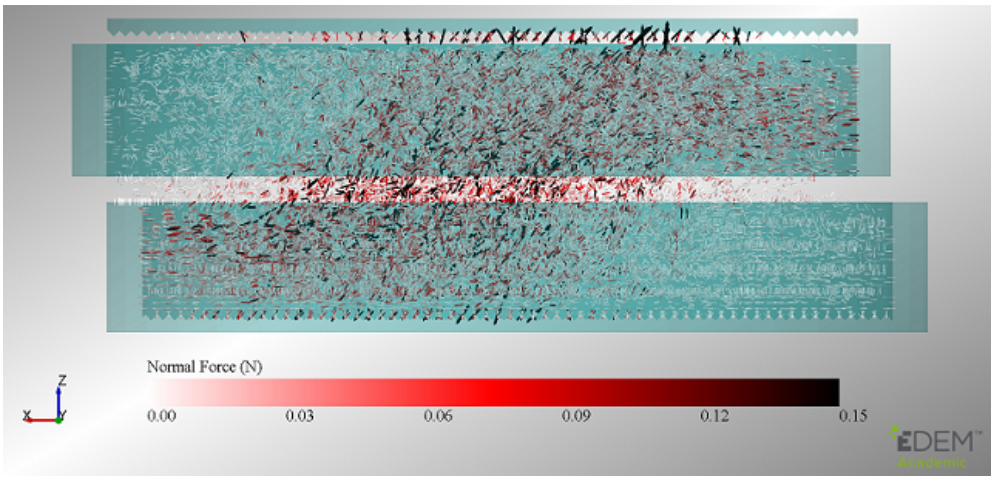

(b)

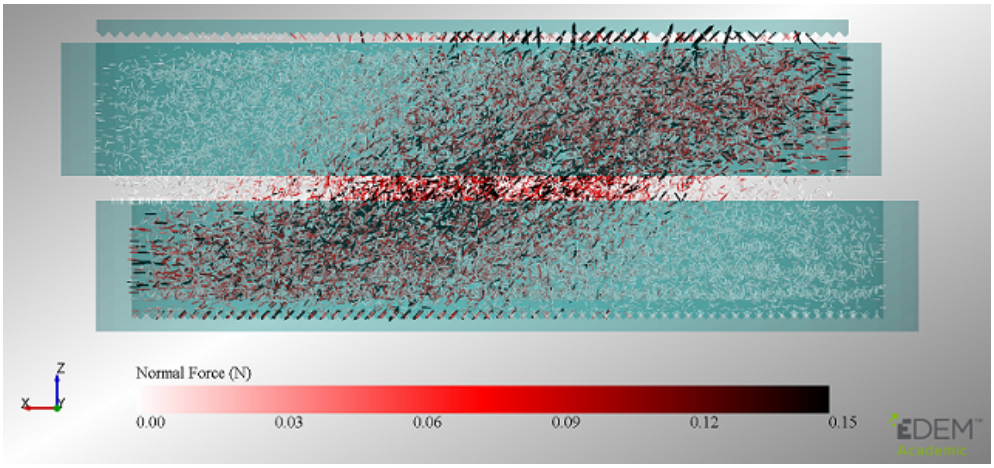

(c)

Figure 4.25 Distribution of normal contact force network a) MS(64) b) MS(27) c) MS(8) MS (note that results are for MS particles, and for displacement of $D = 6$ mm).

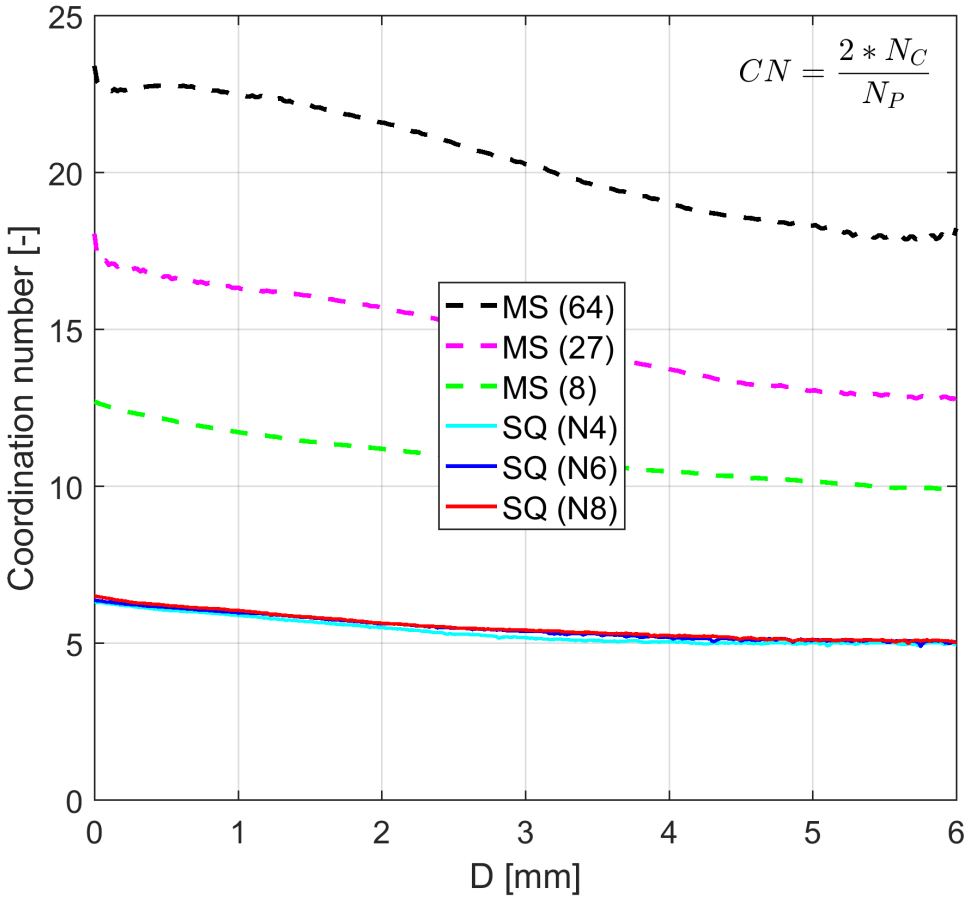

Figure 4.26 Coordination number change during shearing in the Jenike cell.

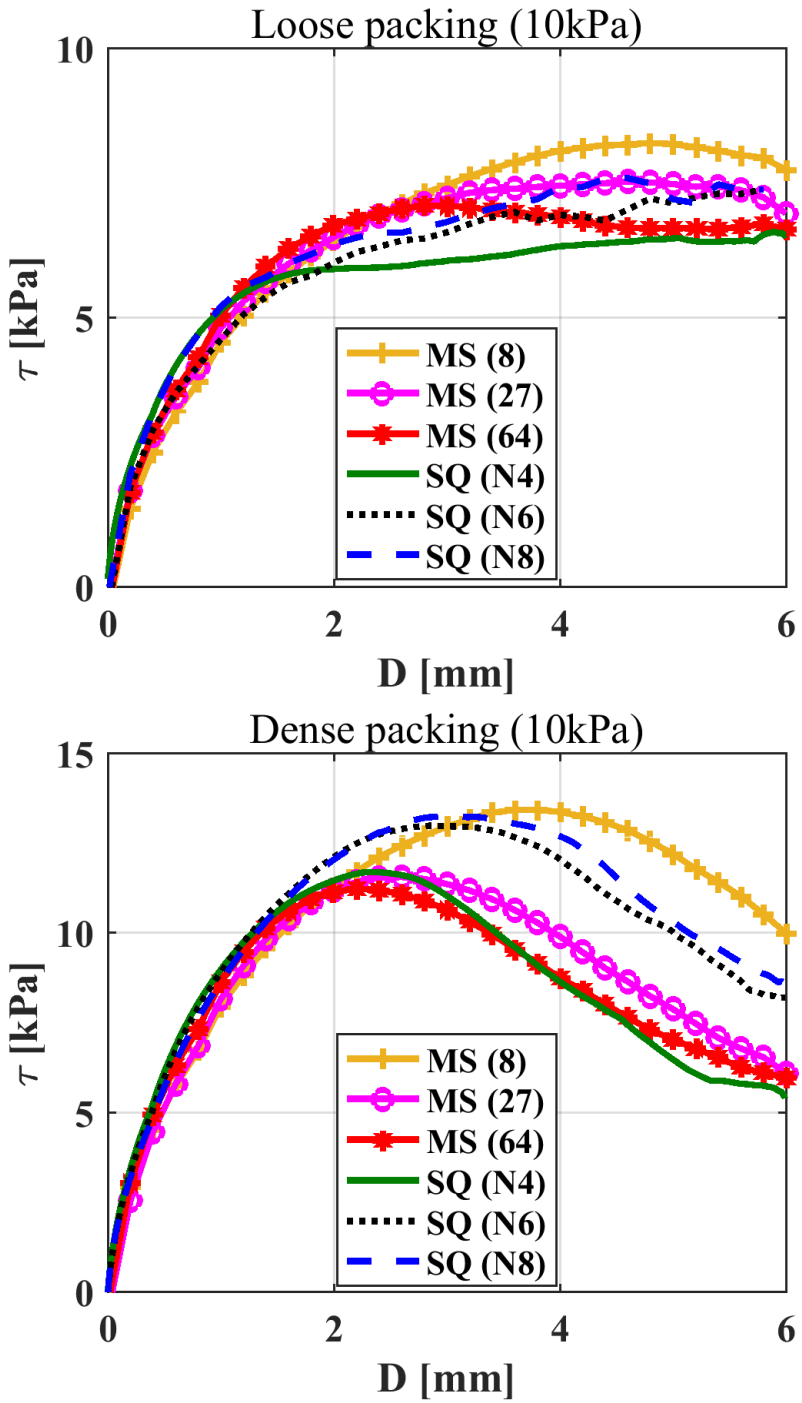

Figure 4.27 Jenike direct shear simulations considering SQ and MS particles a)loose packings b) dense packings.

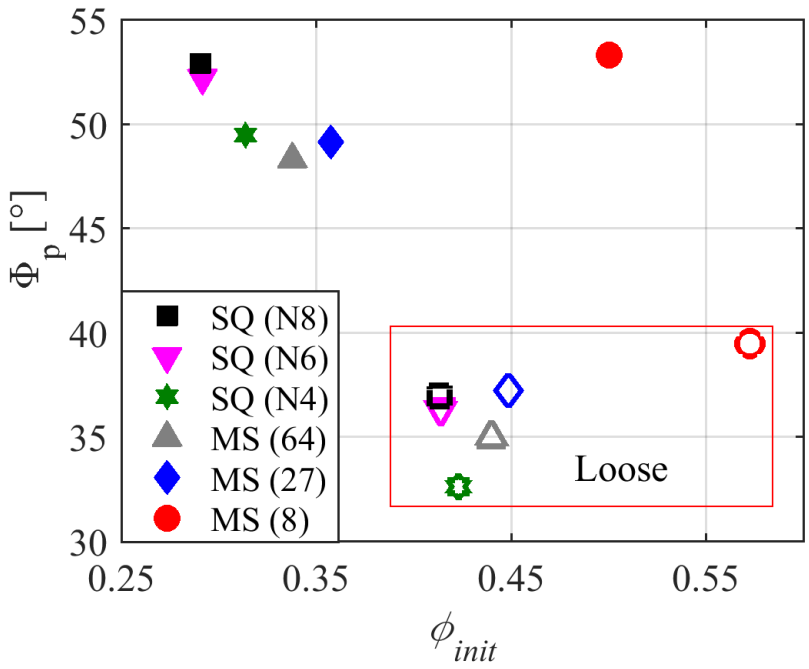

Figure 4.28 Dependence of the peak friction angle (Φ_p) on both particle shape and the initial porosity of the system (the filled markers are for dense packing).

SQ($N8$), however Φ_p for SQ($N6$) and SQ($N8$) only equals MS(27) and MS(64) in loose samples).

A close look into residual strength of the samples in both density states shows that SQ($N4$) and MS(64) present a similar response. On the other hand, it is an established fact that the quasi-static silo discharge can be considered as a dense flow regime (similar to that of Jenike test). Considering this, it is of high interest to investigate the possibility of predicting flow characteristics of the two particles through the shear tests. This will be discussed in detail in section 4.4.3.

Figure 4.29 presents the local distribution of the horizontal stress for the MS and SQ particles (results are only shown for the dense samples, in which a greater shear strength is developed). The pattern for the horizontal stress is similar to the distribution of local porosity and contact network shown in Figure 4.20 and 4.25. Despite the similar residual strength for SQ($N4$) and MS(64), the stress distribution pattern seems to be slightly different for these particles. In general, the increase in shear strength of the material due to change in particle shape can be seen clearly.

The detailed study of the bulk response in the current section and also in Section 4.4.2 reveals the idea that:

Whilst the effect of bumpiness and blockiness may show up more strongly in single particle verification and free flow conditions (e.g. avalanching), in many dense flow situations such as here, the exact shape representation is not so important for all

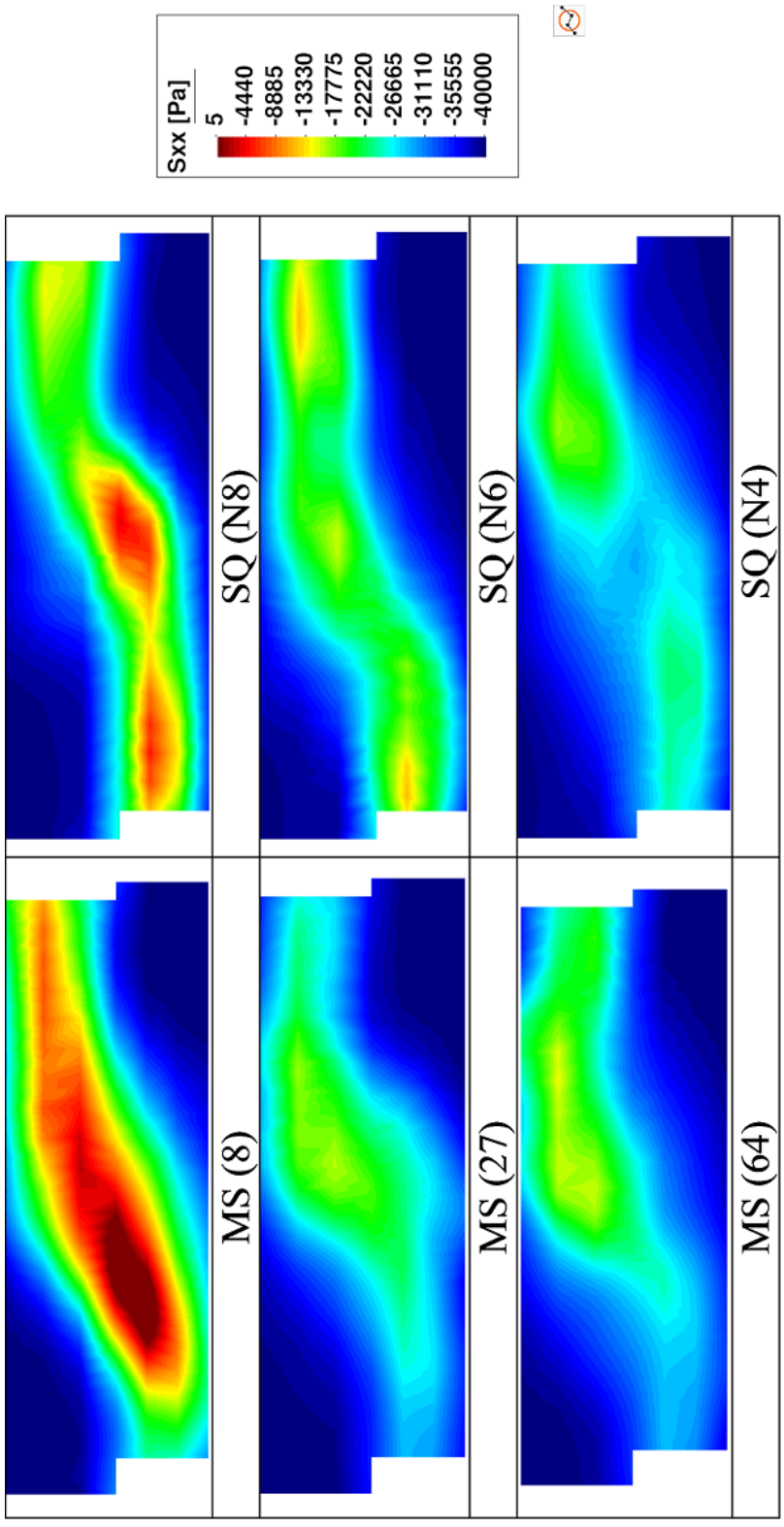

Figure 4.29 Horizontal stress distribution for MS and SQ particles at $D = 6$ mm.

Table 4.4 Number and total mass of particles in silo flow simulation before discharge.

Particle	Number of particles	Total mass, kg
SQ($N4$)	19637	0.5217
SQ($N6$)	17607	0.5205
SQ($N8$)	16652	0.5134
MS(8)	20499	0.5391
MS(27)	18864	0.4965
MS(64)	18475	0.5052

packings (to produce the right shearing response). In other words, once a certain degree of the surface and edge complexities is addressed, further adjustment may not be necessary for predicting the behaviour of dense flow regimes (i.e. once a cube is made out of 3 sub-spheres per edge, increasing the number of sub-spheres to 4 or 5 will not greatly influence the overall behaviour; similarly, for SQ blocks, once an edge sharpness of N=6 is considered, further increase of blockiness is not essential to predict the behaviour of a perfect cube). Additionally, it should be noted that packing density plays a major role in determining the importance of the shape factor (the denser the packing, the more influential is the shape factor on shear strength and porosity of the granular assembly).

4.4.3 Silo flow

This section addresses two objectives: a) evaluating the dependency of quasi-static flow on edge and surface properties of the MS and SQ particles b) assessing the validity of the numerical calibration methodology (through comparing the flow characteristics of particles with similar shearing response in the Jenike test). In this respect, the discharge process of the particles has been monitored inside a flat-bottom silo, which has dimensions $50d \times 5d \times 100d$ in x, y, z directions correspondingly. Periodic boundary conditions are applied in the y direction. The orifice dimension is $10d \times 5d$.

A total of about 21 000 particles were generated in each software to model the filling and discharge of the flat-bottom silo. Particles above the height of 0.2 m in the silo were removed from simulations before discharge in order to have equal bulk volumes, see Table 4.4 for the detailed number of particles. Please note that to address the difference in the volume of the single MS particles, the density of the MS(8) particles has been changed from 4100 to 6279 kg/m^3, to provide a match of the mass of MS(8) particle to the mass of MS(27) particle.

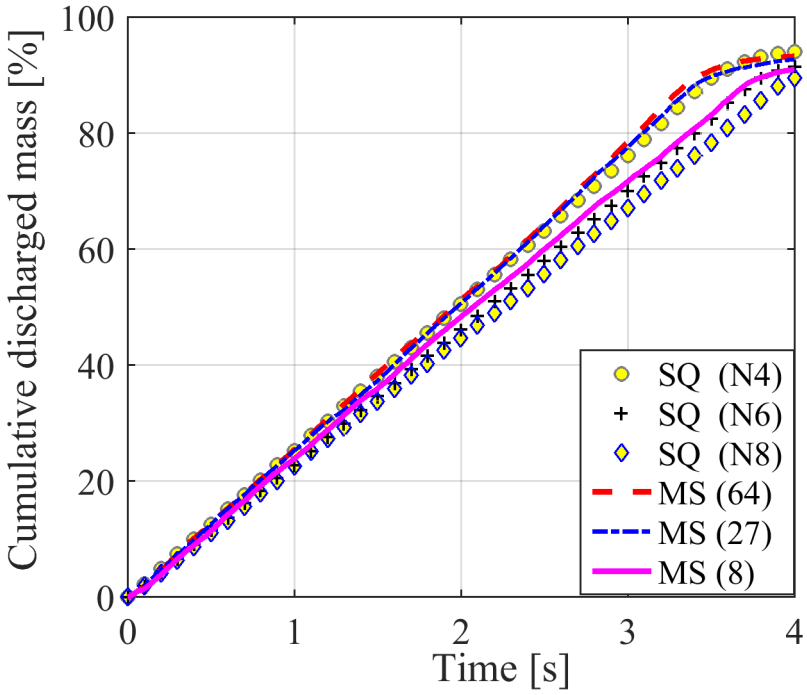

Figure 4.30 Cumulative discharged mass over time.

Discharge process

The discharge rate of the MS and SQ particles are shown in Figure 4.30, shows the effect of blockiness and bumpiness on the discharging process. It is evident that for the SQ particles, the increasing blockiness retards the flow resulting in a decreasing flow-rate For the MS particles, increasing the surface bumpiness also results in a decreasing flow-rate However the effect of bumpiness on flow-rate appears to be much smaller with MS (27) and MS (64) converging to a similar flow-rate. Moreover, the drop in discharge rate, by increasing pseudo-bumpiness, is smaller than the effect of increased blockiness for SQ particles (blockiness is not well captured by bumpiness). Moreover, MS(64) and SQ$(N4)$ (with similar residual shearing response) present an overlapping discharge rates (i.e. the slope of cumulative discharged mass in Figure 4.30). The above results are in line with the Beverloo's equation Beverloo et al. (1961), which predicts the mass flow rate (W) according to the following equation:

$$W = C\rho_b\sqrt{g}(D_o - kd)^{5/2}, \tag{4.18}$$

where, C is constant that depends on the coefficient of friction, ρ_b is the bulk density after filling, g is the gravitational acceleration, D_0 is the opening width, d is the particle diameter, k is generally known to be a constant that depends on particle shape. In this case, kd increases by further bumpiness and blockiness (which results in reduc-

tion of the effective orifice dimension). Another important point is that compared to the significant dependency of the shearing resistance ($\approx 30\%$) on the shape characteristics, discharge rate is affected less ($\approx 10\%$).

Simulation snap-shots have been taken at different instances of the discharged mass (M_D) to provide an insight into flow profiles for both particle types. Figure 4.31 shows the particles inside the silo at 10, 30 and 60 % of the discharge. It can be seen that the flow profiles are a function of the geometry of the particles. Increasing blockiness and bumpiness leads to development of the flow channels to higher elevation (M_D=10 %). Moreover, it is clear that the transition height, of which there is mass flow above this height, is increased (it is important to determine this point, since the maximum horizontal stress distribution is developed in this region). Additionally, it is observable that changing blockiness from 4 to 8 has a small effect on the formation of the dead/not-flowing zones, see M_D=60 %. Unlike for SQ particles, increasing bumpiness leads to formation of larger dead-zones in adjacent of the silo walls (see results at M_D=60%). Additionally, comparing flow pattern for particles with similar shear strength (i.e. SQ($N4$) and MS(64), which were predicted in the direct shear simulations earlier) depicts the similarity of flow kinematics for both particle types. Accordingly, results of this section suggests that for the silo flow situation, which involves large displacement regimes (where residual strength dominates), representation of particle shape using MS or SQ particles can produce matching predictions as long as the relevant residual strength characteristics is captured.

In addition to the above remarks, results indicates that whilst significant differences in single particle behaviour have been shown between the two shape descriptors, they do not lead to significant discrepancy in silo flow kinematics.

Stress distribution

The horizontal (σ_{xx}) and vertical (σ_{zz}) stress distributions inside the silo are obtained through coarse graining as shown in Figure 4.32 (at M_D=30 %). Furthermore, it is an established fact that the continuum fields can be averaged over directions in which the flow is homogeneous. In this respect, since applied periodic boundary in depth of silo provides a homogeneous flow, the results are averaged over y direction. A close look at σ_{zz} distributions for MS and SQ particles reveals that the vertical stress is independent of the particle shape characteristics (this is demonstrated by plotting variation of σ_{zz} over two heights of silo, see Figure 4.33). Additionally, the highest magnitude of the σ_{zz} is developed adjacent to the walls in the stagnant zones (two column of high stress at both sides of the flow channel). This is due to presence of the strong arches in the mass flow region that exerts the overburden pressure to the particles near the side-walls (it is clear that the flow channel cannot carry significant vertical

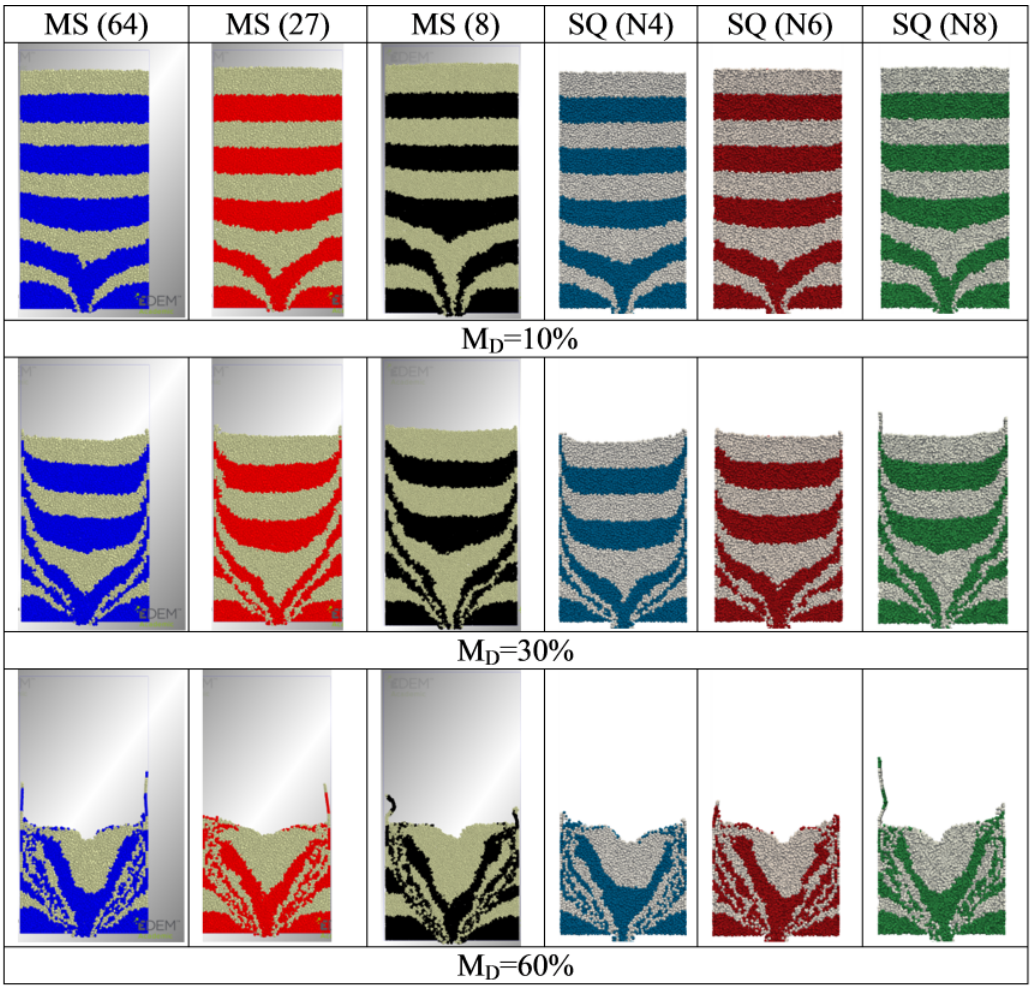

Figure 4.31 Flow profiles for both SQ and MS particles at M_D =10, 30 and 60 %.

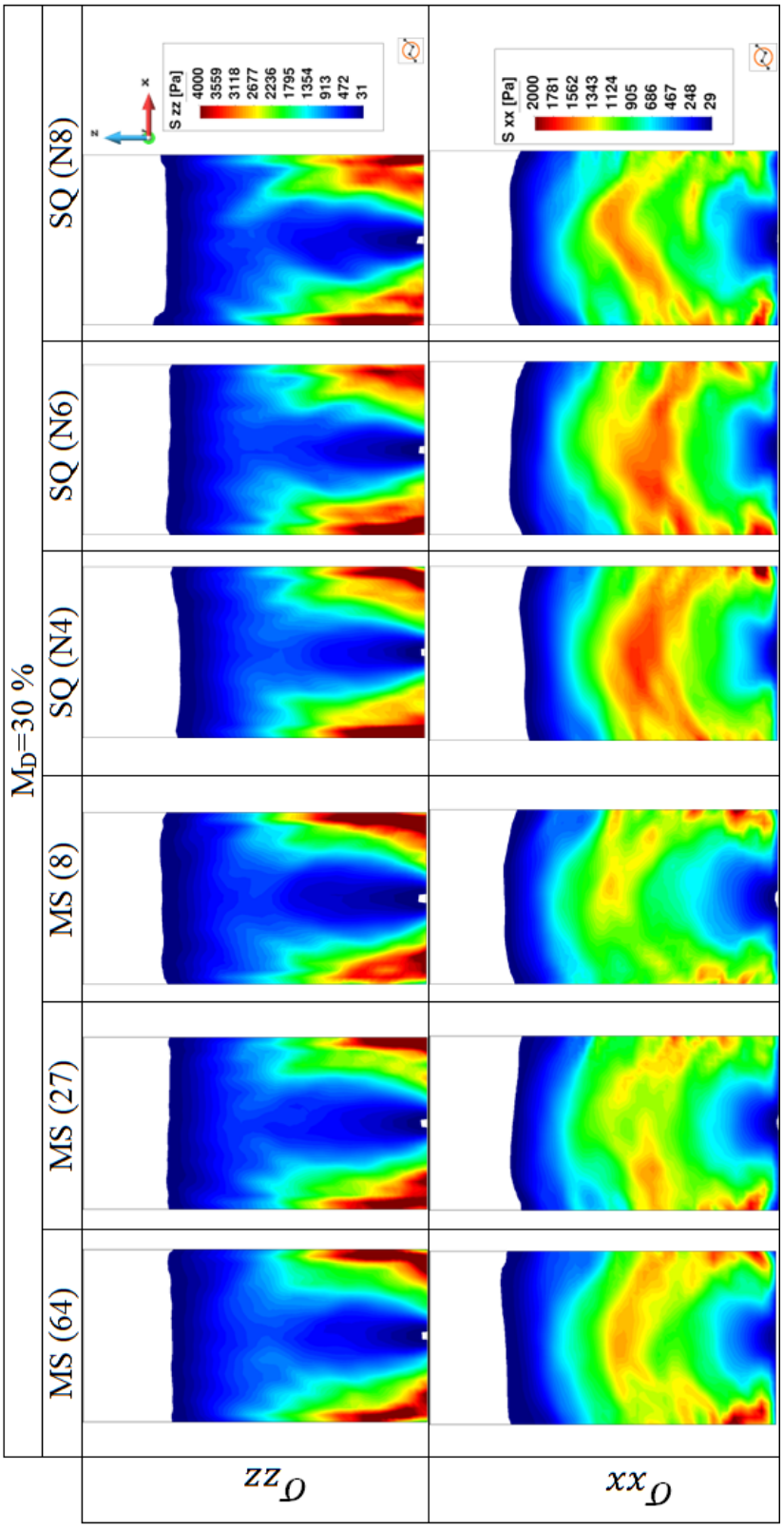

Figure 4.32 Stress distribution inside the silo at M_D =30 %.

.

loads). Furthermore, the σ_{xx} distribution is showing a reduction with the increase in N parameter and decrease of number of sub-spheres. For MS(64) and SQ$(N4)$ particles, even though a similar flow pattern and discharge rate is captured, the distribution of σ_{xx} differs.

4.5 Summary

Multi-spheres and Superquadrics are popular approaches for addressing particle shape effect in DEM. This chapter focused on the mechanical characteristics of cubical particles, modelled by the two methods, through conducting simulations at both single particle and bulk levels. The results of these tests are assessed both at the micro, directly through DEM outputs, and at the meso- and macro- scales, using a coarse graining technique. Accordingly, a better understanding of the micro/macro properties of the MS and SQ particles has been obtained and the potential similarities of the two methods are distinguished.

A series of grain level tests has been carried out and the results emphasize the importance of surface bumpiness and edge sharpness in the single-particle behaviour and are used for informing the bulk response. Additionally, heap formation characteristic of the particles has also been assessed in an angle of repose test. It is seen that the surface inclination of the formed piles increased monotonically with the increase in blockiness. A similar influence is seen by increasing the bumpiness in MS particles. Furthermore, shearing tests in a Jenike shear tester with MS and SQ particles are conducted to determine the role of blockiness in SQ and number of sub-spheres (surface bumpiness) in MS particles. Results suggest that the shape complexity only significantly affects the shear strength, porosity and mode of motion when the packing is dense. Subsequently, the influences of particle edge sharpness and surface roughness on flow characteristics of a granular assembly are investigated. It is observed that the effect of shape features is even less on the flow pattern and mass flow rate but is found to have a significant influence on the stress distribution.

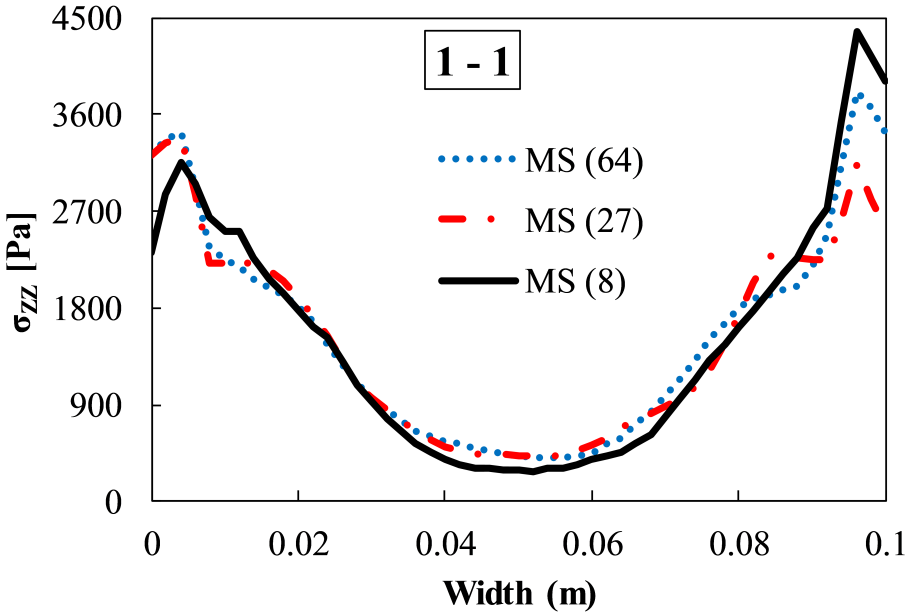

(a)

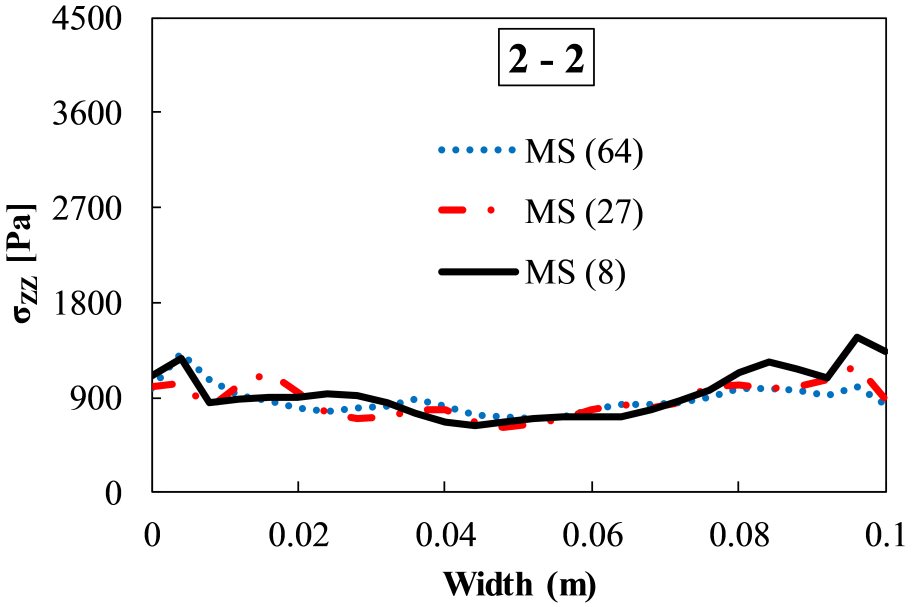

(b)

Figure 4.33 Vertical stress distribution along the width of silo (for MS type particles) a) cross-section 1-1 (H=0.05 m, near the outlet) b) cross-section 2-2 (H=0.1 m, mid-height of silo).

Chapter 5

Applicability of rolling resistance models in addressing the shape complexity of multi-spherical and superquadric approaches[1]

The aim of including either complex particle shapes (i.e. by means of superquadrics or multi-spheres) or having spheres (together with rolling resistance models) in DEM simulations, is to predict realistic behaviour of granular assemblies. Where, the only advantage of the latter approach is to have a faster algorithm for contact detection and force calculation. The influence of both approaches, in the contact level and bulk response, has been discussed in detail throughout Chapters 4 and 3. However, yet it is needed to examine the capabilities of artificial shape representation method (i.e. rolling resistance) in mimicking the characteristics of complex shape particles. Accordingly, this chapter will compare the bulk response from three different rolling resistance models with two types of non-spherical particles (cylinders and cubes). Moreover, influence of aspect ratio, as an additional shape complexity factor, on macro-scale response of the samples will be assessed. The investigations will be addressed through con-

[1]Results of this chapter are included in a paper draft:

Podlozhnyuk, A., Soltanbeigi, B., Papanicolopulos, S.A., Kloss, C., Pirker, S. and Ooi, J.Y., "Characteristics of different particle shape descriptors in predicting avalanching, packing and shearing response of granular material", *To be submitted for Granular Matter*.

Conference proceeding (Section 5.4):

Soltanbeigi, B., Papanicolopulos, S.A. and Ooi, J.Y., "Particle shape effect on deformation localization during quasi-static flow at active state" 5th Int. conf. on Geotechnical Engineering and soil mechanics, Tehran, Iran, November 2016.

Presented in:

Soltanbeigi, B., Podlozhnyuk, A., Papanicolopulos, S.A., Kloss, C. and Ooi, J.Y., "Influence of blockiness and bumpiness on modelling dense granular flows of non-spherical particles", *Particles conference*, Hannover, Germany, September 2017.

ducting angle of repose and Jenike shear test. This way, by knowing the limitations and capabilities of different rolling resistance models, it will be possible to inform the future studies about choosing the most appropriate methodology to address the shape effect.

5.1 Introduction

Traditionally, due to simplicity and computational costs, spheres are used for describing particle shape in DEM. However, it is known that in reality particles are mostly of irregular shapes, which increase the degree of inter-particle interlocking among the particles. Meanwhile, it is known that controlling the rotational freedom can overcome the inherent deficiency of the spheres in providing geometric interlocking (i.e. utilization of rolling resistance models). In the literature, there are several studies that made an effort to evaluate the resemblance of bulk response in spherical particles (in presence of rolling resistance) to that of complex shape particles. A comprehensive literature survey is conducted and presented in Chapter 2. Following is a summary of the most relevant works that have been done by other researchers:

Estrada et al. (2011) compared the response of discs, accompanied by rolling resistance at contacts, with regular polygonal particles (in 2D). The tests were conducted in simple shear condition and various aspects of the bulk response have been assessed. They observed that the rolling friction coefficient can be successfully related to the number of sides in polygonal particles. It is also reported that there exists a good agreement between two types of particle packings in terms of shear strength, solid fraction, force and fabric anisotropies, and probability distribution of contact forces.

Wensrich and Katterfeld (2012) proposed an idea of relating coefficient of rolling friction to a normalized average eccentricity of contact. They evaluated the proposed solution through conducting angle of repose tests and compared the results of spheres, subjected to rolling resistance, with simple clumped particles. It was seen that similar angle of repose with non-spherical particles can be reached for spheres with considering approximately half of the estimated rolling friction. They suggested that the source of discrepancy can be justified by considering the fact that the artificial rolling resistance, applied through proposed methodology, is always acting in the reverse direction of rotation, while real interlocking among particles sometimes can lead to acceleration of the rotation.

Zhou et al. (2013) employed the rolling resistance model, proposed by Iwashita and Oda (1998), for disks and compared the results with the response of irregularly shaped particles (triangle and square clumps). They reported that the two approaches present different localisation modes of particle rotation and shear strain at the peak state. The

sample with disks shows a clear localization band, while the sample with clump particles exhibits a more uniform localization pattern. Moreover, it is stated that, although the consideration of rolling resistance for disks affects the macroscopic strength and dilatancy of the samples, it is not able to reproduce the rotational behaviour as exhibited by irregularly shaped particles.

5.2 Methodology

This section provides information regarding the material properties and the testing procedures that have been followed. The particles consist of spheres (with 10 % of polydispersity and mean radius of 1 mm), cubes and cylinders (both shapes are simulated with various complexities, at aspect ratios (AR) between 1 to 3).

Cubes/cuboids and cylinders are approximated by SQ particles in LIGGGHTS (Kloss et al., 2012; Podlozhnyuk et al., 2017) and using MS particles in EDEM (DEM Solutions Ltd., 2014). Regarding the use of two distinct DEM codes, it should be noted that the contact detection algorithm and force calculation methodology are different for multi-sphere and superquadric particles. Furthermore, for modelling spherical particles, both codes are used to consider various rolling resistance models, see 5.2.3. The considered rolling resistance models are already implemented in the employed codes and are widely used in the literature.

The consistency of the contact models in both codes is evaluated for the spherical particles. In this respect, results of the Jenike test is compared (at bulk-scale) for a set of identical packing and results are summarized in Section 5.3.2.

The material parameters are chosen in a way that the computational cost is reasonable for non-spherical particles. Table 4.1 shows the material properties for all types of particles and the considered geometry.

5.2.1 Superquadrics

The equation that governs the shape of a SQ particle (shape function) in its local coordinate system, given by Barr (1981), is as follows:

$$f(x,y,z) \equiv \left(\left|\frac{x}{a}\right|^{n_2} + \left|\frac{y}{b}\right|^{n_2}\right)^{\frac{n_1}{n_2}} + \left|\frac{z}{c}\right|^{n_1} - 1 = 0, \tag{5.1}$$

where a, b, c are the half-lengths of the particles along its principal axes, and n_1 and n_2 are blockiness parameters that control edge sharpness. For instance, cubical ($a = b = c = d/2$) and prolate cuboidal ($a = b = d/2, c = AR \cdot a$) particles can be modelled by superquadrics and taking $n_1 = n_2 = N > 2$, prolate cylindrical particles ($a = b = d/2, c = AR \cdot a$) can be modelled by taking $n_1 = N > 2, n_2 = 2$, where N controls the

level of edge sharpness (AR is the aspect ratio and d is particle edge length at d =2). Different levels of edge sharpness (between $N = 4$ and $N = 10$, further denoted as SQ(N4),...,SQ(N10)) are used in this paper to study the blockiness effect. Figure 5.1 illustrates SQ cubic particles with $AR = 1$ (top row), and cylinders with $AR = 1.5$ (second row). Note that for both particle shapes the edge sharpness is increased from left to right.

5.2.2 Multi-sphere approach

Cubes, as multi-spheres, were modelled in EDEM software using equal-radius ($d/4$) overlapping sub-spheres. The number of sub-spheres in each edge of the cubes varies between 2 and 4, resulting in 8, 27 and 64 total sub-spheres per particle (further denoted as MS(8), MS(27) and MS(64) correspondingly). Graphical illustrations for MS(8), MS(27), MS(64) are given in Figure 5.1 (these are similar to that of presented at Section). We have also considered an extension in number of sub-spheres around a single axis to investigate the effect of another shape complexity parameter, which is referred as aspect ratio (AR). Due to excessive increase in number of sub-spheres, the extension of MS(64) is not considered (remains with $AR = 1$). Whereas, for the angle of repose test, AR is increased up to 3 (for both MS(8) and MS(27) particles). Moreover, for the Jenike test, the particle extension is considered up to $AR = 2$ (this is due to requirement of high computational time).

Furthermore, the representation of the cylindrical particles is addressed through considering overlapping spheres, which are aligned around a single axis. The particles consist of 2, 3, 4 and 30 sub-spheres, which leads to variation of the bumpiness. For MS(2), MS(3) and MS(4), the bumpiness is changed in circumference of the particles, while for MS(30) an edge (top and bottom) bumpiness is also added, see Figure 5.1.

5.2.3 Rolling friction models

It is known that spherical particles underestimate the interlocking, thus fail to capture formation of stable angles of repose Ai et al. (2011). Consequently, additional rolling friction models are often used by researchers for representing the effects of particle shape. The coefficient of rolling friction μ_r can be considered as a second DEM shape parameter, in addition to particle radius R, when a bulk solid is represented by perfect spheres. Accordingly, μ_r is defined as dimensionless parameter that is proportional to the torque that counterbalances the rotation of the particle produced by gravity on a slope:

$$\mu_r = \tan(\beta), \tag{5.2}$$

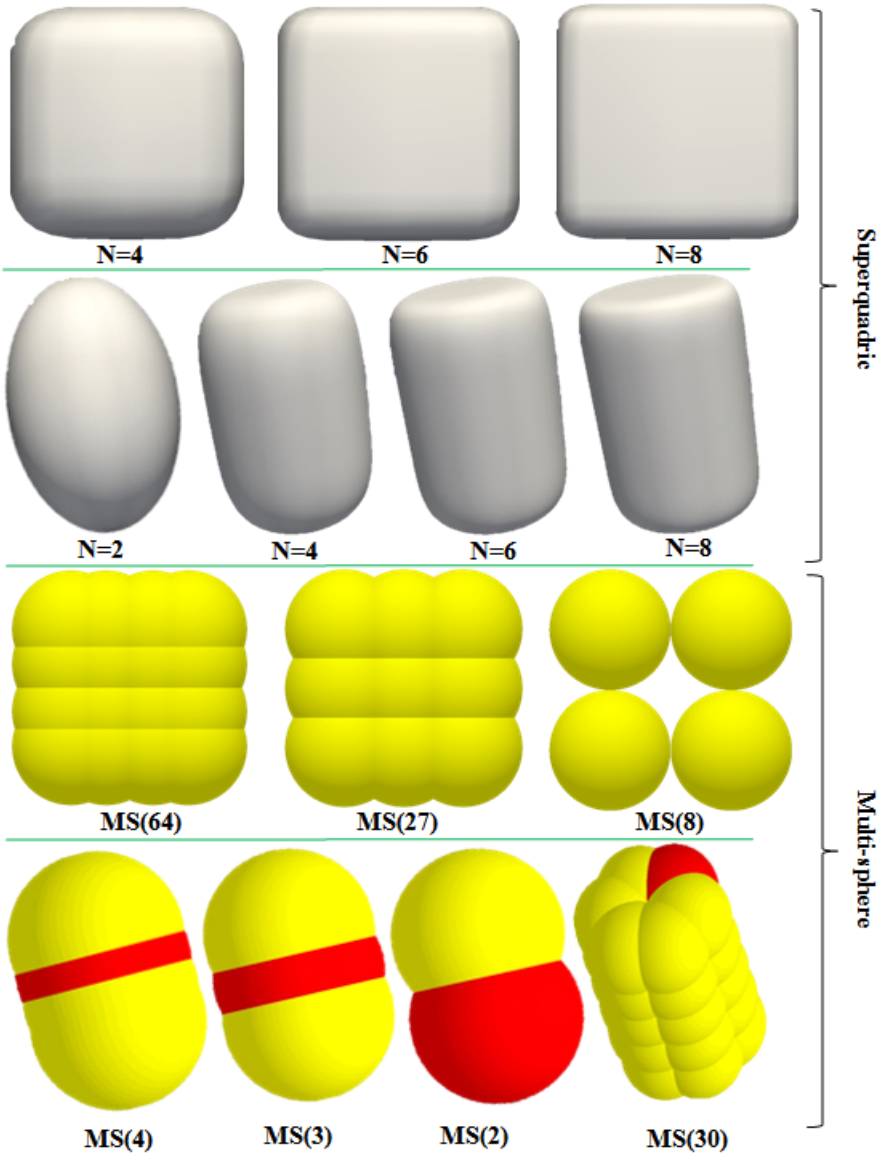

Figure 5.1 Particle shapes used throughout the tests; top/first row: SQ cubes with $AR = 1$, second row: SQ cylinders with $AR = 1.5$ (for both particle shapes from left to right the blockiness increases), third row: MS cubes with $AR = 1$, fourth/bottom row: MS cylinders with $AR = 1.5$ (for both MS type particles, from left to right the surface bumpiness increases).

where, β is the minimum angle of a slope at which the rolling occurs. DEM parameters, including sliding (μ_s) and rolling (μ_r) coefficients of friction, are commonly determined by so called characterization or calibration technique. The macroscopic outcome of large-scale DEM simulations, for example, the static angle of repose of a heap or the "shear stress vs. displacement" curve in the Jenike shear tester, is compared with that for bulk experiments. If DEM simulation results disagree with bulk measurements, the set of contact law parameters must be adjusted until reasonable agreement is achieved.

Here, three different rolling resistance models are considered together with spherical particles. The characteristics of the two models are already discussed in Chapter 3 (Section 3.2). Below is a brief summary of the employed models:

First model is referred as type Model A and applies a torque constantly to each contact to represent rolling resistance (A detailed explanations regarding the model and it characteristics are summarized in Chapter 3).

The second model, as already discussed in Section 2.2.4, is referred as contact-independent in Ai et al. (2011) (called as Model *B* in here and Chapter 3). The fundamental idea behind this models is also to generate a torque ($\boldsymbol{T}$) which opposes the rotation of the particles in contact (this model only considers direction of the rotational velocity for a single particle), see Section 3.2 for more details.

Third considered model is the elastic-plastic spring-dashpot model (EPSD), which was originally proposed by Iwashita and Oda (1998), or type *C* according to Ai et al. (2011) (called as Model *C* from now on). Here, the applied torque consists of two components: a mechanical spring torque $\boldsymbol{T}_r^k$ and a viscous damping torque $\boldsymbol{T}_r^d$:

$$\boldsymbol{T}_r = \boldsymbol{T}_r^k + \boldsymbol{T}_r^d. \tag{5.3}$$

The spring term at time $t+\Delta t$ is computed in an incremental manner:

$$\boldsymbol{T}_{r,t+\Delta t}^k = \boldsymbol{T}_{r,t}^k + \Delta \boldsymbol{T}_r^k, \tag{5.4}$$

where $\Delta \boldsymbol{T}_r^k = -k_r \boldsymbol{\theta}_r$, $\boldsymbol{\theta}_r$ is the incremental relative rotation between two particles and k_r is the rolling stiffness. The magnitude of spring term is bounded by the torque $T_r^m = \mu_r R_r F_n$ which is achieved at a full mobilisation rolling angle $\theta_r^m = T_r^m / k_r$:

$$||\boldsymbol{T}_{r,t+\Delta t}^k|| \leq T_r^m. \tag{5.5}$$

The viscous damping torque T_r^d is assumed to be dependent on the relative rolling angular velocity $\dot{\boldsymbol{\theta}}_r$ between the two particles in contact and the damping constant C_r:

$$\boldsymbol{T}_{r,t+\Delta t}^{d} = \begin{cases} -C_r \dot{\boldsymbol{\theta}}_r \text{ if } ||\boldsymbol{T}_{r,t+\Delta t}^{k}|| < T_r^m \\ -fC_r \dot{\boldsymbol{\theta}}_r \text{ if } ||\boldsymbol{T}_{r,t+\Delta t}^{k}|| = T_r^m. \end{cases} \tag{5.6}$$

Here, $C_r = \eta_r C_r^{crit}$ is the viscous damping coefficient, η_r is the rolling viscous damping ratio and $C_r^{crit} = 2\sqrt{I_r k_r}$ is the rolling critical viscous damping constant. I_r is the equivalent moment of inertia about the contact point between the two contacting spheres which is obtained from the moment of inertia I_i, I_j and masses m_i, m_j of the particles i and j, respectively using Huygens-Steiner theorem:

$$I_r = \left(\frac{1}{I_i + m_j r_i^2} + \frac{1}{I_i + m_j r_j^2} \right)^{-1} \tag{5.7}$$

In LIGGGHTS (Kloss et al., 2012), a modified version (EPSD2) of the elastic-plastic spring-dashpot model is implemented (originally proposed by Iwashita and Oda (1998)). In this modification, the viscous damping term is switched off and the rolling stiffness k_r is calculated as:

$$k_r = k_t R^{*2}, \tag{5.8}$$

It is emphasized by Iwashita and Oda (1998) that there is no rational reason to choose a specific value of the rolling stiffness k_r because no experimental data is available.

5.3 Simulation results

5.3.1 Angle of repose

In this test an assembly of 6000 particles is distributed randomly in a cone. The system is allowed to settle under gravity (in Z-direction) for 1s simulation time. Figure 4.12 shows the simulation set-up and the dimensions used.

Then, after the packing is formed, the orifice is opened, and the discharge is commenced. The simulation continues until a heap is formed. The heap is then analysed, and the angle of repose is estimated.

For the assemblies with Model *A* rolling resistance model, special care must be taken for the simulation period after the formation of the stable heap. According to Ai et al. (2011), particles with Model *A* are susceptible to oscillation in static packings (i.e. the model applies a torque at each time-step even when particle has no rotation). Applying the artificial torque to the single particles, which are at rest, increases the kinetic energy of the system and can lead to instabilities, see Section 3.4. Additionally,

it is already mentioned that similar to Model *A*, Model *B* is also susceptible to oscillations (i.e. by ignoring the state of particle being in motion or static conditions). It is worth mentioning that based on our observations, this deficiency is more problematic for higher values of μ_r. Consequently, the AoR is measured at several instances (after the initial heap is formed) and results suggest that for $\mu_r \leq 0.2$ the difference in AoR is less than 2 degrees (when simulation time increases from 1 to 5 seconds), whereas for larger values of μ_r it is hard to establish the instance when a stable heap is formed. Thus, in order to have analogy between the measured data, all the simulations are stopped at exactly 5 seconds from the opening of the orifice.

The algorithm, which determines the angle of repose for the heaps is already discussed in Section 4.4.1. The angle of repose is found as the inclination angle of $z = z(r)$ using linear regression, see Figure 5.2. The first and the last bins are excluded to avoid the influence of the rounded top and flattened foot of the heap.

It can be seen from Figure 5.2 that the rolling friction models affect the heap formation characteristics of the spherical particles differently. For $\mu_r \leq 0.1$ comparable results can be obtained for the three models. Meanwhile, the difference between AoR for Model *A* and Model *C* is relatively small (specially for $\mu_r \leq 0.2$, which is the most frequently used range of μ_r). Moreover, for $\mu_r > 0.1$, model computes heaps with almost 25 % steeper slopes than those of Model *A* and Model *C*. The very high AoR for the packings with Model B can be explained by the fact that this model applies the torque to every single particle always in the opposite direction of the rotation (ignoring relative rotational velocity of the contacting particles). Further details of the rolling model and its specification is already discussed in Section 3.2.

An other important objective of this study is to evaluate the capability of the rolling resistance models in providing the bulk response of the irregular shape particles. Accordingly, we have considered the simulation of non-spherical particles by means of multi-sphere and superquadric approaches for cubes/cuboids and cylindrical particle shapes. Results for cubic shape particles (with aspect ratio of 1) have already been presented in Chapter 4, in which the influence of surface bumpiness and corner sharpness on AoR results are reported. In this chapter, results for cubes are extended and particles with higher aspect ratios are also considered.

Figure 5.3 provides an understanding regarding the AoR for cube/cuboid shape particles. For $AR = 1$, increasing corner sharpness from 4 to 8, contributes to increase of AoR for almost 7 degrees. Furthermore, the increase of surface bumpiness (from MS(64) to MS(27)) has insignificant effect, whereas MS(8), with higher interlocking, provides a larger AoR value. Additionally, it is clear that varying aspect ratio between 1 to 3 has the consistent increasing influence on AoR for all particle types (note that results for MS(64) are only shown for $AR = 1$ due to requirement of high computational time). Results also suggest that, compared to sharp increase of SQ$(N4)$, SQ$(N6)$ and

MS(27), the AoR for particles with highest bumpiness and blockiness is less affected by the increase of *AR*. Another important observation in Figure 5.3 is that by increase of *AR* (specially for $AR > 2$) the difference for the measured AoR between different particles decreases (compared to values at $AR = 1$).

To further investigate the avalanching characteristics of the non-spherical particles, the AoR test has been also carried out considering cylindrical particles with different aspect ratios. First set of tests have been conducted considering SQ particles with different blockiness, see Figure 5.4. Results show that increasing *N* parameter from 4 to 6 contributes to formation of heaps with higher AoR values (at all aspect ratios). However, having cylindrical particles with further blockiness (i.e. $N = 8 - 10$) has no considerable effect on AoR values (this holds true for all ranges of *AR*). Second set of simulations have been done using MS particles with various number of sub-spheres. These tests are only conducted at $AR = 1.5$ with particles consisting of 2, 3, 4 and 30 sub-spheres, in which the former three types have only bumpiness at circumference, whereas MS(30) has bumpiness both on its edges (top and bottom) and circumference, see Figure 5.1. Results for MS particles suggest that increasing bumpiness at circumference has little influence on AoR (i.e. MS(4), MS(3) and MS(2)), accordingly bumpiness at the top and bottom edges is also required to achieve higher AoR angles (i.e. MS(30)). Having particles similar to MS(30) will definitely increase the computational costs (both due to increasing number of sub-spheres and the need for sub-spheres with smaller radius), whereas changing *N* has no effect on computational performance of SQ particles, see Chapter 4. Consequently, to represent cylinders, MS particles are not further considered with other aspect ratios.

Considering AoR results for cuboidal and cylindrical particles with various *AR* and comparing them with those of spherical particles (accompanied by three rolling resistance models), the following can be pointed out: a) Model *A* and Model *C* can provide a similar AoR to that of $AR = 1$ for cubes with $0.15 < \mu_r < 0.3$ and for cylinders with $0.1 < \mu_r < 0.2$ (see Figure 5.5), b) for $AR > 1$, to compensate a similar AoR (for both cuboid and cylinders), spherical particles need to have a maximum value of $\mu_r = \mu_s = 0.56$ (it is usually suggested that rolling resistance coefficient must be smaller/equal to sliding friction coefficient) c) for Model *B*, it can be seen that assigning $0.05 < \mu_r < 0.2$ can provide AoR values comparable to all range of *AR* (for both cubes and cylinders). Consequently, it is seen in this section that for the angle of repose test, incorporation of rolling resistance models can mimic the avalanching response of non-spherical particles to a great extent. Next section (5.3.2) evaluates the respond of granular systems in a Jenike shear cell and provides detailed information regarding the influence of different rolling resistance models on porosity, shear strength and volume change characteristics of spherical particles. Results from Section 5.3.2 are further compared with respond of MS and SQ particles with various shape complexities.

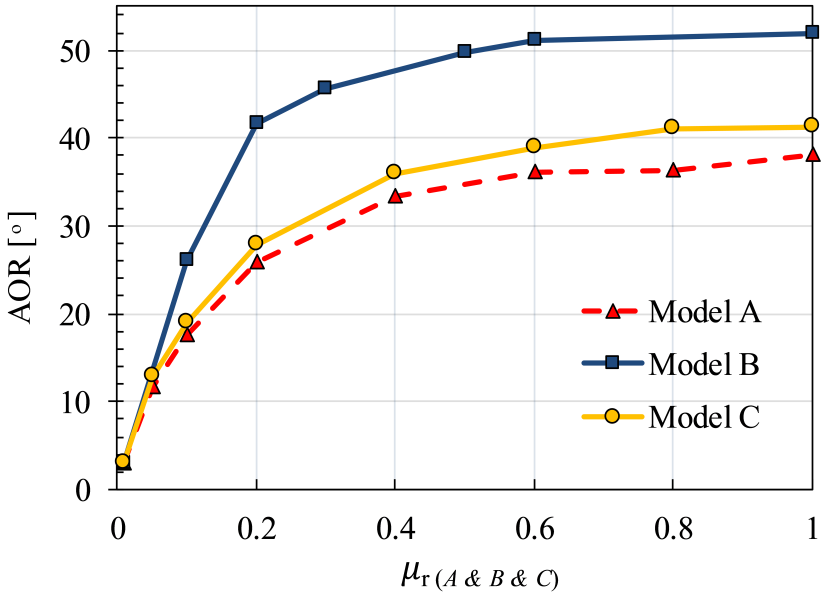

Figure 5.2 Average angle of repose for different μ_r values.

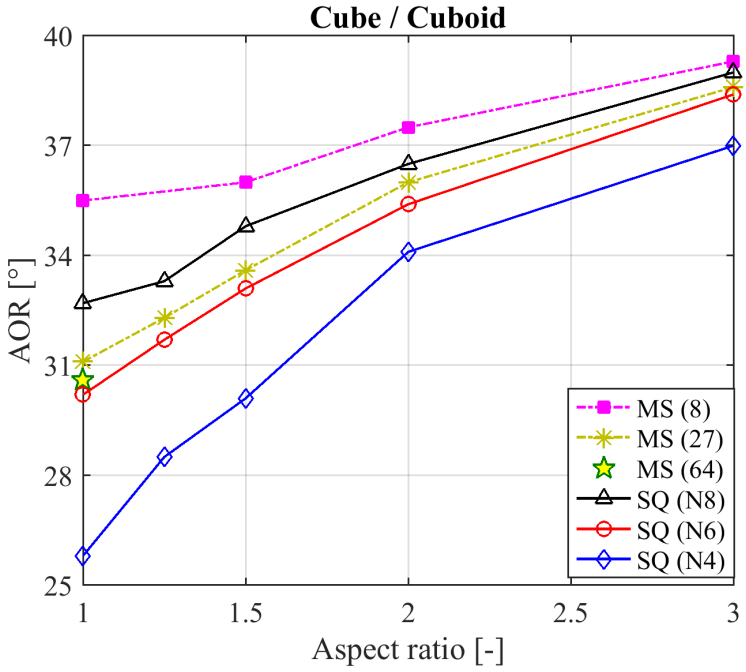

Figure 5.3 Average angle of repose for elongated MS and SQ cubes (cuboids).

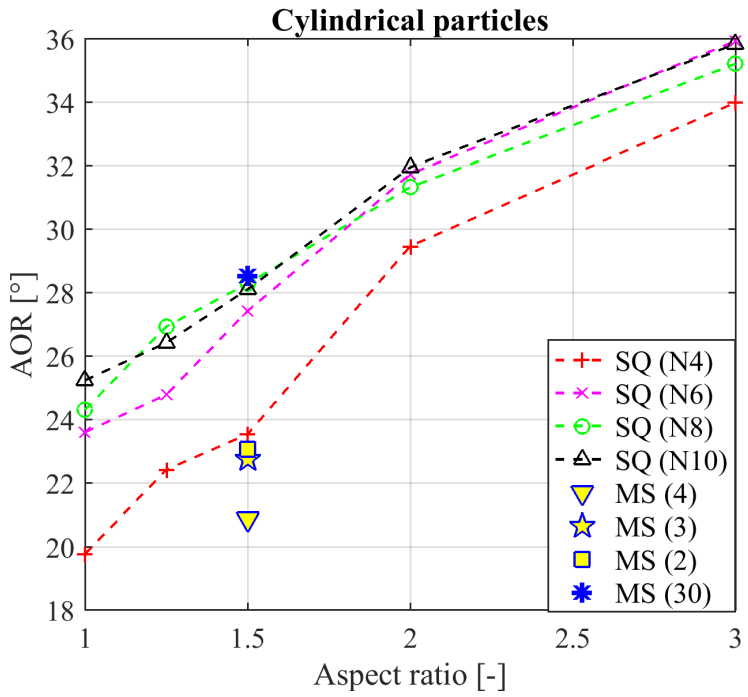

Figure 5.4 Average angle of repose for cylindrical MS and SQ particles.

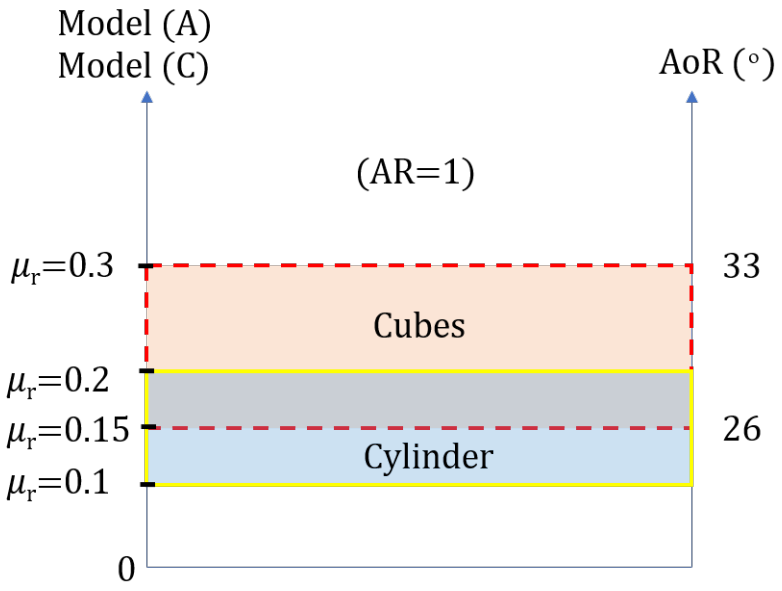

Figure 5.5 Graphical description of equivalent μ_r for obtaining similar AoR values to those of cubes and cylinders.

5.3.2 Jenike shear tester

The Jenike shear tester that is used here is identical to the one discussed in Section 4.4.2. The granular system consists of spherical particles with diameter ranging from 1.8 to 2.2 mm and following a normal distribution (with a mean diameter of 2 mm and a standard deviation of 0.2). The DEM time-step was chosen as $\Delta t = 2 \cdot 10^{-6}$ s (5 % of Rayleigh time) in all simulations. Two types of packing were generated to assess the dependence of the results on density state of the initial packing. In the dense packing, the particle-particle sliding friction μ^s_{pp} and rolling friction μ^r_{pp} coefficients were set to zero at the filling stage (i.e. all simulations were carried out based on a single initial packing). Next, before applying σ_v, μ^s_{pp} is changed back to 0.56 and μ^r_{pp} is systematically increased for individual packing ($\mu^r_{pp} = 0.01, 0.1, 0.2, 0.3, 0.5, 0.8$ and 1). For these packings, system is allowed to rest for half of a second of simulation time, prior to consolidation. Accordingly, this set of simulations are referred as equivalent dense initial packing (EDIP).

On the other hand, a second type of packing is established, which has $\mu^s_{pp} = 0.56$ at all stages of the test. Furthermore, the same values of μ^r_{pp}, as for EDIP during shearing, is applied to the granular assemblies both during filling and shearing (this is as if approximating the inclusion of particle shape during the packing). This is done to clarify the importance of the shape parameter (i.e. rolling resistance) in imposing the arrangement of the particles and further evaluate the shearing response of the relatively loose packings (depending on the incorporated value of μ^r_{pp}).

For all simulations, material properties were kept identical and packings of equivalent bulk volume were generated for all types of particles (for detailed information regarding the packings of MS and SQ cubes refer to Chapter 4). It is worth mentioning that, since it is already seen that shape factor is more effective in densely packed assemblies, the cylindrical and cubical particles are only simulated in the dense state. In the following section (5.3.2), the effects of including an artificial particle shape parameter on the packing density is evaluated. Afterwards, the shearing response of the particles is assessed in section 5.3.2.

Porosity

Spherical particles: it is known that applying any type of rolling resistance model affects particle arrangement, and thus the porosity of the granular packing (this is an inherent feature since all models suppress the movement of single particles). Accordingly, the porosity ϕ of the samples was measured before the start of consolidation state. This scalar quantity is an indication of how densely the particles are packed in the system (i.e. by dividing the total volume of the voids over the volume of the shear tester). There are many studies in the literature for determining the packing charac-

teristics of particles with various properties. For the spherical particles (using DEM), Jerier et al. (2010) varied the ratio of particle radius between 2 and 7 and determined a solid fraction within 0.58 to 0.75 (corresponding to $0.25 < \phi_{init} < 0.42$). Aste (2005) reported that pouring mono-sized spheres into a container, typically a solid fraction between 0.61 and 0.62 ($\phi = 0.38$ and 0.39) is obtained (depending on the geometry of the container, speed and height of filling). It is mentioned that slightly denser packings (i.e. solid fraction of 0.63) can be obtained by gently tapping the container. Additionally, it is reported that to achieve the random close packing limit (i.e. solid fraction of 0.64), the sample must be simultaneously tapped and compressed.

As mentioned before, the packings are prepared in dense and loose states (by turning on/off μ^s_{pp} and μ^r_{pp}). Figure 5.6 presents the dependency of the initial porosity (ϕ_{init}) of the samples on rolling resistance, for different models. For EDIP packings, ϕ_{init} is shown as a single point in Figure 5.6 ($\mu^s_{pp} = \mu^r_{pp} = 0$), of which has the lowest value as $\phi_{init} = 0.377$.

Additionally, it is observed that enabling the sliding friction (i.e. $\mu^s_{pp} = 0.56$) affects the ϕ_{init} (loosens the packing to $\phi_{init} = 0.4$). Moreover, considering higher μ^r_{pp} values, further increases the voidage in the granular system (i.e. by 15 % at most). For Model *A*, ϕ_{init} increases linearly, while its values are smaller than other two models. Model *C* provides the highest ϕ_{init} for small vales of μ_r (for $\mu_r < 0.1$). For $\mu_r \geq 0.2$ results of Model *B* and Model *C* are almost comparable (i.e. both models have similar influence on packing, despite their different rotation retardation mechanisms).

Non-spherical particles: ϕ_{init} for particles with various shapes is also computed and summarized in Figure 5.7 (results of cubes with $AR = 1$ have already been discussed in Chapter 4). For SQ cuboids, it is seen that increasing aspect ratio leads to slightly increased ϕ_{init} for SQ($N6$) and SQ($N8$) with $AR = 1.25$, while SQ($N4$) is independent of the AR value, see Figure 5.7a. In case of MS particles, the sharpest increase in ϕ_{init} is seen for the MS(8) particle. However, MS(27) shows almost a constant value for ϕ_{init} (a slight increase for ϕ_{init} is seen while moving from $AR = 1$ to $AR = 1.25$). Note that, similar to Section 5.3.1, MS(64) is not simulated for $AR > 1$.

Furthermore, the results for cylindrical particles are plotted in Fig. 5.7b. A cylindrical particle with $AR = 1$ and $N = 2$ represents a sphere, and an ellipsoid is formed for larger aspect ratios. The only noticeable change in initial porosity of cylindrical particles is seen when passing from a sphere to an ellipsoid (independent of N parameter). In general, it can be suggested that cylinders, at any level of shape complexity, have lower porosity than spheres. Additionally, the difference in porosity obtained for spheres with only sliding friction in Figures 5.6 and 5.7b can be justified by the fact that the spheres generated by superquadric approach are mono-sized. Moreover, for SQ($N4$), SQ($N6$) and SQ($N8$) the aspect ratio parameter is not affecting the packing porosity (at $AR > 1.5$, identical ϕ_{init} values are obtained for all N values).

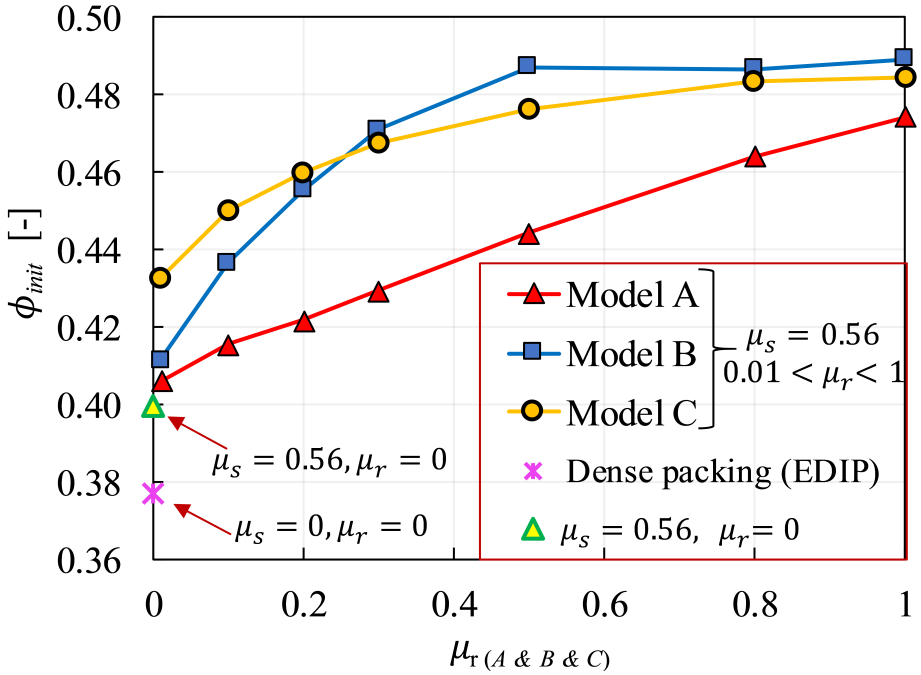

Figure 5.6 Initial porosity of the packings with spherical particles in the presence of rolling friction.

Finally, the packing characteristics of spherical particles (in presence/absence of rolling resistance models), is compared to those of considered cuboids/cylinders through assessing Figures 5.6 and 5.7. It can be pointed out that except for MS(8), which has a pseudo porosity, all cubes/cuboids and cylinders (in dense state) have lower porosities than spheres.

Volume change during shearing: it is also useful to monitor the vertical displacement of the lid, during the shearing of the assembly, to determine the mode of volume change (i.e. contractive or dilative), see Figures 5.8 and 5.9. For the EDIP packings, the contraction of the assemblies seems to be insignificant and dilation is the dominant mode of volume change. Packings with Model *A* are almost independent of the μ^r_{pp} (at shearing stage) and experience a similar lid displacement for all values of μ^r_{pp}. Packings with Model *B* are following a specific trend for the increase of μ^r_{pp}; for the $\mu^r_{pp} = 0.01 - 0.3$, Model *B* presents the same respond as Model *A*, however, for $\mu^r_{pp} > 0.3$, D_L values are descending (that is against the well-established fact that further shape irregularity will contribute to more interlocking which leads to a greater dilative behaviour). However, if we consider the fact that was observed in the Section 5.3.1 (μ^r_{pp} is suggested to be less than 0.2 to get reasonable results for AoR), this shortcoming of Model *B* can be ignored. For packings with Model *C*, it can be seen that increasing rolling resistance has a direct impact on the increase of lid's vertical movement (i.e. further dilation).

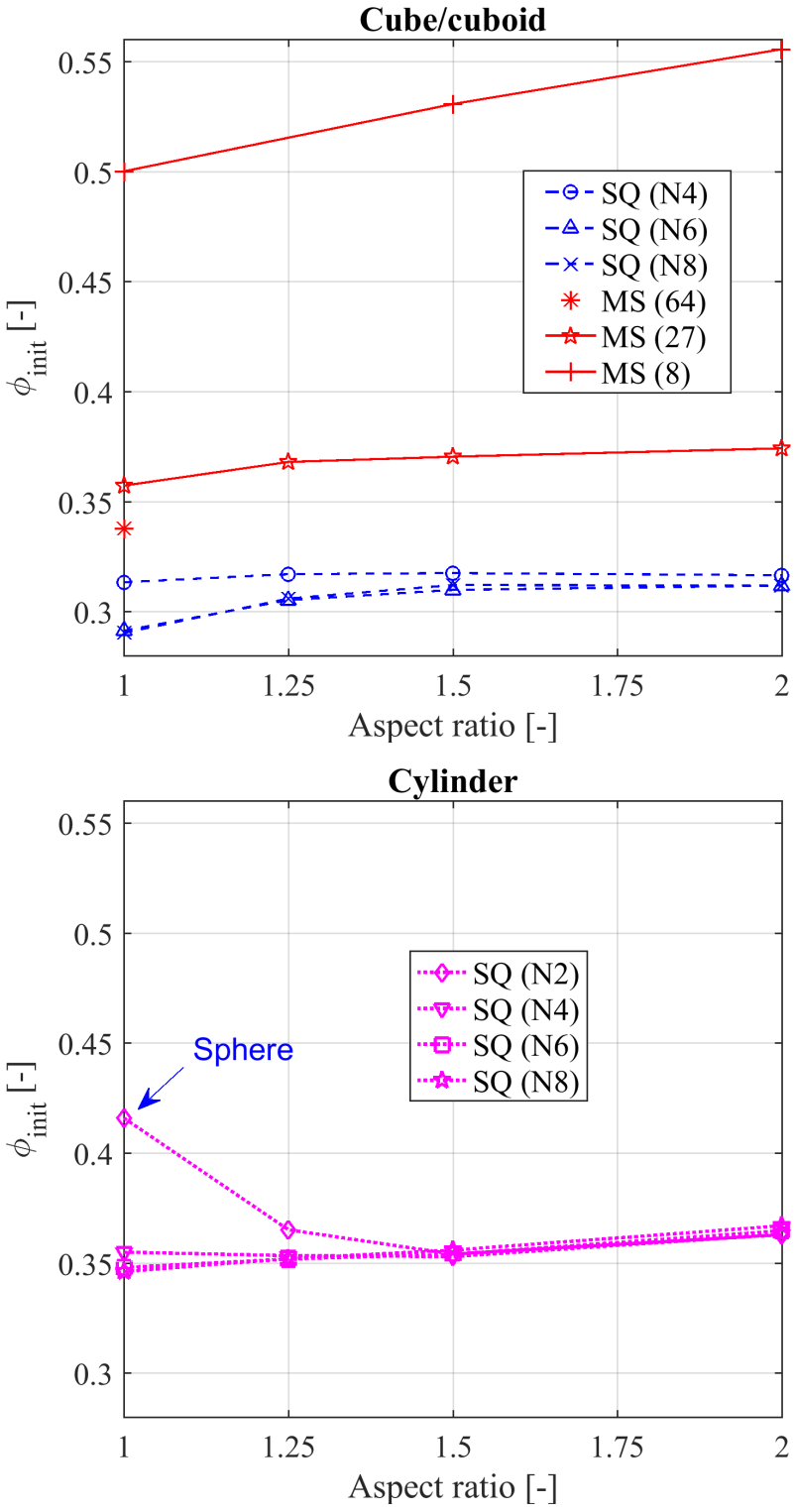

Figure 5.7 Initial porosity of the packings with a) cube/cuboid b) cylindrical particles.

Additionally, for relatively loose packings (with enabled μ^s_{pp} and μ^r_{pp} for both filling and shearing): Model *A* shows a contractive behaviour (i.e. all samples following the characteristics of a loose assembly) for all range of applied μ^r_{pp}, see Figure 5.9. It is only the packing with very small value of rolling friction coefficient (i.e. $\mu^s_{pp} = 0.01$) that undergoes a volume reduction until almost half of the shearing and then starts to present a volume expansion (i.e. behaves approximately similar to a medium dense sample). Consequently, it can be said that although Model *A* contributes to formation of looser packings, it is unable to provide particles with dilative behaviour during the shearing process once $\mu^r_{pp} > 0.01$.

Additionally, it can be seen that Model *B* is approximately following Model *A* (with the exception of the point that higher volume expansion is happening for samples with $0.01 \leq \mu^r_{pp} \leq 0.1$). Meanwhile, packings with Model *C* provided different responses compared to those of Model *A* and Model *B*; it can be seen that, regardless of the initial porosity, all the samples (except $\mu^r_{pp} = 0.01$) are presenting a half-half contractive/dilative behaviour. In other words, until the half of the total shearing distance, samples are compressed and once a threshold for ϕ is reached, dilation is initiated (this represents characteristics of a medium dense sample).

Further insight into volume change characteristics of the different packings is obtained through porosity-displacement plots in Figure 5.10. Results for Model *A* and Model *B* suggest that these packings only provide dilative response for specimens with low porosities (i.e. relatively dense samples). Moreover, it is seen that the porosity results converge towards 0.41-0.46 for Model *A*, and 0.43-47 for Model *B* (at 6mm displacement). In case of Model *C*, irrespective of the initial porosity, almost all samples undergo a contractive behaviour until half of shear displacement distance and then start to dilate.

Shear strength under direct shear

Spherical particles: the corresponding shear stress curves for spherical particles as a function of shear displacement (*D*) are shown in Figures 5.11 and 5.12. It can be seen that in case of EDIP packings, Model *A* has and an insignificant effect on the overall shearing response of the spheres (only the peak strength is increased by 15% for $\mu^r_{pp} > 0.1$). For Model *B*, similarly to the observations in Figure 5.8, for $\mu^r_{pp} = 0.01 - 0.3$ the shearing response is not changed, whereas for larger values of μ^r_{pp} a lower shear strength is observed.

Meanwhile, results from Model *C* are different to those of Model *B* and Model *A*; an increase of μ^r_{pp} results in significantly higher shear strength for the EDIP samples and its effect saturates at $\mu^r_{pp} = 0.5 - 0.8$. Additionally, the largest peak shear strength is almost 2 times the peak strength for Model *B* and Model *A*. It can be suggested that

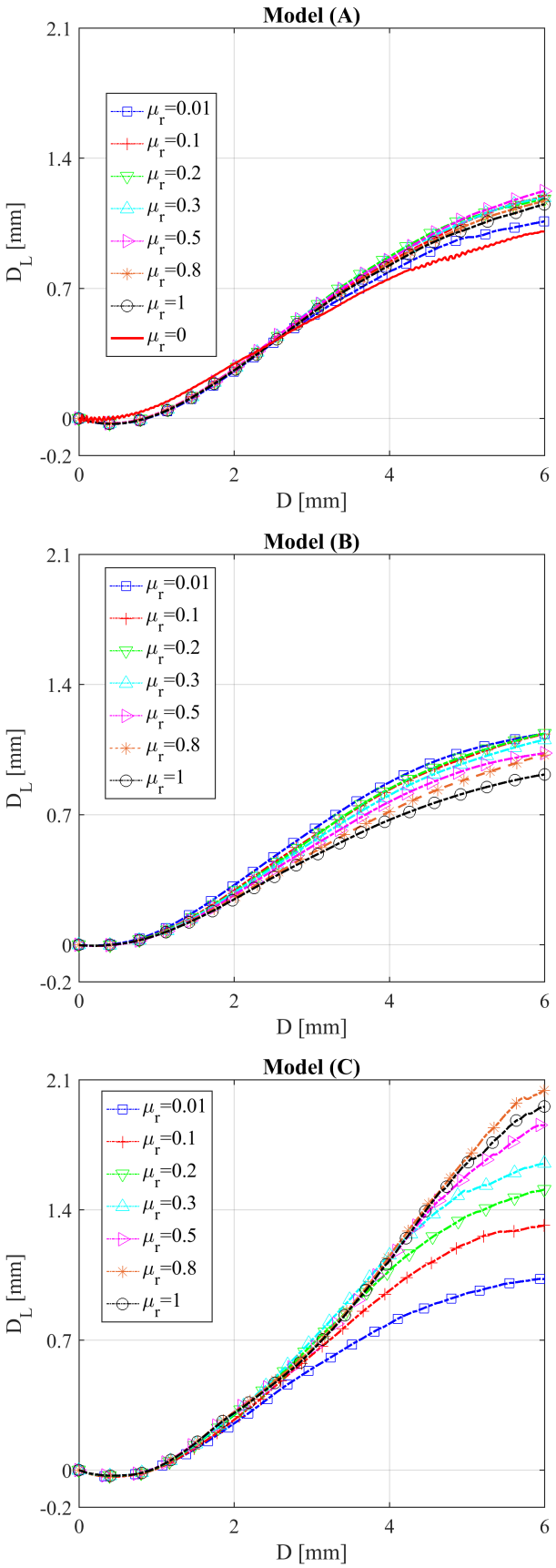

Figure 5.8 The relative vertical displacement of the lid during the shearing for EDIP packings (for all the packings ϕ_{init}=0.37) a) Model *A* b) Model *B* c) Model *C*.

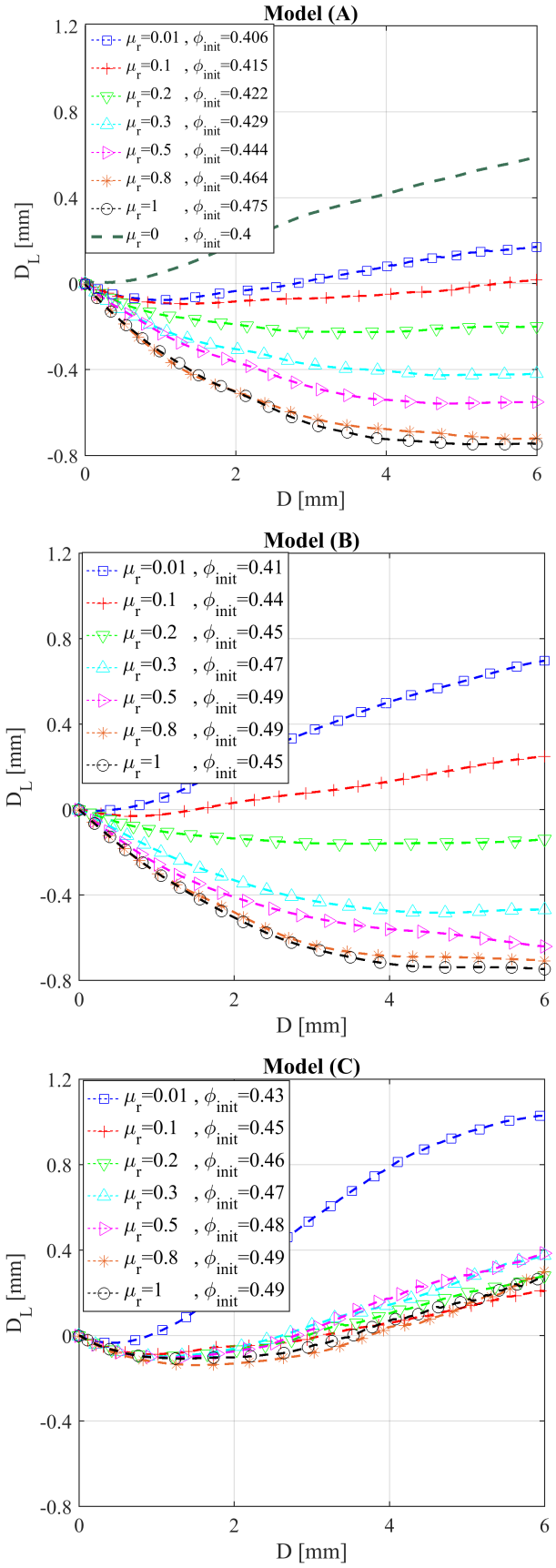

Figure 5.9 The relative vertical displacement of the lid during the shearing for loose packings a) Model *A* b) Model *B* c) Model *C*.

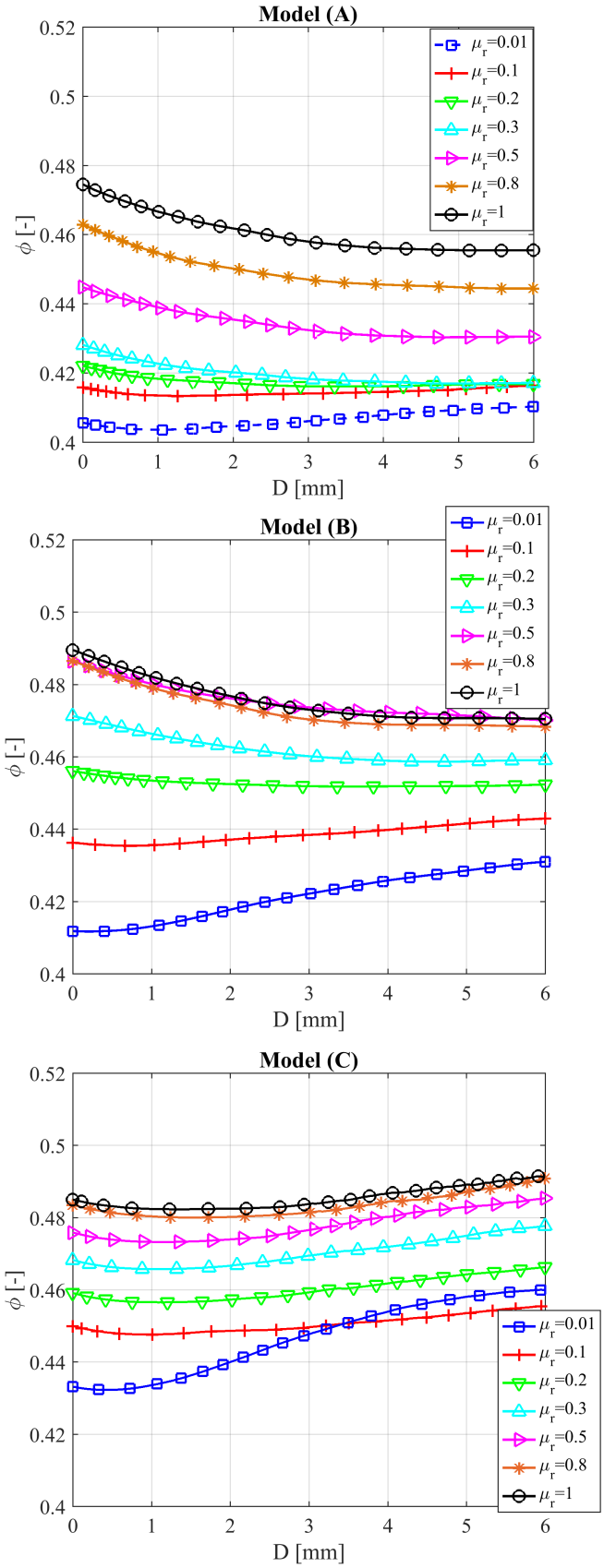

Figure 5.10 Change in porosity with respect to shear displacement (for packings with enabled rolling friction during filling) a) Model *A* b) Model *B* c) Model *C*.

for EDIP packings, only Model *C* has an effective influence on the shear strength of the granular assembly, which follows a trend similar to increase of shape irregularity.

Based on the observations in Figure 5.6, it is known that the incorporation of the rolling resistance models contributes to the formation of loose packings. However, it is not clear that whether applying rolling resistance during shearing will still be able to compensate for the shape effect for these packings. The shearing response of the relatively loose packings are summarized in Figure 5.12. For both Model *A* and Model *B*, it is seen that while increasing μ^r_{pp}, both initial stiffness and peak shear stress for the packings are decreased to a large extent (nonetheless, the shear strength at critical state is approximately comparable). This reduction in shear strength can be partially related to packing density, however it seems that these two models fail to calculate appropriate opposing torques. Moreover, for packings with Model *C*, it is clear that despite the initially loose packings, the shear strength is increased by increasing the rolling resistance coefficient (up to $\mu^r_{pp} = 0.5$).

Coordination number: the coordination number (*CN*) of the samples are also obtained for dense and loose samples and its variation by shear displacement is plotted in Figures 5.13 and 5.14 (since the response of Model *A* is similar to that of Model *B*, results from one case is only presented). It is clear that for dense samples of the both models, due to a dilative response, the coordination number is reduced (some contacts are lost) as the material is sheared. This in agreement with observations of Zhao et al. (2015).

In the case of loose packings, it is seen for both models that as μ^r_{pp} increases, *CN* is reduced for the initial packings (at $D = 0$). Additionally, a small decrease is seen during initial instances of shearing and then *CN* remains constant for the both models, see Figure 5.14.

Non-spherical particles: similar to Section 5.3.1, the effect of aspect ratio on cuboids and cylindrical particles (with various surface and edge properties) is investigated within the Jenike shear test, see Figure 5.15. The peak friction angle (Φ_p) of the packings, which is obtained through dividing the maximum value of τ by σ_n, is plotted with respect to *AR*. For SQ cuboids, the Φ_p increases sharply for SQ$(N4)$ up to $AR = 1.5$, whereas for SQ$(N6)$ and SQ$(N8)$ the change in Φ_p is smaller and limited by $AR = 1.25$. However, MS cuboids show a reduced dependency on the *AR* value (only MS(27) shows an increase for $AR = 1.25$).

On the other hand, the cylinder with $N = 2$ and $AR = 1$ (i.e. sphere) has the lowest Φ_p, which is significantly increased at $AR = 1.25$ (i.e. converting to ellipsoid). For $AR > 1.25$ results for SQ$(N2)$ and SQ$(N4)$ overlap. Other cylindrical particles with sharper edges only show a small change in Φ_p for $AR = 1.25$ (no changes are seen for $AR > 1.25$).

Furthermore, the shear strength for cubes/cuboids and cylinders is compared with spherical particles. Accordingly, the peak friction angle (Φ_p) of the different spherical packings are summarized in Figure 5.16 (since only Model *C* provides reasonable shearing response, results from Model *B* and Model *A* are not included). It is clear that peak friction angle of spheres in both EDIP and loose packings increases almost monotonically with increase of μ^r_{pp}. Considering Figures 5.15 and 5.16, results suggest that it is possible to calibrate the μ^r_{pp} to obtain desired individual macro-scale response of the non-spherical particles (in this case peak friction angle).

5.4 Case study: Particle shape influence on active failure state

It is important to assess the influence of the particle shape parameter in various testing conditions. This section considers a geotechnical application (i.e. behaviour of a backfill behind a retaining structure) and investigates the dependency of the bulk response on the particle shape factor. Accordingly, a cohesionless retained backfill that deforms under a plane strain boundary condition is modelled through DEM using both spherical particles with applied rolling resistance and multi-spherical particles.

The conducted investigations include the following: a) the velocity distribution of the individual particles b) wall pressure distribution along its height c) the total force acting on the wall throughout horizontal wall movement d) determination of the failure surface geometry e) obtaining the shear and volumetric strain distribution along emerged shear bands.

5.4.1 Introduction

Designing soil-retaining structures is among the oldest topics in Civil Engineering. The Coulomb and Rankine theories are the most widely accepted for estimation of the induced loads from the backfill and also to predict the size of the active failure zone (Coulomb, 1776; Rankine, 1857). Both methods are based on limit equilibrium theory and therefore suffer from the inherent deficiency of ignoring the evolution of deformation localization and the heterogeneous characteristics of the stress distribution. To overcome these shortcomings, several studies have been conducted both experimentally (Altunbas et al., 2017; Fang and Ishibashi, 1986; Soltanbeigi et al., 2019; Terzaghi, 1943; Toyosawa et al., 2006) and numerically (Benmeddour et al., 2012; Goel and Patra, 2008; Jiang et al., 2014; Tejchman et al., 2007).

Among previously conducted DEM studies, the characteristics of different shape representation methods, in predicting the backfill failure, is overlooked. Accordingly,

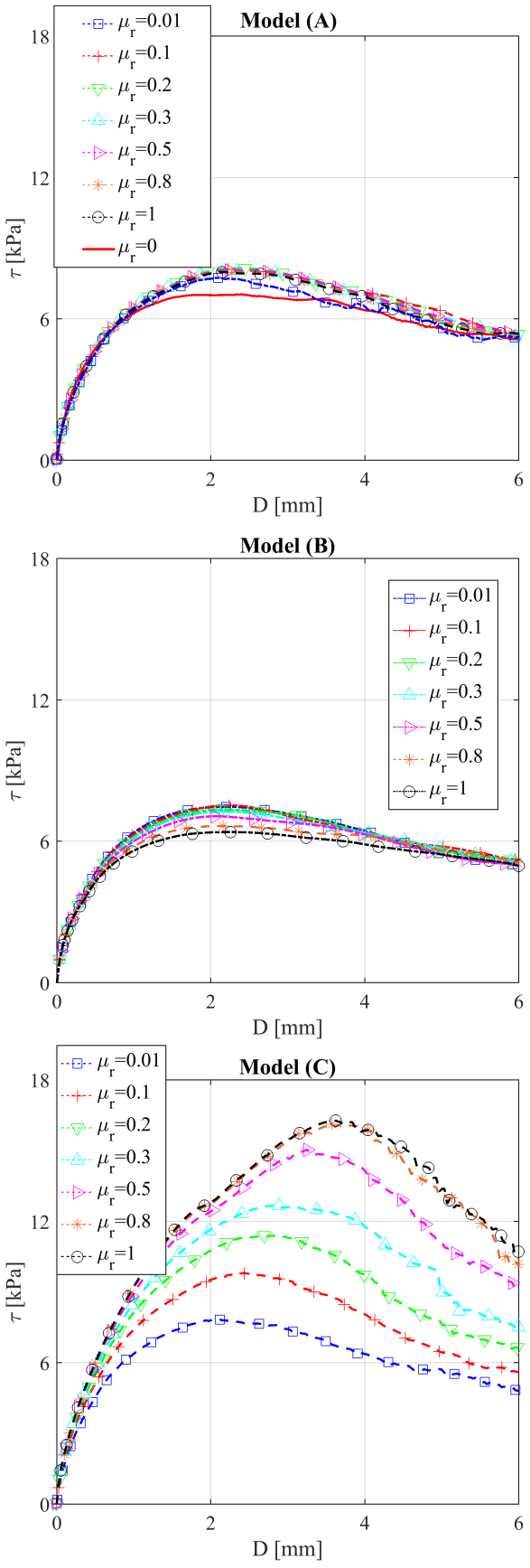

Figure 5.11 The shear stress displacement curves considering various values of μ_{pp}^{r}, for EDIP packings (for all the packings ϕ_{init}=0.37) a) Model *A* b) Model *B* c) Model *C*.

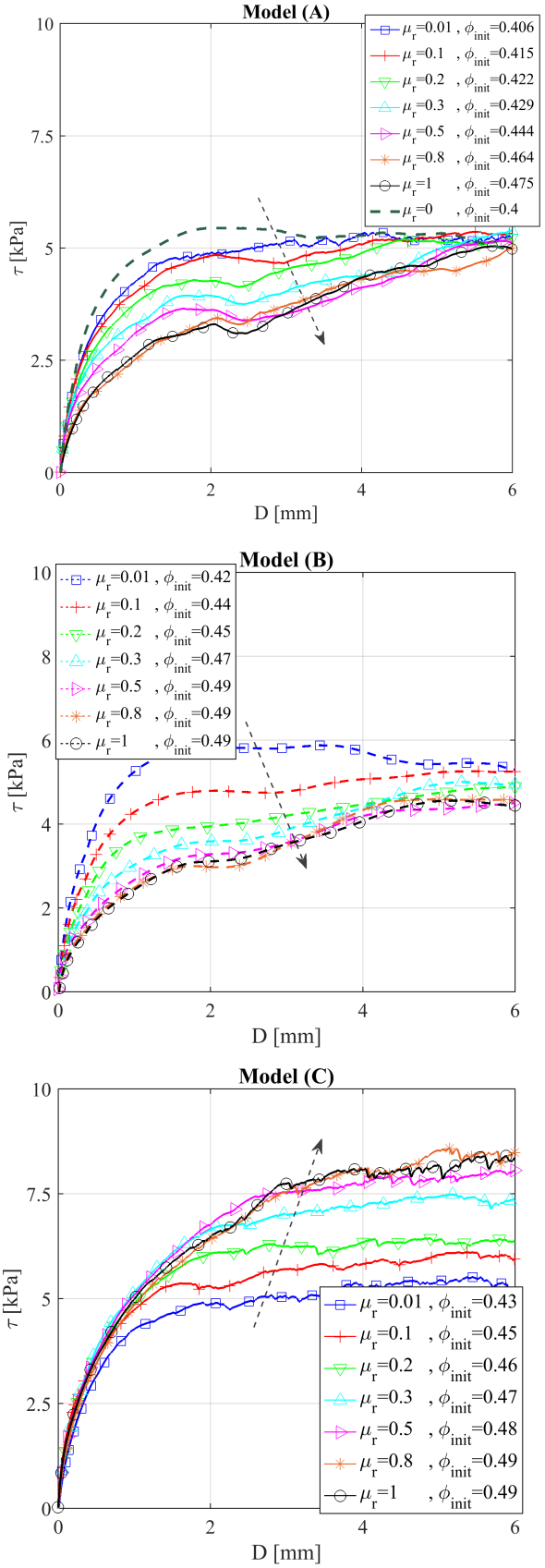

Figure 5.12 The shear stress displacement curves considering various values of μ_{pp}^{r}, for loose packings a) Model *A* b) Model *B* c) Model *C*.

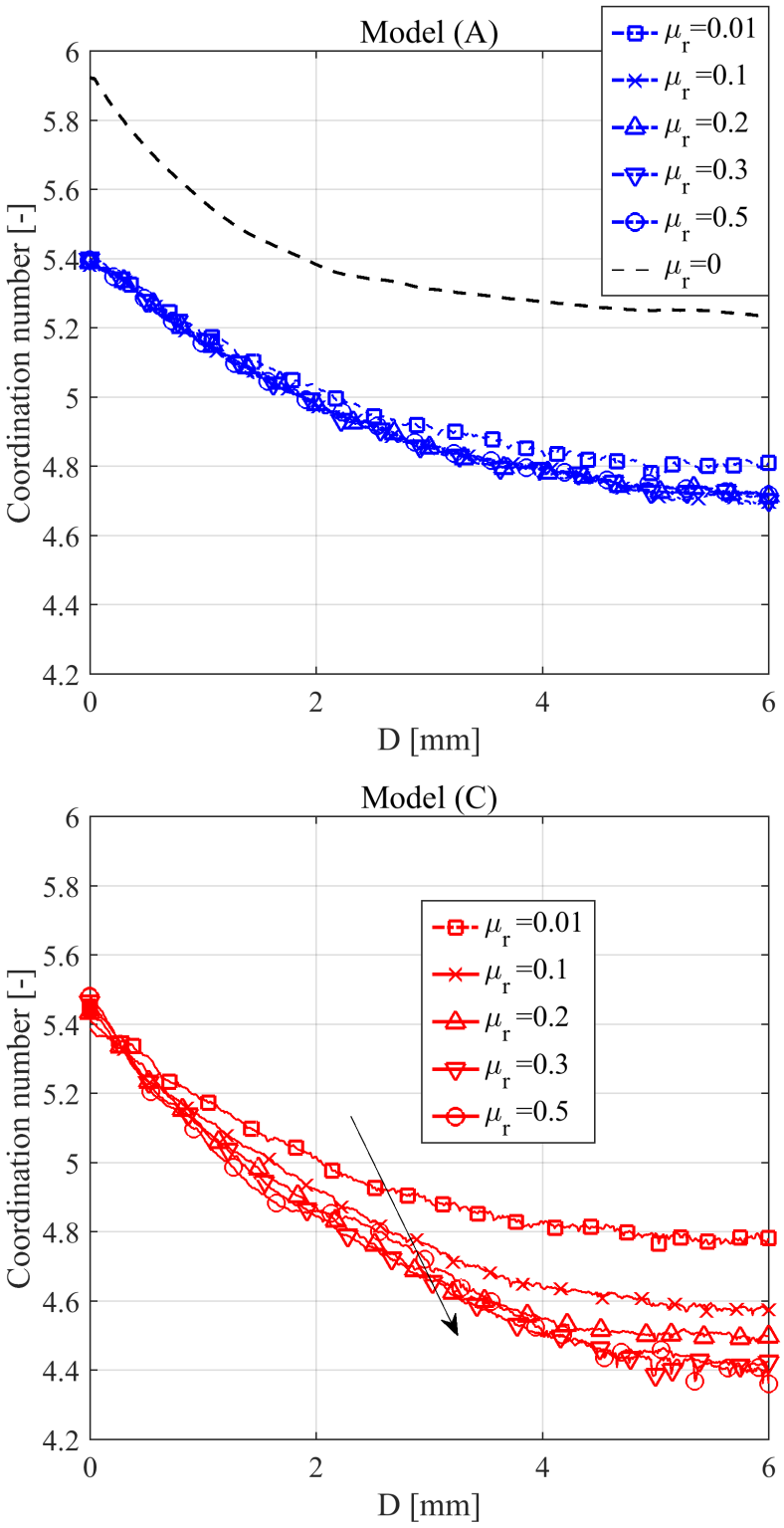

Figure 5.13 Variation of the coordination number with respect to shear displacement for EDIP packings a) Model *A* b) Model *C*.

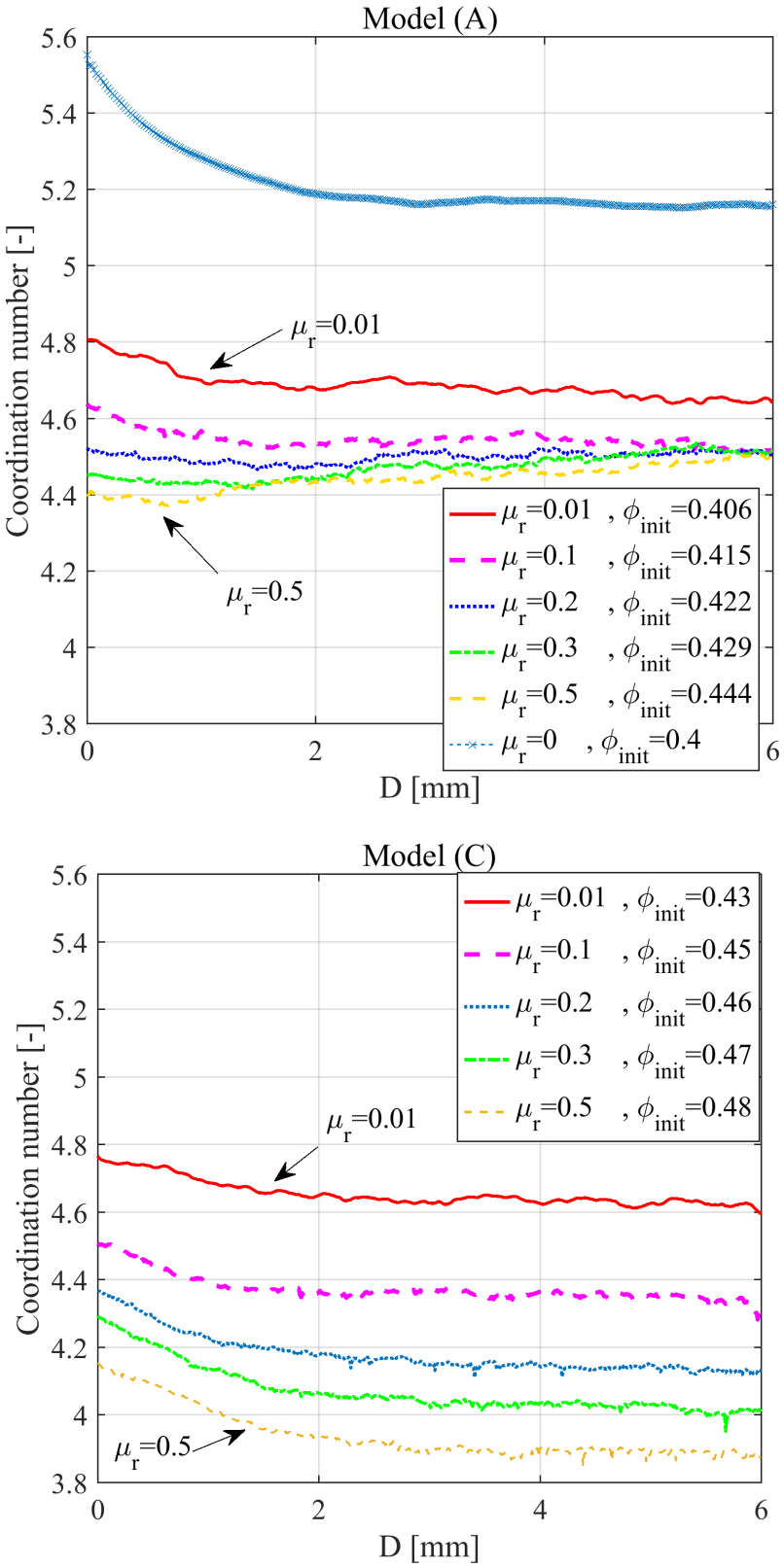

Figure 5.14 Variation of the coordination number with respect to shear displacement for loose packings (with various μ_r values) a) Model *A* b) Model *C*.

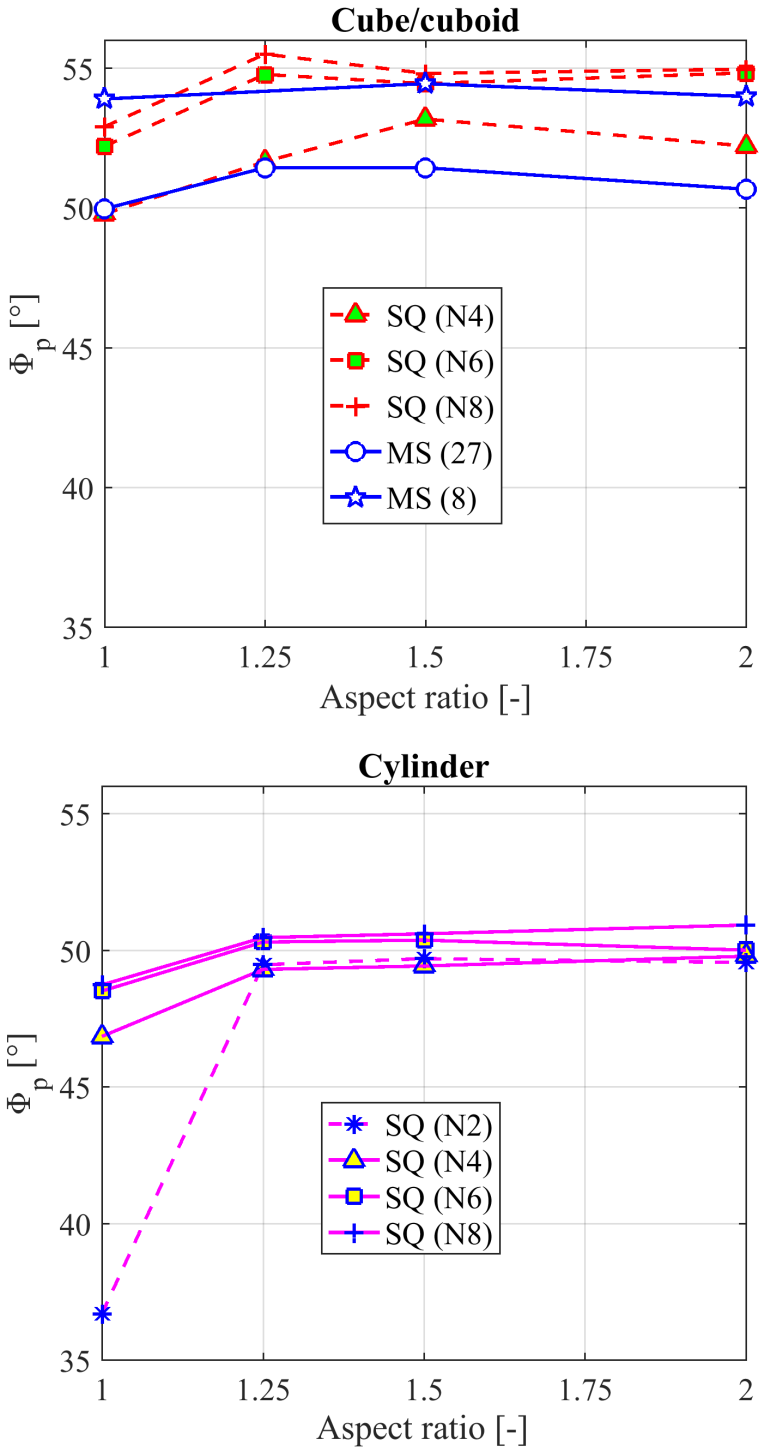

Figure 5.15 Dependency of peak friction angle on aspect ratio for a) cube/cuboids b)cylinders.

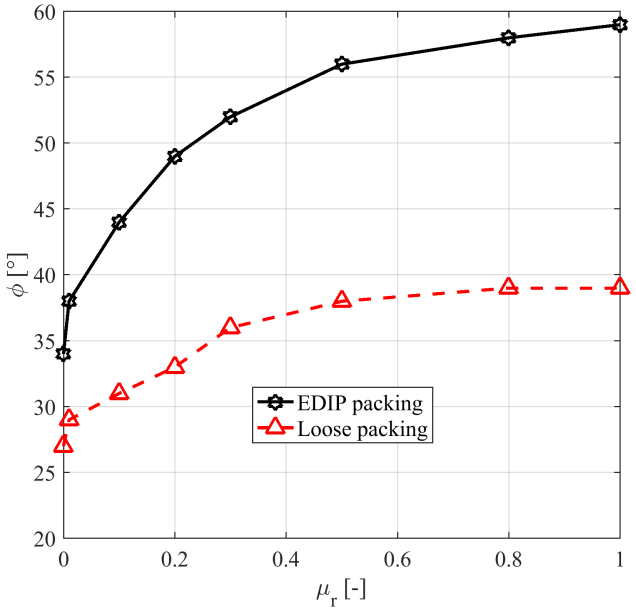

Figure 5.16 Summary of the peak friction angle for various packing densities (for Model *C*).

a series of DEM simulations are performed within a model retaining wall as the main geometry with two types of particles; perfect sphere, with additional rolling resistance feature, and non-spherical particles which are composed of two overlapping spheres. Consequently, the equivalence of computed macroscopic features of both systems is investigated quantitatively and qualitatively.

5.4.2 Methodology

A cohesionless retained backfill that deforms under a plane strain boundary condition is modelled using DEM, as shown in Figure 5.17a. The retaining wall has a rough surface and its outward horizontal translation leads to active state failure. The proposed geometry has a periodic boundary in the depth of the backfill (y direction). Furthermore, the adverse influence of bed boundary effects is minimized by considering a layer of particles in the bottom section of the model. The properties of the particles in this layer are the same as in the backfill and its height is 10 times the mean particle diameter. Table 3.1 summarizes the list of parameters of the DEM simulation. The EDEM® 2.3 particle simulation software is used for running numerical simulations (DEM Solutions Ltd., 2014).

When using spherical particles, the granular system consists of 22000 spherical particles with a mean diameter of 3 mm and a standard deviation of 0.3 mm. Additionally, the simplest multi-sphere particle, which is composed of two overlapping spheres

and will be referred to as paired particle hereafter. The total number of paired particles is approximately 18000 and the aspect ratio is 1.25, see Figure 5.17b.

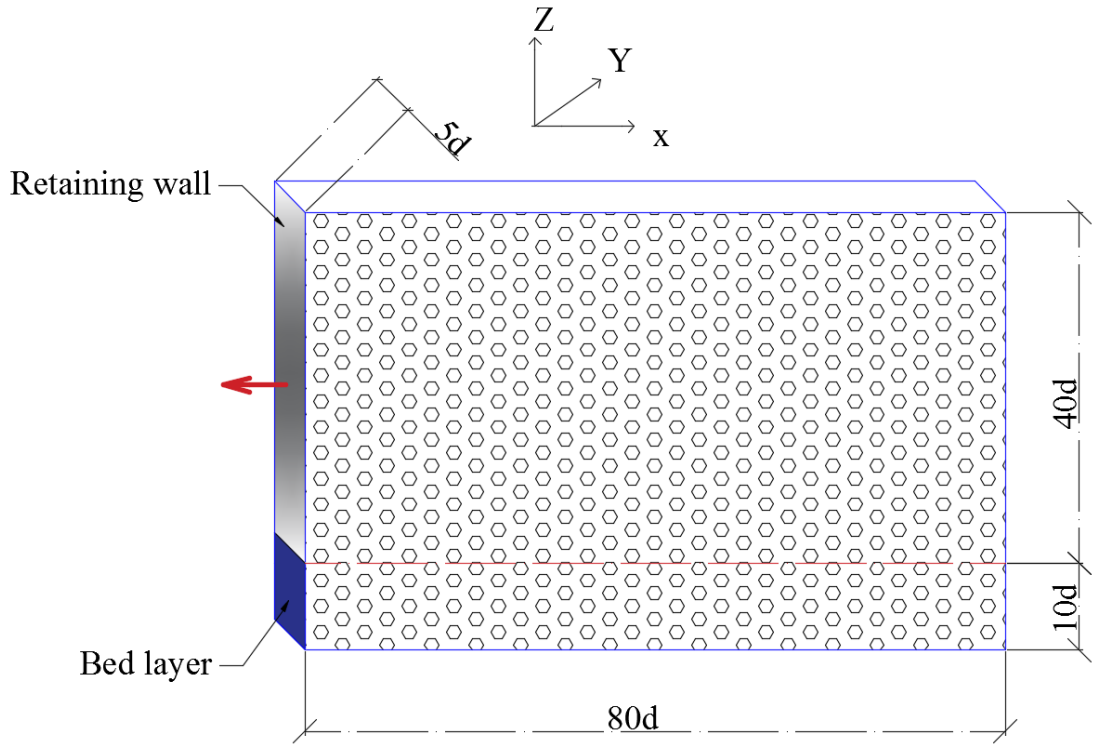

(a)

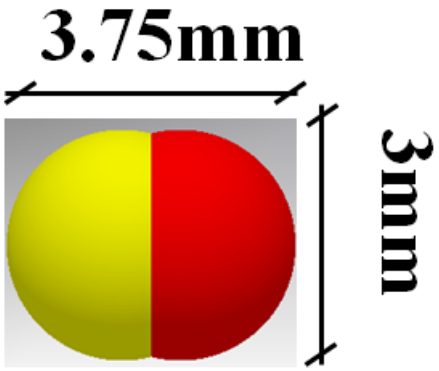

(b)

Figure 5.17 DEM model a) geometry of the retaining wall and modelled backfill b) paired particles.

Based on study of Morrissey (2013), among various particle generation methods that are supported in the EDEM Particle Factory™, the moving dynamic factory has been adopted for filling of the system due to its speed benefits. The wall is translating with a constant speed of 1 mm/s to ensure the quasi-static flow of the particulate system. The particle data is saved with a frequency of 200 Hz. Here, only Model *A* is considered as the main rolling resistance model.

5.4.3 Results

The first objective of the current study is to identify the influence of applying rolling resistance to spherical particles on the bulk characteristics of the backfill. Accordingly, results for two backfills with no rolling resistance (μ_r=0) and a very high value of rolling friction coefficient (μ_r=1) are compared. Furthermore, the consistency of bulk response for the complex shape particles and spheres with reduced rotation is evaluated.

The wall horizontal displacement at any instance of the test is normalized by the wall height (H_w) and is referred to as S/H_w hereafter. Figure 5.18 shows the horizontal velocity distribution in the granular system at a wall translation of 1mm (i.e. at $T = 1s$), for spherical particles with μ_r=0 and μ_r=1, and for paired particles. The dislocation of the wall causes flow of particles in a certain region of the backfill, with particles in the vicinity of the wall having the maximum velocity. Figure 5.18b indicates that including rolling resistance for spheres influences the magnitude of the velocity distribution in a decreasing manner compared to μ_r=0. Moreover, the backfill with μ_r=1 presents a more uniform distribution of velocity, which follows the wall speed (i.e. 10-3 m/s). Comparison of Figures 5.18b and 5.18c suggests that spheres with μ_r=1 show a similar trend to paired particles for the velocity distribution. Additionally, both backfills with spherical particles have a stationary zone which is separated by a transitional low speed zone from the active wedge. However, in the case of paired particles the transition zone is not present and the flow is concentrated within a pronounced area.

Figure 5.19a shows the influence of both restraining the rotational freedom of spheres and use of paired particles and on the lateral pressure distribution (P_h), along the wall height, with respect to magnitude of the wall translation. The case S/H_w=2.08e-4 represents the very initial steps of wall movement, therefore the pressure distribution still overlaps for both spherical cases (i.e. μ_r=0 and μ_r=1). However, the P_h values have dropped to nearly half for paired particles. Additionally, further increase in wall translation results in reduction of the exerted pressure for all cases, which indicates the failure of the backfill and mobilization of the active thrust. Additionally, it can be observed that the presence of rolling resistance is influencing the magnitude of the exerted pressure, and the backfill with μ_r=1 presents lower values for P_h as displayed in Figure 5.19a. This is in line with the numerical results of Jiang et al. (2014). Moreover, results suggest the presence of arching (Goel and Patra, 2008; Terzaghi, 1943), which is originated from relative displacement of the failure wedge and the stationary zone along the slip line.

Figure 5.19b compares the total compressive force (F_T) acting on the retaining wall with respect to wall movement for μ_r=0 and μ_r=1, and for paired particles. The plot shows that a small wall movement results in a sudden drop in F_T, and further wall

displacement reveals an almost constant value for F_T. As expected, the difference in P_h distribution for μ_r=0 and μ_r=1 is also observed for F_T. Additionally, Figure 5.19b indicates that for the similar amount of wall movement, paired particles exert less total force compared to spherical particles. Consequently, Figure 5.19 shows that applying the artificial torque to spherical particles contributes to the reduction of the induced pressure on the retaining wall, and this in line with the effect of non-sphericity. Nonetheless, further studies are needed to address the degree to which the applied rolling resistance provides a similar stress state as for complex shaped particles.

Hybrid PIV-DEM strain measurement

Particle Image Velocimetry (PIV) is a numerical method for the determination of deformations through consecutive images taken from a transparent side of a sample. This technique was developed initially by Adrian (1991) for the field of experimental fluid mechanics.

This study uses GeoPIV for image analysis, which is a MATLAB module developed especially for applying PIV in geotechnical applications (White et al., 2003). GeoPIV tracks the texture of the soil within captured images and provides displacement vector fields, shear and volumetric strain maps throughout the test. The first step in GeoPIV is to determine the area of interest (AOI) and cut it out of the digital image and divide into a grid of square patches, see Figure 5.20a. These patches are distinguished by their unique pixel intensity variation signatures. Subsequently, GeoPIV algorithm searches in a specified zone within the deformed image to find a patch that has maximum similarity to the initial patch's signature. The difference between the target patch, measured in pixels, and the reference patch is visualized by the displacement vector as shown in Figure 5.20b. According to Lesniewska and Wood (2009), the best solution to address related concerns is to consider coarser patches and define them in overlapping distance. Here, we consider patches with size of 150 pixels and centre-to-centre distance of neighbouring patches of 50 pixels.

In this study, a hybrid PIV-DEM solution is employed to obtain the strain distribution field within the numerical model (see Zhou (2011) for a detailed description of the methodology). Successive images of the backfill, with frequency of 10 Hz, are extracted from EDEM and analysed through PIV. Results of shear strain distribution with respect to wall movement are shown in Figure 5.21 for the backfill with μ_r=1. The deformation localization is observed in the plots, which starts from the toe and continues up to the surface of the backfill. It can be seen that the shear band formation is initiated from early stages of the test and as the wall moves further, the intensity of shear strain along the shear band increases. To compare the failure surface geometries of the backfills, the outer edge of the active failure zone is identified. The extracted geometry

(normalized by the wall height H_w) is plotted in Figure 5.22, showing a continuous parabolic failure surface for all cases, which matches experimental observations by Cinicioglu et al. (2015). Additionally, the results suggest that the inclusion of rolling resistance has negligible effect on the geometry and the location of the failure surface. Paired particles present a smaller wedge that can justify the lower active thrust.

Volumetric strain maps give an interpretation of dilative behaviour of the backfill during the active failure. For volumetric strain maps, the distribution of expansive behaviour (blue areas) is dominant along the shear band for paired particles, which is apparent in Figure 5.23c. Furthermore, it seems that the backfill with rolling resistance is presenting a more dilative deformation along formed shear band compared to μ_r=0. Nonetheless, it can be seen that the results of the volumetric expansion in the backfill with μ_r=1 stands relatively far from results of paired particles. Accordingly, a more detailed quantitative study may better highlight the defects of current rolling resistance model in predicting shear band evolution.

5.5 Summary

This chapter evaluated the potential for different rolling resistance models in predicting avalanching, packing and shearing characteristics of non-spherical particles with different degrees of shape complexity. Three popular types of rolling resistance models are employed together with spherical particles and two types of complex shapes, as cubes and cylinders, are simulated using superquadric and multi-sphere approaches. The complexity of non-spherical particles are varied by means of corner sharpness, surface bumpiness and aspect ratio.

Accordingly, results from angle of repose test suggested that incorporation of the artificial torque (provided with all three models) can approximate the avalanching characteristics of the simulated cube/cuboid and cylindrical particles. Moreover, the obtained results for the Jenike test suggest that except for porosity, both the shear strength and dilative response of the considered non-spherical particles can be predicted with only one of the employed models (elastic-plastic spring-dashpot model (EPSD)). The other two simple rolling resistance models (i.e. Model *A* and Model *B*) affect the initial porosity of the system, however fail to provide reasonable results in terms of volume expansion and shear strength.

Comparing AoR results with those of Jenike shear, it can be depicted that Model *A* and Model *B* rolling resistance models are problem dependent. In other words, these simple models are effective only when the system is not externally loaded (i.e. only contribute to initial packing and heap formation).

Furthermore, as an additional case study, the sensitivity of the bulk behaviour in a cohesionless backfill, to the particle shape is assessed. The simulations represented an active failure state, where the rigid frictional retaining wall translates away from the backfill. The particle shape is addressed using spherical (with and without rolling resistance) and paired (two overlapping sphere) particles. The results show that spheres with rolling resistance follow the behaviour of paired particles in case of total pressure exerted on the wall and uniformity of the velocity distribution. In contrast, the response of paired particles, in terms of failure surface geometry and dilative behaviour of the sample, is not predictable by considering spherical particles and the respective rolling resistance model.

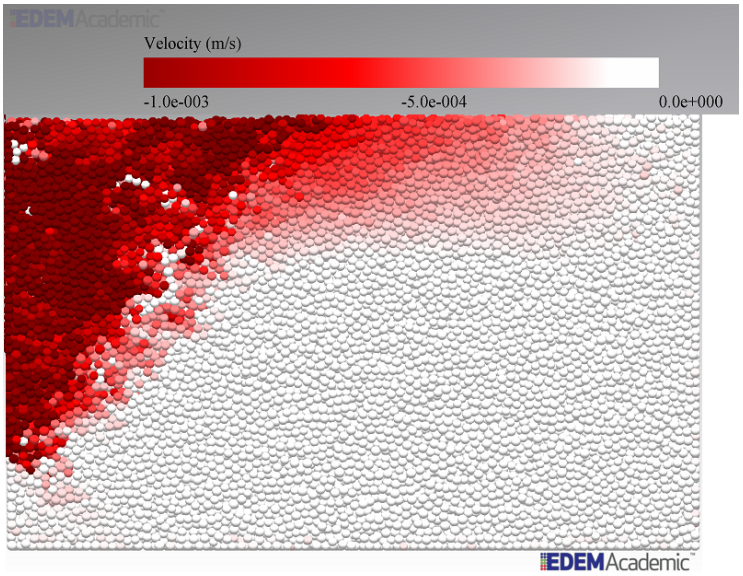

(a)

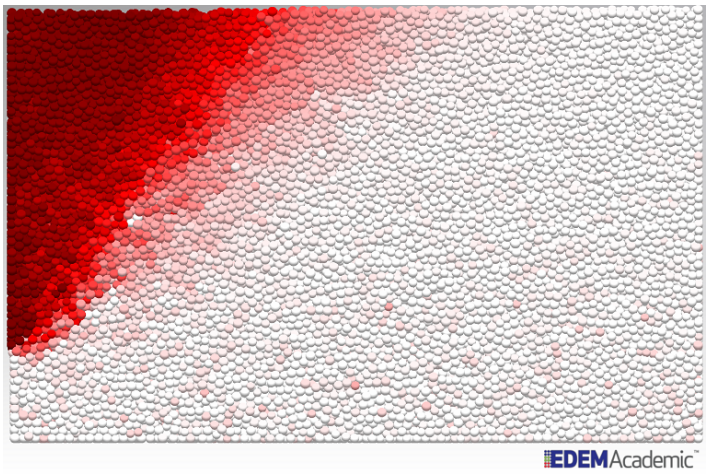

(b)

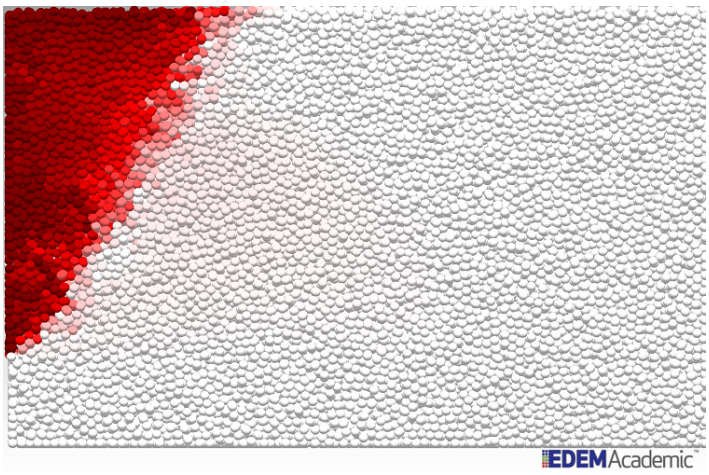

(c)

Figure 5.18 Horizontal velocity distribution at 1 mm of the wall movement (i.e. at $T = 1s$) for a) μ_r=0 b) μ_r=1 c) paired particles.

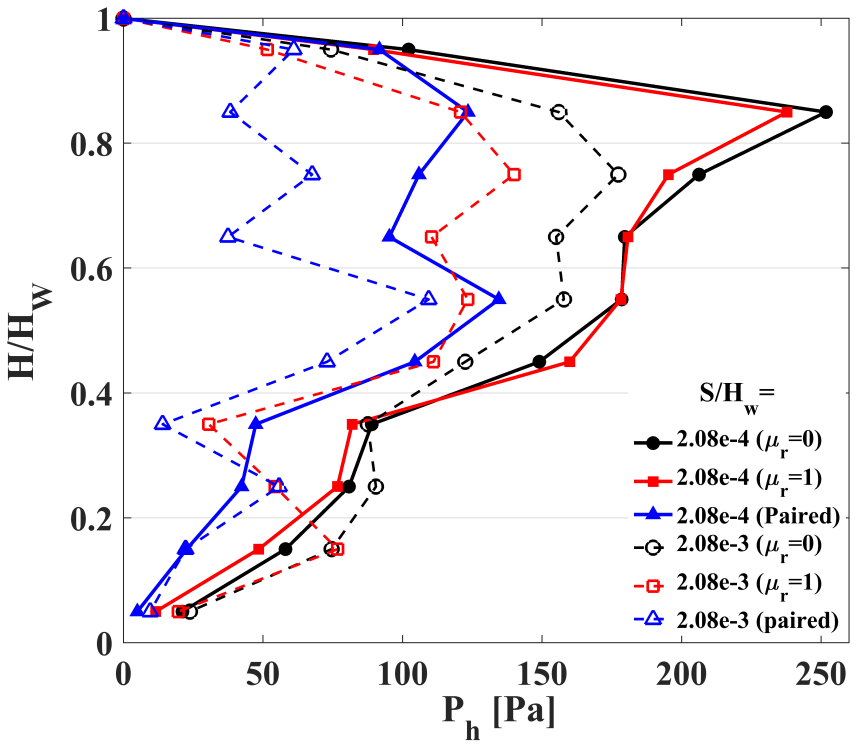

(a)

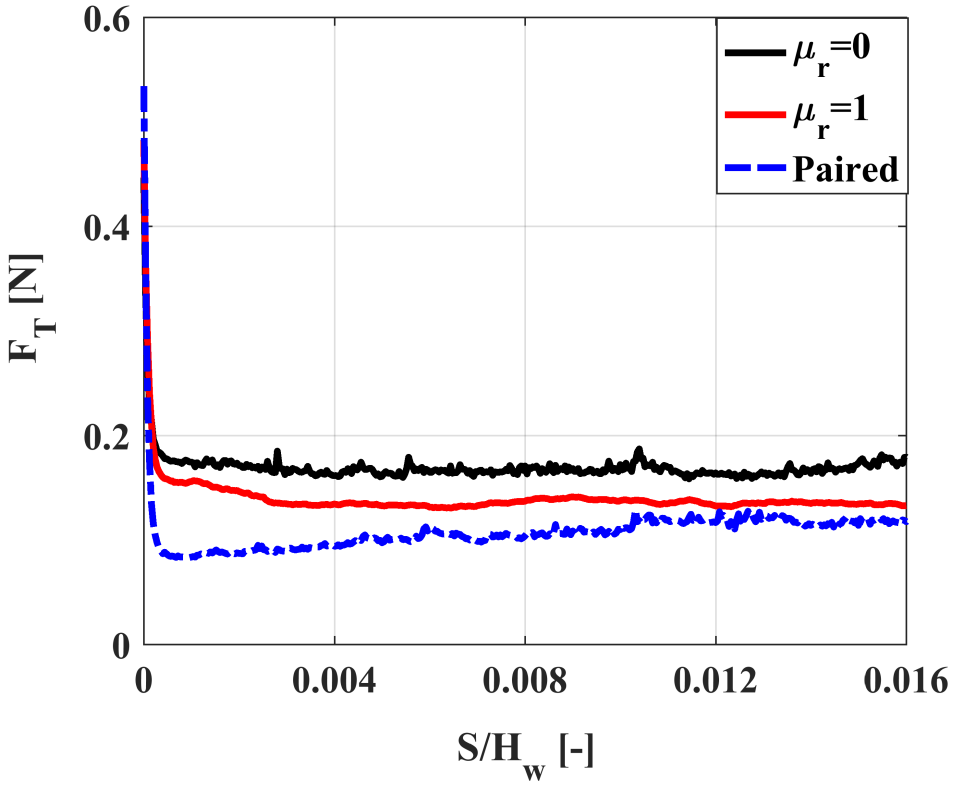

(b)

Figure 5.19 Dependency of the pressure distribution on particle shape a) wall pressure distribution b) total normal force exerted on wall.

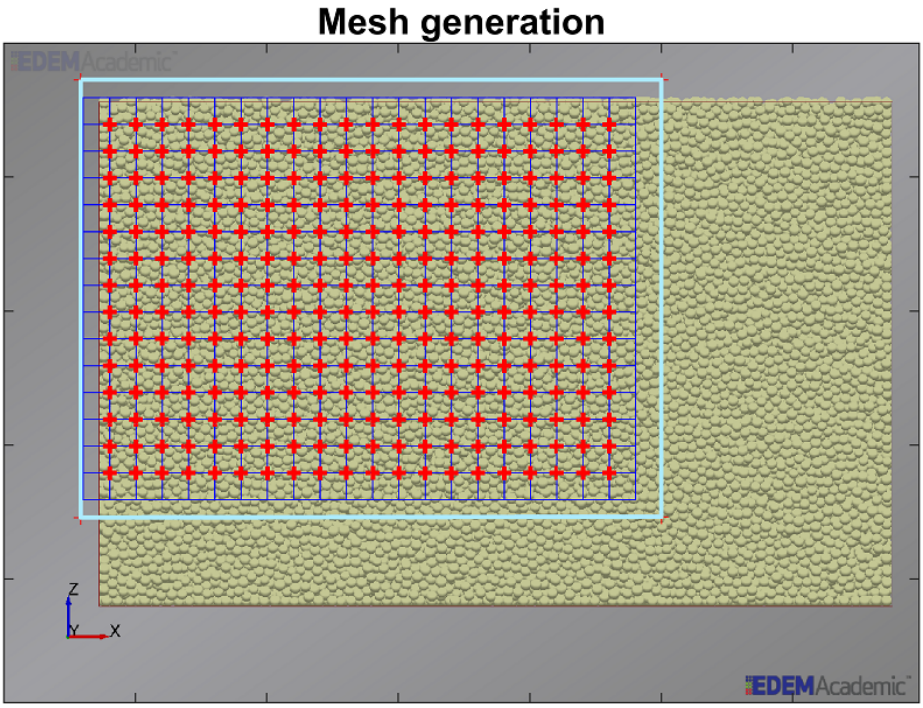

(a)

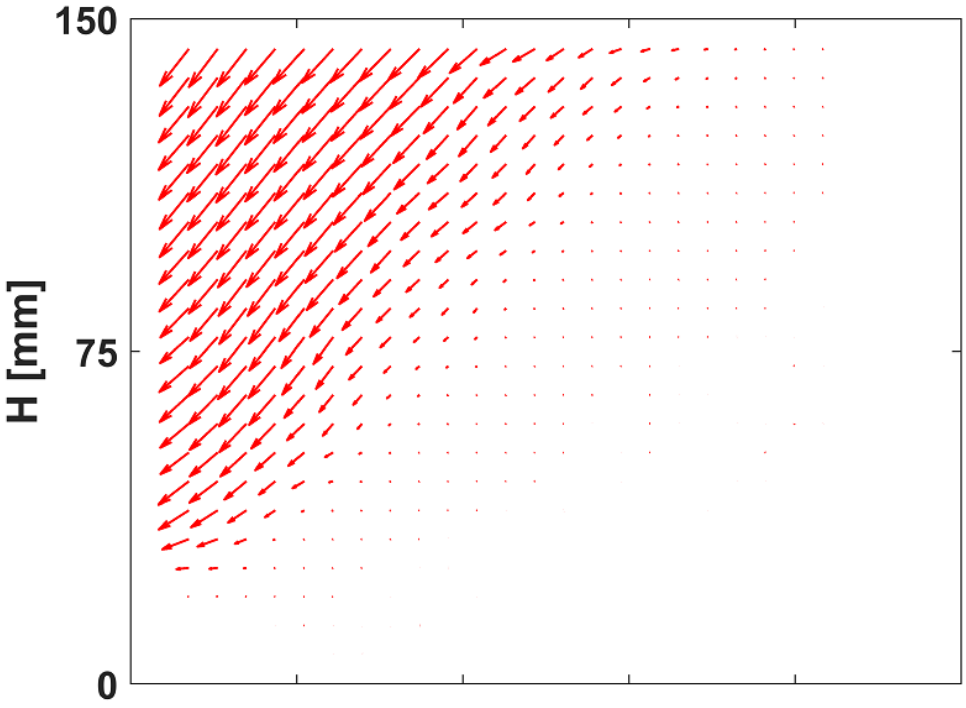

(b)

Figure 5.20 Graphical representation of PIV a) AOI and patches b) vector field for the deforming media.

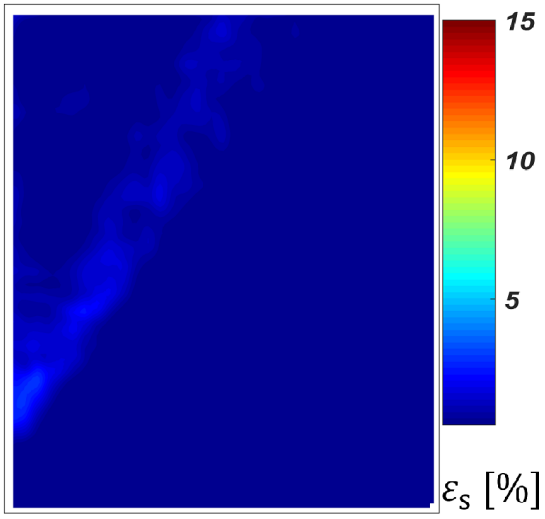

(a)

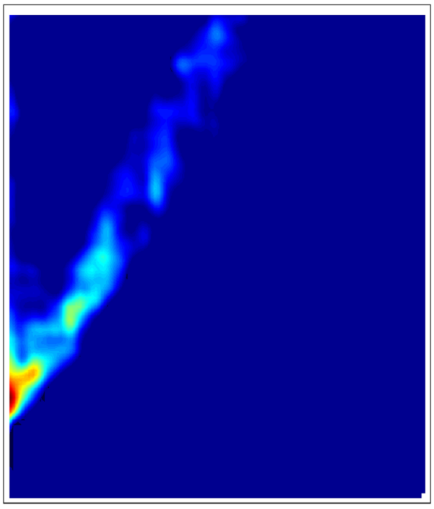

(b)

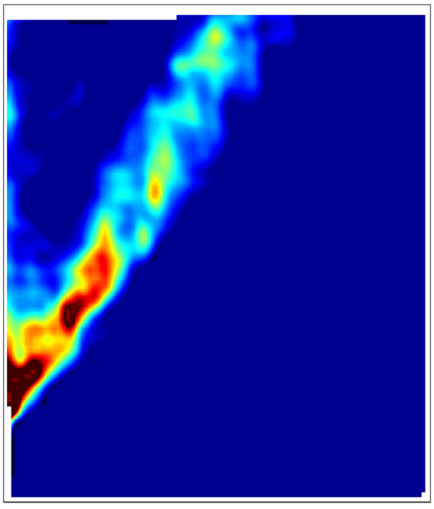

(c)

Figure 5.21 Shear strain distribution with respect to wall movement.

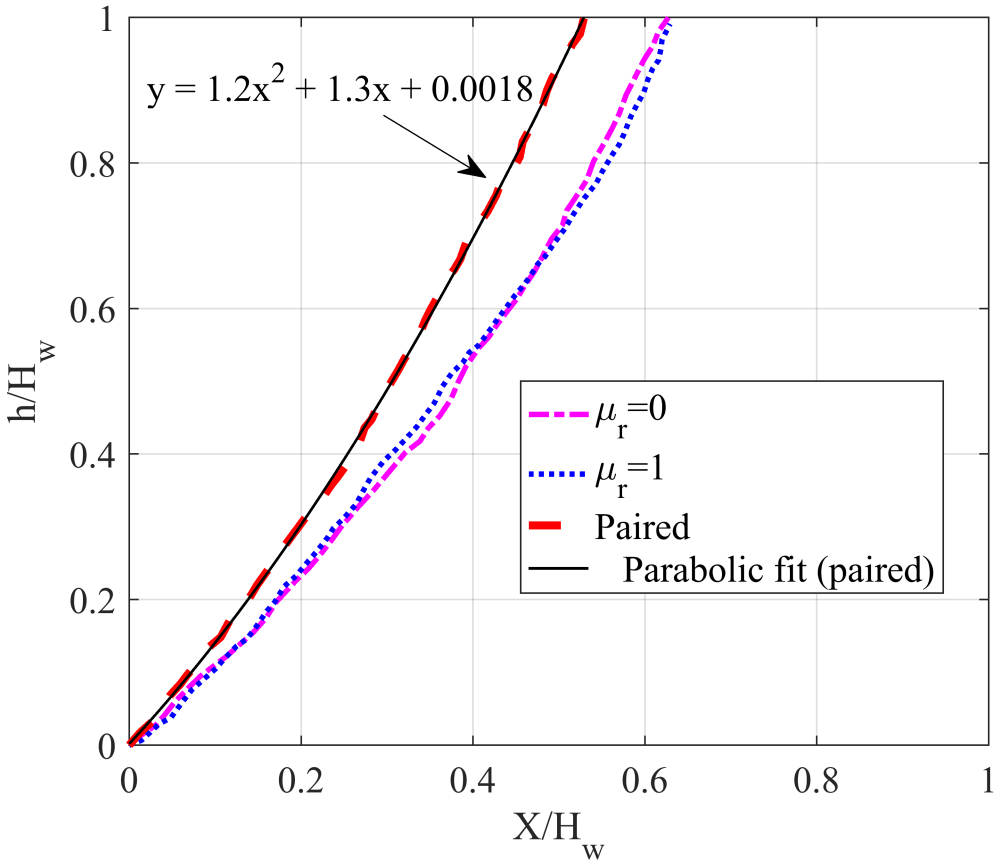

Figure 5.22 Quantitative comparison of failure surfaces.

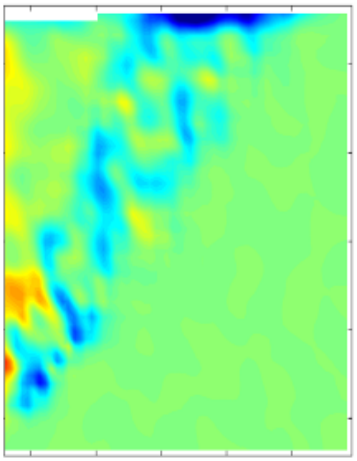

(a)

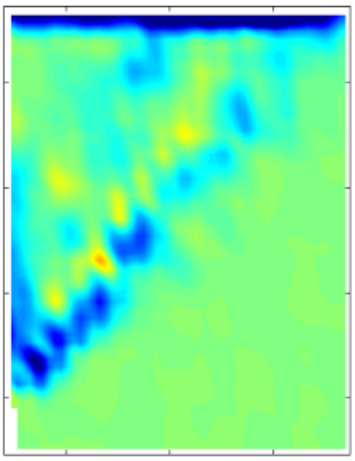

(b)

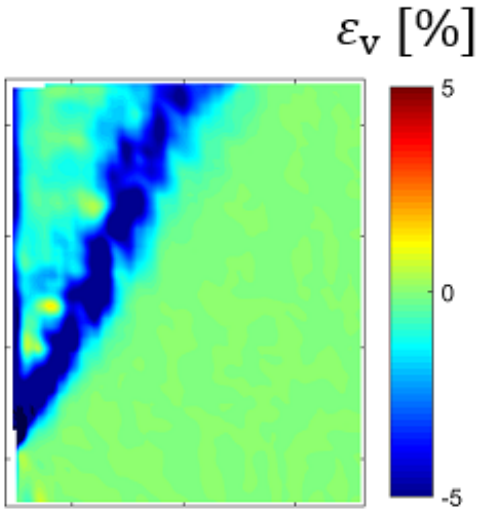

(c)

Figure 5.23 Hybrid PIV-DEM volumetric strain measurement results (at S/H_w=0.016) a) μ_r=0 b) μ_r=1 c) paired.

Chapter 6

Experimental and numerical study of flow under high gravity condition [1]

To characterize the considered granular materials and also to validate the numerical observations, it is essential to conduct experimental studies. Similar to the previous chapters, the main factor that will be investigated here is the particle shape. The first part of this chapter will explain the tests and methodologies that are followed to study the flowing and shearing properties of the granular samples. Later, results from angle of repose, Jenike shear test and 1g silo and their dependency on particle shape will be discussed. Simultaneously, in all silo tests, the discharge of particles is recorded and analysed through image processing. However, it is known that lab-scale $1g$ silo tests suffer from boundary effects, since the stress state differs significantly from that of industrial scale silo. In this respect, a set of tests has been conducted in a silo centrifuge device (with both flat-bottom and a wedge shape hopper), which is capable of increasing the acceleration up to 100 times. The obtained results from four types of material (with various particle shapes) will be compared to Beverloo's equation, which suggests that the outflow of granular materials at higher gravity is proportional to square root of gravity ratio. Finally, the micro-scale behaviour of the granular assembly, in the presence of higher gravities, will be assessed through conducting DEM analyses.

[1] Results of this chapter are partially presented in:
Soltanbeigi, B., Papanicolopulos, S.A., Zetzener, H., Ooi, J.Y. and Kwade, A., "Experimental study of particle shape effect on flow characteristics of granular materials" 1st International Conference of the Greek Society of Experimental Mechanics of Materials, Athens, Greece, May 2018.

6.1 Methods and instrumentations

6.1.1 Angle of repose test

Among various calibration tests, angle of repose (AoR) is considered as a quick, cheap and relatively reliable test. The test provides an understanding about the maximum stable slope that material can form, see Figure 6.1. Accordingly, it is regarded as an indication of the internal friction angle for the material.

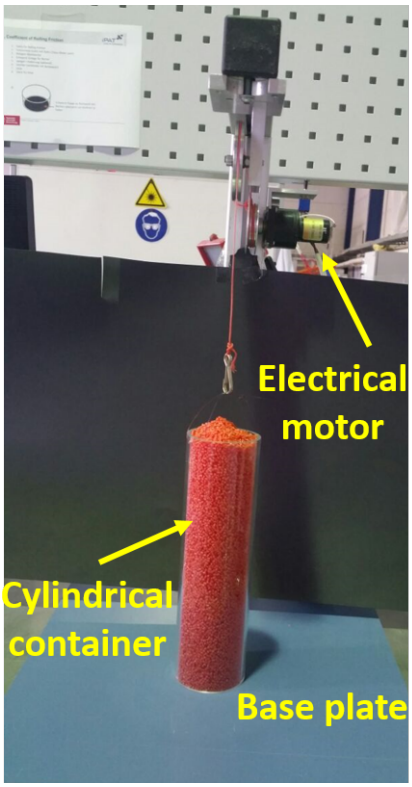

(a)

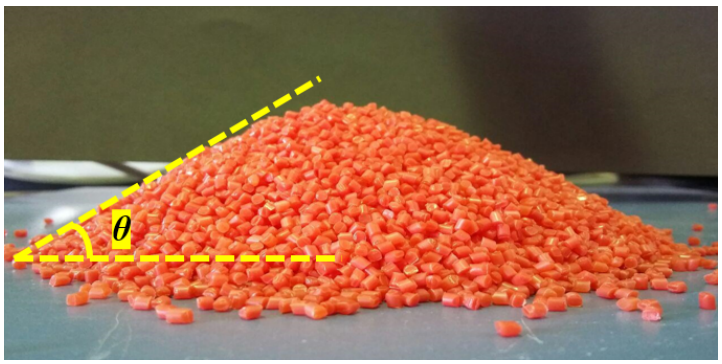

(b)

Figure 6.1 Angle of repose a) test set-up b) pile formation and AoR measurement.

The angle of repose is a function of the material properties (such as: shape, surface morphology, size distribution and existence of cohesion), and it is also sensitive to the

boundary conditions (e.g. surface roughness of the base plate, geometry of the base plate, speed of container movement or height of discharge), for more details refer to Al-Hashemi and Al-Amoudi (2018).

The container is filled with equal volume of particles (a funnel is used for filling the container and then levelled), as shown in Figure 6.1. The container has 8 cm diameter and 30 cm height. Then, container is elevated with a constant speed until all the particles are discharged and a stable heap is formed.

6.1.2 Jenike shear test

The Jenike shear tester is a well-known apparatus for evaluating the shear strength of granular materials. According to ASTM D6128 (2006), most of the unwanted flow problems, such as ratholing, segregation and flooding, can be prevented by characterizing the bulk material through Jenike test. Here, the processes of sample preparation, test procedure and result interpretation are presented:

- *Filling and trimming:* after fixing the position of each section, the bulk solid is filled within the base, upper ring and filling mould, and particles above the filling mould are removed carefully, see Figure 6.2a.
- *Pre-consolidation:* the twisting lid is located on the levelled surface of the sample (Figure 6.2b), the hanger with desired dead-load is placed on the lid, the twisting arm is pulled down and fixed to the lid (Figure 6.2c), twisting the arm for 20 cycles *ASTM D6773-16, Standard Test Method for Bulk Solids Using Schulze Ring Shear Tester* (2016).
- *Pre-shearing:* shearing of the sample starts with the horizontal movement of the upper ring. The shearing continues up to a certain distance, where the sample reaches the steady state (see Figure 6.3 part I). Here, the shearing is stopped, the stem is moved backward until zero shear stress is reached (see Figure 6.3 part II), and the pre-consolidation load is substituted with a smaller load (i.e. usually between 80 to 20 % of the pre-consolidation load).
- *Shearing:* after substituting the vertical load, the movement of the upper ring starts and the main shearing step happens (see Figure 6.3 part III). The shearing continues up to the maximum movement capacity (i.e. 6 mm).

6.1.3 1g silo discharge

A lab-scale silo is already designed and built at the Institute for Particle Technology (iPAT), which can simulate both flat bottom and inclined (wedge-shape) hoppers (i.e.

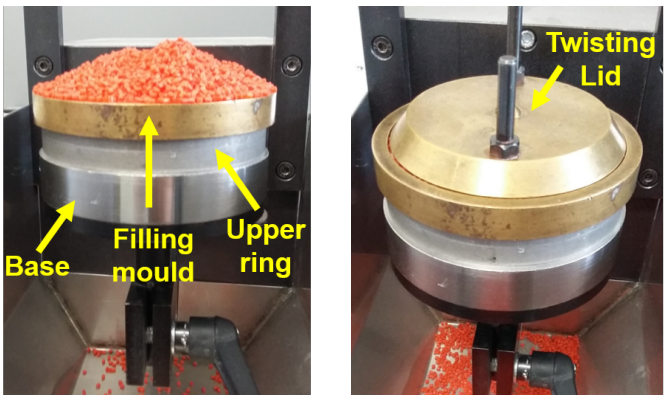

(a) (b)

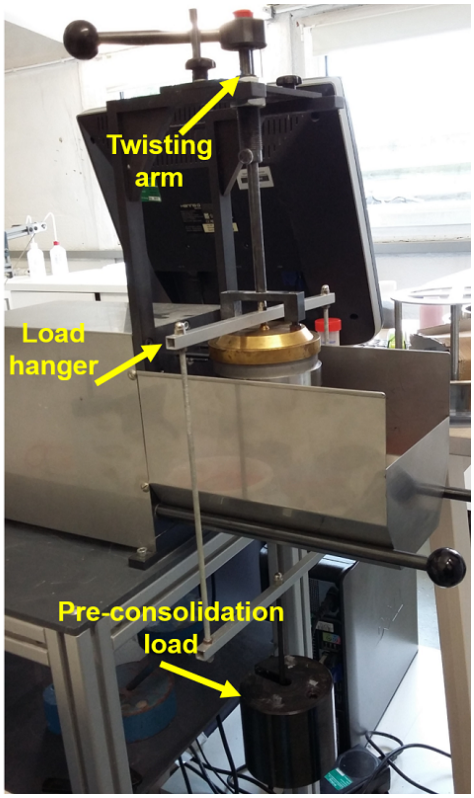

(c)

Figure 6.2 Test set-up for Jenike shear test a) filling state b) levelling and twisting lid c) consolidation state.

20° to 60° against the vertical and the outlet width from 20 to 60 mm). The built silo has transparent walls and allows the observation of the flow during discharge, see Figure 6.4. In this study we only carry out the tests in the flat-bottom case, which has an inherent funnel flow. There are various non-destructive testing methodologies that can be used to monitor the flow characteristics, among which PIV (Slominski et al., 2007) and X-ray (Grudzień et al., 2011) techniques are the most favourable.

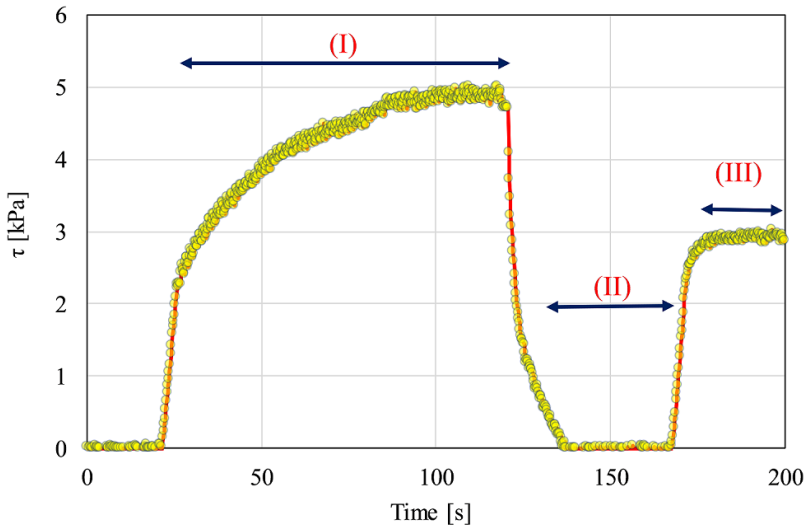

Figure 6.3 A sample of Jenike shear test result (pre-consolidation vertical pressure= 7.5 kPa, vertical pressure during shear= 4 kPa).

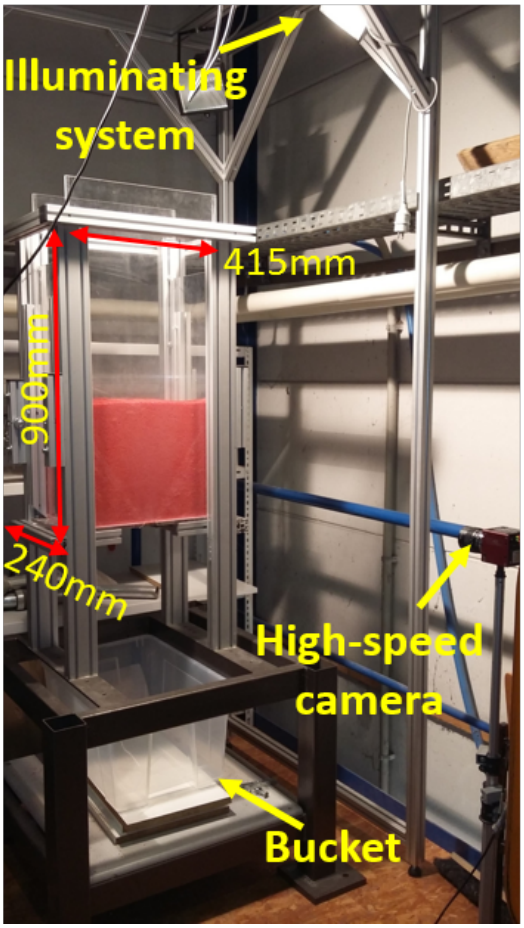

Figure 6.4 1*g* flat-bottom silo test set-up.

6.1.4 Silo centrifuge

Characterizing the flow of the granular materials under reduced scale (in laboratory) can lead to error in optimum design of the silos. The main reason for this inconsistency can be related to the difference in stress distribution between lab-scale and real silos. The higher stresses inside the silo can affect the flow characteristics of both cohesive and cohesionless particles. For cohesive bulk solids, special care must be taken to address the actual stress state, since the material strength depends highly on the consolidation stresses, see Großstück and Schwedes (2005). On the other hand, for the cohesionless material arching occurs in silos with insufficient outlet dimensions (due to particle interlocking), which might be overlooked in a small-scale silo. The simplest approach to overcome this issue is to increase outlet dimensions, but this leads to increase of stresses at the silo walls.

Figure 6.5 is a graphical description of how the silo centrifuge simulates the realistic stress state in the sample. In short, the model silo is Z times smaller than actual silo, by increasing the acceleration by Z times, the stress distribution in the model follows the realistic values. Following is the explanation on how rotation in centrifuge is converted to the acceleration:

$$\alpha = Zg = r\omega^2 \tag{6.1}$$

where, α is centrifugal acceleration, ω is angular velocity, Z is the multiple of the gravity and r is the radius (from centre of rotation to the outlet). Additionally, ω and Z are calculated as:

$$\omega = \frac{2n\pi}{60}, \tag{6.2}$$

$$Z = \frac{4rn^2\pi^2}{g60^2} \tag{6.3}$$

where, n is the number of rotations per minute. Different sections of the employed silo centrifuge are presented in Figure 6.6.

6.1.5 Image processing

Image processing can be used as a non-intrusive tool for measuring the displacements or deformations in engineering. An outstanding feature of this method is the possibility of non-contact measurement (i.e. unlike the ordinary strain gauges, which need direct contact with the material, this method makes distant detection of the displacements). Both advances in computational power, and the availability of digital high-

Figure 6.5 Graphical description of simulation realistic stress state in the model silo centrifuge.

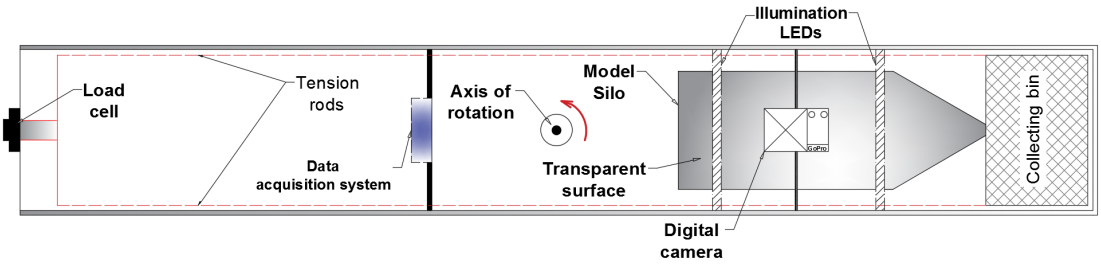

Figure 6.6 Schematic of silo centrifuge set-up.

speed cameras, have encouraged many researchers to utilize this method in various research fields.

In Geotechnical Engineering and Powder Technology fields, image processing is used for monitoring the motion of the particles. Following is two examples of different applications for this method:

In a recent study, using Particle Image Velocimetry (PIV) method, the failure surface of cohesionless backfills are determined for active state by Altunbas et al. (2017). Moreover, segregation of the particles during the discharge process is visualized and studied in detail by Combarros Garcia et al. (2016).

There exist various software for conducting the image analyses, each with different capabilities. Among these, we have used two free software PIVLab and GeoPIV. PIVLab is known as a fast and user friendly software, which provides detailed information regarding the velocity distribution, see (Thielicke, 2014; Thielicke and Stamhuis, 2014). On the other hand, GeoPIV is known best as the software which provides the strain maps (shear and volumetric), developed by (Stanier et al., 2016; White et al., 2003).

PIVLab

An overview on capabilities and functionality of the software is summarized in this section. The steps are briefly stated here:

Importing of images: Initially, the captured video must be converted to still frames and saved as images (this can be done by MATLAB). PIVLab reads the source files only if the images have certain format (e.g. .bmp, .tiff, .jpeg) and they need to be named in a sequential order.

Analysis settings: Once desired set of images are imported to the software, it is essential to apply some adjustments before running the analyses. Three steps are foreseen for this purpose *Exclusions (ROI, Mask)*: which enables the selection of the region of interest or apply a mask to the region that needs to be excluded, *Image pre-processing*: used for enhancing the quality of the analyses and user may vary contrast in this step to make the particles more distinguishable, *PIV settings*: provides two options for the

cross-correlation algorithm (i.e. the DCC (single pass direct cross correlation) and FFT window deformation (direct Fourier transform correlation with multiple passes and deforming windows)), and additionally, the size of the interrogation area (patch size) can be defined here.

Analysis: This step starts the analysis and has two options of only current frame or all frames. This process will take some time, depending on number of frames, the size of interrogation area and performance of the considered work station.

Calibration: The initial unit is the pixel/frame and it requires a calibration to obtain SI units (m/s). The frequency of recorded images must be defined her (number of frames captured per second). Additionally, based on a known distance on the image, it is possible to convert the displacement unit from pixels to m.

Data validation: There are several approaches to eliminate the wild vectors (i.e. with enormous values); the simplest way is to click on *display all frames in scatter plot* and apply an acceptance limit and remove vectors larger than this limit. Moreover, it is possible to move through the frames and manually reject the vectors that are looking larger than expected value. Additionally, there is a statistical option, in which standard deviation filter is activated.

Plot, Extraction and Statistics: These steps are referred as post-processing tools and can be used to plot: Vector field, Vorticity, U velocity, V velocity, Divergence, Streamlines and some other parameters. Another useful feature is the possibility for calculation of the mean over desired number of frames (this is necessary for applying temporal average in study of quasi-static flow conditions).

GeoPIV

GeoPIV is a widely used software mostly in Geotechnical Engineering applications. A detailed explanation of GeoPIV is provided in Section 5.4.3 and will not be discussed here.

6.2 Material properties

Best practice for this part of the study is to consider material with similar properties, where the only varying factor is shape. Nonetheless, limitations of each test constrained our choices; for instance, Jenike shear cell, with diameter of 93 mm, needs particles at least 20 times smaller (maximum diameter). An extensive material investigation lead to Aluminium Oxide that had spheres, tablets and extrudes (produced from exactly the same material). But, the available minimum length of the tablets was 5 mm, and extrudes had a length distribution of 2 to 7 mm.

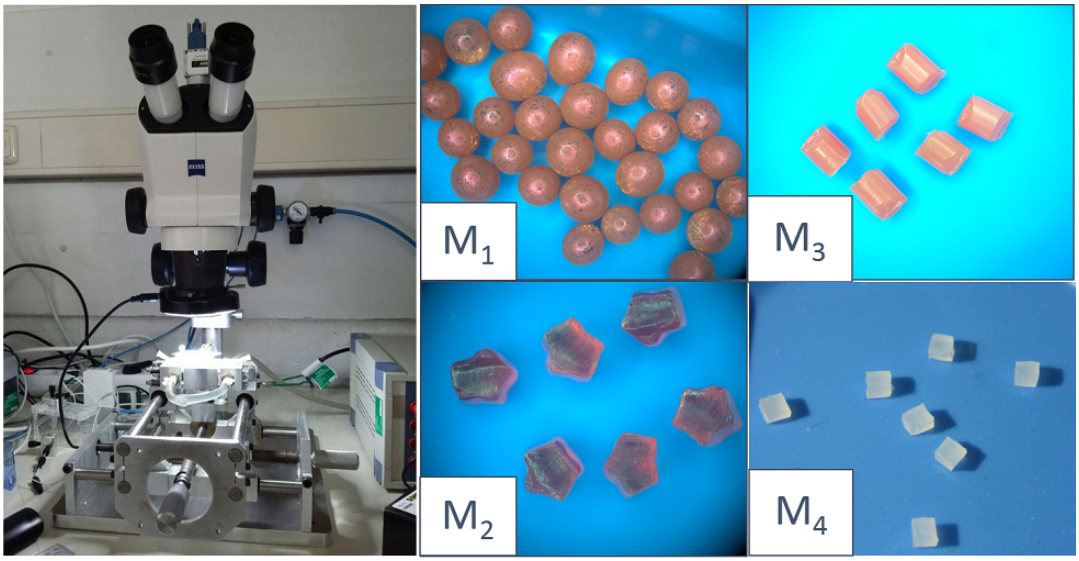

Figure 6.7 Considered material for the experiments (pictures are taken with an optical microscope).

Table 6.1 Properties of the materials used for the experimental study.

Abbreviation	Shape	Material	Size, mm	Bulk density, kg/m^3
M_1	Sphere	Sodalime-glass	2.4-2.9	1530
M_2	Pentagon	PA6 Plastic	1.5	1350
M_3	Cylinder	Polyamid	1.9-2.3	650
M_4	Cube	Polyamid	1.5	650

Tests in this chapter are conducted for 4 types of material with various particle shapes, see Figure 6.7. Properties of the materials are summarized in Table 6.1.

6.3 Results and discussion

Following sections summarize the test results of the angle of repose, Jenike shear tester, 1g flat-bottom silo and silo centrifuge.

6.3.1 Angle of repose

All the samples are prepared with equal bulk volume (i.e. the cylindrical container is filled completely and levelled). The container is then raised with a constant speed and a heap is formed. Later, using a digital camera, from a constant distance, pictures are taken from all tests. Finally, using image analyses the inclination of the heap is measured with respect to the horizontal (tests are repeated 5 times and an average value is taken). Raw images are shown in Figure 6.8, it is clear that the shape factor

influences the heap formation characteristics of the particles. M_1 has a distinct single-particle layer spread on the base plate and the heap is only made in the centre, which makes it hard to measure the exact angle of repose. The steepest slants are formed for M_4. The quantified results for the measured values of AoR are summarized in Figure 6.9. Results confirm that interlocking is highly contributing to the avalanching properties of granular material.

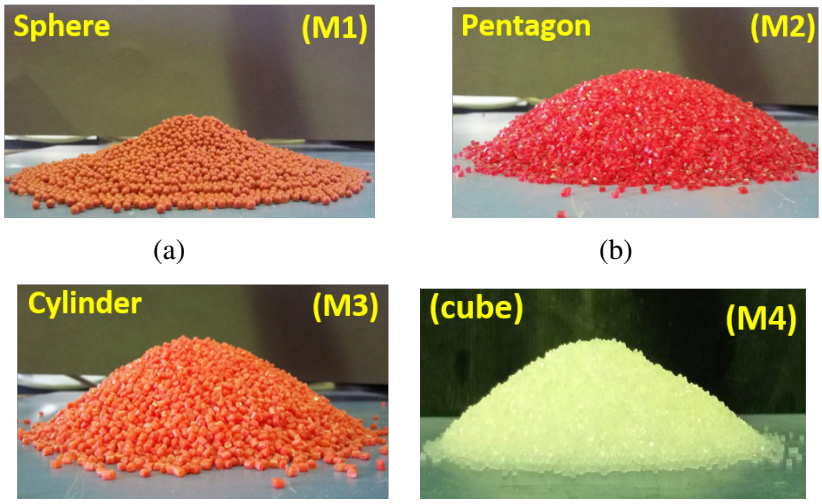

Figure 6.8 Heap formation for the considered four type of granular materials.

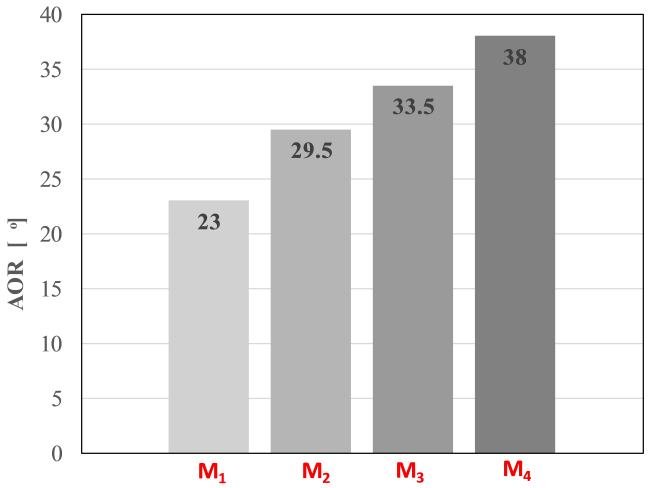

Figure 6.9 Measured values of AoR for the considered materials.

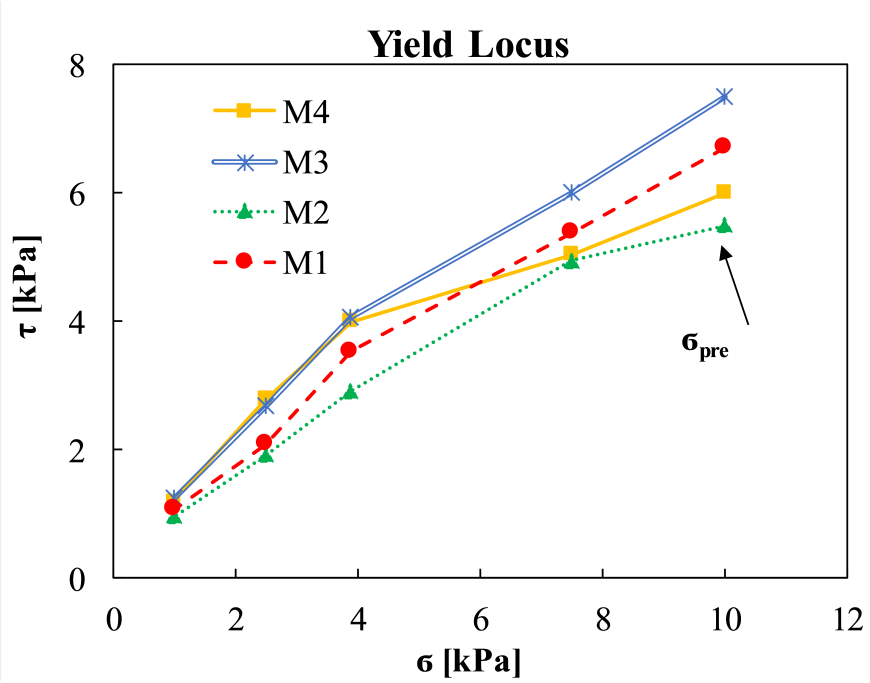

Figure 6.10 Results of Jenike shear test.

6.3.2 Jenike shear test

Similar to the conducted DEM simulations, the dependence of material shear strength on shape characteristics is evaluated in the Jenike shear cell. Results in Figure 6.10 are obtained within a similar testing condition; samples are prepared with air-pluviation technique, pre-consolidation is applied at 10kPa to all samples, shearing is followed with different vertical pressures.

Results indicate that particle shape is affecting the shearing response, however, influence of shape parameter is not following the same trend as AoR test. This might be justified due to the limitations that were faced during material selection (as discussed in Section 6.2). In other words, the varying parameter is not only the shape of particles and this affects the conclusions here. It is seen from results that M_3, instead of M_4, yield the highest shear strength, which can be due to higher aspect ratio of the particles (i.e. M_4 has unity aspect ratio, while M_3 particles have 1.2 aspect ratio).

6.3.3 1g silo (flat-bottom)

A set of preliminary tests have been conducted to determine the importance of the particle shape in governing the discharge process. The obtained images are analysed through GeoPIV and a set of typical results are shown in Figure 6.11.

Accordingly, the flow characteristics for M_1 and M_3 are compared in this section. Figure 6.12a presents displacement vector fields for the two materials at 10 % of the

discharge. There is a clear distinction between both materials in developing flow channels, where M_1 is having a wider channel compared to M_3. Moreover, particles from near the walls (near the surface) are contributing to the flow of M_1, while M_3 particles are only discharging along the height of the channel and a larger stagnant zone emerges. This is due to higher interlocking among M_3 particles, which hinders the motion of the particles and leads to creation of an unstable rathole. Additionally, the repose angle at the end of the discharge process has been compared in Figure 6.12b, which provide similar observation to that in angle of repose test. A quantitative comparison between the flow profiles of the considered particles suggests that flow boundaries are direct function of the particle shape, as shown in Figure 6.12c.

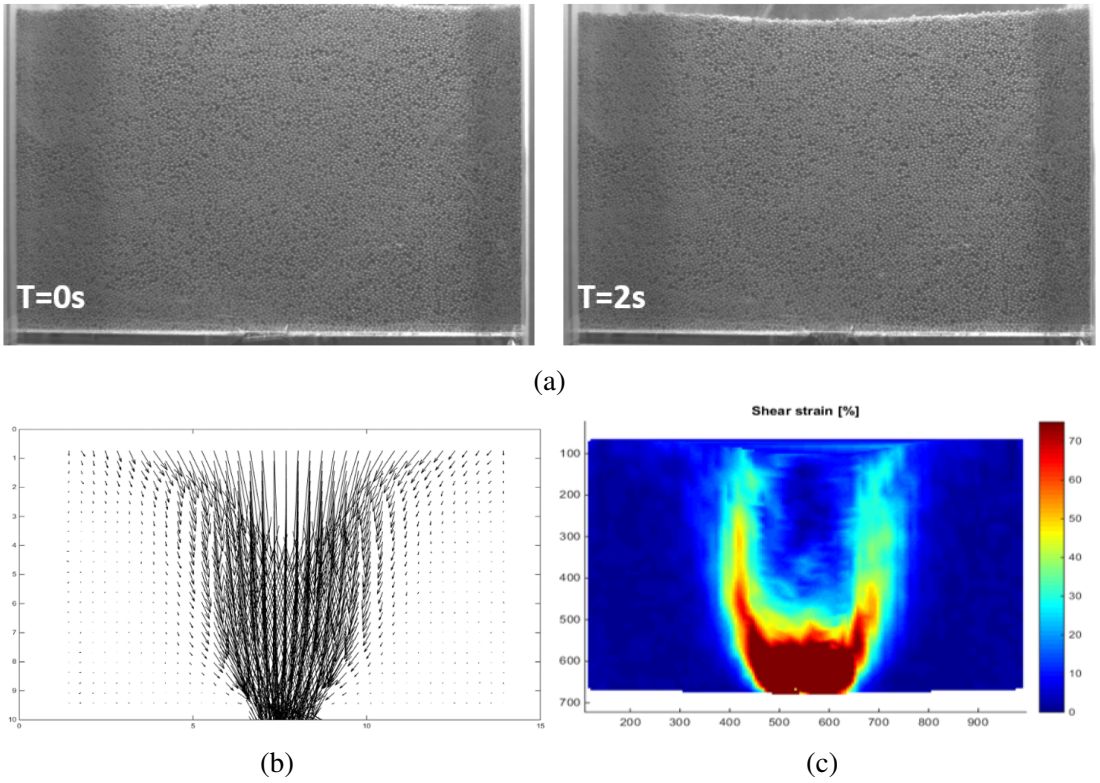

Figure 6.11 Image processing procedure (using GeoPIV) on discharge process a) raw images at two instances of discharge b) resulting displacement vector filled c) resulting shear strain map (results are for M_1).

6.3.4 Silo centrifuge

The available silo centrifuge at Technische Universität Braunschweig is used to better understand the flow characteristics of the granular materials under higher stress conditions. This experimental set-up was uniquely designed almost 20 years ago, to scale-up the stress state in the sample and simulate a realistic testing condition (similar to that of industrial-size silos). The initial applicability of the available silo centrifuge was

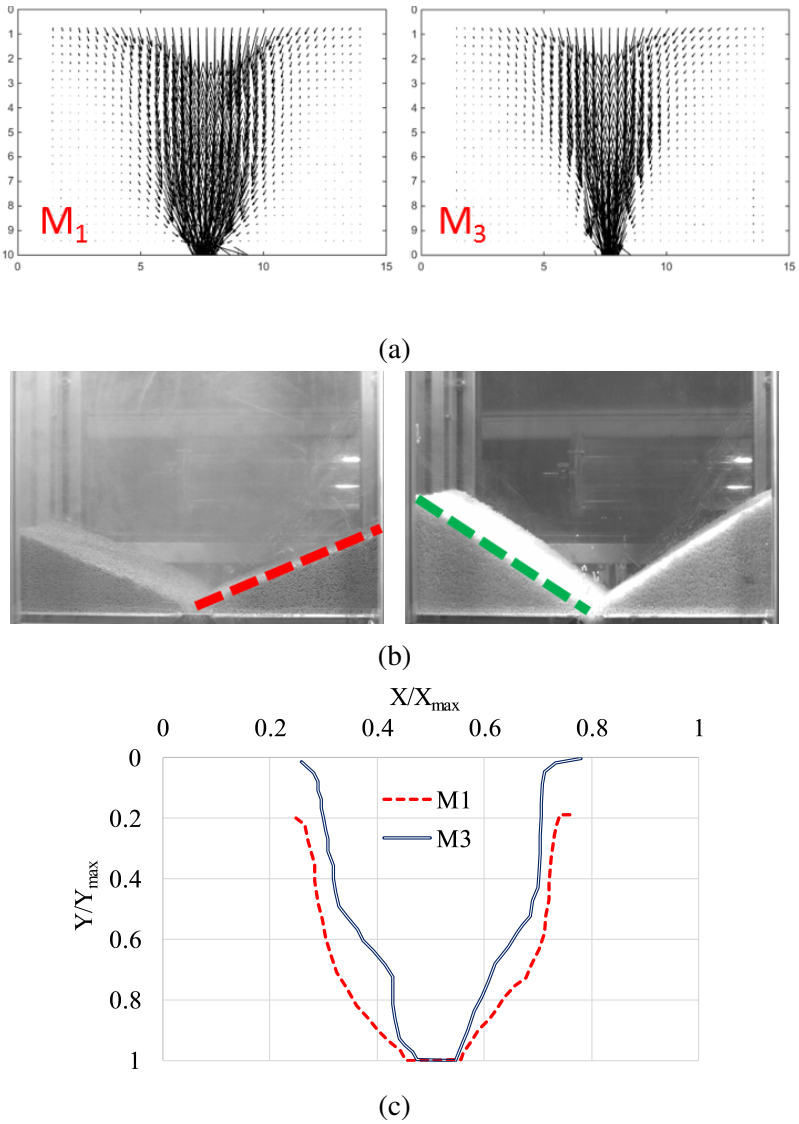

Figure 6.12 Comparison of flow characteristics for particles with different shapes (M_1 and M_3) a) Displacement vector field b) end of discharge and repose angle c) extraction of flow profiles and quantitative comparison.

limited to the study of cohesive powders. However, the initial intention (during this PhD project) was to change some parts of the silo and make it possible to visualise the out-flow of cohesionless material. Accordingly, the first step was to re-design the transparent silo. Next, a considerable time was allocated for selection, calibration and execution of an affordable high-speed camera which could satisfy demanding testing conditions (i.e. being safe to use in high accelerations, having a light weight, supporting wireless recording). The initial results did not meet the expected standards which led to fitting an illumination system for improved visualization of the results (see Figure 6.13). The same limitations for selection of the appropriate camera was

also present for the lightening system, since the accelerations were going up to 50 times the gravitational force on Earth.

Successively, possibility of predicting the mass flow rate and flow profiles under higher gravity levels are investigated for different shape particles. A set of tests has been conducted using the silo centrifuge and results are presented in this section. The device is utilized with a load-cell, which measures the discharge of particles over time (as shown in Figure 6.6, the discharged material is collected in a bin that is connected to the load-cell). Two types of geometry are utilized for the model silo, namely a flat-bottom and a wedge shaped hopper (in which inclined sides make 15° with vertical). Following is the summary of the experimental observations:

Wedge shape hopper: Tests are conducted with three types of materials at three different gravitational acceleration levels (15, 30 and 40g). For each test the cumulative mass discharge is calculated and plotted in Figure 6.14. Results show the change in cumulative mass discharge as a function of increased acceleration (the higher the acceleration, the steeper the cumulative mass discharge, which indicates higher mass discharge rate).

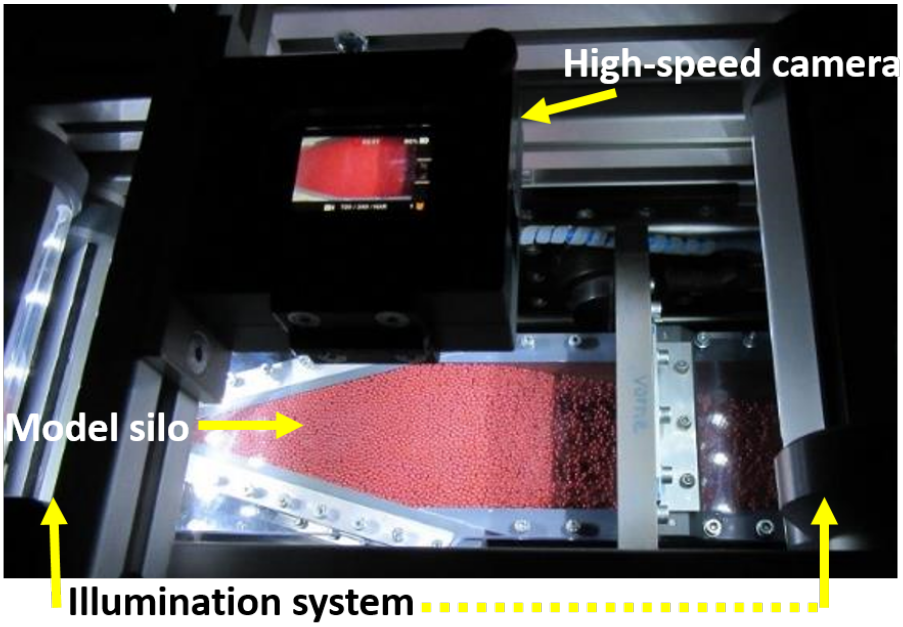

Figure 6.13 Test set-up for the Silo centrifuge (presenting model silo with inclined hopper, high-speed camera and illumination system).

Additionally, the image processing technique allows detection of the motion of particles along the transparent surface. As the first characterizing step, using PIVLab, the velocity of the discharging particles is obtained for the considered materials at 1g. Figure 6.15 presents the spatial distribution of velocity (toward the opening). It is seen that M_1 (with spherical particles) shows slower zones near the walls, whereas, M_2 and

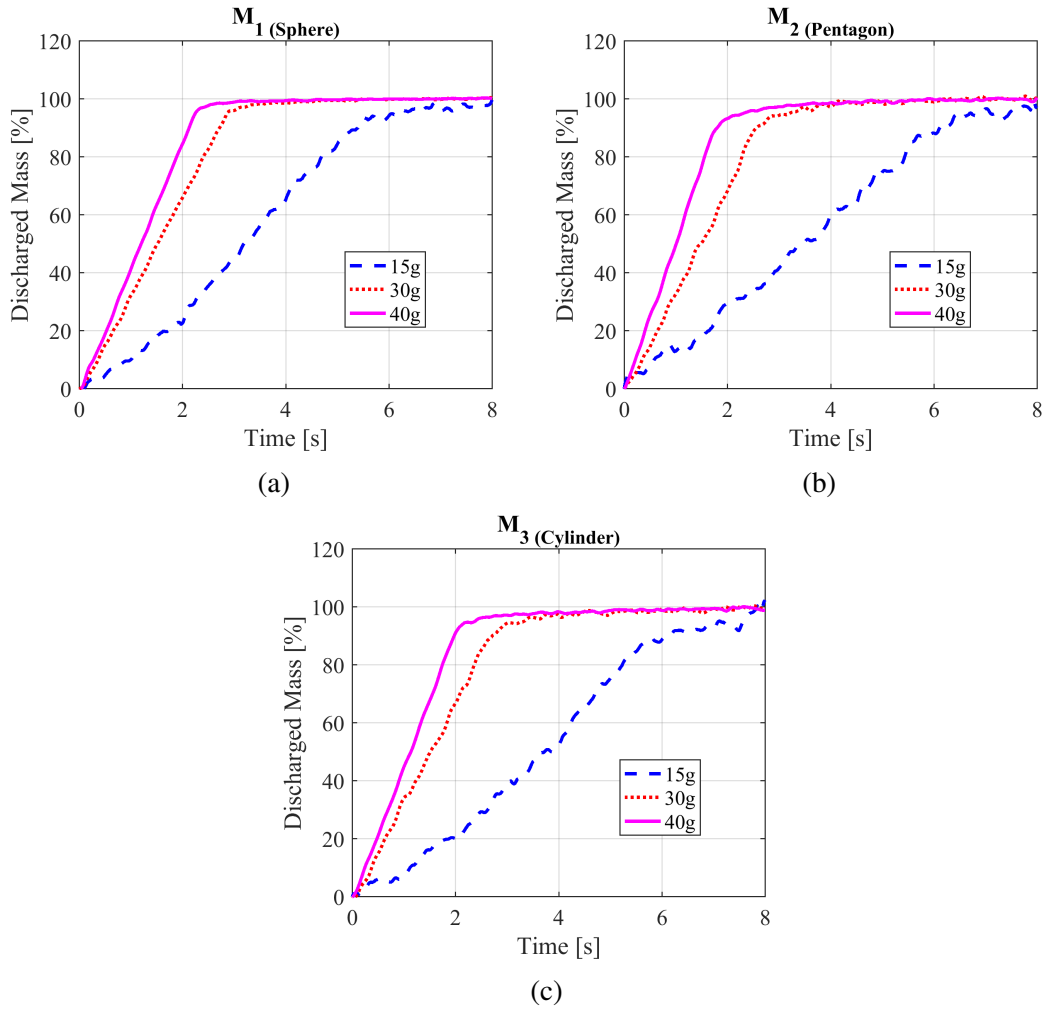

Figure 6.14 Cumulative mass discharge over time at different gravitational accelerations (for wedge shape hopper) a) for M_1 b) for M_2 c) for M_3.

M_3 are less affected by the boundary effect and present mass flow. A possible explanation for this issue is that the surface coating of the spherical particles is affecting the flow characteristic (at the end of each test some of the coated material was remaining on the silo walls and collecting bin).

Moreover, two cross-sections have been defined at two different heights of the model silo and velocity distributions are quantitatively compared (both V and U components), see Figures 6.16 and 6.17. Clearly, in case of V component, M_1 present a large variation from the boundaries toward the centre of the silo (contrary to M_2 and M_3). Additionally, at height H_1 (intersection of the hopper with vertical section), M_1 has the highest velocities at the centre of silo (as a result of the least interlocking). The U component, on the other hand, does not vary much for the studied materials. As shown in Figure 6.17, the horizontal velocity varies between a positive and negative value (moving along width of the silo, from left to right). This is due to the fact that

while discharging, all the particles tend to move toward the centre of the silo. Thus, particles moving from left side of the silo toward the centre have positive velocity sign. Whereas, particles moving from right side of the silo toward the centre have negative velocity sign.

Flat-bottom silo: An attempt has been made to design a small-scale flat-bottom silo, which is then fitted into the silo centrifuge device, see Figure 6.18. A flat-bottom silo has an inherent funnel flow, thus it is important to study the evolution of dead-zone formation and their dependency on the stress state. It is worth mentioning that at this stage of the tests, M_2 particles are replaced with M_4 (which has similar material to M_3).

The discharge rate of particles from the flat-bottom silo, at 30 and 45g, is recorded and reported in Figure 6.19. The results suggest that M_4 type of particles provide the slowest outflow, which can be an indication of the higher degree of interlocking among particles (this is in line with AoR results). Additionally, using PIV analyses, velocity profiles of the particles are quantified and further studied. Accordingly, the velocity distribution along the width of the silo is obtained at two different cross-sections (CS), where the first one is located at $H/3$ from bottom of the silo ($CS1 = H/3$), and the second is at mid height ($CS2 = H/2$). The velocity distribution at 1g are representing 10% of the total discharge (results are time averaged over 25 frames or 0.5s). In the case of the outward velocity it can be seen that M_4 has the lowest velocity values, which is in agreement with discharge rate results (in both CS1 and CS2), see Figure 6.20. The horizontal velocity of the discharged particles is evaluated in Figure 6.21. In this case, it is seen that at CS1 spherical particles have the largest velocity variation along the width of the silo (indication of lower inter-particle interlocking). At CS2 all particles present mass flow.

Beverloo's equation (applicability for various gravity levels)

Beverloo's correlation, which is used for the prediction of the discharge rate (W), suggests that the increase in mass discharge rate between two identical silos (at different gravities, as g_1 and g_2) can be calculated by considering Equation 2.8, as follows:

$$\frac{W_1}{W_2} = \sqrt{\frac{g_1}{g_2}} \tag{6.4}$$

In other words, the mass discharge rate ratio, at any value of the acceleration, is proportional to square root of the gravity ratio. The validity of this approach is investigated, by considering the mass discharge rate at two different g levels, for the tested materials.

Additionally, the dependency of flow profiles on the gravitational acceleration is still not completely addressed in the literature. Work from Mathews and Wu (2016)

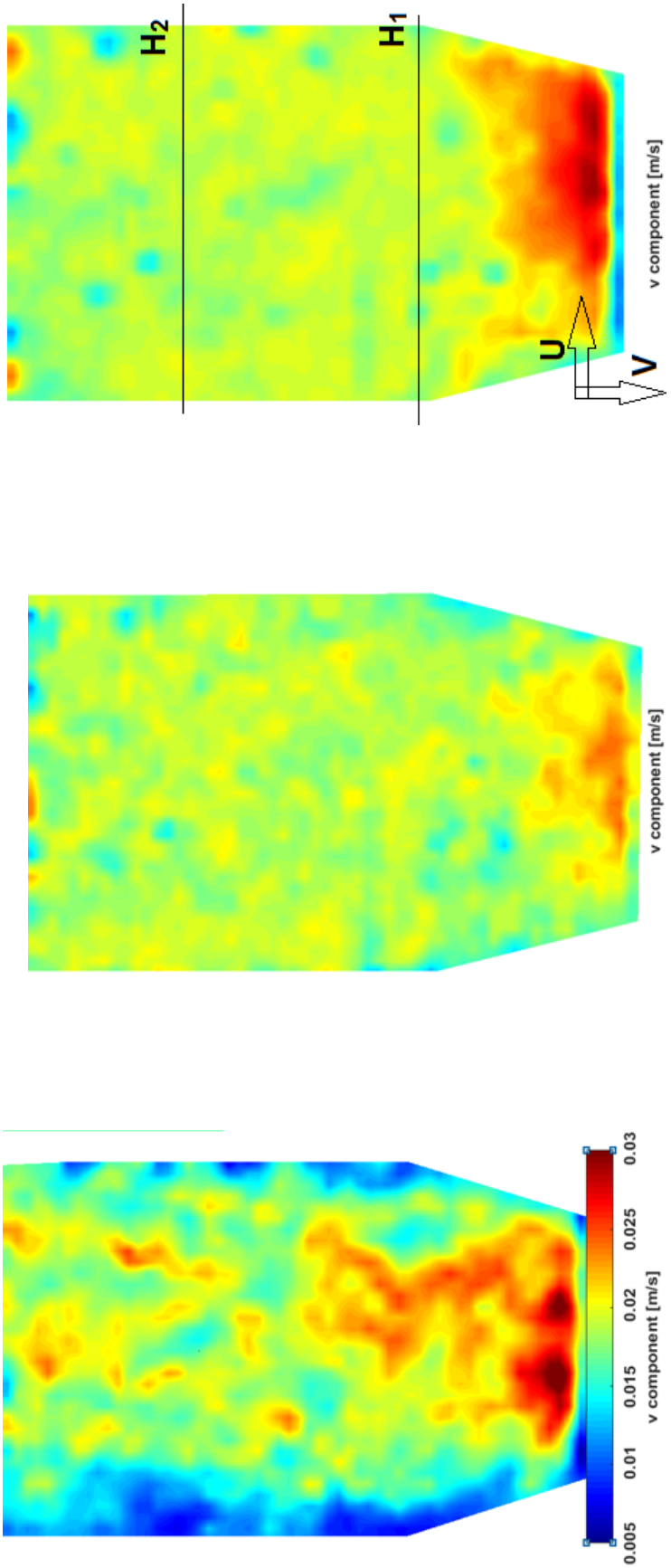

Figure 6.15 Spatial distribution of velocity (V component) at 10 % of discharge for the considered materials (for wedge shape hopper), from left to right M_1, M_2 and M_3.

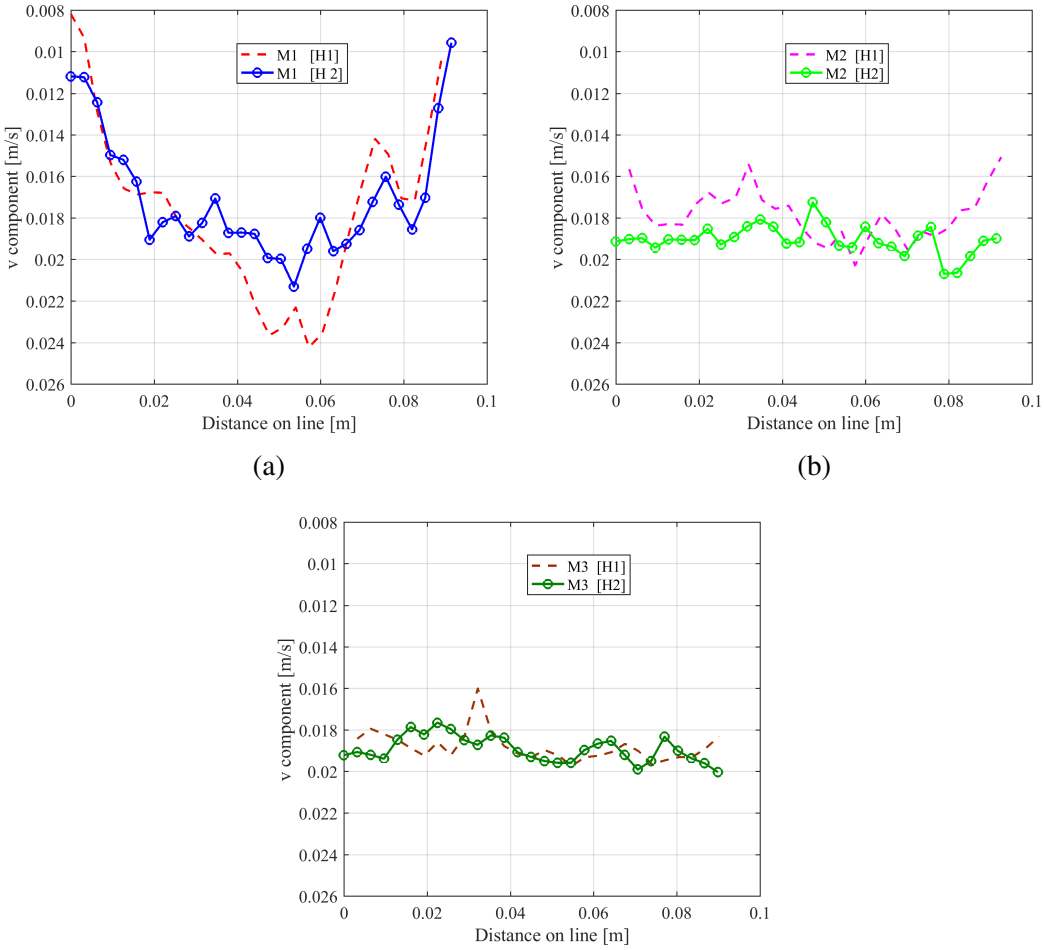

Figure 6.16 Cross-sections at two different heights (H_1 and H_2) for V component (outward) of the velocity distribution (for wedge shape hopper) a) for M_1 b)for M_2 c) for M_3.

can be considered as the only recent study that has visualised flow profiles. However, summary of their work leaves many unanswered questions regarding predictability of the flow profiles in high g conditions. Their observation suggests that the transition height is independent of the gravity. Additionally, it is mentioned that the vertical and horizontal components of velocity often have an asymmetric distribution (about the silo's vertical axis), however, the reason is unknown for this. Therefore, an effort has been made to revisit this issue both experimentally and by means of DEM.

Wedge shaped hopper: In Figure 6.22, the square root of gravity ratio is displayed for all the considered materials and compared with the ratio of mass flow rates. Results suggest that only in case of spheres (after discharge reaches to steady state) Beverloo's prediction holds true. For M_2 and M_3 (with irregular shapes) Beverloo's prediction is not leading to a precise mass flow rate ratio. Dorbolo et al. (2013), conducting silo

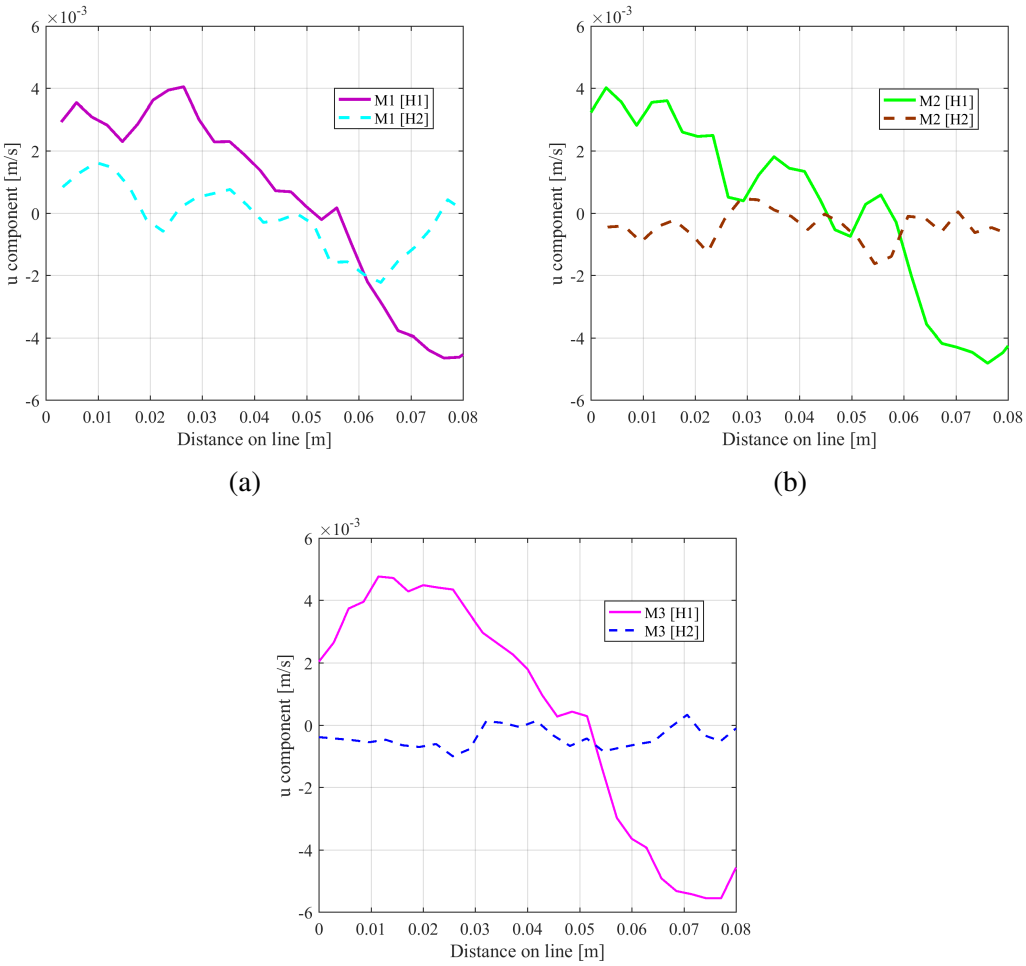

Figure 6.17 Cross-sections at two different heights (H_1 and H_2) for U component of the velocity distribution a) for M_1 b)for M_2 c) for M_3.

centrifuge tests, confirmed the applicability of Beverloo's approach for spherical particles. Furthermore, observing the discharge of sand particles at different gravity levels, Mathews and Wu (2016) concluded that for a 30° hopper, the discrepancy between recorded and predicted discharge rates is not proportional to the gravity. However, Mathews and Wu (2016) reported that for spherical glass beads the predicted results are in good agreement with the measured values.

Using PIVLab, it is possible to compare the velocity distribution of the particles within different gravity levels. Thus, the distribution of velocity at different g levels are obtained for three types of materials. Since variation of the horizontal velocity was very small, the magnitude of velocity vector is considered here. Moreover, the velocities for the higher g cases are normalized by the square root of the gravity ratio. Figure 6.23 shows histogram graphs, which present the frequency of particles discharging with various velocities over the whole silo. It is seen that M_1 (with spherical parti-

Figure 6.18 Test set-up for the flat-bottom silo.

cles) has the widest velocity distribution at $1g$ among all materials. For M_1, on the other hand, the normalized velocities are approximately following the velocities at $1g$. In contrast, for M_2 and M_3, the normalized velocities are larger than the velocities at $1g$. Mathews and Wu (2016) made a similar observation for the spherical particles, in which the normalized velocities of the higher g cases are almost overlapping the velocities of the $1g$ case.

Nonetheless, it is clear that, for all materials, the normalized velocities for 30 and 40g are almost equal. This observations is also reported by Mathews and Wu (2016), where it is shown that normalizing vertical and horizontal velocity components (by square root of gravity multiplied by width of the silo outlet), for higher g cases, provides approximately overlapping results, but they are not following the results for 1g.

Flat-bottom silo: Similar to the previous section (study of flow in inclined hopper), the mass discharge rate of the considered materials is monitored from a flat-bottom silo. It is seen in Figure 6.24 that Beverloo's prediction is underestimating the ratio of mass flow rate for two different tests with different accelerations. Nonetheless, among the three material types, M_1 with spherical particles provide the closest agreement with that of Beverloo's approach (this is seen also in case of the inclined hopper). Observing the

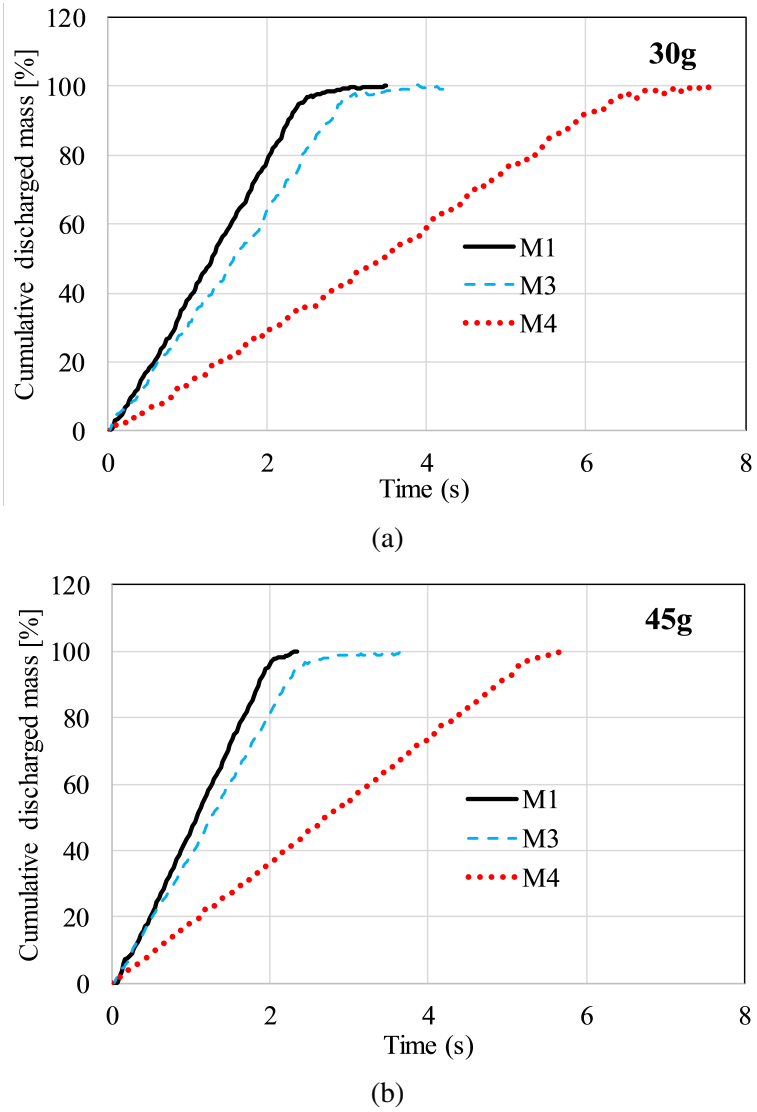

Figure 6.19 Cumulative mass discharged over time at different gravitational accelerations for flat-bottom silo (for M_1, M_3 and M_4) a) 30g b) 45g.

discharge of sand particles at different gravity levels in a flat bottom silo, Mathews and Wu (2016) stated that the Beverloo's discharge rate is applicable (i.e. more accurate) when the applied gravities are low.

Furthermore, the velocity distribution of the conducted tests has been obtained through PIV analysis. This way, the validity of the Beverloo's approach in predicting velocity profiles, inside a flat-bottom silo, has been investigated. The velocity distribution is obtained along two different cross-sections through the width of the silo. This enables the evaluation of the formed dead zones at different gravity levels. Here, the two cases that are compared consists of 1g and 30g tests, where the case with higher acceleration is normalized by the square root of gravity ratio. Results at $CS1$ in Figure 6.25 show: a) M_1 is well predicted at both sides of the flow channel, whereas there

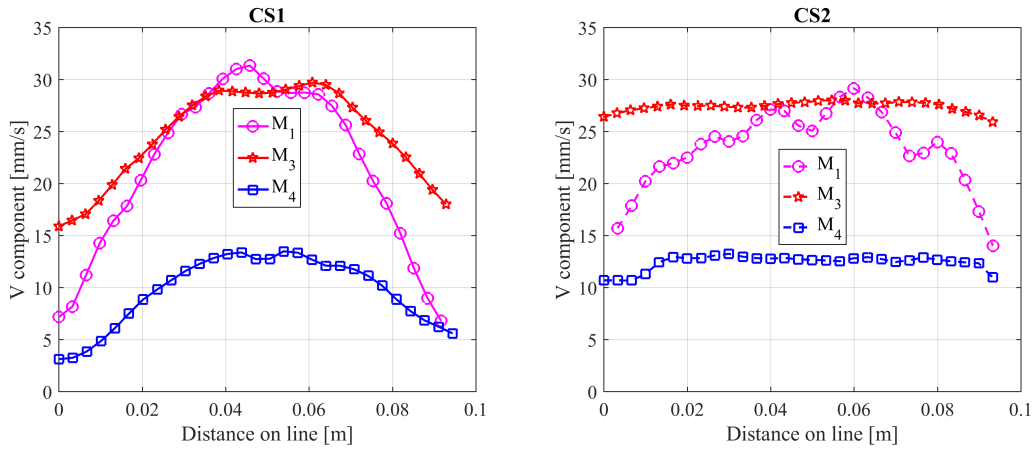

Figure 6.20 Distribution of the outward velocity at 1g along cross-sections at two different heights (for flat-bottom silo) a) CS1 (at H/3 from bottom) b) CS2 (mid-height of silo).

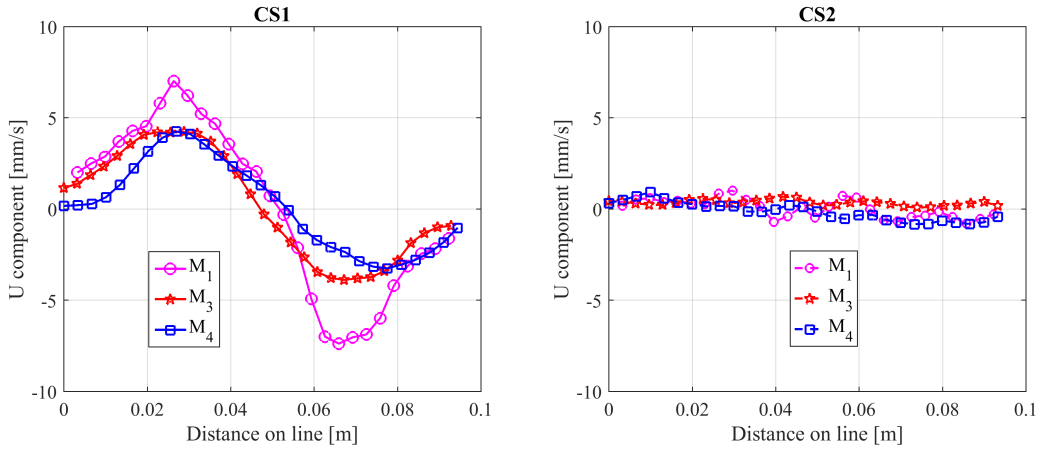

Figure 6.21 Distribution of horizontal velocity at 1g along cross-sections at two different heights (for flat-bottom silo) a) CS1 (at H/3 from bottom) b) CS2 (mid-height of silo).

is a discrepancy in the flow channel itself (normalized case is slower) b) both M_3 and M_4 built a stable dead-zone in higher gravities and normalized values are well below the velocities at 1g. At *CS*2, on the other hand, it is seen that: a) results for spherical particles at 1g are in agreement to some extent with the predicted values, b) for M_3 and M_4, at increased acceleration, the dead-zone is further developed and changed the mass flow zone at 1g case to a funnel flow. Mathews and Wu (2016) observed a similar discrepancy in velocity distribution between the normalized and 1g case.

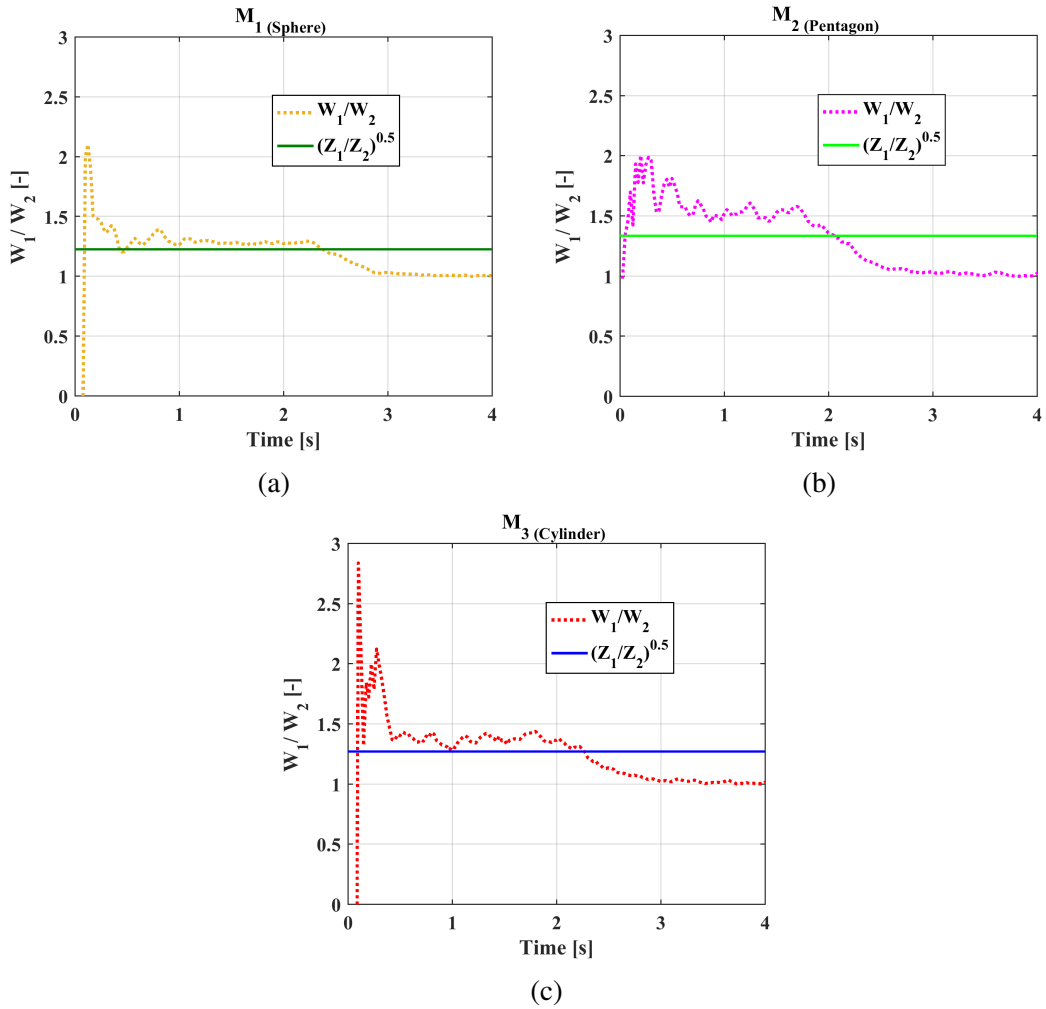

Figure 6.22 Comparison of predicted results by Beverloo's approach and normalized mass discharge rate over time for wedge shape hopper (ratio of mass flow rate (W) for two different gravitational accelerations as $30g$ and $40g$) a) for M_1 b) for M_2 c) for M_3.

6.3.5 DEM simulations

Experimental results indicate that there are still uncertainties regarding predictability of flow characteristics in the presence of higher gravitational accelerations (particularly for non-spherical particles). Accordingly, a set of DEM simulations has been conducted to verify the experimental observations and investigate the problem at micro-scale (all material and particle properties are identical to Chapter 4).

The first step in DEM simulations was to determine the differences between the procedures that provide increased g levels. The first approach applies the gravity numerically to all particles, where the second approach (similar to the experimental approach) rotates the whole granular system with respect to a certain axis (with r distance from the opening) and increases the acceleration. The rotational speed of the system is

assigned so that the resultant gravitation acceleration equals to the numerical increase of g (i.e. 200rpm equals to 30g and 335rpm equals to 50g).

Results in Figure 6.27, for both particle shapes (spherical and cubical particles MS(27)), suggest that both approaches provide a similar cumulative discharge over time (there is a very small underestimation in the rotated case). For simulations hereafter, the method with increasing the gravity numerically for each particle is considered.

Next, the influence of particle shape factor is evaluated at different g conditions. Mass flow rate for spherical and cubical particles are compared for $1g$ and $50g$. Results for $50g$ are normalized both in terms of time and mass flow rate. Normalization is conducted by dividing mass flow rate with square root of gravity and multiplying time by square root of gravity.

Flat-bottom silo: In case of spherical particles (6.28a), results for mass flow rate are almost overlapping (small deviation can be related to the difference in initial packing density of the samples). For cubic particles, however, there is a inconsistency between two cases up to half of discharge time (normalized data are over-predicting).

The cumulative discharged mass is also provided for all tests, and shown in Figure 6.29. For the spherical particles results at $1g$ are overlapping with that of normalized values. In contrast, for MS(27) normalized values at $50g$ are deviating from results in $1g$.

The velocity distribution is also evaluated for the considered particles. The width and height of the silo are divided to equal volumes (cube bins), in which downward velocity of the particles are averaged over this volume. Additionally, result are averaged over 5 % of discharge to reduce the temporal fluctuations (temporal average). To consider change in flow profiles, seven cross-sections have been chosen and results are shown in Figures 6.31 and 6.32.

It is seen from Figure 6.31a that, velocity of the spherical particles near the boundaries and outlet are deviating (indication of a larger dead-zone for normalized case). Meanwhile, Figure 6.31b shows that from mid height of the silo towards free surface (above H=0.105m), where there is mass flow, normalization provides overlapping results to a high extent. This is in-line with the experimental observations in Figure 6.26a.

For MS(27) particles, the asymmetric flow is observable in Figure 6.32a. Moreover, similar to the spherical particles, lower values of normalized velocity suggest the existence of larger dead-zones. The inconsistency between the two cases is seen even above the mid-height of the silo, which indicates development of a dead-zone nearly up to the free surface. This is following the experimental observations for both M_3 and M_4 in Figures 6.26b and 6.26c.

Results suggest that change in velocity profiles are not proportional to the square root of gravity and further assessments are required. Additionally, while studying this issue, particles with non-spherical shapes must be treated different to that of spherical particles.

Wedge shape hopper: A similar hopper to that of experimental set-up is simulated and the discharge of both spherical and non-spherical particles is evaluated (comparison is only carried out for the mass flow rate). Following the previous sections, the results at higher accelerations are normalized by the square root of gravity ratio. Results in 6.33 suggest that in case of an inclined hopper, Beverloo's prediction is well overlapping with results at 1g (both in case of mass flow rate and cumulative discharged mass).

6.4 Summary

An important factor that governs the interaction of individual particles is the shape complexity. In this regard, this chapter considered a set of experiments to characterize the influence of shape on the bulk response of granular assemblies (DEM simulation are also conducted only for studying the flow properties during high g conditions).

Initially, heap formation characteristics of the considered materials have been investigated. Results indicate that M_4 with cube shape, has the highest degree of interlocking, which led to highest angle of repose. Results from the Jenike shear cell are also affected by shape factor, however they are not following AoR results, which indicates that influence of shape parameter is also problem dependent.

Flow properties of the particles with different shapes are assessed within a $1g$ flat-bottom silo. It is seen that flow profiles are highly dependent on the shape factor and particles with higher interlocking develop a flow channel up to the free surface of the packing, which is in agreement with DEM results observed in Chapters 3 and 4.

Further studies have been done on flow characteristics of the considered materials in the presence of higher gravitational accelerations. Using a load-cell, out-flow of the particles was measured over time. The obtained results depicted the change in mass discharge rate as function of particle shape irregularity (lower mass discharge rate is resulted). Moreover, Beverloo's theory seems to provide a good approximation for the mass flow rate for increased gravities only in case of spherical particles (this is a mutual observation for both flat-bottom and wedge shape hopper). Both in experimental and numerical results, normalized velocity profiles (with square root of gravity) is relatively following the results at 1g. This is not holding true in case of non-spherical particles (at both silo geometries), where normalization always leads to underestimated velocity profiles (compared to that of spherical particles).

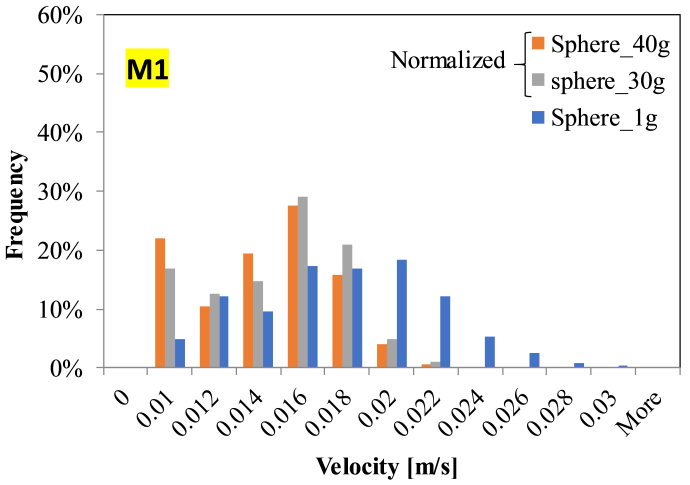

(a)

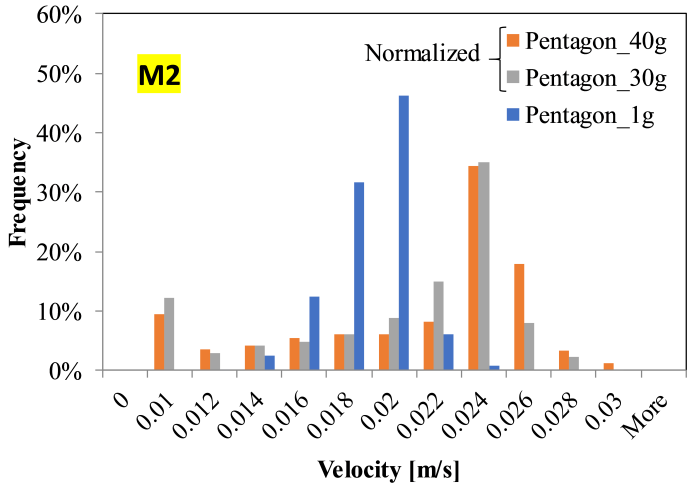

(b)

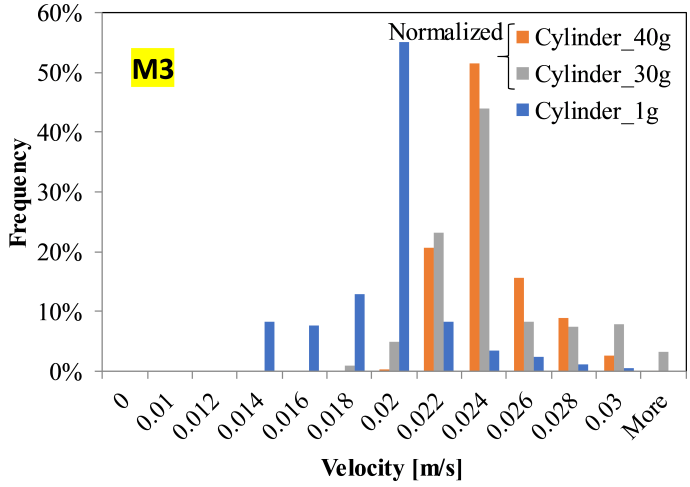

(c)

Figure 6.23 Histogram representation for magnitude of velocity distribution for wedge shape hopper (except for 1g case, all results are normalized by square root of gravity) a) for M_1 b)for M_2 c) for M_3.

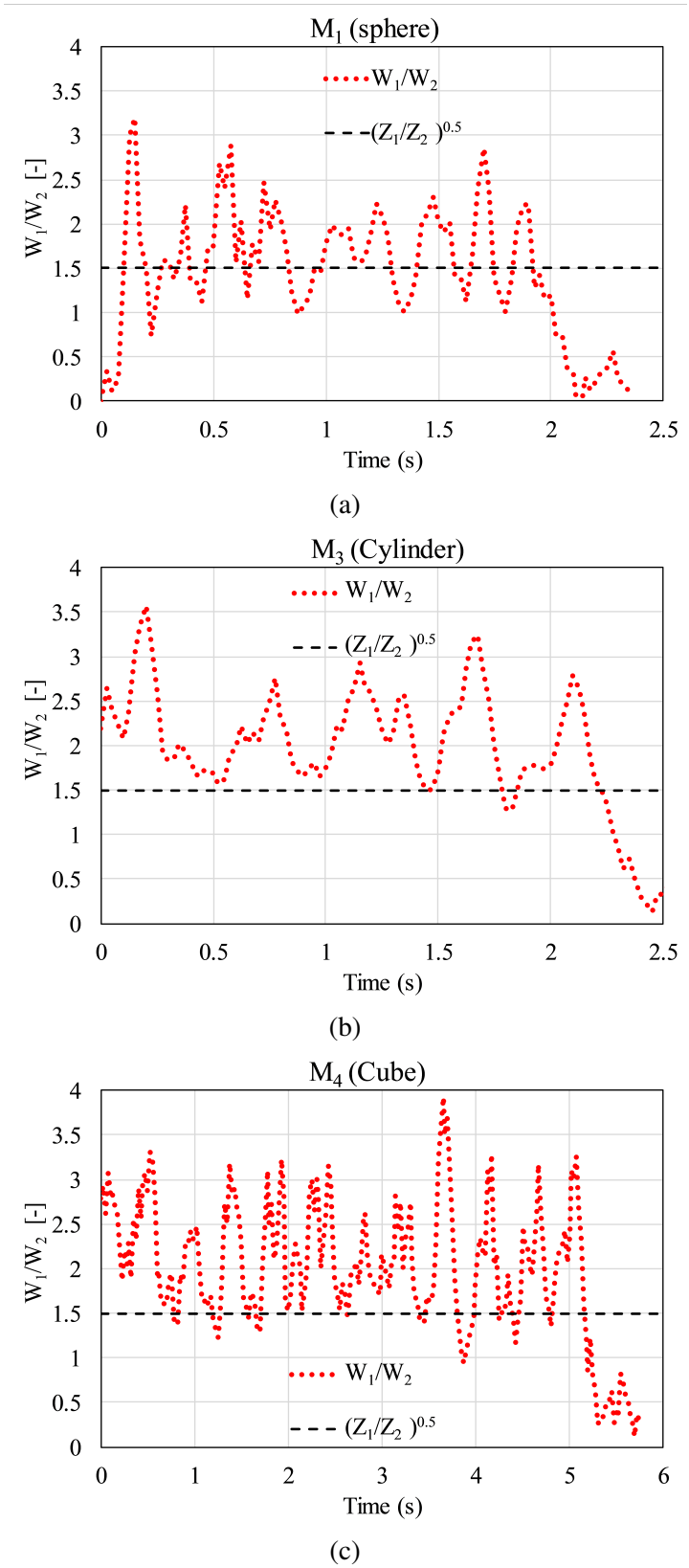

Figure 6.24 Comparison of Beverloo's approach and normalized mass discharge rate over time for flat bottom silo (ratio of mass flow rate (W) for two different gravitational acceleration) a) for M_1 b) for M_3 c) for M_4.

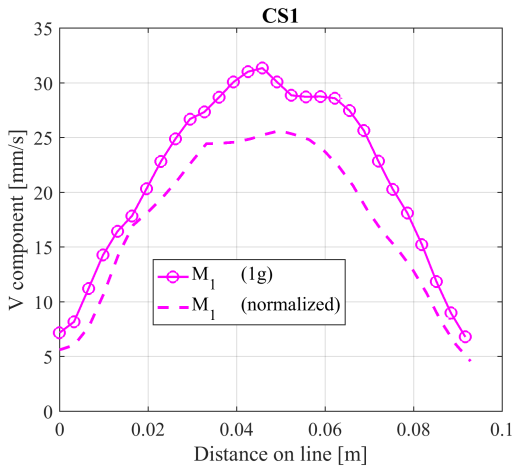

(a)

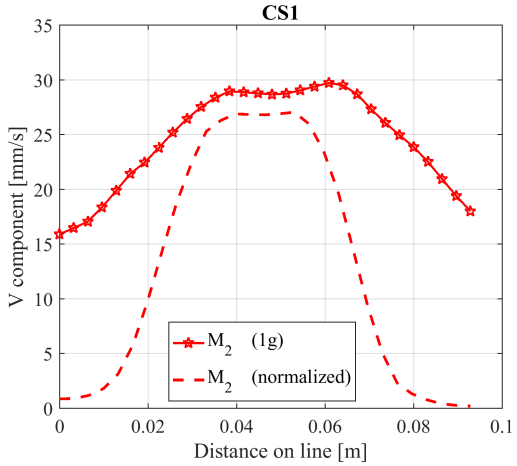

(b)

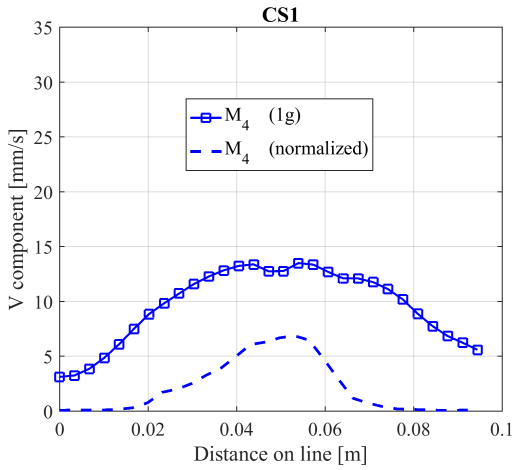

(c)

Figure 6.25 Velocity distribution along the width of silo (at CS1=H/3); comparison of the outward velocity at 1g and 30g for flat bottom silo (normalized by square root of gravity ratio) a) for M_1 b) for M_3 c) for M_4.

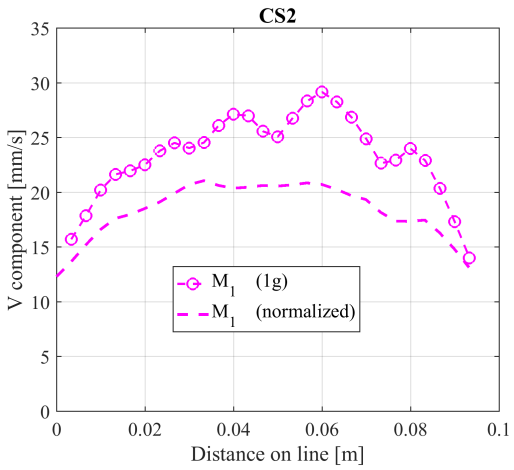

(a)

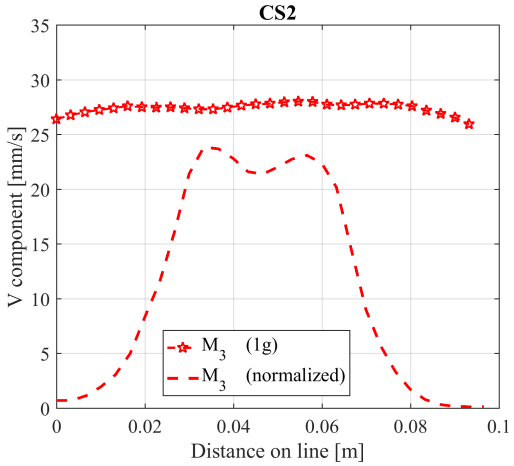

(b)

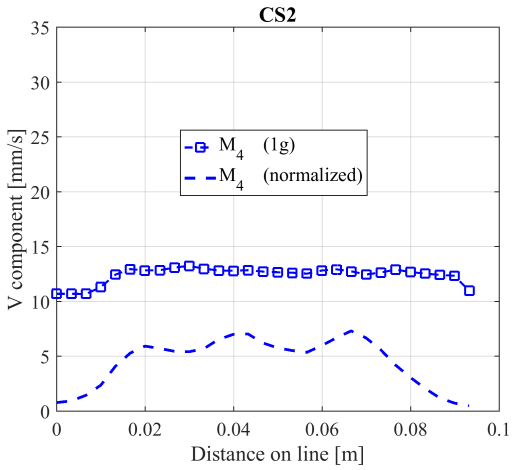

(c)

Figure 6.26 Velocity distribution along the width of silo (at CS2=H/2); comparison of the outward velocity at 1g and 30g for flat bottom silo (normalized by square root of gravity ratio) a) for M_1 b) for M_3 c) for M_4.

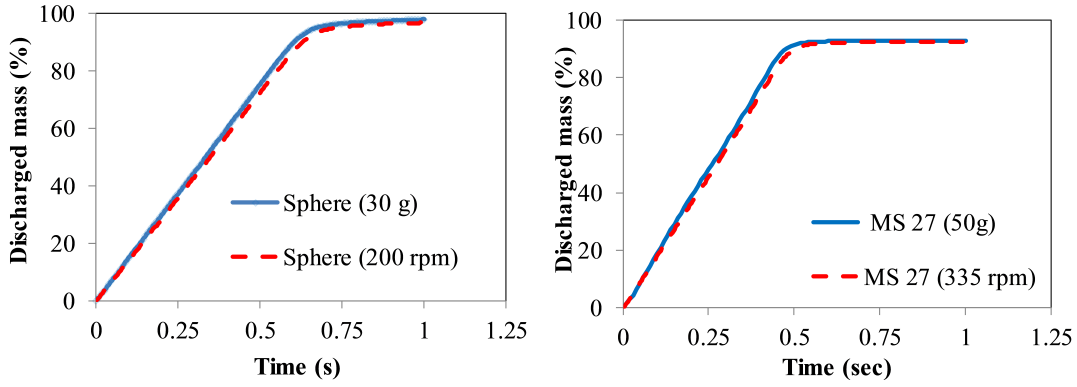

(a) (b)

Figure 6.27 Influence of applying accelerations with different approaches on the cumulative mass discharge (in flat bottom silo) a) spherical particles b) cubical shaped particles.

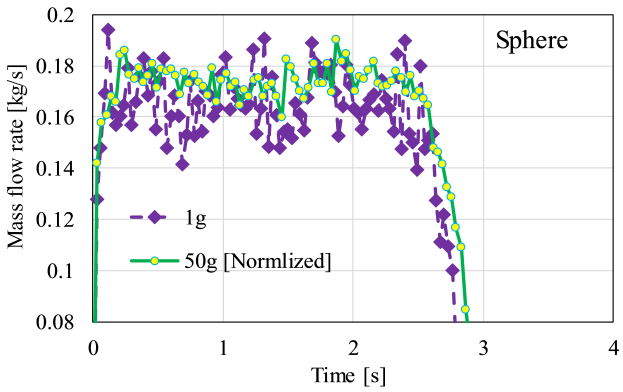

(a)

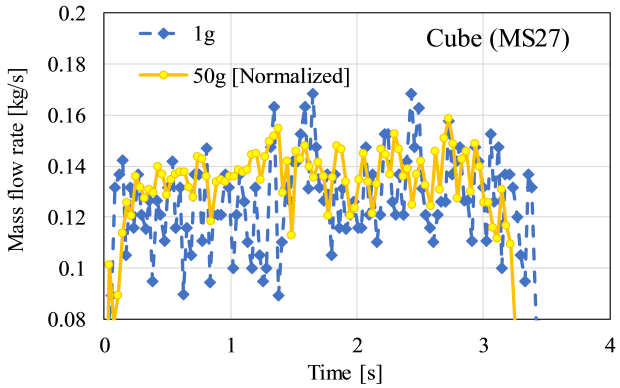

(b)

Figure 6.28 Mass flow rate for particles at different gravity acceleration levels for flat bottom silo (results of 50*g* are normalized by square root of gravity) a) spherical particles b) cubical shaped particles.

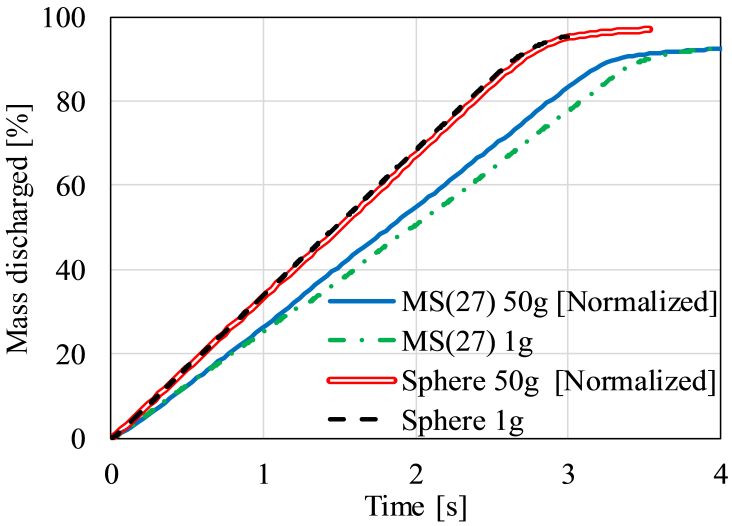

Figure 6.29 Cumulative discharge for different shape particles at different gravities for flat bottom silo (results of 50g are normalized by square root of gravity).

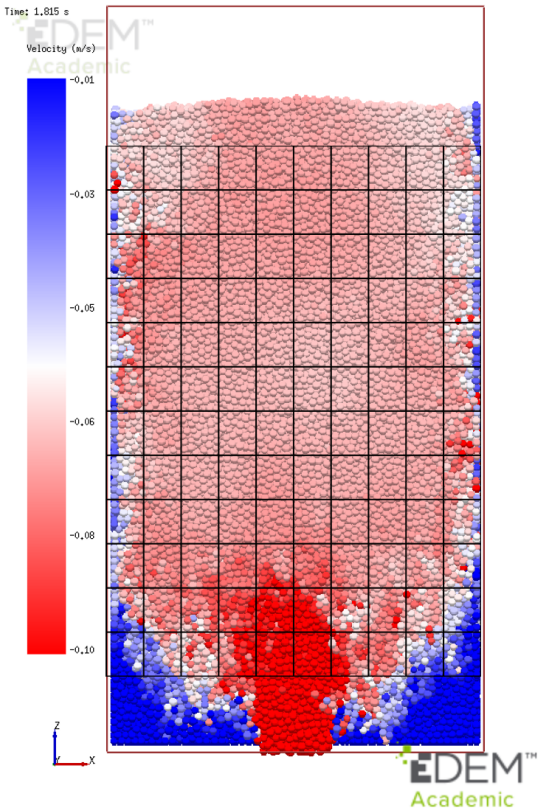

Figure 6.30 Discharge of spherical particles at 1g condition (colouring of the particles are based on the magnitude of vertical velocity).

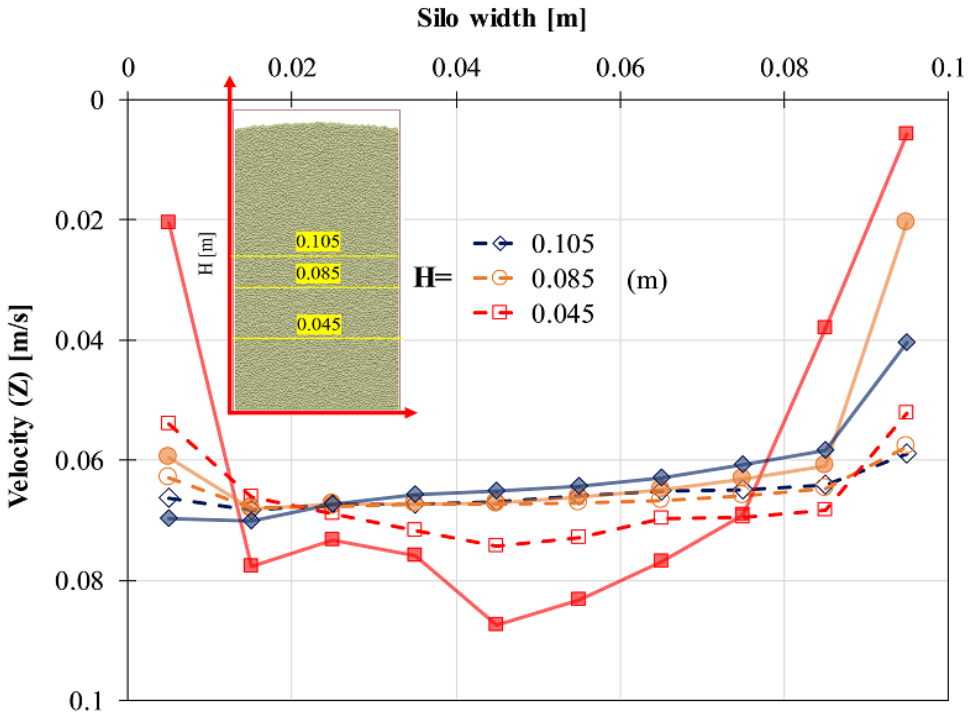

(a)

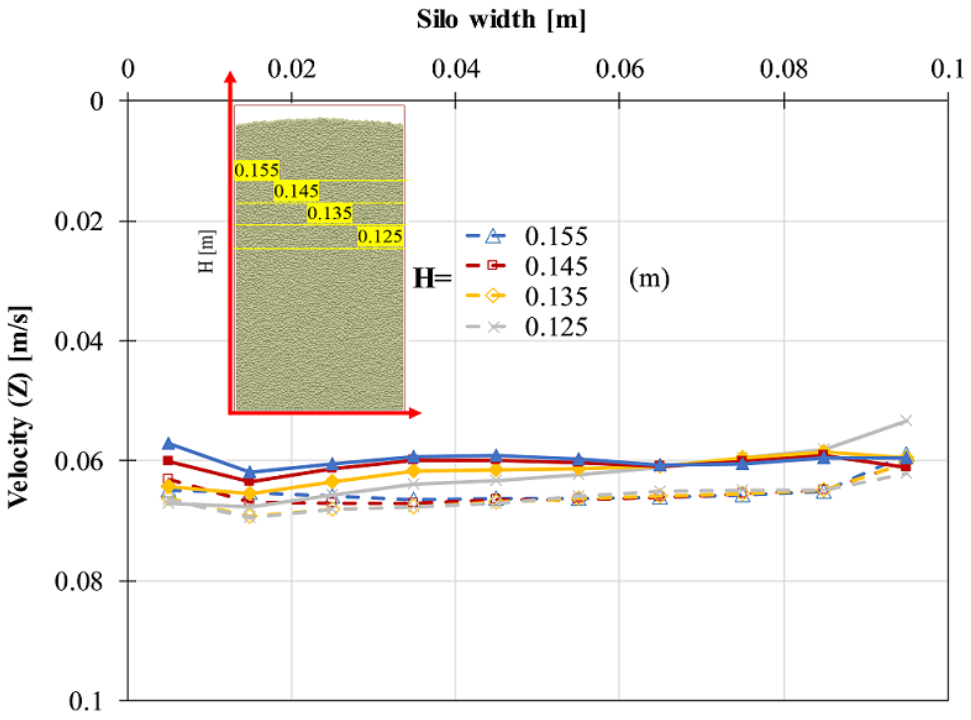

(b)

Figure 6.31 Velocity distribution of spherical particles over width of silo for flat bottom case (at various heights), filled markers and solid lines present results of normalized case (i.e. 50g), a) lower half b) upper half of the silo.

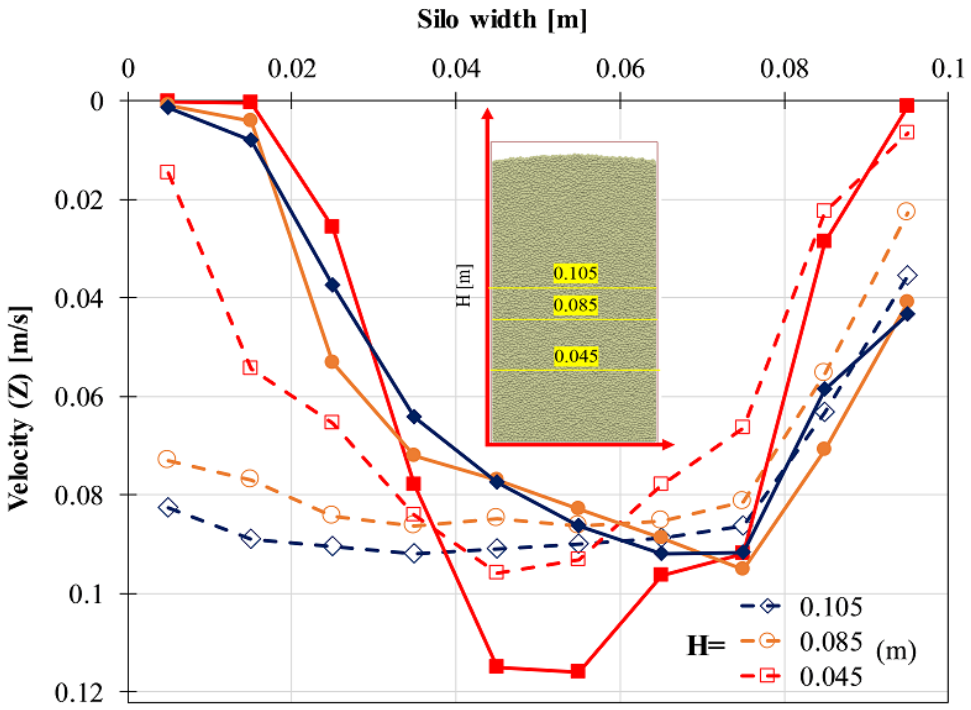

(a)

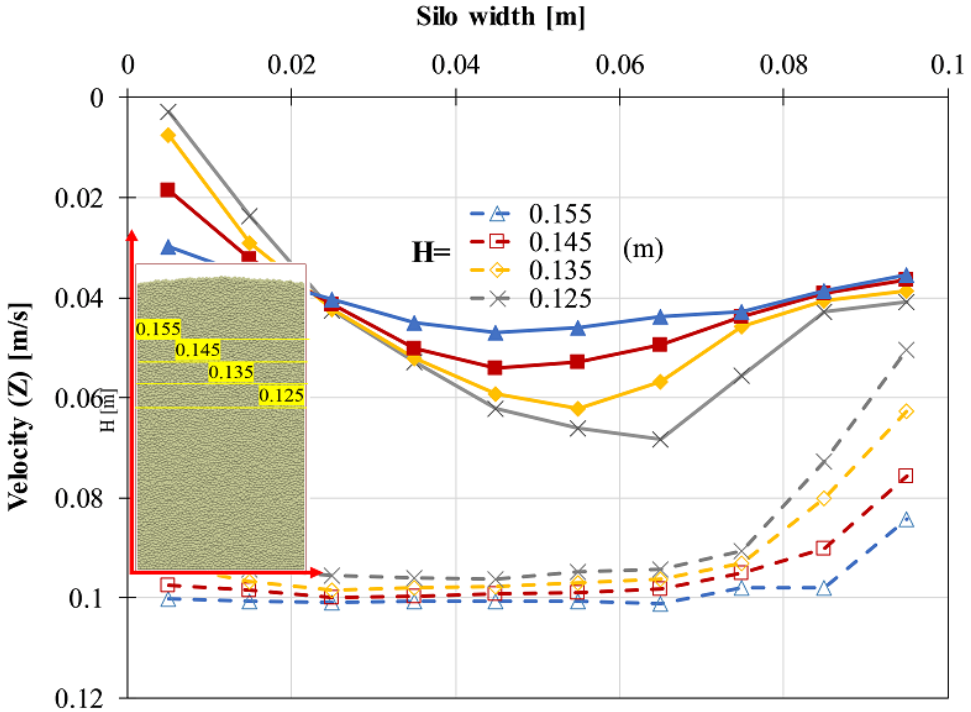

(b)

Figure 6.32 Velocity distribution of cubical particles over width of silo for flat bottom case (at various heights), filled markers and solid lines present results of normalized case (i.e. 50g), a) lower half b) upper half of the silo.

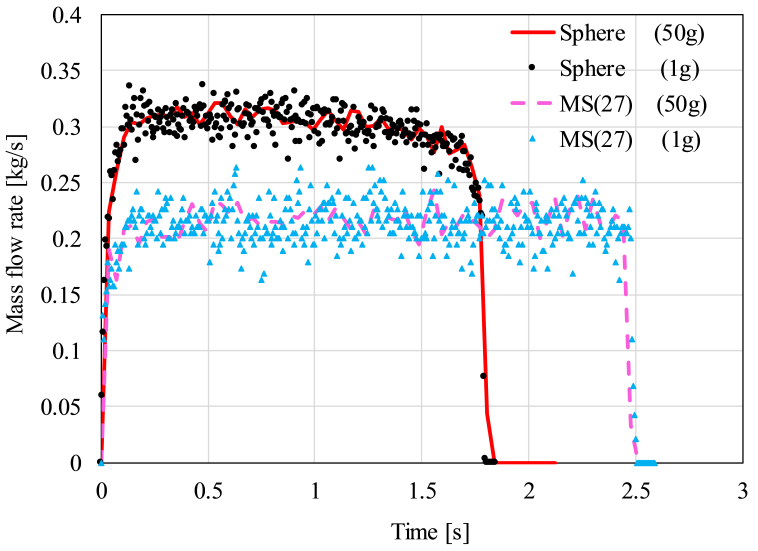

(a)

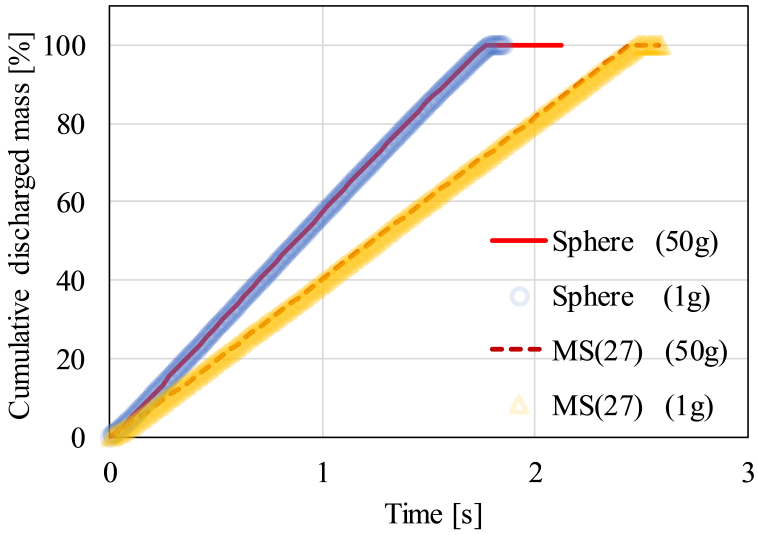

(b)

Figure 6.33 Discharge of particles with different shapes (at different *g* levels from) from wedge shaped hopper a) mass flow rate b) cumulative mass discharge over time.

Chapter 7

Conclusions and Recommendations

The core focus of this thesis was to investigate the importance of the shape factor in the micro- and macro-scale response of granular materials. The numerical part of the study has been conducted using DEM, where there exist various shape representation approaches. The employed methods include spheres (with/without presence of rolling resistance), multi-spheres and superquadrics. The particle and bulk-scale characteristics of all methods are assessed within different testing scenarios. Additionally, comparing the response of all the approaches, the possibility of predicting similar behaviour, with the use of each method, has been studied. Moreover, a set of experimental studies has been conducted to determine the dependence of flowing and shearing behaviour of granular materials on the particle shape factor. Further analysis has been carried out on the flow characteristics by utilizing image processing techniques. Finally, the predictability of flow under realistic stress states has been evaluated (i.e. by enabling gravitational accelerations) for the ensiled granular assemblies.

7.1 Conclusions

The novel findings of the thesis are first briefly discussed below and then explained in detail in terms of the key conclusions of each chapter.

The influence of incorporating rolling resistance models, during a quasi-static flow, was not clearly addressed in the literature. The current study has performed a comprehensive sensitivity analysis on the discharge process. It is shown that almost all the macro-scale characteristics of the spherical particles are affected by the inclusion of rolling resistance, especially the flow characteristics. Moreover, the influence of particle shape is assessed by considering two different shape representation techniques, namely multi-spheres and superquadrics. It is shown that varying shape complexity

(i.e. by changing surface bumpiness or edge sharpness) has approximately similar effects on the flowing and shearing characteristics of granular assemblies. Additionally, an important uncertainty regarding the applicability of rolling resistance models in mimicking the behaviour of complex shape particles is answered. It is shown that relatively simple rolling resistance models are not successful in presenting shape effect during dense shearing scenarios. On the other hand, more complex type of rolling resistance models can mimic successfully the bulk response of irregular shape particles (i.e. in terms of shear strength and dilative behaviour). Furthermore, results from experimental tests have shown the great influence of shape parameter on the avalanching and shear strength of granular material. Finally, results from a silo centrifuge test suggested that Beverloo's empirical approach, for predicting the mass flow rate of granular assemblies under higher gravitational accelerations, may need a modification for predicting the response of non-spherical particles.

The individual conclusions drawn from each chapter are:

Behaviour of spherical particles with restrained rotation

In this part of the study, the effect of two rolling resistance models on both packing and discharge characteristics of spherical particles has been investigated. Accordingly, the rolling resistance coefficient for both models is systematically increased and the resulting bulk scale responses are compared. The key observations are:

- Solid fraction decreases with increase in rolling resistance in both models.
- Utilization of both rolling resistance models for spherical particles results in lower mass discharge.
- Increasing the μ_r value affects the flow profiles to a large extent; a fast flow channel is built and additionally the not flowing (stagnant) zone is enlarged.
- The horizontal stress distribution is mainly dependent on the flow kinematics; μ_r>0 results in formation of a flow channel in the centre of the silo, which causes the breakage of the formed arches and reduces the horizontal stress distribution.
- Both models can be calibrated to get similar cumulative discharges (i.e. with identical mass flow rates). The coefficient that must be multiplied to $\mu_{r(B)}$ to obtain equivalent $\mu_{r(A)}$ varies between 4 to 2 (for $\mu_{r(A)}$<0.2 is around 4 and then for $\mu_{r(A)}$>0.2 decreases linearly up to 2).
- Calibrated models are also evaluated by means of stress distribution, velocity profiles and solid fractions in a common range that is obtained through a detailed

survey in the literature $0.01<\mu_{r(A)}<0.2$. There is a good match for mentioned bulk scale results between calibrated models in the featured range.

- The initial packing effect on the bulk behaviour is also studied. The results suggest that the discharge rate and the solid fraction is governed by the rolling resistance model and the respective flow channel rather than the initial packing.

Addressing shape parameter by means of multi-spheres and superquadrics

Due to advances in computational power, it is now possible to run simulations with non-spherical particles (a couple of thousands or in some cases a couple of ten thousands) in relatively reasonable time. Accordingly, the number of researchers considering shape factor in their studies is highly increasing. Among different shape representation approaches, multi-spheres and superquadrics are the most popular ones so far. However, each method has its own features in addressing shape complexity, where multi-spheres represent best surface bumpiness and superquadrics are well-producing sharp edges. Meantime, there is a vague knowledge behind the selection process of each method (i.e. it is not yet clear which approach is more appropriate for a certain application). Accordingly, a comprehensive study has been performed by varying the surface and edge properties of cubic shape particles and results are compared in multi-scale. The testing scenarios cover particle-scale tests, such as: inclined surface, degree of interlocking, particle-wall impact and particle-particle sliding. In bulk-scale, on the other hand, angle of repose, Jenike shear tester and silo discharge tests have been carried out. Following is a summary of the key observations:

- At the grain-level, several test cases were simulated with MS and SQ particles, which led to a better understanding of impact, interlocking, sliding and tilting characteristics of the single particles. Tests revealed the dependence of particle behaviour at the micro-scale on the particle edge and surface properties. For example, it has been shown that, at low friction coefficients, interlocking of MS particles can have significant effect on particle motion.

- In the angle of repose test, the surface inclination of the formed piles increases monotonically with the increase in blockiness. A similar influence is seen by increasing the bumpiness in MS particles.

- Measuring the simulation time for particles with different shape properties, it is shown that the SQ blockiness has no significant influence on the computational costs. On the contrary, the computational time for MS particles strongly depends on the number of sub-spheres. It is seen that only $\mathrm{MS}(8)$ (among all MS particles) have computational time comparable to that for SQ particles, which

is approximately 10 times slower than spherical particles. The use of SQ particles can therefore be beneficial for modelling non-spherical particles in DEM (especially for blocky types of particles).

- Further assessment of bulk behaviour of the MS and SQ particles is performed through conducting the Jenike shear test. Results suggest that the surface roughness, in MS particles, and edge sharpness, in SQ particles, can dictate the material response only in certain density states. Namely, for porosity, dilation and shear strength of the material a dense packing is more susceptible to the variation in blockiness and bumpiness of particle.

- For the silo flow, it is shown that the discharge rate, flow profiles and stress are affected by the shape to varying degrees. With increasing blockiness and surface bumpiness, the flow is retarded to some extent, of the order of 10 % in this study. Moreover, the horizontal stress reduces whilst the vertical stress is much less sensitive to the shape characteristics.

- The flow properties of the particles with similar residual shear strength have been assessed and an identical flow pattern and discharge rate is recorded. Nevertheless, the inherent difference in total number of contacts in MS particles (which acts as additional frictional resistance) could potentially give a different stress field.

Possibility of addressing shape complexities by means of rolling resistance models

The avalanching, packing and shearing response from three rolling resistance models is compared with common non-spherical particles with aspect ratio of one and higher (cylinders and cubes/cuboids). The non-spherical shapes are simulated by means of MS and SQ particles, each of which have unique shape irregularities. Accordingly, it was possible to examine the capabilities of artificial shape representation scenario in mimicking the real shape factor. Following are the main observations:

- For the AoR test, results suggest that tuning the unitless shape parameter (μ^r_{pp}) for the three models can lead to the desired heap, which is comparable to the results of non-spherical particles (with various bumpiness, blockiness and aspect ratios).

- Based on the results, it is shown that the incorporation of the rolling resistance models contributes to formation of the loose packings. However, it is seen that the exact match for the spheres and cubes and cylinders is not obtainable.

- The capability of the considered models in providing dilative response during shearing is evaluated. Results suggest that Model *A* and Model *B* are addressing

this phenomenon only for packing with a limited packing density. However, Model *C* is well capable of providing dilation for the granular assemblies almost for the whole range of packing densities.

- For the shear strength, it holds true to claim that once μ_{pp}^{r} is varied, only Model *C* is providing reasonable results and the obtained peak friction angles for the this model are well in agreement with those of cubical and cylindrical shape particles.

- Results suggest that in the conducted tests, it is possible to calibrate the μ_{pp}^{r} in order to obtain the desired individual macro-scale response of non-spherical particles. However, special care must be taken to characterize each rolling resistance model and determine the area of influence of models in different testing conditions.

Furthermore, as an additional case study, the sensitivity of the bulk behaviour, in a cohesionless backfill, to the particle shape is assessed. Active failure state has been simulated, where the rigid frictional retaining wall translates away from the backfill at a constant speed. The particle shape is addressed using spherical (with and without rolling resistance) and paired (two overlapping sphere) particles. Comparing the results for μ_r=0, μ_r=1 (with spheres) and paired particles, the capability of the rolling resistance in providing shape effect is evaluated. Following is a list of principal findings:

- It is observed that the paired particles show a uniform velocity distribution for individual particles over a distinct area. The presence of rolling resistance is mimicking this attitude to some extent.

- It is shown that the stress distribution is excessively influenced by the shape effect; by employing paired particles, the total force on the wall is reduced and this is similar to the effect of including rolling resistance for the spherical particles.

- Compared to spherical particles, the failure wedge for paired particles is smaller, which can justify the lower active thrust for these particles.

- The geometry of the failure surface remains the same for μ_r=0 and μ_r=1.

- The volumetric strain distribution suggests that the paired particles tend to dilate more along the shear band. Spherical particles with μ_r=0 are not efficient in capturing the dilative features of the soil and adding the rotational constraints seems to improve this deficiency.

Experimental observation of the flow and its dependence on shape factor

An important factor that governs the interaction of individual particles is the geometrical interlocking, which is due to irregular shapes. In this regard, we have considered an experimental study to characterize the influence of shape irregularity on the bulk response and also to validate DEM observations. Considered materials have spherical, pentagon, cylindrical and cubical shapes. Initially, avalanching and shearing characteristics of the materials are obtained through angle of repose and Jenike shear tests. Next, a flat-bottom silo is used for investigating the particle shape effect on the flow kinematics at earth gravity. The silo has transparent walls and allows visualization of the flow during the discharge. A high-speed camera is utilized to capture successive images at all the stages of the test. Later, using PIV, the displacement field is tracked and plotted as vectors. This allows the flow channel geometry for all the packings to be compared. Finally, flow characteristics of the considered materials are evaluated in a silo centrifuge device (with flat-bottom and wedge shaped hopper). This is done to investigate the predictability of the mass flow rate and flow profiles in the presence of realistic stress distribution (similar to industrial size silos). The main conclusions are summarized as follows:

- Interlocking between single particles results in a higher angle of repose (similar observation was obtained in DEM simulations in Chapter 4).
- In terms of the Jenike shear test, results are not exactly following AoR; here cylindrical particles show the highest shear strength. The difference in shear strength of cubes and cylinders is likely related to the difference in aspect ratio (where the latter has a larger aspect ratio).
- Flow profiles are affected to a high extent by the shape parameter, non-spherical particles result in a narrower flow channel. Spherical particles, on the other hand show a wider flow channel and particles from near the walls (near the surface) are contributing to the flow.
- It is shown that Beverloo's approach for predicting mass flow rates (at higher gravitational accelerations) holds true for only spherical shape particles (both in case of flat-bottom silo and wedge shape hopper).
- In case of velocity profiles, similar to mass flow results, only spherical particles present relatively comparable values between 1g and normalized cases.
- Comparing results of spherical and cubical shape particles in DEM, a similar discrepancy is seen between results from 1g and those of obtained through normalization of higher g cases.

7.2 Suggestions for future work

Stability of a silo is primarily affected by non-symmetrical flow of the bulk solid and uncontrolled volume changes in the hopper. To avoid any damages on the silo, it is essential to characterize flow profiles. Additionally, it is a well-established fact that flow characteristics in a silo are a function of various factors, such as particle size, shape, cohesion and boundary conditions. Numerous studies have been conducted to attain the influence of different factors on the bulk response of granular assemblies. However, it is yet challenging to predict the flow profiles based on the single-particle properties. Accordingly, a future study can follow a multi-scale procedure to correlate the micro-scale properties to the macro-scale response of the granular assemblies. In this respect, a set of reference materials, with varying size distribution and shape, must be examined both experimentally and numerically. Eventually, a mathematical description can be likely suggested for predicting flow profiles.

Further research could investigate the effect of increasing shape complexity and its effect on the bulk response of the backfill during passive states. The obtained pressure distribution and also captured failure surfaces should be compared to the available experimental results and analytical approaches to further validate the DEM outputs. Moreover, the results of the hybrid PIV-DEM could be checked by comparing the current results with the strain distribution obtained through particle scale data from DEM simulations.

Another outlook to future research could be finding bulk granular materials which are from exactly the same substance and the only varying parameter is the shape. Then, the conducted characterizing tests could be repeated to draw more robust conclusions.

References

Abbaspour-Fard, M. (2004), 'Theoretical Validation of a Multi-sphere, Discrete Element Model Suitable for Biomaterials Handling Simulation', *Biosystems Engineering* **88**(2), 153–161.

Abbaspour-Fard, M. H. (2000), Discrete element modelling of the dynamic behaviour of non-spherical particulate materials, PhD thesis, The University of Newcastle upon Tyne.

Adrian, R. J. (1991), 'Particle-imaging techniques for experimental fluid mechanics', *Annual review of fluid mechanics* **23**(1), 261–304.

Ai, J., Chen, J.-F., Rotter, M. and Ooi, J. Y. (2011), 'Assessment of rolling resistance models in discrete element simulations', *Powder Technology* **206**(3), 269–282.

Aigner, A., Schneiderbauer, S., Kloss, C. and Pirker, S. (2013), Determining the coefficient of friction by shear tester simulation, *in* '3rd International Conference on Particle-Based Methods', Vol. 1, pp. 335–342.

Al-Hashemi, H. M. B. and Al-Amoudi, O. S. B. (2018), 'A review on the angle of repose of granular materials', *Powder Technology* **330**, 397–417.

Altunbas, A., Soltanbeigi, B. and Cinicioglu, O. (2017), 'Determination of active failure surface geometry for cohesionless backfills', *Geomechanics and Engineering* **12**(6), 983–1001.

Anand, A., Curtis, J. S., Wassgren, C. R., Hancock, B. C. and Ketterhagen, W. R. (2008), 'Predicting discharge dynamics from a rectangular hopper using the discrete element method (DEM)', *Chemical Engineering Science* **63**(24), 5821–5830.

Aste, T. (2005), 'Variations around disordered close packing', *Journal of Physics: Condensed Matter* **17**(24), S2361.

ASTM D6128 (2006), 'Standard Test Method for Shear Testing of Bulk Solids Using the Jenike Shear Cell'.

ASTM D6773-16, Standard Test Method for Bulk Solids Using Schulze Ring Shear Tester (2016), ASTM International, West Conshohocken.
URL: *http://www.astm.org/cgi-bin/resolver.cgi?D6773-16*

Azéma, E., Radjai, F. and Saussine, G. (2009), Quasistatic behavior and force transmission in packing of irregular polyhedral particles, *in* 'AIP Conference Proceedings', Vol. 1145, AIP, pp. 273–276.

Babic, M. (1997), 'Average balance equations for granular materials', *International journal of engineering science* **35**(5), 523–548.

Babout, L., Grudzien, K., Maire, E. and Withers, P. J. (2013), 'Influence of wall roughness and packing density on stagnant zone formation during funnel flow discharge from a silo: An X-ray imaging study', *Chemical Engineering Science* **97**, 210–224.

Balevičius, R., Sielamowicz, I., Mróz, Z. and Kačianauskas, R. (2012), 'Effect of rolling friction on wall pressure, discharge velocity and outflow of granular material from a flat-bottomed bin', *Particuology* **10**(6), 672–682.

Bardet, J. P. (1994), 'Observations on the effects of particle rotations on the failure of idealized granular materials', *Mechanics of materials* **18**(2), 159–182.

Barr, A. H. (1981), 'Superquadrics and angle-preserving transformations', *IEEE Computer Graphics and Applications* **1**(January), 11–23.

Barrios, G. K. P., de Carvalho, R. M., Kwade, A. and Tavares, L. M. (2013), 'Contact parameter estimation for DEM simulation of iron ore pellet handling', *Powder technology* **248**, 84–93.

Baxter, G. W., Behringer, R. P., Fagert, T. and Johnson, G. A. (1990), Pattern formation and time-dependence in flowing sand, *in* 'Two phase flows and waves', Springer, pp. 1–29.

Beer, F. P., Johnston Jr, E. R., Mazurek, D. F., Cornwell, P. J., Eisenberg, E. R. and Sanghi, S. (1972), *Vector mechanics for engineers*, Vol. 1, Tata McGraw-Hill Education.

Benmeddour, D., Mellas, M., Frank, R. and Mabrouki, a. (2012), 'Numerical study of passive and active earth pressures of sands', *Computers and Geotechnics* **40**, 34–44. **URL:** *http://dx.doi.org/10.1016/j.compgeo.2011.10.002*

Benvenuti, L. (2014), Establishing the predictive capabilities of DEM simulations: sliding and rolling friction coefficients of non-spherical particles, *in* 'CFD 2014 Proceedings', number June, pp. 1–7.

Benvenuti, L., Kloss, C. and Pirker, S. (2016), 'Identification of DEM simulation parameters by Artificial Neural Networks and bulk experiments', *Powder Technology* **291**, 456–465.

Beverloo, W. A., Leniger, H. A. and de Velde, J. (1961), 'The flow of granular solids through orifices', *Chemical engineering science* **15**(3-4), 260–269.

Börzsönyi, T., Somfai, E., Szabó, B., Wegner, S., Mier, P., Rose, G. and Stannarius, R. (2016), 'Packing, alignment and flow of shape-anisotropic grains in a 3D silo experiment', *New Journal of Physics* **18**(9), 93017.

Brilliantov, N. V. and Pöschel, T. (1998), 'Rolling friction of a viscous sphere on a hard plane', *Europhysics Letters* **42**(5), 511–516.

Brilliantov, N. V., Spahn, F., Hertzsch, J.-M. and Pöschel, T. (1996), 'Model for collisions in granular gases', *Physical review E* **53**(5), 5382.

Brown, R. L. and Richards, J. C. (1970), Principle of Powder Mechanics, number 73, Pergamon press, p. 99993.

Cabiscol, R., Finke, J. H. and Kwade, A. (2018), 'Calibration and interpretation of DEM parameters for simulations of cylindrical tablets with multi-sphere approach', *Powder Technology* **327**, 232–245.

Calderón, C. A., Olivares, M. C. V., Uñac, R. O. and Vidales, A. M. (2017), 'Correlations between flow rate parameters and the shape of the grains in a silo discharge', *Powder technology* **320**, 43–50.

Calvetti, F., Combe, G. and Lanier, J. (1997), 'Experimental micromechanical analysis of a 2D granular material: relation between structure evolution and loading path', *Mechanics of Cohesive frictional Materials An International Journal on Experiments Modelling and Computation of Materials and Structures* **2**(2), 121–163.

Chang, Y.-L., Chen, T.-H. and Weng, M.-C. (2012), 'Modeling particle rolling behavior by the modified eccentric circle model of DEM', *Rock mechanics and rock engineering* **45**(5), 851–862.

Chen, J. F., Yu, S. K., Ooi, J. Y. and Rotter, J. M. (2001), 'Finite-element modeling of filling pressures in a full-scale silo', *Journal of engineering mechanics* **127**(10), 1058–1066.

Chung, Y.-C. (2006), Discrete element modelling and experimental validation of a granular solid subject to different loading conditions, PhD thesis, University of Edinburgh.

Cinicioglu, O., Altunbas, A., Soltanbeigi, B. and Gezgin, A. T. (2015), Dilatancy based similitude of small-scale 1g models and prototypes for cohesionless soils, *in* 'Geomechanics from Micro to Macro', number 2013, CRC Press, Cambridge, pp. 1641–1645.

Cleary, P. W. (2004), 'Large scale industrial DEM modelling', *Engineering Computations* **21**(2/3/4), 169–204.

Cleary, P. W. (2010), 'DEM prediction of industrial and geophysical particle flows', *Particuology* **8**(2), 106–118.

Cleary, P. W. and Sawley, M. L. (2002), 'DEM modelling of industrial granular flows: 3D case studies and the effect of particle shape on hopper discharge', *Applied Mathematical Modelling* **26**(2), 89–111.

Coe, C. J., Prevost, J. H. and Scanlan, R. H. (1985), 'Dynamic stress wave reflections/attenuation: earthquake simulation in centrifuge soil models', *Earthquake engineering & structural dynamics* **13**(1), 109–128.

Coetzee, C. J. (2017), 'Calibration of the discrete element method', *Powder Technology* **310**, 104–142.

Combarros Garcia, M., Feise, H. J., Strege, S. and Kwade, A. (2016), 'Segregation in heaps and silos: Comparison between experiment, simulation and continuum model', *Powder Technology* **293**, 26–36.

Coulomb, C. (1776), *Essai sur une application des regles des maximis et minimis a quelues problemes de statique relatifs a larchitecture*, De l'Imprimerie Royale.

Cundall, P. A. and Strack, O. D. L. (1979), 'A discrete numerical model for granular assemblies', *Geotechnique* **29**(1), 47–65.

DEM Solutions Ltd. (2014), EDEM 2.6 theory reference guide, Technical report.

Di Renzo, A. and Di Maio, F. P. (2004), 'Comparison of contact-force models for the simulation of collisions in DEM-based granular flow codes', *Chemical Engineering Science* **59**(3), 525–541.

Dogangun, A., Karaca, Z., Durmus, A. and Sezen, H. (2009), 'Cause of damage and failures in silo structures', *Journal of performance of constructed facilities* **23**(2), 65–71.

Dorbolo, S., Maquet, L., Brandenbourger, M., Ludewig, F., Lumay, G., Caps, H., Vandewalle, N., Rondia, S., Mélard, M. and Van Loon, J. (2013), 'Influence of the gravity on the discharge of a silo', *Granular matter* **15**(3), 263–273.

Drescher, A. (1992), 'On the criteria for mass flow in hoppers', *Powder Technology* **73**(3), 251–260.

Drescher, A. (1998), 'Some aspects of flow of granular materials in hoppers', *Philosophical transactions-royal society of london series a mathematical physical and engineering sciences* pp. 2649–2666.

Drescher, A., Cousens, T. W. and Bransby, P. L. (1978), 'Kinematics of the mass flow of granular material through a plane hopper', *Geotechnique* **28**(1), 27–42.

Estrada, N., Azéma, E., Radjai, F. and Taboada, A. (2011), 'Identification of rolling resistance as a shape parameter in sheared granular media', *Physical Review E* **84**(1), 11306.

Estrada, N., Azéma, E., Radjai, F. and Taboada, A. (2013), Comparison of the effects of rolling resistance and angularity in sheared granular media, *in* 'AIP Conference Proceedings', Vol. 1542, AIP, pp. 891–894.

Fang, Y. and Ishibashi, I. (1986), 'Static earth pressures with various wall movements', *Journal of Geotechnical Engineering* **112**(3), 317–333.
URL: *http://ascelibrary.org/doi/abs/10.1061/(ASCE)0733-9410(1986)112:3(317)*

Favier, J., Abbaspourfard, M., Kremmer, M. and Raji, A. (1999), 'Shape representation of axisymmetrical, nonspherical particles in discrete element simulation using multielement model particles', *Engineering Computations* **16**(4), 467–480.

Fleischmann, J. A., Drugan, W. J. and Plesha, M. E. (2013), 'Direct micromechanics derivation and DEM confirmation of the elastic moduli of isotropic particulate materials: Part I No particle rotation', *Journal of the Mechanics and Physics of Solids* **61**(7), 1569–1584.

Freireich, B., Li, J., Litster, J. and Wassgren, C. (2011), 'Incorporating particle flow information from discrete element simulations in population balance models of mixer-coaters', *Chemical Engineering Science* **66**(16), 3592–3604.

Fukumoto, Y., Sakaguchi, H. and Murakami, A. (2013), 'The role of rolling friction in granular packing', *Granular Matter* **15**(2), 175–182.

Fulchini, F., Zafar, U., Hare, C., Ghadiri, M., Tantawy, H., Ahmadian, H. and Poletto, M. (2017), 'Relationship between surface area coverage of flow-aids and flowability of cohesive particles', *Powder Technology* **322**, 417–427.

Goel, S. and Patra, N. R. (2008), 'Effect of Arching on Active Earth Pressure for Rigid Retaining Walls Considering Translation Mode', *International Journal of Geomechanics* **8**(2), 123–133.

Goldhirsch, I. (2010), 'Stress, stress asymmetry and couple stress: From discrete particles to continuous fields', *Granular Matter* **12**(3), 239–252.

Goniva, C., Kloss, C., Deen, N. G., Kuipers, J. A. M. and Pirker, S. (2012), 'Influence of rolling friction on single spout fluidized bed simulation', *Particuology* **10**(5), 582–591.

González-Montellano, C., Ayuga, F. and Ooi, J. Y. (2011), 'Discrete element modelling of grain flow in a planar silo: influence of simulation parameters', *Granular Matter* **13**(2), 149–158.

Großstück, M. and Schwedes, J. (2005), 'Application of model tests on cohesive bulk solids using silo centrifuge technique', *Powder technology* **157**(1-3), 149–155.

Grudzień, K., Niedostatkiewicz, M., Adrien, J., Tejchman, J. and Maire, E. (2011), 'Quantitative estimation of volume changes of granular materials during silo flow using X-ray tomography', *Chemical Engineering and Processing: Process Intensification* **50**(1), 59–67.

Hagen, G. H. L. (1852), 'Aber den Druck und die Bewegung des trocknen Sandes', *Bericht uber die zur Bekanntmachung geeigneten Verhandlungen der Koniglich Preussischen Akademie der Wissenschaften zu Berlin* **35**(1852), 35–42.

Hanley, K. J., Huang, X. and O'Sullivan, C. (2017), 'Comparing the effects of interparticle friction coefficient and intermediate stress ratio on critical-state DEM simulations using Delaunay triangulations', *EPJ Web of Conferences* **140**, 12003.

Härtl, J. and Ooi, J. Y. (2011), 'Numerical investigation of particle shape and particle friction on limiting bulk friction in direct shear tests and comparison with experiments', *Powder Technology* **212**(1), 231–239.

Hastie, D. B. (2013), 'Experimental measurement of the coefficient of restitution of irregular shaped particles impacting on horizontal surfaces', *Chemical Engineering Science* **101**, 828–836.

Höhner, D., Wirtz, S., Kruggel-Emden, H. and Scherer, V. (2011), 'Comparison of the multi-sphere and polyhedral approach to simulate non-spherical particles within the discrete element method: Influence on temporal force evolution for multiple contacts', *Powder Technology* **208**(3), 643–656.

Höhner, D., Wirtz, S. and Scherer, V. (2012), 'A numerical study on the influence of particle shape on hopper discharge within the polyhedral and multi-sphere discrete element method', *Powder Technology* **226**, 16–28.

Höhner, D., Wirtz, S. and Scherer, V. (2013), 'Experimental and numerical investigation on the influence of particle shape and shape approximation on hopper discharge using the discrete element method', *Powder Technology* **235**, 614–627.

Holst, J. M. F. G., Ooi, J. Y., Rotter, J. M. and Rong, G. H. (1999), 'Numerical modeling of silo filling. I: continuum analyses', *Journal of engineering mechanics* **125**(1), 94–103.

Horabik, J., Parafiniuk, P. and Molenda, M. (2018), 'Stress profile in bulk of seeds in a shallow model silo as influenced by mobilisation of particle-particle and particle-wall friction: Experiments and DEM simulations', *Powder Technology* **327**, 320–334.

Huang, X., Hanley, K. J., O'Sullivan, C. and Kwok, C. Y. (2014), 'Exploring the influence of interparticle friction on critical state behaviour using DEM', *International Journal for Numerical and Analytical Methods in Geomechanics* **38**(12), 1276–1297.

Idinger, G., Aklik, P., Wu, W. and Borja, R. I. (2011), 'Centrifuge model test on the face stability of shallow tunnel', *Acta Geotechnica* **6**(2), 105–117.

Ittershagen, T., Zetzener, H., Schwedes, J. and Kwade, A. (2013), 'Anisotropic behaviour of bulk solids and its effect on silo design', *Powder Technology* **247**, 260–264.

Iwashita, K. and Oda, M. (1998), 'Rolling resistance at contacts in simulation of shear band development by DEM', *Journal of engineering mechanics* **124**(3), 285–292.

Jaeger, H. M., Nagel, S. R. and Behringer, R. P. (1996), 'Granular solids, liquids, and gases', *Reviews of Modern Physics* **68**(4), 1259.

Jaelee, S. (2014), developments in large scale discrete element with polyhedral particles simulations, PhD thesis, University of Illinois at Urbana-Champaign.

Jaky, J. (1948), Pressure in silos, *in* 'Proceedings of the 2nd international conference on soil mechanics and foundation engineering', Vol. 1, pp. 103–107.

Janssen, H. A. (1895), 'Versuche uber getreidedruck in silozellen', *Z. Ver. Dtsch. Ing.* **39**(35), 1045–1049.

Jenike, A. W. (1964), 'Storage and flow of bulk solids', *Bulletin* **123**.

Jenike, A. W., Elsey, P. J. and Wooley, R. H. (1960), Flow properties of bulk solids, *in* 'Proc American Soc Testing Materials', Vol. 60, p. 1168.

Jerier, J.-F., Richefeu, V., Imbault, D. and Donzé, F.-V. (2010), 'Packing spherical discrete elements for large scale simulations', *Computer Methods in Applied Mechanics and Engineering* **199**(25-28), 1668–1676.

Jia, X., Gan, M., Williams, R. A. and Rhodes, D. (2007), 'Validation of a digital packing algorithm in predicting powder packing densities', *Powder Technology* **174**(1-2), 10–13.

Jiang, M., He, J., Wang, J., Liu, F. and Zhang, W. (2014), 'Distinct simulation of earth pressure against a rigid retaining wall considering inter-particle rolling resistance in sandy backfill', *Granular Matter* **16**(5), 797–814.

Jiang, M. J., Yu, H.-S. and Harris, D. (2005), 'A novel discrete model for granular material incorporating rolling resistance', *Computers and Geotechnics* **32**(5), 340–357.

Johanson, J. R. (1966), 'The use of flow-corrective inserts in bins', *Journal of Engineering for Industry* **88**(2), 224–230.

Ketterhagen, W. R., Curtis, J. S., Wassgren, C. R. and Hancock, B. C. (2009), 'Predicting the flow mode from hoppers using the discrete element method', *Powder technology* **195**(1), 1–10.

Kloss, C., Goniva, C., Hager, A., Amberger, S. and Pirker, S. (2012), 'Models, algorithms and validation for opensource DEM and CFD-DEM', *Progress in Computational Fluid Dynamics, An International Journal* **12**(2/3), 140.

Kodam, M., Bharadwaj, R., Curtis, J., Hancock, B. and Wassgren, C. (2009), 'Force model considerations for glued-sphere discrete element method simulations', *Chemical Engineering Science* **64**(15), 3466–3475.

Kremmer, M. and Favier, J. F. (2001), 'A method for representing boundaries in discrete element modelling—part I: Geometry and contact detection', *International Journal for Numerical Methods in Engineering* **51**(12), 1407–1421.
URL: *http://doi.wiley.com/10.1002/nme.184*

Kristiansen, N. O., Munch-Andersen, J. and Nielsen, J. (1988), A centrifuge study of load and flow conditions in silos with cohesive media, *in* 'Centrifuge', Vol. 88, Balkema Rotterdam, pp. 593–600.

Kruggel-Emden, H., Rickelt, S., Wirtz, S. and Scherer, V. (2008), 'A study on the validity of the multi-sphere Discrete Element Method', *Powder Technology* **188**(2), 153–165.

Kruggel-Emden, H., Wirtz, S. and Scherer, V. (2008), 'A study on tangential force laws applicable to the discrete element method (DEM) for materials with viscoelastic or plastic behavior', *Chemical Engineering Science* **63**, 1523–1541.

Kwade, A., Schulze, D. and Schwedes, J. (1994), 'Determination of the stress ratio in uniaxial compression tests-Part 2', *Powder Handling & Processing* **6**(2), 199–203.

Labra, C., Ooi, J. Y. and Sun, J. (2013), 'Spatial and temporal coarse-graining for DEM analysis', *AIP Conference Proceedings* **1542**(1).

Langston, P. A., Tüzün, U. and Heyes, D. M. (1995), 'Discrete element simulation of internal stress and flow fields in funnel flow hoppers', *Powder Technology* **85**(2), 153–169.

Lesniewska, D. and Wood, D. M. (2009), 'Observations of Stresses and Strains in a Granular Material', *Journal of Engineering Mechanics* **135**(9), 1038–1054.

Li, J., Langston, P. A., Webb, C. and Dyakowski, T. (2004), 'Flow of sphero-disc particles in rectangular hoppers—a DEM and experimental comparison in 3D', *Chemical Engineering Science* **59**(24), 5917–5929.

Li, S., Zhao, J., Lu, P. and Xie, Y. (2010), 'Maximum packing densities of basic 3D objects', *Chinese Science Bulletin* **55**(2), 114–119.

Liu, S. D., Zhou, Z. Y., Zou, R. P., Pinson, D. and Yu, A. B. (2014), 'Flow characteristics and discharge rate of ellipsoidal particles in a flat bottom hopper', *Powder Technology* **253**, 70–79.

Loganathan, N., Poulos, H. G. and Stewart, D. P. (2000), 'Centrifuge model testing of tunnelling-induced ground and pile deformations', *Geotechnique* **50**(3), 283–294.

Lu, G., Third, J. R. and Müller, C. R. (2015), 'Discrete element models for non-spherical particle systems: From theoretical developments to applications', *Chemical Engineering Science* **127**, 425–465.

Madabhushi, G. (2014), *Centrifuge modelling for civil engineers*, CRC Press.

Maiti, R., Das, G. and Das, P. K. (2016), 'Experiments on eccentric granular discharge from a quasi-two-dimensional silo', *Powder Technology* **301**, 1054–1066.

Marigo, M., Cairns, D. L., Davies, M., Ingram, A. and Stitt, E. H. (2011), 'Developing mechanistic understanding of granular behaviour in complex moving geometry using the Discrete Element Method: Part B: Investigation of flow and mixing in the Turbula® mixer', *Powder technology* **212**(1), 17–24.

Marigo, M. and Stitt, E. H. (2015), 'Discrete Element Method (DEM) for Industrial Applications: Comments on Calibration and Validation for the Modelling of Cylindrical Pellets', *KONA Powder and Particle Journal* **32**(0), 236–252.

Markauskas, D., Kačianauskas, R., Džiugys, A. and Navakas, R. (2009), 'Investigation of adequacy of multi-sphere approximation of elliptical particles for DEM simulations', *Granular Matter* **12**(1), 107–123.

Masson, S. and Martinez, J. (2000), 'Effect of particle mechanical properties on silo flow and stresses from distinct element simulations', *Powder Technology* **109**(1), 164–178.

Mathews, J. C. and Wu, W. (2016), 'Model tests of silo discharge in a geotechnical centrifuge', *Powder Technology* **293**, 3–14.

Matuttis, H.-G. and Chen, J. (2014), *Understanding the discrete element method: simulation of non-spherical particles for granular and multi-body systems*, John Wiley & Sons.

McGlinchey, D. (2008), *Bulk solids handling*, Wiley-Blackwell.

Mindlin, R. D. and Deresiewicz, H. (1953), 'Elastic Spheres in Contact Under Varying Oblique Forces', *J. Appl. Mech.* **327**, 327–344.

Mohamed, A. and Gutierrez, M. (2010), 'Comprehensive study of the effects of rolling resistance on the stress–strain and strain localization behavior of granular materials', *Granular Matter* **12**(5), 527–541.

Molerus, O. and Schöneborn, P. R. (1977), 'Bunker design based on experiments in a bunker-centrifuge', *Powder Technology* **16**(2), 265–272.

Moreno-Atanasio, R., Antony, S. J. and Ghadiri, M. (2005), 'Analysis of flowability of cohesive powders using Distinct Element Method', *Powder Technology* **158**(1-3), 51–57.

Morrissey, J. P. (2013), 'Discrete element modelling of iron ore pellets to include the effects of moisture and fines, PhD thesis, University of Edinburgh'.

Nedderman, R. M. (1992), *Static and kinematics of granular materials*, Cambridge University Press.

Nedderman, R. M. and Laohakul, C. (1980), 'The thickness of the shear zone of flowing granular materials', *Powder Technology* **25**(1), 91–100.

Nedderman, R. M., Tüzün, U., Savage, S. B. and Houlsby, G. T. (1982), 'The flow of granular materials—I: Discharge rates from hoppers', *Chemical Engineering Science* **37**(11), 1597–1609.

Niedostatkiewicz, M., Tejchman, J., Chaniecki, Z. and Grudzień, K. (2009), 'Determination of bulk solid concentration changes during granular flow in a model silo with ECT sensors', *Chemical Engineering Science* **64**(1), 20–30.

Niedostatkiewicz, M., Tejchman, J., Grudzień, K. and Chaniecki, Z. (2010), 'Application of ECT to solid concentration measurements during granular flow in a rectangular model silo', *Chemical Engineering Research and Design* **88**(8), 1037–1048.

Nielsen, J. and Askegaard, V. (1977), 'Scale errors in model tests on granular media with special reference to silo models', *Powder technology* **16**(1), 123–130.

Oda, M. and Kazama, H. (1998), 'Microstructure of shear bands and its relation to the mechanisms of dilatancy and failure of dense granular soils', *Géotechnique* **48**(4), 465–481.

Oda, M., Konishi, J. and Nemat-Nasser, S. (1982), 'Experimental micromechanical evaluation of strength of granular materials: effects of particle rolling', *Mechanics of materials* **1**(4), 269–283.

Ooi, J. Y. and Rotter, J. M. (1990), 'Wall pressures in squat steel silos from simple finite element analysis', *Computers & Structures* **37**(4), 361–374.

Ooi, J. Y. and Rotter, J. M. (1991), 'Elastic predictions of pressures in conical silo hoppers', *Engineering Structures* **13**(1), 2–12.

Ostendorf, M. and Schwedes, J. (2005), 'Application of particle image velocimetry for velocity measurements during silo discharge', *Powder Technology* **158**(1-3), 69–75.

O'Sullivan, C. (2011), 'Particle-based discrete element modeling: geomechanics perspective', *International Journal of Geomechanics* **11**(6), 449–464.

Pereira, G. G. and Cleary, P. W. (2017), 'Segregation due to particle shape of a granular mixture in a slowly rotating tumbler', *Granular Matter* **19**(2).

Podlozhnyuk, A., Pirker, S. and Kloss, C. (2017), 'Efficient implementation of superquadric particles in Discrete Element Method within an open-source framework', *Computational Particle Mechanics* **4**(1), 101–118.

Popescu, R. and Prevost, J. H. (1993), 'Centrifuge validation of a numerical model for dynamic soil liquefaction', *Soil Dynamics and Earthquake Engineering* **12**(2), 73–90.

Porbaha, A. and Goodings, D. J. (1996), 'Centrifuge modeling of geotextile-reinforced cohesive soil retaining walls', *Journal of Geotechnical Engineering* **122**(10), 840–848.

Pournin, L., Weber, M., Tsukahara, M., Ferrez, J.-A., Ramaioli, M. and Liebling, T. M. (2005), 'Three-dimensional distinct element simulation of spherocylinder crystallization', *Granular Matter* **7**(2-3), 119–126.

Powrie, W. and Daly, M. P. (2007), 'Centrifuge modelling of embedded retaining walls with stabilising bases', *Geotechnique* **57**(6), 485–497.

Rankine, W. J. M. (1857), 'On the Stability of Loose Earth', *Philosophical Transactions of the Royal Society of London* **147**(84), 9–27.

Ravenet, J. (1981), 'Silo problems', *Bulk Solids Handling* **1**(4), 667–679.

Rotter, J. M. (2008), '3 Silo and hopper design for strength', *Bulk Solids Handling* p. 99.

Sakaguchi, H., Ozaki, E. and Igarashi, T. (1993), 'Plugging of the flow of granular materials during the discharge from a silo', *International Journal of Modern Physics B* **7**(09n10), 1949–1963.

Sanad, A. M., Ooi, J. Y., Holst, J. and Rotter, J. M. (2001), 'Computations of granular flow and pressures in a flat-bottomed silo', *Journal of engineering mechanics* **127**(10), 1033–1043.

Schulze, D. (2008), 'Discussion of testers and test procedures', *Powders and Bulk Solids: Behavior, Characterization, Storage and Flow* pp. 163–198.

Schwedes, J. (1975), 'Shearing behaviour of slightly compressed cohesive granular materials', *Powder Technology* **11**(1), 59–67.

Shamsi, M. M. M. and Mirghasemi, A. A. (2012), 'Numerical simulation of 3D semi-real-shaped granular particle assembly', *Powder technology* **221**, 431–446.

Shen, H. H. (2013), Rolling resistance effect for sheared granular materials in the inertial regime, *in* 'AIP Conference Proceedings', Vol. 1542, AIP, pp. 827–830.

Singh, D. N. and Kuriyan, S. J. (2002), 'Estimation of hydraulic conductivity of unsaturated soils using a geotechnical centrifuge', *Canadian Geotechnical Journal* **39**(3), 684–694.

Slominski, C., Niedostatkiewicz, M. and Tejchman, J. (2007), 'Application of particle image velocimetry (PIV) for deformation measurement during granular silo flow', *Powder Technology* **173**(1), 1–18.

Soltanbeigi, B., Altunbas, A. and Cinicioglu, O. (2019), 'Influence of dilatancy on shear band characteristics of granular backfills', *European Journal of Environmental and Civil Engineering* pp. 1–18.

Soltanbeigi, B., Podlozhnyuk, A., Ooi, J. Y., Kloss, C. and Papanicolopulos, S.-A. (2017), 'Comparison of multi-sphere and superquadric particle representation for modelling shearing and flow characteristics of granular assemblies', *EPJ Web of Conferences* **140**, 06015.

Soltanbeigi, B., Podlozhnyuk, A., Papanicolopulos, S.-A., Kloss, C., Pirker, S. and Ooi, J. Y. (2018), 'DEM study of mechanical characteristics of multi-spherical and superquadric particles at micro and macro scales', *Powder Technology* **329**, 288–303.

Sonnenberg, R., Bransby, M. F., Hallett, P. D., Bengough, A. G., Mickovski, S. B. and Davies, M. C. R. (2010), 'Centrifuge modelling of soil slopes reinforced with vegetation', *Canadian Geotechnical Journal* **47**(12), 1415–1430.

Stanier, S., Blaber, J., Take, W. and White, D. (2016), 'Improved image-based deformation measurement for geotechnical applications', *Canadian Geotechnical Journal* **53**(5), 727–739.

StanleyWood, N. (2008), Bulk powder properties: instrumentation and techniques, *in* 'Bulk Solids Handling: Equipment Selection and Operation', Wiley Online Library, pp. 1–67.

Sukumaran, B. and Ashmawy, A. K. (2003), 'Influence of inherent particle characteristics on hopper flow rate', *Powder Technology* **138**(1), 46–50.

Taghizadeh, K., Kumar, N., Magnanimo, V. and Luding, S. (2015), Understanding the effects of inter-particle contact friction on the elastic moduli of granular materials, *in* 'IOP Conference Series: Earth and Environmental Science', Vol. 26, IOP Publishing, p. 12008.

Tao, H., Jin, B., Zhong, W., Wang, X., Ren, B., Zhang, Y. and Xiao, R. (2010), 'Discrete element method modeling of non-spherical granular flow in rectangular hopper', *Chemical Engineering and Processing: Process Intensification* **49**(2), 151–158.

Tejchman, J. (2008), *Shear localization in granular bodies with micro-polar hypoplasticity*, Springer Science & Business Media.

Tejchman, J. (2013), *Confined granular flow in silos: experimental and numerical investigations*, Springer Science & Business Media.

Tejchman, J., Bauer, E. and Tantono, S. F. (2007), 'Influence of initial density of cohesionless soil on evolution of passive earth pressure', *Acta Geotechnica* **2**, 53–63.

Tejchman, J. and Gudehus, G. (2000), 'Verspannung, Scherfugenbildung und Selbsterregung bei der Siloentleerung', *Silobauwerke und ihre spezifischen Beanspruchungen* pp. 243–287.

Tejchman, J. and Wu, W. (2009), 'FE-investigation of shear localization in granular bodies under high shear rate', *Granular Matter* **11**(2), 115–128.

Terzaghi, K. (1943), *Theoretical Soil Mechanics*, Chapman And Hall, Limited.; London.

Thakur, S. C., Ooi, J. Y. and Ahmadian, H. (2016), 'Scaling of discrete element model parameters for cohesionless and cohesive solid', *Powder Technology* **293**, 130–137.

Thielicke, W. (2014), The flapping flight of birds: Analysis and application, Doctor of philosophy, University of Groningen.

Thielicke, W. and Stamhuis, E. J. (2014), 'PIVlab – Towards User-friendly, Affordable and Accurate Digital Particle Image Velocimetry in MATLAB', *Journal of Open Research Software* **2**(1).

Torricelli, E. (1644), *Opera geometrica*, Masse & de Landis.

Toyosawa, Y., Itoh, K. and Tamrakar, S. B. (2006), 'Redistribution of active earth pressures using movable earth support apparatus in centrifuge', (4), 1113–1118.

Vidyapati, V. and Subramaniam, S. (2013), 'Granular flow in silo discharge: discrete element method simulations and model assessment', *Industrial & Engineering Chemistry Research* **52**(36), 13171–13182.

Wang, J., Yu, H. S., Langston, P. and Fraige, F. (2011), 'Particle shape effects in discrete element modelling of cohesive angular particles', *Granular Matter* **13**(1), 1–12.
URL: *http://link.springer.com/10.1007/s10035-010-0217-4*

Wang, L., Li, R., Wu, B., Wu, Z. and Ding, Z. (2017), 'Determination of the coefficient of rolling friction of an irregularly shaped maize particle group using physical experiment and simulations', *Particuology* .

Wang, Y., Lu, Y. and Ooi, J. Y. (2014), 'Finite element modelling of wall pressures in a cylindrical silo with conical hopper using an Arbitrary Lagrangian-Eulerian formulation', *Powder Technology* **257**, 181–190.

Wang, Y., Lu, Y. and Ooi, J. Y. (2015), 'A numerical study of wall pressure and granular flow in a flat-bottomed silo', *Powder Technology* **282**, 43–54.

Weinhart, T., Labra, C., Luding, S. and Ooi, J. Y. (2016), 'Influence of coarse-graining parameters on the analysis of DEM simulations of silo flow', *Powder technology* **293**, 138–148.

Wensrich, C. and Katterfeld, A. (2012), 'Rolling friction as a technique for modelling particle shape in DEM', *Powder Technology* **217**, 409–417.

White, D., Take, W. and Bolton, M. (2003), 'Soil deformation measurement using particle image velocimetry (PIV) and photogrammetry', *Geothechnique* **53**(7), 619–631.

Williams, J. C. (1977), 'The rate of discharge of coarse granular materials from conical mass flow hoppers', *Chemical Engineering Science* **32**(3), 247–255.

Williams, J. R. and Pentland, A. P. (1992), 'Superquadratics and Modal Dynamics for Discrete Elements in Interactive Design', *Engineering Computations* **9**(2), 115–127.

Wójcik, M., Tejchman, J. and Enstad, G. G. (2012), 'Confined granular flow in silos with inserts—Full-scale experiments', *Powder technology* **222**, 15–36.

Wood, D. M. (1991), *Soil Behaviour and Critical State Soil Mechanics*, Cambridge university press.

Yan, Z., Wilkinson, S. K., Stitt, E. H. and Marigo, M. (2015), 'Discrete element modelling (DEM) input parameters: understanding their impact on model predictions using statistical analysis', *Computational Particle Mechanics* **2**(3), 283–299.

Yang, Y., Ooi, J. Y., Rotter, M. and Wang, Y. (2011), 'Numerical analysis of silo behavior using non-coaxial models', *Chemical engineering science* **66**(8), 1715–1727.

You, Y. and Zhao, Y. (2018), 'Discrete element modelling of ellipsoidal particles using super-ellipsoids and multi-spheres: A comparative study', *Powder Technology* **331**, 179–191.

Yu, Y. and Saxén, H. (2014), 'Segregation behavior of particles in a top hopper of a blast furnace', *Powder Technology* **262**, 233–241.

Zafar, U., Hare, C., Calvert, G., Ghadiri, M., Girimonte, R., Formisani, B., Quintanilla, M. A. S. and Valverde, J. M. (2015), 'Comparison of cohesive powder flowability measured by Schulze shear cell, raining bed method, Sevilla powder tester and new ball indentation method', *Powder Technology* **286**, 807–816.

Zafar, U., Hare, C., Hassanpour, A. and Ghadiri, M. (2017), 'Ball indentation on powder beds for assessing powder flowability: Analysis of operation window', *Powder Technology* **310**, 300–306.

Zhang, K. F. and Ooi, J. Y. (1998), 'A kinematic model for solids flow in flat-bottomed silos', *Geotechnique* **48**(4), 545–553.

Zhang, L. and Thornton, C. (2007), 'A numerical examination of the direct shear test', *Geotechnique* **57**(4), 343–354.

Zhao, J. and Guo, N. (2014), 'Rotational resistance and shear-induced anisotropy in granular media', *Acta Mechanica Solida Sinica* **27**(1), 1–14.

Zhao, S., Zhou, X. and Liu, W. (2015), 'Discrete element simulations of direct shear tests with particle angularity effect', *Granular Matter* **17**(6), 793–806.

Zhong, W., Yu, A., Liu, X., Tong, Z. and Zhang, H. (2016), 'DEM/CFD-DEM Modelling of Non-spherical Particulate Systems: Theoretical Developments and Applications', *Powder Technology* **302**, 108–152.

Zhou, B., Huang, R., Wang, H. and Wang, J. (2013), 'DEM investigation of particle anti-rotation effects on the micromechanical response of granular materials', *Granular Matter* **15**(3), 315–326.

Zhou, C. (2011), 'PhD thesis:Investigation of micro- and macro-phenomena in densely packed granular media using the discrete element method , PhD thesis, University of Edinburgh'.

Zhou, C. and Ooi, J. Y. (2009), 'Numerical investigation of progressive development of granular pile with spherical and non-spherical particles', *Mechanics of Materials* **41**(6), 707–714.

Zhou, Y. C., Wright, B. D., Yang, R. Y., Xu, B. H. and Yu, A. B. (1999), 'Rolling friction in the dynamic simulation of sandpile formation', *Physica A: Statistical Mechanics and its Applications* **269**(2), 536–553.

Zuriguel, I., Garcimartín, A., Maza, D., Pugnaloni, L. A. and Pastor, J. M. (2005), 'Jamming during the discharge of granular matter from a silo', *Physical Review E* **71**(5), 51303.